Investigation of Seismic Failure Modes in Flexural Concrete Walls Using Finite Element Analysis

Zachary J. Whitman

A thesis submitted in partial fulfillment
of the requirements for the degree of

Master of Science in Civil Engineering

University of Washington

2015

Committee:
Laura N. Lowes
Dawn E. Lehman
Michael R. Motley

Program Authorized to Offer Degree
Civil & Environmental Engineering

University of Washington

ABSTRACT

Investigation of Seismic Failure Modes in Flexural Concrete Walls Using Finite Element Analysis

Zachary J. Whitman

Co-Chairs of the Supervisory Committee:

Professor Laura Lowes

Professor Dawn Lehman

Civil & Environmental Engineering

Reinforced concrete structural walls are a common seismic lateral force resisting system in concrete buildings. They possess high strength and stiffness, which are desirable in resisting low-to-moderate seismic demands. When subjected to larger seismic demands, walls are assumed to develop a flexural response mechanism controlled by tensile failure of the longitudinal reinforcement. However, in recent earthquakes (2010 Chile, 2011 New Zealand) compression failures have been observed in the boundary elements at the ends of the wall, in the interior web region of the wall, or both. These failure modes have been observed in experimental tests as well.

In lab settings, the size of the wall specimen and the magnitude of the applied loads (vertical and lateral loads) are limited by the capacity of the laboratory equipment. This study utilized nonlinear high-resolution finite element modeling to enable investigation of the influence of a wide range of design parameters on the behavior of planar walls, including failure mechanisms. The finite element model was developed and calibrated using data from multiple laboratory tests of walls.

The calibrated model was used to conduct an extensive parameter study. The results of this study were used to develop new shear stress limits and boundary element length requirements to prevent walls from developing non-ductile failure modes.

TABLE OF CONTENTS

LIST OF FIGURES

LIST OF TABLES

LIST OF SYMBOLS

ACI BE: classification of boundary element confinement per ACI 318-14 (i.e., NBE (non-compliant BE), OBE (ordinary boundary element), SBE (special boundary element))

ALR: axial load ratio (%), where the applied axial load is normalized by $A_g f'_c$

$A_{s,sm}$: area of smeared reinforcement crossing the concrete surface

$A_{c,proj}$: concrete surface on which reinforcement is smeared

c_{ATENA}: location of the neutral axis from the extreme compressive fiber in ATENA simulation

COV: coefficient of variation

c_{PSRP}: location of the neutral axis from the extreme compressive fiber in a PSRP analysis

CSAR: cross-sectional aspect ratio, l_w/t_w

C_{ts}: residual concrete tensile stress divided by peak concrete tensile stress (tension stiffening)

d_b: diameter of longitudinal reinforcement for wall end region

$E_{c,f}$: elastic modulus of elastic foundation material

E_c: concrete elastic modulus

E_h: steel hardening ratio

E_s: elastic modulus of reinforcing steel

$E_{s,BE}$: elastic modulus of longitudinal boundary element reinforcing steel

$E_{s,v}$: elastic modulus of longitudinal web reinforcing steel

Eps zz: vertical strain

f'_c: concrete compressive strength

f'_{c0}: concrete compressive strength at zero plastic deformation

FM: failure mode, including Bar Rupture (BR), Compression-Buckling (CB), Compression-Shear (CS)

f'_t, $f_t^{'ef}$: concrete tensile strength

f_u; steel ultimate strength

f_y: steel yield strength

$f_{y,BE}$: yield strength of longitudinal boundary element reinforcing steel

$f_{y,v}$: yield strength of longitudinal web reinforcing steel

$f_{u,BE}$: ultimate strength of longitudinal boundary element reinforcing steel

$f_{u,v}$: ultimate strength of longitudinal web reinforcing steel

Gamma yz: in-plane shear strain

G_f: concrete fracture energy

G^P: plastic potential function

h: specimen height

h_{eff}: effective wall height, defined as the constant ratio between the base moment and base shear

h_x: horizontal spacing of vertical reinforcement for wall end region

I_1: first invariant of stress tensor

J_2: second invariant of deviatoric stress tensor

K_s: shear stiffness parallel to the crack surface

K_t: tensile stiffness normal to the crack surface

l_{be}: length of boundary element region

L_c: characteristic length of finite element mesh in compression

L_d: characteristic length of finite element mesh

l_w: length of wall in direction parallel to web region

L_t: characteristic length of finite element mesh in tension

M_b: base moment resisted by the wall

NC2: ATENA concrete constitutive model “NonLinearCementitious2”

M_n: nominal moment strength for the base section, defined by the extreme compression fiber strain in the boundary element core reaching a strain value of -0.003 in/in

PSRP: plane sections remain plane

s_1, s_2, and s_3: principal values of the deviatoric stress tensor

S_F: shear retention parameter

Shear Span: $M_b/V_b l_w$ (h_{eff}/l_w)

Sigma zz: vertical stress

Sigma yz: in-plane shear stress

s_{vert}: longitudinal spacing of confining reinforcement for wall end region.

TS: c_{ts} expressed as a percentage (tension stiffening)

t_f: foundation thickness

t_w: wall thickness

V_b: base shear resisted by the wall

V_{max}: peak base shear

V_n: nominal shear strength of the wall per ACI 318-14

V_y: base shear the point of system yield as defined by yield on the longitudinal reinforcement in the ATENA model

$w_{d:}$ concrete plastic deformation at zero compressive stress

w_t, w_{tc} : length of concrete crack opening

α_{BE}; parameter that defines required length of confined region for prevention of CS failure (Chapter 6)

β: concrete dilation parameter

$\Delta_{j:}$ maximum story drift demand for specimen j in fragility curve calculation

Δ_{shear}: shear deformation at a height $l_w/2$ (hinge length) from the wall base.

Δ_{story}: story drift, drift recorded one story height above the specimen base

Δ_u: specimen drift capacity, defined as the drift at which the lateral load-carrying capacity of the wall drops to 80% of the historic maximum

Δ_y: specimen drift at section yield as defined by PSRP analysis

ε_c^P: strain at peak concrete compressive strength

ε_{eq}^P: equivalent plastic strain

ε^f: concrete fracturing strain

ε_{pl}: plastic strain limit of concrete

ε_t; tensile strain in the longitudinal boundary element reinforcement at point of experimental wall failure

$\varepsilon_{t,ATENA}$: extreme tensile strain observed at M_n in the ATENA simulation

$\varepsilon_{t,PSRP}$: extreme tensile strain observed at M_n in PSRP analysis

ε_u : steel fracture strain

$\varepsilon_{u,BE}$: fracture strain of the boundary element reinforcement

$\varepsilon_{u,v}$: rupture strain of longitudinal web reinforcing steel

ε_y: steel yield strain

ρ_{gross}: total gross longitudinal reinforcement ratio

ρ_{sm}: smeared reinforcement ratio

$\rho_{t,web}$: transverse reinforcement ratio for wall web

$\rho_{vert,BE}$: longitudinal reinforcement ratio for wall end region

$\rho_{vert,web}$: longitudinal reinforcement ratio for wall web

ρ_{vol}: volumetric reinforcement ratio for wall end region

σ_{ij}^{t}: elastic predictor

σ_{ij}^{n}: stress state at step n

σ_{ij}^{n-1}: stress state at step n-1

σ_1, σ_2, and σ_3: principal values of the stress tensor

θ_{hinge}: hinge rotation at failure, where the hinge length is assumed to be $l_w/2$

θ_j: maximum hinge rotation demand for specimen j in fragility curve calculation

μ and σ: parameters used to define fragility curves, defined such that the sample mean equals $e^{\mu+\frac{\sigma^2}{2}}$ and sample median equals e^{μ}

ACKNOWLEDGEMENTS

The funding for this research was provided by the National Institute for Standards and Technology.

I would like to express gratitude to my advisors Professors Laura Lowes and Dawn Lehman for their help, guidance, and advice over the last two years. Thanks to Professor Mike Motley for serving on my committee and providing helpful comments that improved this thesis. I'm also thankful for the instruction of Professors John Stanton, Pedro Arduino, and Marc Eberhard, all of whom taught excellent courses in concrete and modeling and greatly improved my understanding in these areas.

I've received wonderful help from a number of mentors and peers over my time at the University of Washington. I'm thankful for the constant mentorship of Tim and Samantha, who provided excellent advice and free lunches in equal measure. Morgan Knighton has been a great friend and calming influence through my collegiate experience. As someone who processes information verbally, I should also thank my graduate officemates: Kevin Martin, Ryan Ballard, Ryan Ganey, Nasser Marafi, and Kamal Ahmed. Thank you for (mostly voluntarily) helping me process through the different issues encountered in research.

None of this would be possible if not for my wonderful family. My parents established the importance and value of education in my life, teaching me the importance of setting goals at a young age; their expectations have always been high, but those expectations have always managed to provide encouragement rather than act as a burden. I'm proud to have parents who are unfailing in their support, encouragement, and love. I'm also blessed to have siblings that genuinely care and want the best for me; Thank you to Cameron, Matthew, and Gabrielle for being so thoroughly and consistently supportive.

1 INTRODUCTION

Reinforced concrete structural walls are a common seismic lateral force resisting system. They possess high strength and stiffness, which are desirable in resisting low-to-moderate seismic demands. When subjected to larger seismic demands, walls are assumed to act in a flexural mode dominated by tensile failure of the longitudinal reinforcement. However, in recent earthquakes (e.g., 2010 Chile, 2011 New Zealand), compression failures have been observed in the boundary element and/or web of walls. Experimental studies support the potential for compression failures in walls (e.g., Birely 2012).

In lab settings, the size of the wall specimen and applied loads (vertical and lateral loads) are limited; this limits the range of design parameters that can be investigated. Additionally, previous experimental tests have typically employed specimens with configurations and design details that are not representative of walls constructed in actual buildings. Thus, to improve understanding of the flexural response of walls and the design parameters that determine flexural failure modes and deformation capacity, a numerical study was undertaken. The study investigated the impact on wall response of design parameters found previously (e.g., Birely 2012) to correlate with flexural failure mode and/or deformation capacity: cross-sectional aspect ratio (CSAR), shear stress demand, and axial load ratio. The study employed nonlinear three-dimensional continuum-type finite element analysis and the commercial software program ATENA (http://cervenka.cz). Initially, the finite element model was developed and calibrated using a database of planar experimental wall specimens. The database covered a range of flexural failure modes, including tensile fracture of the longitudinal reinforcement and compressive failure to the boundary element, web or both. This validated model was then used to conduct an extensive parameter study. The results provide new recommendations for shear stress limits and boundary element lengths to increase the deformation capacity of walls.

The primary objectives of the research presented in this thesis are:

1. To develop a nonlinear three-dimensional finite element (FE) model capable of predicting the stiffness, strength, deformation capacity, and failure mode of wall test specimens that yield in flexure prior to failure.
2. To use this model to determine the influence of untested parameters on walls expected to respond primarily in flexure, including cross-sectionally slender walls, walls with high shear stress demand and walls with high axial load ratios.
3. To provide design recommendations that inhibit undesirable failure modes and maximize the deformation capacity of walls.

1.1 THESIS ORGANIZATION

This research is phased into three primary categories: model development and validation, parameter study, and development of design recommendations for flexural concrete walls.

Chapter 2 motivates the development of a FE wall model by reviewing the response of flexural walls observed in the laboratory and field. The capabilities of previously developed wall models are reviewed, a limited study is undertaken to investigate the capabilities of the ATENA and Abaqus software, and the ATENA software is identified as the preferred FE software for this research effort.

Development and validation of the FE model is presented in Chapter 3. An experimental data set for use in model calibration and validation is presented; this includes details of the geometry, reinforcement, loading, and measured response quantities for each specimen. This is followed by a broad discussion of the key characteristics of the ATENA model, including the constitutive material models, basic model layout, reinforcement configuration, loading protocol, and mesh scheme. This leads into a calibration of the reinforcement configuration and a number of concrete material parameters. The most crucial of the concrete material parameters is the plastic deformation; this value controls the deformation capacity exhibited by the concrete model, a behavior that is critical to correctly predicting compression failures that exhibit a softening response. A method is then defined to determine the failure mode of simulations conducted in ATENA, with two failure modes considered: compression-buckling (CB) and bar rupture (BR). With a calibrated model and defined method of determining failure mode, the model is evaluated on the ability to accurately predict the results of specimens from the experimental data set introduced earlier in the chapter.

Chapter 4 presents the results of FE analyses, using the model presented in Chapter 3, to investigate wall behavior and failure modes. To facilitate the investigation, five reference walls are selected from the larger dataset presented in Chapter 3; these reference walls represent a range of salient design parameters including axial load ratio, maximum shear stress, shear span, and cross-sectional aspect ratio as well as exhibit all identified flexural failure modes. Both the global (e.g., load-displacement response, prediction error of stiffness, strength, and deformation capacity) and local results (e.g., contour stress and strain plots) are investigated. It is observed that difference failure modes are associated with different stress and strain fields and that variation in salient design parameters, particularly normalized shear stress demand and CSAR, results in significant variation in the stress and strain fields. The results of this investigation is the identification of a third failure mode, described as a compression-shear failure, in which diagonal shear stress impacts the likelihood and premature compression failure of the wall cross section.

Chapter 5 uses the validated numerical modeling approach to conduct a parameter study that investigates and quantifies the influence of shear stress demand, axial load ratio, and CSAR on development of a particular failure mode and drift capacity. The results provide further understanding of the shear-influenced compression failure identified in Chapter 4, with the shear stress demand and cross-sectional aspect ratio of a wall identified as the two parameters that lead to reduced deformation capacity for flexural walls.

Chapter 6 investigates design to prevent compression-shear failure in flexural walls. The parameter study from Chapter 5 is extended to investigate the impact of boundary element length (i.e., length along the wall cross section that is provided with confining reinforcement) on both deformation capacity and observed failure mode. The results of this study are compared with the minimum boundary element length specified in ACI 318-14. The chapter concludes by providing design recommendations for prevention of compression-shear failure at high shear demands.

Chapter 7 summarizes all research presented in the thesis, outlines the key conclusions reached in analysis, and makes recommendations for future work to advance understanding of and design procedures for flexural concrete walls.

2 WALL BEHAVIOR AND ANALYSIS

This chapter presents the motivation for the research project and for the use of the ATENA software package to simulate the nonlinear response of slender walls. The results of previous experimental investigations of concrete walls and of post-earthquake investigations of damaged and undamaged concrete wall buildings are reviewed to demonstrate the need for research to improve understanding of wall behavior and failure mechanisms. Analysis methods and software used in previous research studies are then reviewed and evaluated with respect to the current study objective of understanding the impact of various design parameters on failure mechanism and ductility. Two software programs, Abaqus and ATENA are identified as potentially being appropriate for use on the study. These two programs are evaluated, and the results of this evaluation are presented.

2.1 MOTIVATION FOR DEVELOPMENT OF WALL MODEL

The purpose of this section is to determine the key parameters of interest in this research. Past observations from the laboratory and field are examined to identify key parameters in wall deformation capacity and failure mode.

2.1.1 Birely Study

Birely et al. (2011) conducted an extensive study of experimental wall specimens and investigated the relationship between wall behavior and several key parameters. Several of these parameters correlated to wall deformation capacity and/or failure mode. These included:

- Axial load ratio ($P/A_g f'_c$), where P is the axial load, A_g is the gross area of the section, and f'_c is the compressive stress of the concrete.
- Shear demand ($V_{max}/A_{cv} f'_c{}^{0.5}$), where V_{max} is the maximum base shear resisted by the wall and A_{cv} is the effective shear area of the section (equal to the gross area for planar walls).
- Shear span ($M_b/V_b l_w$), where M_b is the base moment, V_b is the base shear, and l_w is the wall length.
- Cross-sectional aspect ratio (l_w/t_w), where t_w is the wall thickness.
- Boundary element configuration (l_{be}/t_w), where l_{be} is the boundary element length.
- Confining boundary element reinforcement ($\rho_{vol}\sqrt{l_{be}/s_{vert}}$), where ρ_{vol} is the volumetric confining reinforcement ratio and s_{vert} is the vertical spacing of confining reinforcement.

Birely summarized this research with two key findings:

1. *Drift capacity is inversely proportional to shear stress demand and shear demand-capacity ratio.*
2. *The presence of axial load increases the rate at which drift capacity diminishes with increasing axial demand.*

The basis for the first result is shown in Figure 2.1, in which there exists a clear relationship between the shear stress demand and deformation capacity of the walls. Note that Birely considers two failure modes in this specific analysis: Flexure-Fracture and Flexure-Compression. These walls are expected to respond primarily in flexure, with failure occurring due to either fracture in the tensile reinforcement or concrete crushing in the boundary element core.

The main points drawn are that (1) there is a significant influence of shear on wall behavior and (2) axial load plays a secondary role in response, diminishing wall deformation capacity (Figure 2.2). The influence of shear in wall response necessitates the development of a model that does not decouple shear response and flexural response. Prior models developed, such as those discussed in Section 2.2, have simplified analysis by assuming that shear response and flexural response in walls can be assumed to act separately.

While the key findings related to axial load ratio and shear demand, the other parameters defined above also correlated with drift capacity:

- Shear span: Drift capacity increased with increased shear span. This can be interpreted as taller walls having lower stiffness and thus achieving greater drift capacity; this phenomenon is captured in wall models developed previously. However, taller walls also have lesser shear demands than equivalent shorter walls, and the impact of shear demand on deformation capacity and failure mode is not captured by models that decouple flexural and shear response. This research will focus on the latter concern, studying how increased shear demands affect deformation capacity and failure mode.
- Wall Configuration: Both the cross-sectional aspect ratio (CSAR) and boundary element length correlated to wall deformation capacity. As shown in Figure 2.3, walls of high CSAR (i.e., cross-sectionally slender) exhibit less deformation capacity than those with a low CSAR (i.e., cross-sectionally stout). The high R^2 correlations ($R^2 = 0.76$ for flexural-compression failures) show the potential significance of this parameter, but available data is again limited. Both of these parameters will be investigated in this research.
- Confining Reinforcement: The impact of confining reinforcement detailing on wall response is investigated by Welt (2015) and will not be considered in the scope of this research.

The Birely study thus identifies three key parameters which are considered in this research: shear demand, axial load ratio, and wall configuration (both CSAR and boundary element geometry).

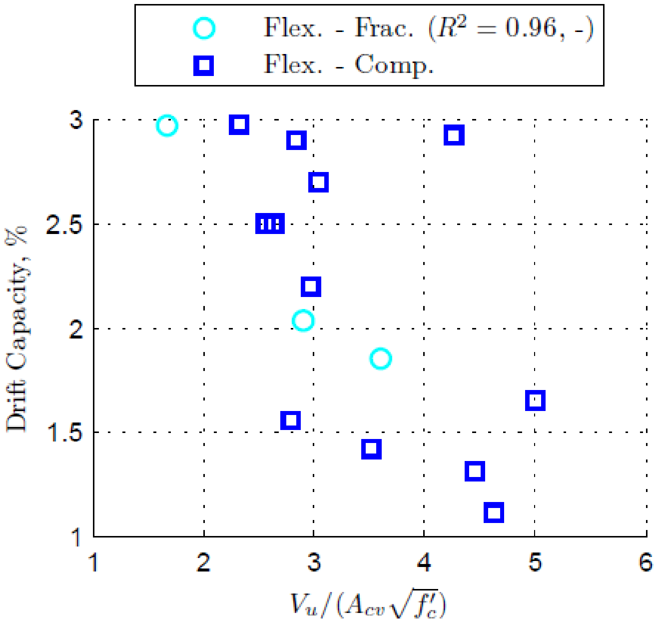

Figure 2.1 – Relationship between Drift and Peak Shear Stress (Birely et al. 2011)

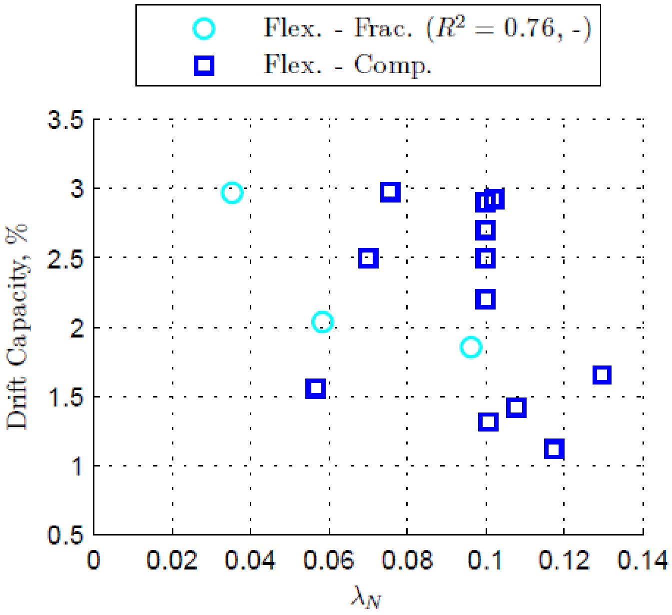

Figure 2.2 – Relationship between Drift and Axial Load Ratio (Birely et al. 2011)

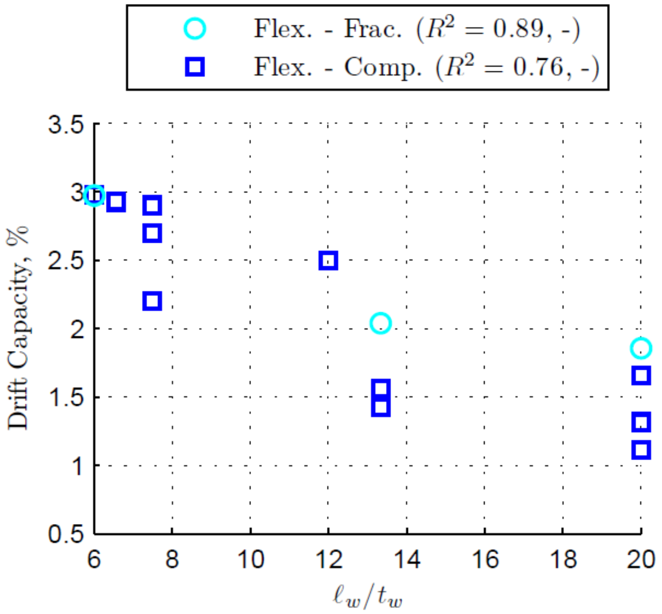

Figure 2.3 – Relationship between Drift and Cross-Sectional Aspect Ratio (Birely et al. 2011)

2.1.2 Wallace Study

The influence of shear on wall response was also studied by Wallace (2012), who noted that:

- Engineers have pushed limits in recent years, producing walls with higher shear demands and more slender profiles than have been verified in past testing or field experience.
- Observed damage in recent earthquakes exceeded expectations, with diagonal shear cracks and web damage apparent in walls after the 2010 Chile earthquake (Figure 2.5).

- Relatively thin wall boundaries failed to develop ductile behavior in compression, even if they complied with ACI 318 special boundary element requirements.

These findings are in line with those of Birely, with Wallace agreeing that (1) shear plays a role in the failure of flexural walls and (2) high-CSAR (“thin”) sections exhibit lower deformation capacities than are observed in low-CSAR sections. Also noted is the idea that experimentally-tested specimens do not reflect the structural walls currently being designed in practice, which are often designs to resist greater shear demands with a larger CSAR than is typical of laboratory designs.

2.1.3 Failure Modes for Flexural Walls

Compressive demands in the boundary element are the cause of most major damage that occurs in U.S. structural walls, but the damage observed after the 2010 Chile earthquake included large diagonal shear cracks and web crushing, as observed in Figure 2.4 (Birely 2012). This presents an issue of missing data; experimental tests have focused on specimens subjected to shear stresses less than $5\sqrt{f'c}$ psi ($0.42\sqrt{f'c}$ MPa), and these results show that failure mode is not a key factor in wall deformation capacity. However, tests of walls subjected to greater peak shear stresses must be conducted to fully understand the impact of shear and failure mode on deformation capacity. It is necessary to use a model to extend this analysis as there are limits on laboratory testing, with funding and equipment making it difficult to test specimens at high levels of shear demand.

Both Birely and Wallace discuss the idea that damage observed experimentally in flexural-compression failures does not match that which was exhibited in the Chile and New Zealand earthquakes. This necessitates the consideration of a third failure mode, a compression failure in which shear plays a significant role in the loss of load-carrying capacity. The research presented here will thus consider the possibility of three distinct failure modes:

- Bar Rupture (BR): Wall responds primarily in flexure and fails due to rupture of the longitudinal boundary element reinforcement.
- Compression-Buckling (CB): Wall responds primarily in flexure and fails due to concrete crushing the boundary element core.
- Compression-Shear (CS): Wall responds in both shear and flexure and fails due to concrete crushing in the web and/or boundary element core.

Figure 2.4 – Structural Wall Damage in 2010 Chile Earthquake (Moehle 2011)

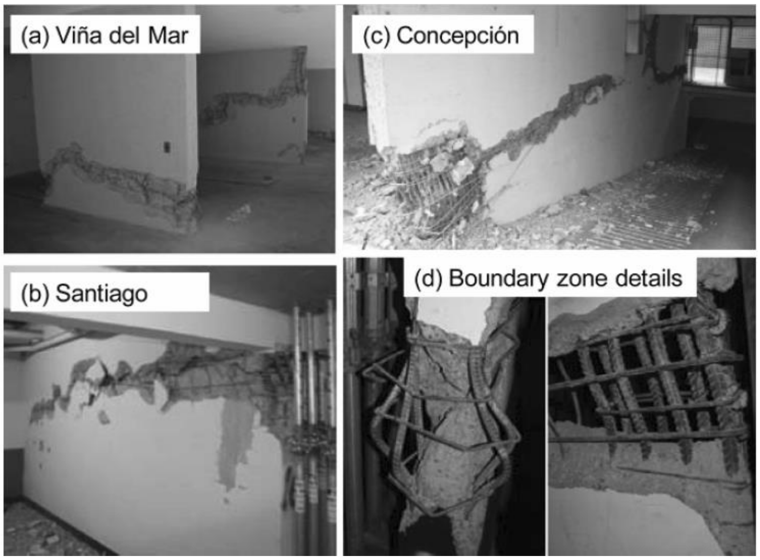

Figure 2.5 – Typical Wall Damage in Chile Earthquake (Wallace 2012)

2.2 PREVIOUS WALL ANALYSES

A review of previous research shows the need to investigate the impact on flexural wall response and failure of shear demand, axial load demand and cross-section configuration. As previously discussed, this is best done via numerical modeling. There are a number of existing numerical models that are appropriate for use in investigating wall response. Table identifies these models, provides one or more references in which they have been used to simulate wall response, and lists the strengths and weaknesses of each model with respect to the objective of the current study. With respect to the strengths and weaknesses of the models, it should be noted that many do not simulate flexure-shear interaction, which is required to investigate the impact of shear on flexural failure modes and deformation capacity.

Table 2.1 – Summary of Capabilities for Different Model Types

Model Type	Strengths	Weaknesses
Either Fiber-Hinge Model or Lumped-Plasticity Fiber-Type Beam-Column Element (Berry et al. 2008)	• Computationally efficient. • Provides accurate prediction of strength.	• Assumption that plane sections remain plane • Uses two-node line elements to model 3D geometry. • Cannot account for localization of failure. • Does not provide an accurate prediction of stiffness and deformation capacity.
Regularized Distributed-Plasticity Beam-Column Element w/ Fiber Section (Pugh 2012, Welt 2015)	• Computationally efficient. • Provides accurate prediction of strength, stiffness, and deformation capacity. • Can account for localization of failure.	• Plane sections remain plane • Uses two-node line elements to model 3D geometry.
Multi-Vertical Line Element (Orakcal and Wallace 2006)	• Computationally efficient. • Provides accurate prediction of strength and stiffness.	• Assumption that plane sections remain plane. • Uses two-node line elements to model 3D geometry. • Cannot account for localization of failure. • Does not provide an accurate prediction of deformation capacity.
2D Continuum Model using VecTor2 (Palermo and Vecchio 2007, Pugh 2012)	• Does not assume that plane sections remain plane. • Provides accurate prediction of strength • Uses 3D elements to model 3D geometry.	• Computationally expensive. • Cannot account for localization of failure. • Does not provide an accurate prediction of stiffness and deformation capacity.
Perform3D Fiber Shell Element (NIST 2013)	• Does not assume that plane sections remain plane • Provides accurate prediction of strength • Uses 2D shell elements to model 3D geometry.	• Computationally expensive. • Cannot account for localization of failure. • Does not provide an accurate prediction of stiffness and deformation capacity.

Model Type	Strengths	Weaknesses
3D Continuum Analysis	• Does not assume that plane sections remain plane. • Provides accurate prediction of stiffness, strength, deformation capacity, and failure mode. • Uses 3D elements to model 3D geometry. • Can account for localization of failure.	• Computationally expensive.

2.3 INVESTIGATION OF FE ANALYSIS IN ATENA AND ABAQUS

Given that finite element analysis using three-dimensional continuum-type elements is the only analysis method that meets the needs of the current study, two software packages that provide this capability and were readily available to the research team were investigated further. These software packages are ATENA and Abaqus.

- ATENA is a commercial nonlinear finite element analysis program specifically designed for the nonlinear analysis of reinforced concrete continua (http://www.cervenka.cz). It is published by Cervenka Consulting and includes the capability to model advanced topics such as shrinkage and temperature effects, post-tensioned cables, and several reinforcement bond models in addition to all basic concrete analysis features.

- Abaqus is a general, multi-purpose simulation program that can be used in a wide variety of finite element applications (http://3ds.com). The program includes several concrete models, an extensive element library, and excellent pre- and post-processing capability.

These two software programs were evaluated on the basis of their ability to effectively model confining reinforcement and provide concrete models that exhibit numerical stability in planar wall applications.

2.3.1 Confinement Study

Both models were evaluated with respect to the accuracy and robustness with which the impact of confinement on concrete response is simulated. A series of plain concrete rectangular prisms, confined by rectangular ties with no cover concrete provided were modeled. The basic ATENA model for a prism is shown in Figure 2.8. The full prism study is included as Appendix C in this document.

The prism study investigated the ability of the Abaqus and ATENA programs to simulate the impact on confined concrete strength and deformation capacity of

- Vertical spacing and bar area of confining reinforcement,
- Confining reinforcement ratio, and
- Smeared versus discrete reinforcement (ATENA only).

Representative results of the Abaqus and ATENA analyses are presented in Figure 2.6-Figure 2.7, respectively. The Abaqus prism analysis results showed that:

- The confining reinforcement had no impact on the concrete peak strength. Models run with significant confinement had no strength gain over those run with no confining reinforcement.
- Confining reinforcement had a significant impact on the deformation capacity of the concrete.

The ATENA prism analysis results showed that:

- The confining reinforcement was influential in both the concrete deformation capacity and peak strength.

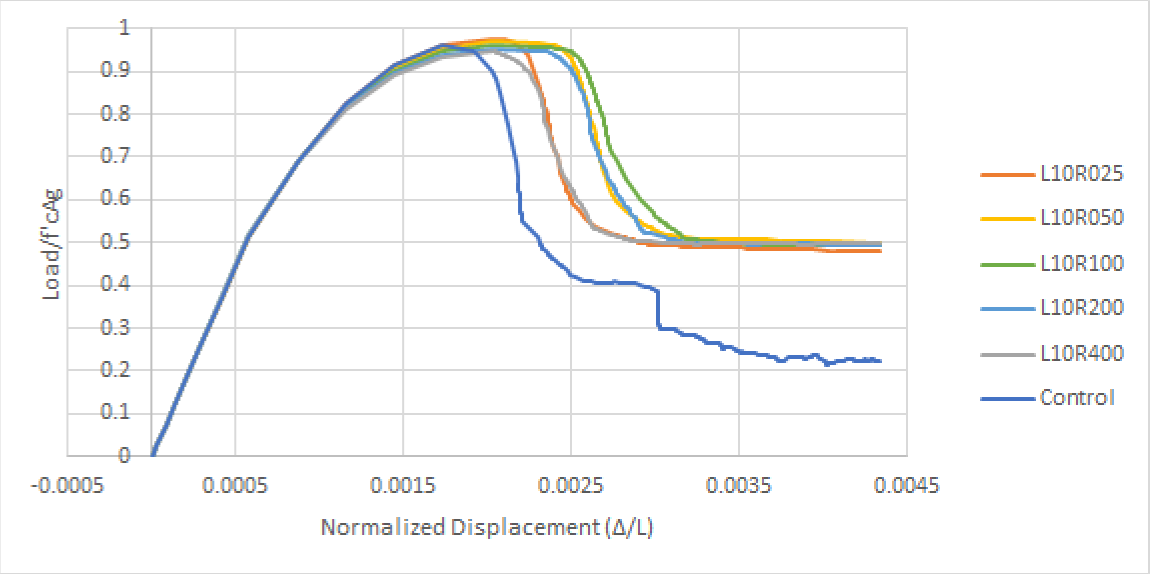

Figure 2.6 – Representive Abaqus Results of Prism Study (Load-displacement response for 3 in. (76.2 mm) tie spacing)

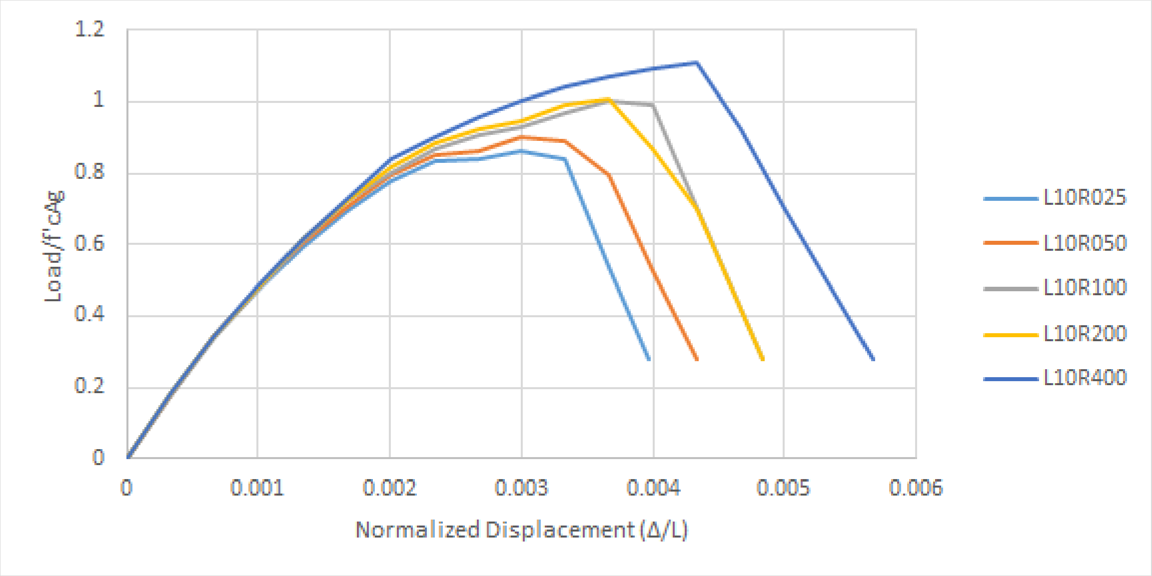

Figure 2.7 – Representive ATENA Results of Prism Study (Load-displacement response for 3 in. (76.2 mm) tie spacing)

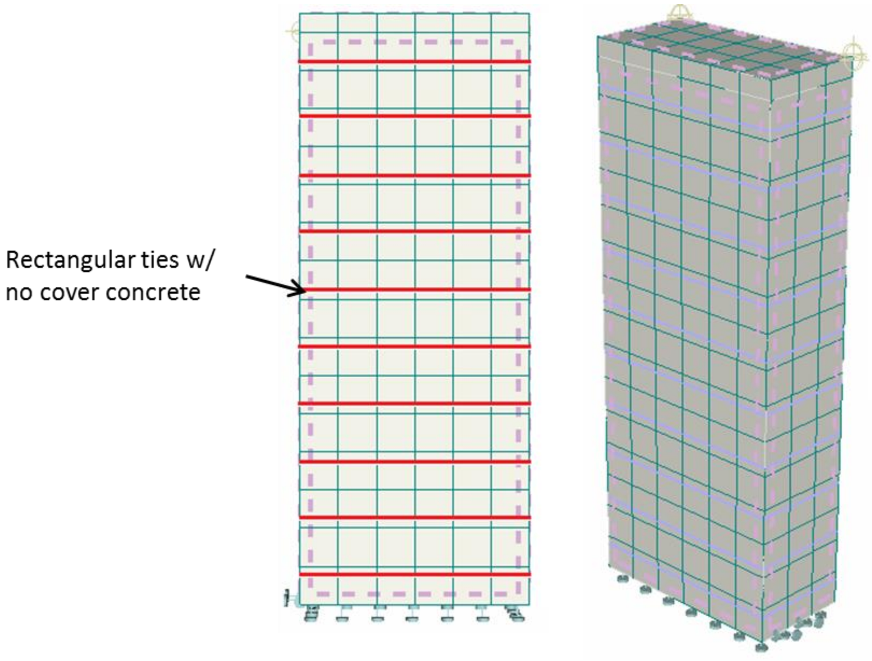

Figure 2.8 – Layout of Study Prism in ATENA

2.3.2 Wall Study

Basic wall models were conducted in both software packages to determine the ability of each program to exhibit numerical stability in planar wall applications.

- Abaqus models exhibited numerical instability prior to or at the point of section yield.
- ATENA models exhibited numerically stable behavior and accurate prediction of strength and deformation capacity for a specimen subjected to monotonic loading. The models exhibited numerical instability when subjected to cyclic load protocols.

Abaqus did not exhibit the ability to stably model walls or simulate the expected behavior of confined regions. ATENA was thus selected as the program for the development of the FE continuum planar wall model.

2.4 SUMMARY AND CONCLUSIONS

Previous research shows that the current understanding of wall behavior is not sufficient to explain recent observations in both laboratory and field settings. The following parameters are thus investigated in this research:

- Shear demand
- Axial load ratio
- Wall configuration (CSAR and boundary element geometry)

To enable investigation of these parameters and provide further insight into wall failure mechanisms, a numerical model that provides the following was required:

- No assumption of plane sections remaining plane.
- Able to provide accurate predictions for wall strength, stiffness, and deformation capacity.
- Able to account for localization of behavior.

- Uses 3D elements to model 3D geometry.

A review of analysis software used previously shows that Abaqus and ATENA, which were readily available to the research team, had the greatest potential for meeting analysis needs. An investigation of the capabilities of Abaqus and ATENA was conducted with each software package evaluated on the ability to (1) correctly predict behavior of confined concrete subjected to compression and (2) exhibit numerical stability in planar wall application. ATENA was identified as the preferred software package for this project.

3 MODEL DEVELOPMENT AND CALIBRATION

The research presented in this chapter focuses on developing a nonlinear three-dimensional continuum-type finite element (FE) model for modeling slender walls using the ATENA software package (www.cervenka.cz). The ultimate intent of this model is to (1) accurately and robustly predict the response of planar walls, including walls tested in the laboratory and (2) enable investigation of the impact of various design parameters on the flexural response of walls, including wall failure mode. Model accuracy and robustness are judged by the ability of the model to predict specimen strength, stiffness, deformation capacity, and failure mode while achieving numerical stability. While laboratory test specimens are subjected to quasi-static reversed cyclic loading, it was found that the software could not robustly simulate cyclic response. Thus, the results of analyses of walls subjected to lateral loading under monotonically increasing displacement demand were compared with data from cyclic tests to validate the model and were used to investigate wall behavior.

As discussed in Chapter 2, the FE model is developed in the ATENA software package. The FE model is defined by the meshing of the geometry, the material models, and material model parameters, all of which are discussed in this chapter. Specifically, this model employs three-dimensional brick elements in meshing and a concrete constitutive model that simulates softening in tension and compression. This enables simulation of the interaction of shear and flexural response mechanisms. This aspect of wall behavior determines failure for some wall designs and is either not represented or represented poorly by most models proposed previously for use in analysis of concrete walls.

Accurate and consistent simulation of the nonlinear response of concrete walls using continuum-type finite element analysis is challenging. Accurate prediction of response requires calibration of some concrete constitutive model parameters that are not easily determined from material testing. These include the deformation capacity of plain concrete, which determines the post-peak response of concrete under compression loading and is required for accurate, mesh-objective prediction of compression-controlled failure, as well as shear resistance across concrete crack surfaces. In this chapter, appropriate values for all material parameters used in the ATENA material models are determined to achieve accurate and numerically stable simulation of response. Model meshing to represent wall geometry and achieve accurate simulation of response is also addressed.

ATENA includes several different concrete material models that may be used to simulate the response of plain concrete subjected to multi-dimensional cyclic loading. The “Nonlinear Cementitious 2” (NC2) model was chosen for use in this study as this material model supports automated regularization of concrete response to both compression and tension loading using a mesh-dependent length. This automated regularization results in mesh-independent response prediction in which the drift at failure is not significantly affected by element size and the level of mesh refinement.

Section 3.1 introduces the 26 experimental walls used to calibrate the model. A discussion of ATENA is provided in Section 3.2, discussing the different material models, model layout, and mesh scheme used in the reference model. All parameters used in the reference model are discussed in Section 3.3. This is then followed by the definition of failure modes in Section 3.4. Section 3.5 covers the post-processing procedure used to isolate CB and BR failures in ATENA. A discussion of numerical instability encountered in the wall database is presented in Section 3.6. Results for the full wall database are detailed in Section 3.7

3.1 EXPERIMENTAL SPECIMENS USED TO DEVELOP THE WALL MODELING PROCEDURE

Data from experimental tests of planar concrete walls subjected to quasi-static cyclic lateral loading were used to determine appropriate modeling procedures and calibrate model parameters. The dataset included 23 planar wall tests specimens from eight experimental test programs conducted by researchers around the world with results published from 1976 until 2012.

The dataset included 18 wall test specimens assembled by Pugh (2012) to develop a regularized distributed-plasticity beam-column element wall model. The five criteria used to qualify walls for the database are as follows:

- Specimens exhibited flexure-controlled response with loss of lateral load carrying capacity resulting from tensile rupture of longitudinal reinforcement (prior to or following buckling) or crushing of the boundary element concrete.
- Specimens were sufficiently thick, at least 3 in. (76.2 mm) to ensure that wall thickness would not adversely affect construction or response.
- Reinforcing steel is not spliced at the base of the wall where moment demand is greatest and inelastic action is expected.
- Sufficient data were available in the literature to fully define a numerical model; data deemed necessary included concrete compressive strength, data defining reinforcing steels stress-strain response, specimen geometry and reinforcement layout, and test specimen boundary conditions in the laboratory.
- Sufficient data were provided to enable evaluation of simulation results; data deemed necessary included global load-displacement response as well as the observed failure mechanism.

These 18 test specimens are supplemented by five wall specimens tested recently by Tran (2012). These five specimens tested by Tran meet the five criteria above.

Figure 3.1 provides, for each wall in the dataset, material, geometric, design and response data of particular interest to the current study. Note that wall specimens were constructed of normal strength concrete and reinforcing steels; concrete compressive strengths ranging from 4270 to 10250 psi (29.4-70.7MPa) with an average concrete compressive strength of 6030 psi (41.6 MPa), and steel yield strength ranged from 63.0 to 87.2 ksi (434-601 MPa) with an average value of 71.7 ksi (494 MPa). All data essential to model development and evaluation, including experimental load-displacement histories, are presented in Appendix A. Parameters in Table 3.1 are defined as follows:

- Cross-Sectional Aspect Ratio (CSAR): l_w/t_w, where l_w is the wall in-plan length and t_w is the wall thickness.
- ALR: axial load ratio.
- V_b: base shear resisted by the wall.
- M_b: base moment resisted by the wall.
- Shear Span: h_{eff}/l_w, where h_{eff} is the effective height, defined as the constant ratio between the base moment and base shear.
- V_{max}: maximum base shear resisted by the wall.
- V_n: nominal shear strength of the wall per ACI 318-14. Calculated using reported material strengths.
- M_n: nominal moment strength for the base section, defined by the extreme compression fiber strain in the boundary element core reaching a strain value of -0.003 in/in.

- Δ_u: specimen drift capacity. Defined as the drift at which the lateral load-carrying capacity of the wall dropped to 80% of the historic maximum.
- FM: failure mode, defined as either BR, CB, or CS (Section 3.4, Section 4.3).
- ACI BE: classification of boundary element confinement per ACI 318-14 (i.e., NBE, OBE, SBE).

Table 3.1 – Geometry and Loading Information for Experimental Wall Database

Specimen	**Author**	**Loading**						**Results**		**ACI BE**
		CSAR	**Shear Span**	**ALR**	$V_{max}/A_{cv}f'_c$	V_b/V_n	M_b/M_n	Δ_u	**FM**	
		--	--	%	psi	--	--	%	--	--
WSH1	Dazio et al.	13.3	2.3	5.5	2.01	0.44	1.03	1.04	BR	NBE
WSH2	Dazio et al.	13.3	2.3	6.3	2.27	0.53	1.12	1.75	BR	NBE
WSH3	Dazio et al.	13.3	2.3	6.4	2.92	0.67	1.10	2.07	BR	OBE
WSH4	Dazio et al.	13.3	2.3	6.3	2.77	0.62	1.06	1.60	CB	NBE
WSH5	Dazio et al.	13.3	2.3	13.7	2.81	0.62	1.08	1.52	BR	OBE
WSH6	Dazio et al.	13.3	2.3	11.4	3.58	0.83	1.11	2.04	CB	NBE
W1	Liu	6.0	3.1	7.6	2.31	0.39	0.98	2.98	CB	OBE
W2	Liu	6.0	3.1	3.5	1.67	0.33	0.97	2.91	BR	NBE
PW4	Birely	20.0	2.0	12.2	4.63	0.88	1.19	1.01	CB	SBE
RW1	Thomsen et al.	12.0	3.1	10.5	2.57	0.50	1.07	2.26	BR	NBE
RW2	Thomsen et al.	12.0	3.1	9.2	2.65	0.52	1.16	2.35	CB	NBE
S5	Vallenas et al.	21.1	1.6	4.8	6.81	0.88	1.18	1.47	CS	SBE
S6	Vallenas et al.	21.1	1.6	4.8	6.42	0.83	1.12	1.65	CS	SBE
WR20	Oh et al.	7.5	2.0	10.4	3.00	0.76	1.11	2.82	CB	NBE
WR10	Oh et al.	7.5	2.0	9.8	2.87	0.64	1.08	2.82	CB	OBE
WR0	Oh et al.	7.5	2.0	10.8	2.97	0.74	1.08	2.14	CB	NBE
R1	Oesterle et al.	18.8	2.4	0.0	1.10	0.23	1.17	2.52	BR	NBE
R2	Oesterle et al.	18.8	2.4	0.0	2.00	0.42	1.23	3.25	BR	SBE
RW-A20-P10-S38	Tran	8.0	2.0	7.3	3.60	0.81	1.26	3.14	CB	SBE
RW-A20-P10-S63	Tran	8.0	2.0	7.3	6.10	0.91	1.13	3.00	CB	SBE
RW-A15-P10-S51	Tran	8.0	1.5	7.7	4.90	0.83	1.15	3.31	CB	SBE
RW-A15-P10-S78	Tran	8.0	1.5	6.4	7.00	0.85	1.07	3.00	CB	SBE
RW-A15-P2.5-S64	Tran	8.0	1.5	1.6	5.80	0.79	0.99	3.00	CB	SBE
Mean		12.1	2.2	7.1	3.60	0.65	1.11	2.33	--	--
Standard Deviation		5.0	0.52	3.7	1.75	0.20	0.07	0.72	--	--
COV		0.41	0.24	0.52	0.49	0.31	0.06	0.31	--	--

3.1.1 Summary of Experimental Test Programs

The wall specimens listed in Table 3.1 were tested as part of eight different experimental investigations conducted since 1976. The objective of these experimental test programs are summarized below

- Dazio et al. (2009): The experimental program was designed to investigate the performance of wall designs typical of regions of moderate seismicity in Central Europe. The main parameters varied were the material properties, reinforcement ratios, and the axial load ratio.
- Liu (2004): The experimental program was designed to investigate the impact of concrete compressive strength on wall performance for specimens subjected to cyclic lateral load protocols. The only significant difference in the construction of Specimens W1 and W2 is the concrete compressive strength. Note that the applied axial load was held constant; thus, Specimen W2 has a lower axial load ratio than Specimen W1 as Specimen W2 has a higher concrete compressive strength than Specimen W1.
- Birely (2012): The experimental program was designed to evaluate the performance of walls in modern midrise buildings in regions of high seismicity in the United States. The main parameters varied were the shear span and concentration of steel in the boundary element. The tests also studied the impact of reinforcement lap splices on wall response.
- Thomsen et al. (1995): The experimental program was design to evaluate the impact of spacing and confining reinforcement configuration on wall performance. The only significant parameter varied is the detailing of the boundary element confining reinforcement.
- Vallenas et al. (1979): The experimental program was designed to evaluate the impact of load protocol on the response of planar walls with heavily reinforced and confined boundary element regions. The only significant difference between Specimens S5 and S6 is in the load protocol; Specimen S5 was subjected to an essentially monotonic load protocol and Specimen S6 was subjected to a fully cyclic load protocol.
- Oh et al. (2002): The experimental program was designed to study the effect of boundary element confinement on wall response. The main parameter varied between the specimens was the spacing of transverse reinforcement in the boundary element region. Specifically studied is the impact of no defined boundary element (Specimen WR0), confining reinforcement with large vertical spacing (7.87 in. (200 mm), Specimen WR20), and confining reinforcement with a moderate vertical spacing (3.94 in. (100 mm), Specimen WR10).
- Oesterle et al. (1976): The experimental program was designed to study the effect of boundary element reinforcement on the response of specimens not subjected to an axial load. Specimen R1 is lightly-reinforced in both longitudinal and confining boundary element reinforcement; both longitudinal and confining reinforcement are increased in Specimen R2.
- Tran (2012): The experimental program was designed to evaluate the impact of shear span, axial load ratio, and peak shear stress on wall response for specimens with a relatively low cross-sectional aspect ratio (CSAR = 8.0). The parameters are varied as follows: shear spans from 1.5 to 2.0, ALRs from 2.5% to 7.5%, and peak shear stresses from roughly $4\sqrt{f'c}$ to $8\sqrt{f'c}$ psi ($0.33\sqrt{f'c}$-$0.66\sqrt{f'c}$ MPa).

3.2 SIMULATING CONCRETE WALL RESPONSE USING ATENA

The ATENA software package includes constitutive models, element formulations and solution algorithms to enable analysis of reinforced concrete components subjected to quasi-static monotonic and cyclic load histories and exhibiting a range of response and failure modes. Details of the material models, element formulations and solution algorithms relevant to the current study are presented in the following subsections.

3.2.1 Model Layout and Meshing Scheme

Each wall model is split into the following sections: (1) lower boundary element, (2) upper boundary elements, (3) web, (4) loading region, and (5) foundation. This layout is shown in Figure 3.1.

1. Lower boundary element: The lower boundary element exhibits significant inelastic response; thus, this region of the wall requires highly refined modeling to ensure accurate simulation of response. Typically the bottom 25-40% of the wall height experiences significant inelastic action; in this region, most of the vertical and confining reinforcement is modeled explicitly. A small portion of the reinforcement is modeled by smearing the reinforcement area across the entire region. This was found to have minimal impact on simulated response but significant impact on numerical stability; this is discussed in more detail in Section 3.3.5. Element size is the smallest in the lower boundary element region of the wall (element size is approximately 1.5 in. (38.1 mm)); at least 2 elements are used to model half of the thickness of the wall.
2. Upper boundary element: Significant nonlinear response is not expected or observed in the upper boundary element. As such, the impact of confining reinforcement is not significant and modeling this reinforced as smeared reinforcement rather than discrete bars has minimal impact on simulated response. Thus, in the upper boundary element, confining reinforcement is modeled as smeared reinforcement to reduce computational demands. Longitudinal reinforcement is modeled with primarily discrete reinforcement, matching the lower boundary element. To reduce computational demands, the upper boundary element is modeled more coarsely (element size is approximately 3 in. (76.2 mm)); only 1 element is used to model half the thickness of the wall.
3. Web: The web region of the wall is lightly reinforced in both the vertical and horizontal directions. As such, modeling reinforcement as smeared over the entire web regions does not significantly affect simulated response. Thus, to reduce computational demand, horizontal and vertical web reinforcement is modeled as smeared reinforcement. In some cases, to improve numerical stability, some web reinforcement is modeled using discrete bars; this is discussed in Section 3.6. Element size in the web varies to be consistent with element size in the lower and upper boundary element regions of the wall.
4. Loading region: This is defined as the region between the wall height (h) and effective wall height (h_{eff}). It is modeled using an elastic material with an elastic modulus that equals that used for the concrete elsewhere within the wall. This ensures that loads applied to individual nodes are transferred across the entire width of the wall and prevents the localization of damage near the applied load. Elements in this portion of the wall are relatively large (element size exceeds 4 in. (101.6 mm)). Given that concrete is assumed to be elastic, it is not necessary to model reinforcing steel.
5. Foundation: Minimal inelastic action is observed in the foundation of the wall; thus, the foundation is modeled using an elastic material. To facilitate model building and reduce computational effort, the wall foundation is modeled as having the same thickness as the wall. Thus, to simulate the additional stiffness provided by a foundation that is thicker than the wall, the foundation material is modeled using an artificially large elastic modulus defined as follows:

   $$E_{c,f} = E_c(t_f/t_w) \qquad \textit{(Eq. 3.1)}$$

   where $E_{c,f}$ = the elastic modulus of the elastic foundation material, E_c = the elastic modulus of the foundation concrete, t_f = the foundation thickness, and t_w = the wall thickness. The foundation is modeled using relatively large elements (element size exceeds 4 in. (101.6 mm)) in this region.

The element formulations used in this model are defined by ATENA as “3D Brick” or “CCIsoBrick” for all concrete elements and “Reinforcement” for all reinforcing bars. The brick elements are categorized as

"C3D8" and have eight nodes, linear shape functions, and are fully integrated (2x2x2 integration points). The reinforcement elements are categorized as "T2D2" and are two-dimensional truss elements. The reinforcing bars are generated as embedded elements within the existing mesh of 3D solid elements; the reinforcement mesh is governed by the concrete mesh and is not explicitly defined by the user.

A characteristic mesh scheme is shown in Figure 3.2. Note that the different meshed regions are tied together by contact surfaces that are defined with a "perfect connection," ensuring continuity across mesh boundaries. The contact relationship should be defined such that the coarser mesh (i.e., larger finite elements) is the master in the master-slave relationship.

The planar wall specimens have a plane of symmetry that is parallel the face of the wall. This is exploited to reduce model size and computational demand. The symmetric boundary condition applied in ATENA is shown in Figure 3.3.

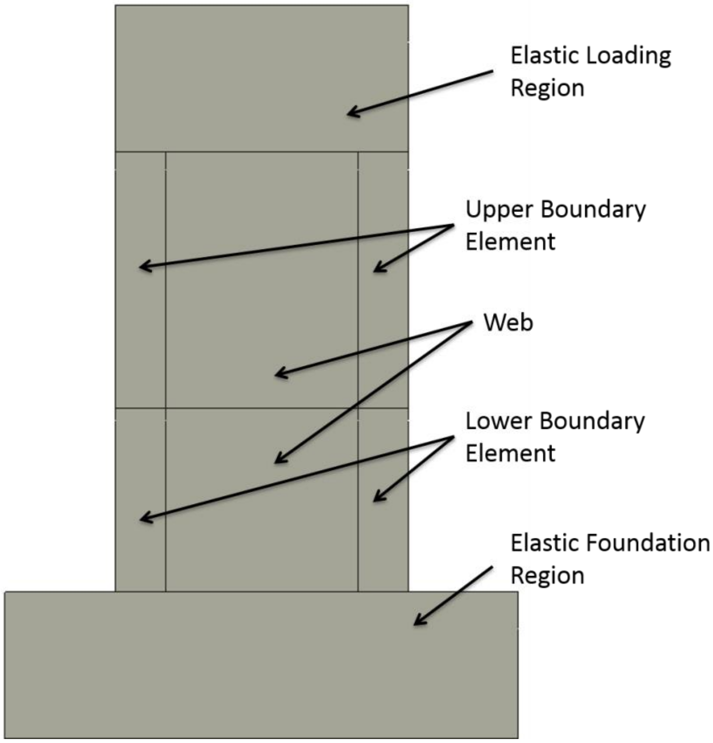

Figure 3.1 – Geometric Layout of ATENA Model (Specimen RW-A20-P10-S63)

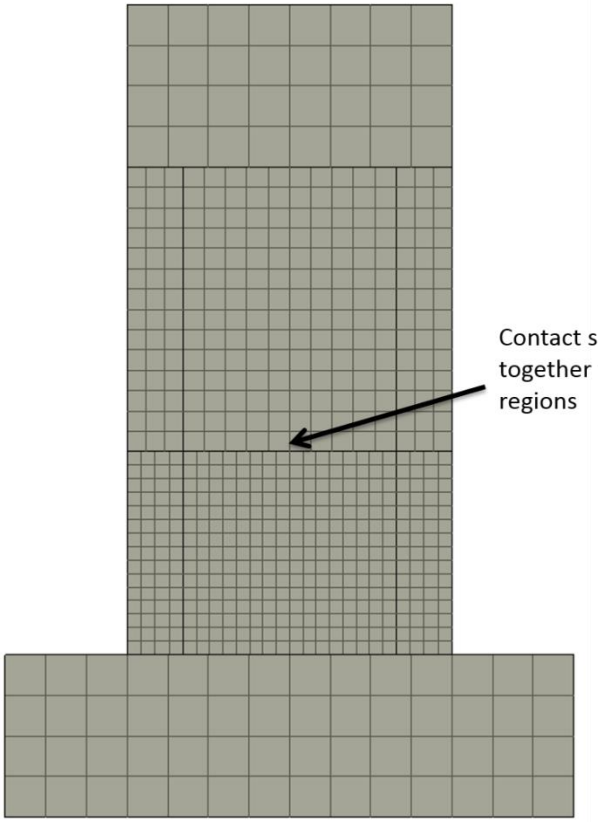

Figure 3.2 – Characteristic Mesh Scheme in ATENA Model (Specimen RW-A20-P10-S63)

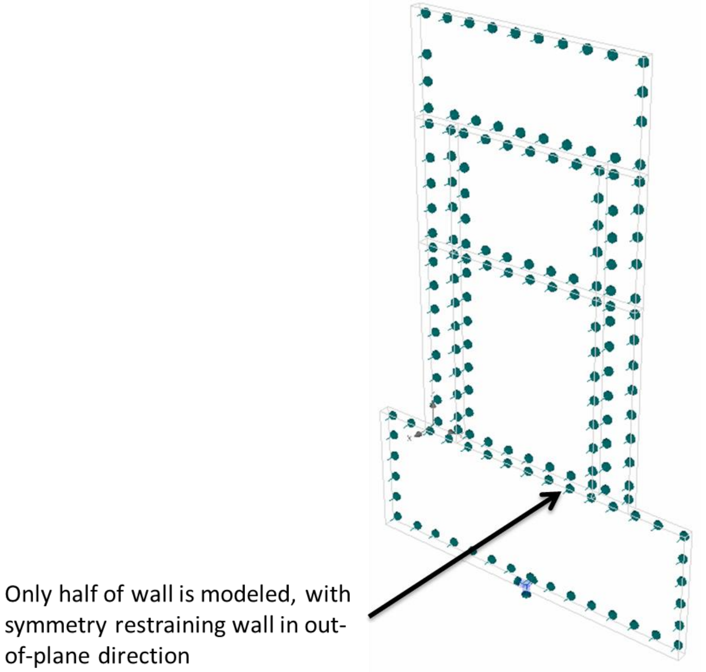

Figure 3.3 – Out-of-Plane Symmetric Boundary Condition for Simulated Wall Models

3.2.2 Loading Protocol

Axial load is applied as a constant surface load that acts across the top surface of the wall. Lateral load is applied to the top surface of the wall via displacement control; multiple nodes on the top surface of the wall are defined to follow the same lateral displacement history. As this load is applied to an elastic material, it effectively acts as a uniform load across the top surface of the wall. The top surface of the wall is defined by the effective height of the applied shear.

Cyclic load protocols were attempted in the development of this model, but the concrete material model became unstable after several cycles of the load protocol had completed. Successful model simulations were only achieved with walls subjected to monotonic load protocols. Discussions with Cervenka Consulting did result in improved behavior of specimens subjected to cyclic protocols, but issues with numerical instability persisted. All models in this study are thus subjected to only monotonic load protocols.

3.2.3 Modeling Concrete Material Response Using ATENA

The ATENA software package includes multiple concrete constitutive models. Of these models, NC2 model is most appropriate for the current study as it is appropriate for concrete that is subjected to a range of three-dimensional stress states and is capable of producing mesh-objective results through material regularization. The NC2 model employs continuum damage mechanics with fixed or rotating cracks to simulate response in tension, plasticity theory with hardening and softening to simulate response in compression and the strain decomposition method proposed by deBorst (1986) to combine tensile and compressive response.

Using the NC2 Model, concrete response under tensile loading is defined by continuum damage mechanics with the concrete fracture energy and a mesh-dependent characteristic length used to regularize material response and ensure mesh-objective simulation of response. Cracking is determined using the Rankine criterion, which results in the onset of cracking when the principal tensile stress exceeds the user-defined concrete tensile strength and crack opening or widening occurring when the tensile stress normal to the crack surface exceeds the post-cracking concrete tensile strength (Figure 3.5). For a fixed-crack model, the orientation of the crack surface is fixed at the onset of cracking, and multiple cracks may develop with the maximum angle between crack surfaces defined by the user; for a rotating crack model, the crack surface rotates to be normal to the maximum principal strain for each load step. Tension softening is simulated; concrete tensile strength normal to the crack surface reduces with increasing crack width, w_{tc}, as shown in Figure 3.4. Crack width is related to strain normal to the crack surface via a mesh-dependent characteristic length, L_t, which is defined as the length of the element in the direction normal to the crack surface (Figure 3.4). The user may choose exponential tensile strength loss per Hordijk (1991) as shown in Figure 3.4 and Figure 3.5 or linear softening. As shown in as shown in Figure 3.4, both curves are defined by the concrete fracture energy, G_f, which is assumed to be a characteristic material property. Nonlinear response under tensile loading is assumed to be due entirely to material damage. For a fixed-crack model, this equates to the material stiffness equaling the material strength divided by the total strain in the direction normal to the crack surface (Figure 3.5); for a rotating crack model, the material compliance tensor is increased incrementally in the current crack-normal direction.

The following symbols are used in Figures 3.4-3.5.

- L_t: characteristic length of finite element mesh.
- f'_t, $f_t^{'ef}$: concrete tensile strength.
- ε^f: concrete fracturing strain.

- G_f: concrete fracture energy.
- w_t, w_{tc} : length of concrete crack opening.
- E_c: concrete elastic modulus.

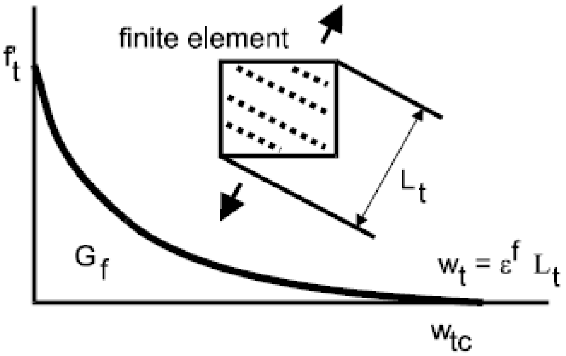

Figure 3.4 – Tensile Softening and Characteristic Length (Cervenka et al. 2013)

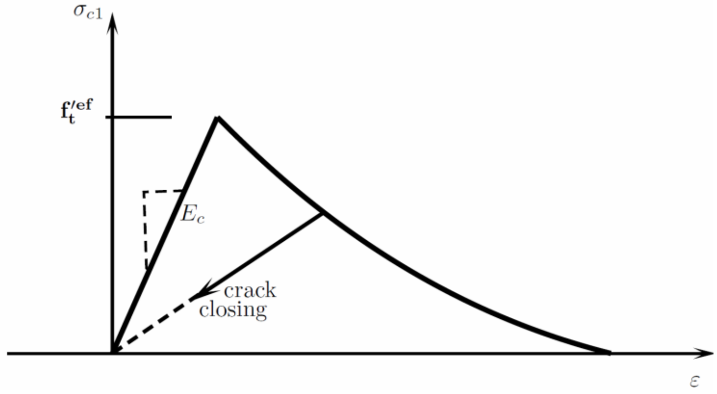

Figure 3.5 – Stages of Crack Opening (Cervenka et al. 2013)

Nonlinear response under compressive loading is defined using plasticity theory and the assumption of non-associated flow. As is done for tension softening, post-peak compression response is defined by a stress versus deformation curve and a mesh-dependent characteristic length. To simulate the impact of confinement on concrete compressive strength, the yield surface by Menétrey and Willam (1995) is used to define the elastic domain (Figure 3.6). The yield surface expands (hardening) and contracts (softening) with increasing equivalent plastic strain. The Drucker-Prager surface is used to define the plastic potential (Figure 3.6); thus the plastic model employs a non-associated flow rule. Hardening and softening with increasing equivalent plastic strain are defined based on data from uniaxial plain concrete compression tests. In the hardening regime, a second-order curve is used to define the stress versus plastic strain history (Figure 3.7). In the softening regime, fundamental material response is assumed to be defined by a linear stress versus deformation curve (Figure 3.7). The area under this curve is the crushing energy described by Jansen and Shah (1997), Coleman and Spacone (2001) and Pugh (2012). As is done for concrete softening in tension, compressive strain is related to compressive deformation via a mesh-dependent characteristic length, $L_{c.}$

Ultimately, characterization of concrete material response using the above model requires specification of several material parameters, all of which are listed in Table 3.2. These are discussed in greater detail in Section 3.3.

The following symbols are used in Figures 3.6-3.7.

- β: concrete dilation parameter.
- σ_{ij}^{t}: elastic predictor.
- σ_{ij}^{n}: stress state at step n.
- σ_{ij}^{n-1}: stress state at step n-1.
- I_1: first invariant of stress tensor.
- J_2: second invariant of deviatoric stress tensor.
- f'_c: concrete compressive strength.
- w_d: concrete plastic deformation at zero compressive stress.
- L_c: characteristic length of finite element mesh.
- E: concrete elastic modulus.
- f'_{c0}: concrete compressive strength at zero plastic deformation.
- ε_c^P: strain at peak concrete compressive strength.
- ε_{eq}^P: equivalent plastic strain.

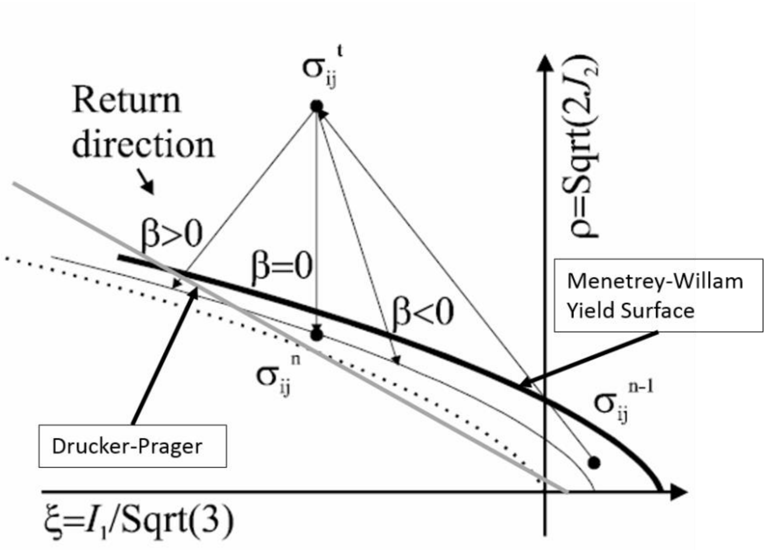

Figure 3.6 – Direction of the Yield Surface and Plastic Strain Vector (Cervenka et al. 2013)

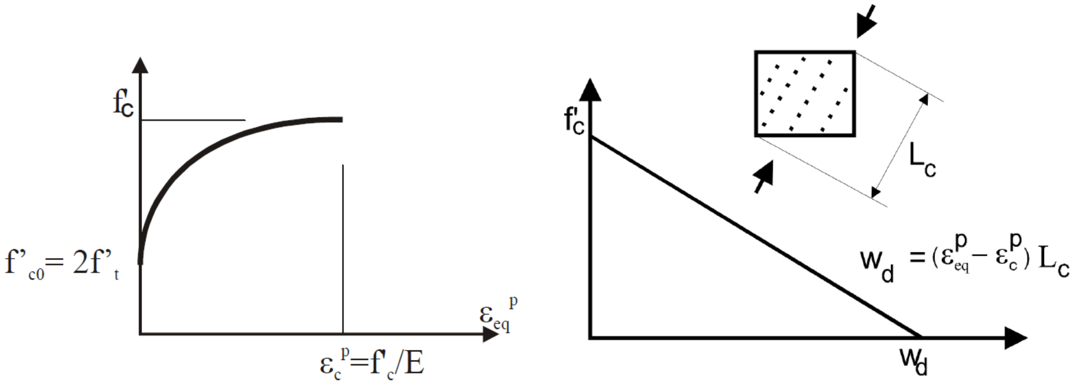

Figure 3.7 – Compressive Hardening/Softening and Comp. Characteristic Length (Cervenka et al. 2013)

Table 3.2 – List of Concrete Parameters Used in ATENA Analysis

Concrete Parameter	Description	Value
Comp. Strength, f'_c	Determines the peak compressive strength of concrete.	Determined by experimental testing of 6"x12" cylinders.
Tensile Strength, f'_t	Determines the peak tensile strength of concrete.	Computed per the recommendations of CEB-FIP (1990), (Eq. 3.3).
Elastic Modulus, E_c	Determines elastic modulus of concrete.	Calculated according to ACI 318-14, (Eq. 3.2)
Fracture Energy, G_f	Determines the fracture energy of concrete; enables material regularization in tension.	Computed per the recommendations of Vos (1983), (Eq. 3.4).
Plastic Deformation, w_d	Determines the plastic deformation capacity of concrete at zero compressive stress; enables material regularization in compression.	Range of potential values (w_d = 0.025 in. to 0.125 in. (0.635 mm to 3.175 mm)) determined by recommendations per ATENA and Pugh (2012); calibrated in Section 3.3.1.
Dilation Parameter, β	Determines the extent to which concrete dilates under inelastic compression loading.	Determined by ATENA recommendation (β = 0 to 0.7) and calibrated in Section 3.3.2.
Shear Retention Factor, S_F	Determines the shear stiffness of cracked concrete.	Range of potential values (S_F = 20 to 200) determined by ATENA recommendation; calibrated in Section 3.3.3.
Tension Softening, c_{ts}	Determines the residual tensile strength of concrete.	Range of potential values (c_{ts} = 0.00 to 0.05) determined by ATENA recommendation; calibrated in Section 3.3.4.

$$E_c = 57000\sqrt{f'c}\ (\text{psi}) \qquad (4700\sqrt{f'c}\ MPa) \qquad \textit{(Eq. 3.2)}$$

$$f'_t = 1.26{f'_{cu}}^{2/3}(\text{psi}) \qquad (0.24{f'_{cu}}^{2/3} MPa) \qquad \textit{(Eq. 3.3)}$$

$$G_f = 0.000143f'_t\ (\text{psi}) \qquad (0.000025f'_t\ MPa) \qquad \textit{(Eq. 3.4)}$$

3.2.4 Modeling Steel Material Response Using ATENA

ATENA provides a reinforcing steel material model based on the work of Menegotto and Pinto (1973). The Menegotto-Pinto model is extended in ATENA to account for isotropic hardening by the specification of an arbitrary hardening constant. However, as all analyses ultimately conducted in ATENA utilized monotonic load protocols (Section 3.2.2), the reinforcement model is essentially a simple multi-linear stress-strain curve. The steel hardening ratio, E_h, is defined as:

$$E_h = \frac{f_u - f_y}{\varepsilon_u - \varepsilon_y} \qquad \textit{(Eq. 3.5)}$$

Where E_s is the steel elastic modulus, f_y is the steel yield strength, f_u is the steel fracture stress, ε_y is the steel yield strain, and ε_u is the steel fracture strain.

3.3 INVESTIGATION AND CALIBRATION OF MODEL PARAMETERS USING EXPERIMENTAL DATA

As noted in Section 3.2, the characterization of concrete material response requires specification of several material parameters; these parameters are described and listed in Table 3.2. For many of these parameters, there are neither simple material tests for determining nor consensus within the community as to appropriate values for use in analysis. To determine the best values for use in this model, calibration studies are conducted to investigate the impact of each parameter on predicted response, the sensitivity of response prediction to variation in the parameters, and identify the parameter value that results in an accurate prediction of response and stable simulation.

The plastic deformation parameter (w_d) determines how rapidly concrete compressive strength is lost. Eight experimental specimens exhibiting compression-controlled failure were considered for the calibration of this parameter as other compression-controlled failures had not yet been successfully modeled (i.e., exhibited sufficient numerical stability to reach failure) at the time of calibration.

Specimens S6, WR0, and RW2 were selected for use in investigating additional concrete material model parameters for the following reasons:

- ALR: The axial load ratios span from 4.8% to 10.8%, showing the behavior of specimens across the range of axial load ratios present for CB failures in the wall database.
- Shear span: this set includes models with shear spans from 1.60 to 3.13, showing the behavior of specimens across the range of shear spans present in the wall database.
- CSAR: The cross-sectional aspect ratios of the three walls are representative of the low (WR0, CSAR = 7.5), moderate (RW2, CSAR = 12), and high (S6, CSAR =21) values present in the wall database.
- Confining reinforcement: WR0 does not have a defined boundary element, RW2 provides a boundary element which does not meet ACI 318-14 SBE criteria, and S6 provides a boundary element which does meet ACI 318-14 SBE criteria.
- Shear stress demand: this set includes models with peak shear stresses from $2.65\sqrt{f'c}$ to $6.42\sqrt{f'c}$ psi ($0.22\sqrt{f'c}$-$0.53\sqrt{f'c}$ MPa), among the highest peak shear stresses present in CB failures in the wall database.
- Failure mode: all represent compression-buckling failure. The investigation of numerical instability and impact of parameters of failure and deformation mainly pertains to walls exhibiting CB failure.

Table 3.3 shows the list of walls used to calibrate the parameters below; Table 3.4 lists recommendations for these parameters.

Table 3.3 – List of Simulations Used for Parameter Study and Calibration

Specimen	w_d	β	S_F	Tension Stiffening	$\rho_{sm,vert}$	$\rho_{sm,horiz}$
S6	X	X	X	X	X	X
RW2	X	X	X	X	X	X
WR0	X	X	X	X	X	X
WR10	X					
WSH4	X					
WSH6	X					
RW-A20-P10-S63	X					
RW-A20-P10-S78	X					

Table 3.4– Summary of Recommendations for Calibrated Model Parameters

Concrete Parameter	Recommendation
Plastic Deformation, w_d	w_d = 0.0425 in. (1.080 mm)
Beta Factor, β	β = 0, may increase up to 0.25
Shear Retention Factor, S_F	S_F = 50
Tension Softening, c_{ts}	c_{ts} = 0.00, may increase up to 0.01
Long. Smeared Reinf.	10% of total
Conf. Smeared Reinf.	25% of total (not to exceed 0.20% gross)

3.3.1 Concrete Deformation Capacity

As discussed in Section 3.2.1, it is necessary to calibrate the deformation capacity of the concrete. The parameter used commonly (Jansen and Shah (1997), Coleman and Spacone (2001) and Pugh (2012)) is the concrete crushing energy, G_{fc}. An increase in crushing energy increases the deformation at which concrete loses compressive strength; this could be expected to increase the deformation capacity of wall exhibiting a compression-controlled failure mode. In ATENA, concrete post-peak response in compression is defined by a compression stress versus displacement model.

To achieve mesh-objective simulation of response for components exhibiting compression-controlled failure, the compression softening response of concrete is defined by a compression stress versus displacement model (Figure 3.7). Linear softening is assumed and the model is defined by the unconfined compressive strength of the concrete and w_d, which is the plastic deformation at zero compressive strength. The area under the compression-softening curve is the concrete crushing energy, which is considered to be a fundamental material property (Jansen and Shah 1997). The compression stress versus deformation curve is transformed to a stress versus strain curve for use in the finite element model via an element-dependent characteristic length, L_d, which is defined as the element length in the direction of the minimal principal strain:

$$\varepsilon_{pl} = \frac{w_d}{L_d} \qquad \textit{(Eq. 3.6)}$$

Relatively little research has addressed concrete crushing energy. Jansen and Shah (1997) conducted compression tests of concrete cylinders with constant cross-sectional area and varying length, and concluded that the concrete crushing energy of unconfined concrete ranges from 114 to 171 lb/in (20-30 N/mm). Pugh (2012) determined that an unconfined concrete crushing energy of $0.078f'_c$ (psi) ($2f'_c$ MPa) (60-80 N/mm for normal strength concrete) results in accurate prediction of the deformation capacity of compression-controlled concrete walls when fiber-type line-element models are used.

Given the wide variation in the valued determined by Jansen and Shah and Pugh, a calibration study was undertaken to determine an appropriate crushing energy for use in defining the ATENA concrete model. Analyses were conducted of nine wall specimens that exhibited compression-controlled, i.e. compression-buckling, failure in the laboratory. For each wall specimen, analyses were conducted for values ranging from 0.025 in. to 0.125 in. (0.635 mm to 3.175 mm), which correspond approximately to crushing energies ranging from 12 N/mm to 80 N/mm for normal strength concrete. Results of this study are shown in Figures 3.8-3.10. These figures show that:

- For some specimens (RW-A20-P10-S63, RW-A15-P10-S78, WSH4, WR0, WR10), at large w_d values, increasing w_d has minimal impact on drift capacity; this behavior is attributed to the failure mode shifting from compression-controlled (i.e. compression-buckling) failure to tension-controlled (i.e. buckling-rupture) such that increasing concrete deformation capacity has minimal impact on wall deformation capacity.
- The range of ideal w_d values ranges from 0.03 in. to 0.05 in. (0.76 mm to 1.27 mm), which corresponds to crushing energies of 15 N/mm to 30 N/mm for normal strength concrete.
- The results do not show a relationship between the concrete compressive strength and w_d; thus, the plastic deformation capacity is independent of the concrete compressive strength.

Ultimately, based on the data in Table 3.5, a w_d of 0.0425 in. (1.08 mm) is chosen for use in all wall analyses. This corresponds to a crushing energy ranging from 114 lb/in (20 N/mm) to 257 lb/in (45 N/mm) (f'_c = 4200-10250 psi (29.0-70.7 MPa)) for concrete compressive strengths of the data set, which is consistent with the crushing energy range of 114 to 171 lb/in (20-30 N/mm) measured by Jansen and Shah (1997) (Note that the Jansen and Shah study used concrete with compressive strengths ranging from 6530 to 13050 psi (45.0-90.0 MPa).

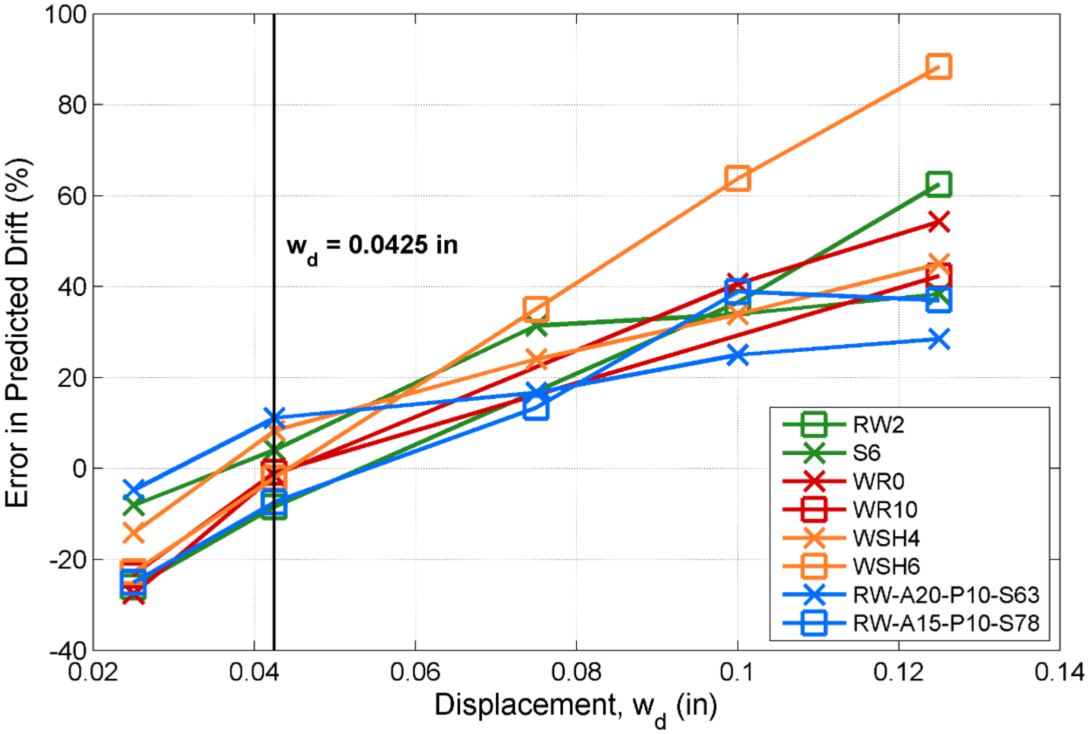

Figure 3.8 –Prediction Error vs. Value of Displacement, w_d

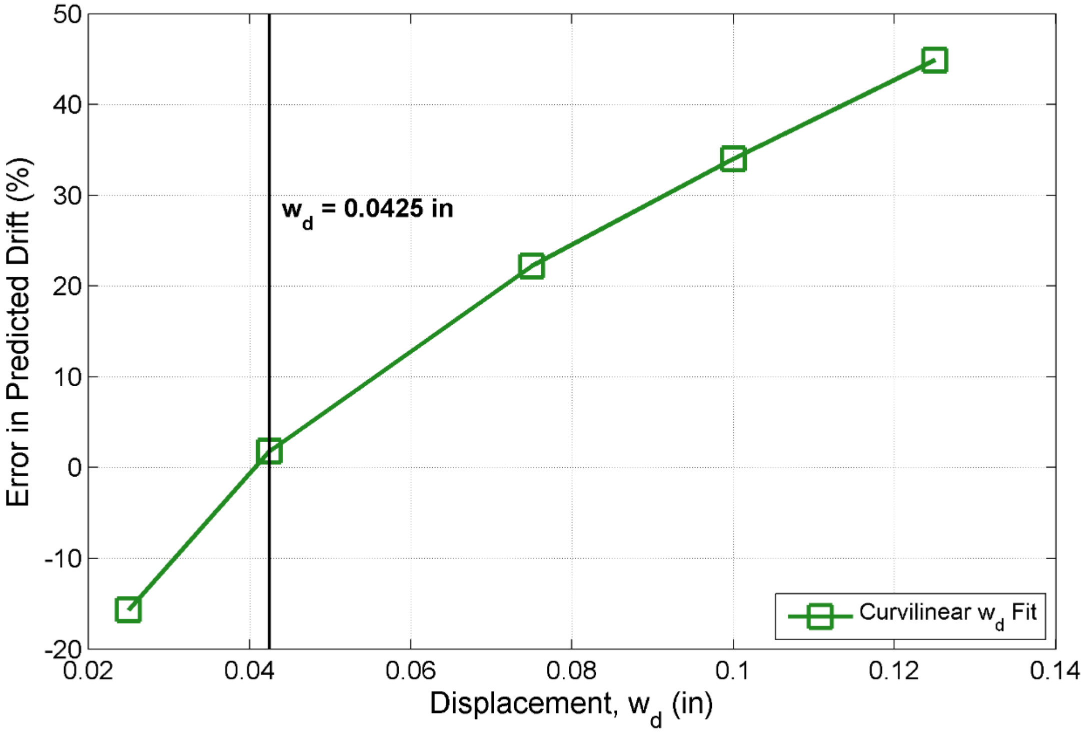

Figure 3.9 – Prediction Error Value of Displacement, w_d, Curvilinear Fit

Table 3.5 – Simulated vs. Experimental Drift for CB Specimens at Varied w_d

Specimen	Error, w_d = 0.025	Error, w_d = 0.0425	Error, w_d = 0.075	Error, w_d = 0.100	Error, w_d = 0.125	Ideal w_d
--	%	%	%	%	%	In
PW3	-3.2	6.4	NA	19.5	36.6	0.0300
RW2	-26.1	-8.4	NA	36.5	62.5	0.0425
S6	-8.1	4.1	31.4	33.9	38.4	0.0350
WR0	-27.6	-1.5	NA	40.6	54.3	0.0425
WR10	-23.4	-0.9	NA	NA	42.3	0.0425
WSH4	-14.1	8.3	24.1	33.9	45.0	0.0300
WSH6	-22.8	-2.1	35.0	63.7	88.4	0.0500
RW-A20-P10-S63	-4.7	11.1	16.7	25.0	28.5	0.0300
RW-A15-P10-S78	-25.0	-7.4	13.4	38.9	NA	0.0500

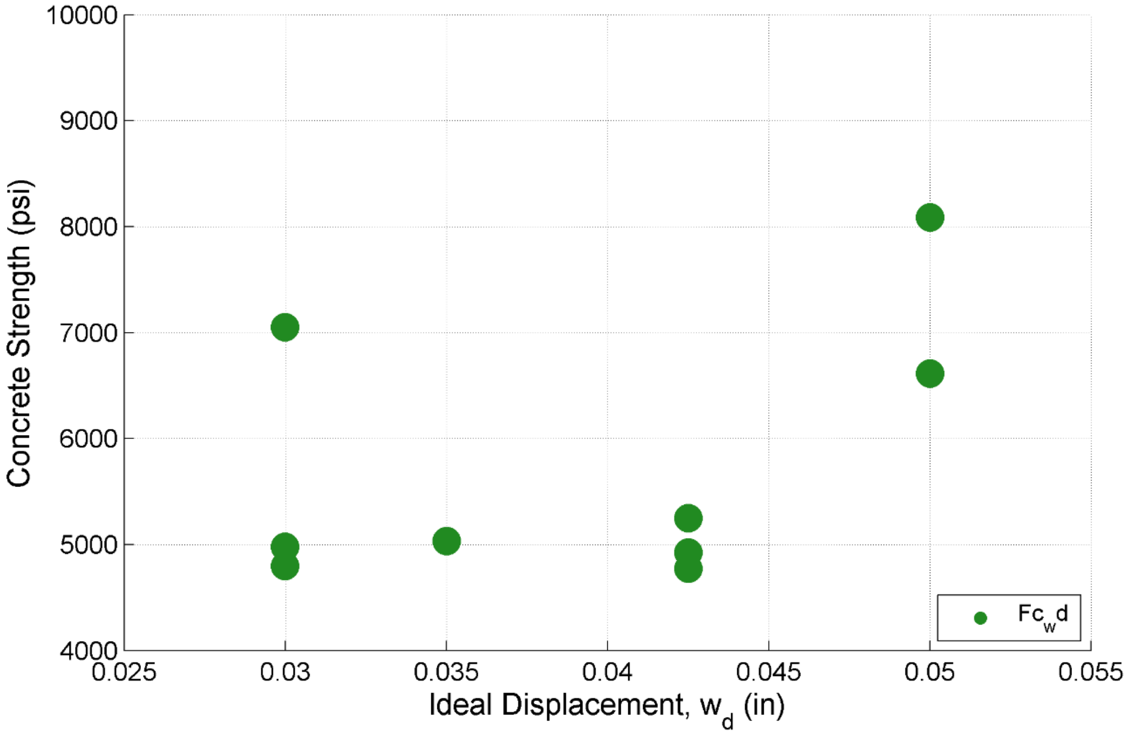

Figure 3.10 –Concrete Compressive Strength vs. Displacement, w_d

3.3.2 Dilation Parameter

The dilation parameter (β) controls concrete dilation associated with plastic compressive response: if $\beta < 0$ the material is compacted and volume decreases during crushing, if $\beta > 0$ the material dilates during crushing, and if $\beta = 0$ the material volume does not change during crushing.

As discussed previously, for the ATENA NC2 concrete model, plastic strain during inelastic compressive response is defined by the plastic potential:

$$G^{P}(\sigma_{ij}) = \beta\frac{1}{\sqrt{3}}I_1 + \sqrt{2J_2} \qquad \textit{(Eq. 3.7)}$$

Where I1 is the first invariant of the stress tensor (Eq. 3.8) and J2 is the second invariant of the deviatoric stress tensor (Eq. 3.9).

$$I_1 = \sigma_1 + \sigma_2 + \sigma_3 \qquad \textit{(Eq. 3.8)}$$

$$J_2 = \frac{1}{2}(s_1^2 + s_2^2 + s_3^2) \qquad \textit{(Eq. 3.9)}$$

Where σ_1, σ_2, and σ_3 are the principal values of the stress tensor and s_1, s_2, and s_3 are the principal values of the deviatoric stress tensor.

This plastic potential is not the same function used to define the yield surface; thus the NC2 concrete model employs a non-associated plastic flow model. Given this plastic potential, in the event of plastic deformation, β determines the direction of the plastic flow as $\varepsilon^p = dG/d\sigma$. The direction of the plastic flow is also the "return direction" to the yield surface from an inadmissible trial stress state outside the yield surface. Figure 3.5 shows the solution path for the "return map algorithm" used to determine the stress state and location of the yield surface during a nonlinear load step. In Figure 3.5, σ_{ij}^{n-1} is the initial stress state in the elastic domain, σ_{ij}^{t} is the inadmissible trial stress state that is outside the yield surface and determined assuming an elastic load increment, and σ_{ij}^{n} is the final stress state on the yield surface, which has evolved due to plastic deformation. The location of σ_{ij}^{n} is determined by β, which defines the slope of the stress increment that "returns" the stress state to the yield surface.

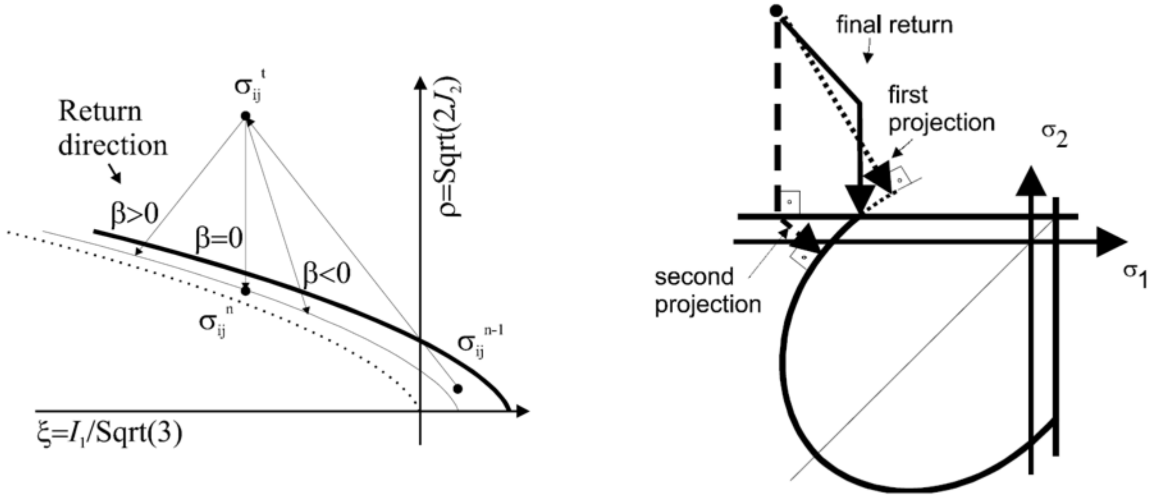

Figure 3.11 – ATENA Documentation for β Parameter (Cervenka et al. 2013)

Based on work by Cervenka et al. (2008), the ATENA user's manual recommends 0 ≤ β ≤ 0.7, such that inelastic compressive response results in zero to positive volumetric expansion. For concrete walls, β could be expected to most significantly affect the behavior of confined concrete in the boundary elements. Boundary element concrete expands under high compressive demands due to the Poisson effect as well as due to plastic dilation; this expansion activates confining reinforcement and the confining pressure increases the compressive strength and compressive strain capacity of the boundary element concrete. Too little expansion and the concrete could be expected to exhibit little gain in strength or deformation capacity; too much expansion and the concrete could be expected to exhibit premature crushing failure due to overestimation of strength gain and plastic strain accumulation.

Data published by Kupfer et al. (1969) on the expansion of concrete under uniaxial compression is shown in is plotted versus different ATENA simulations of plain concrete subjected to uniaxial loading in Figure 3.12. It is clear from the data in Figure 3.12 that a value of β = 0.10 best matches the experimental data for plain concrete subjected to uniaxial compression.

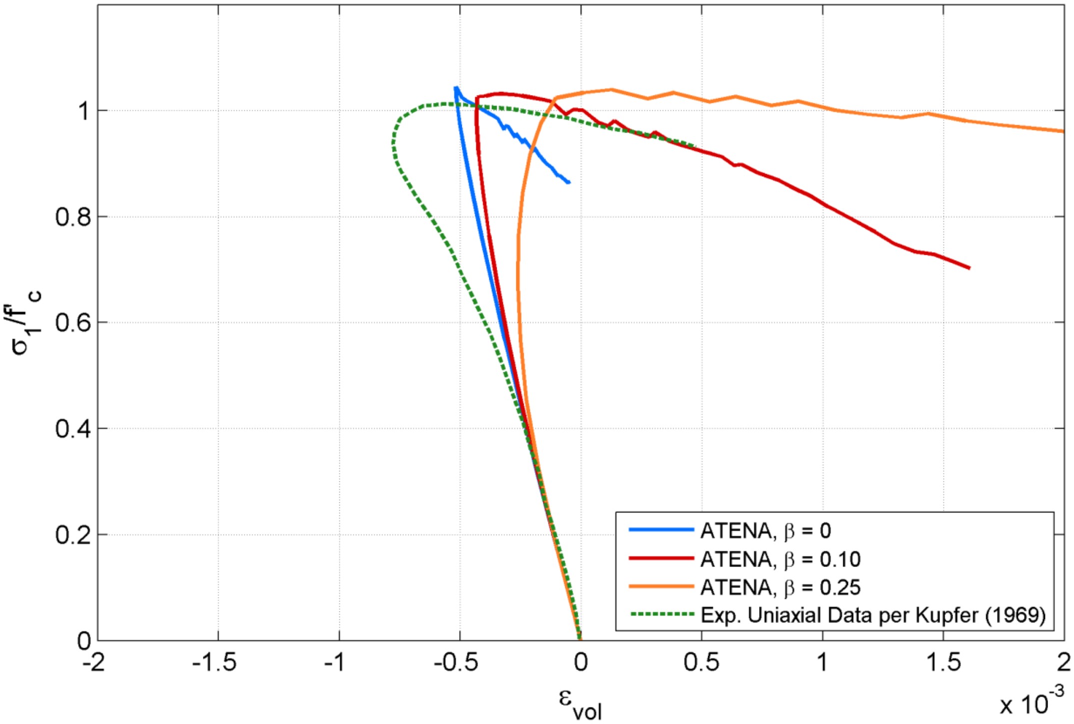

Figure 3.12 – Concrete Compressive Stress vs. Volumetric Strain for ATENA Simulations and Experimental Data per Kupfer et al. (1969)

Figures 3.13-3.15 show the impact of β on simulated response for the three reference walls specimens that exhibited compression-controlled failure. The data in these figures show

- The impact of β on response is approximately the same for β = 0 and β = 0.25.
- Increasing β above 0 can increase wall strength (Figure 3.14).
- Deformation capacity is significantly reduced for β = 0.5 and β = 0.7 and there is the possibility of unstable response (Figure 3.14)

While a value of β = 0.10 best fits experimental data, β = 0 typically provides the greatest level of numerical stability and response is insensitive to this parameter from β = 0 to 0.25. As such, β = 0 is recommended for use. This parameter can be increased if numerical instability is encountered at β = 0, with 0.25 as the upper limit.

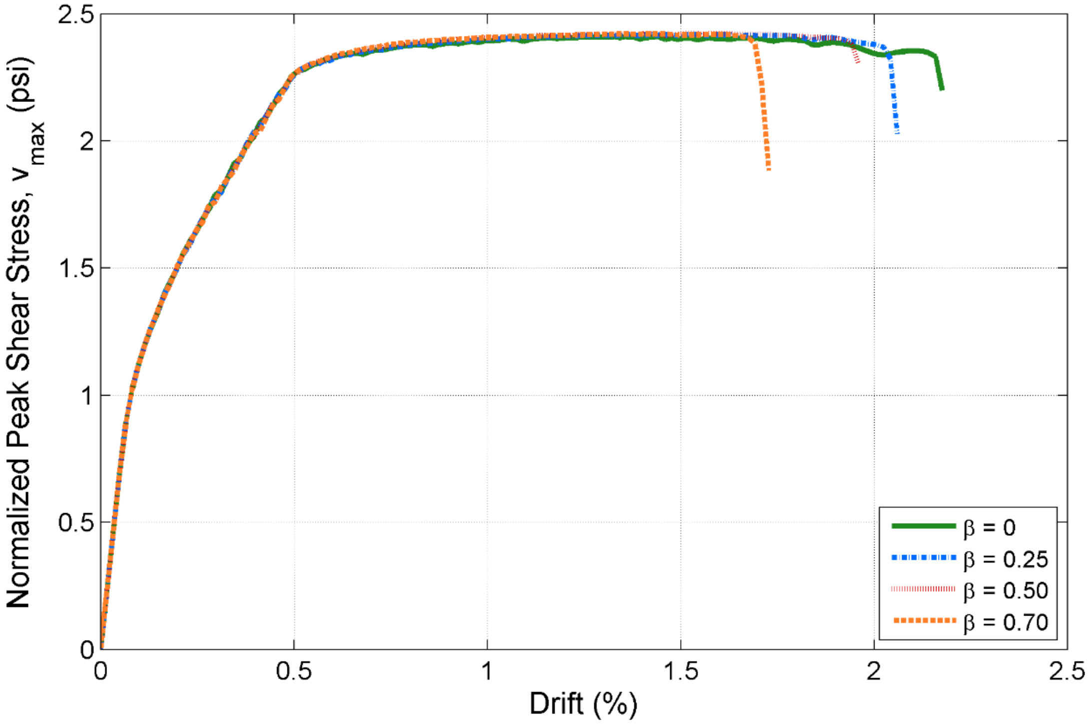

Figure 3.13 – Specimen S6 Normalized Peak Shear Stress vs. Drift for Varied β

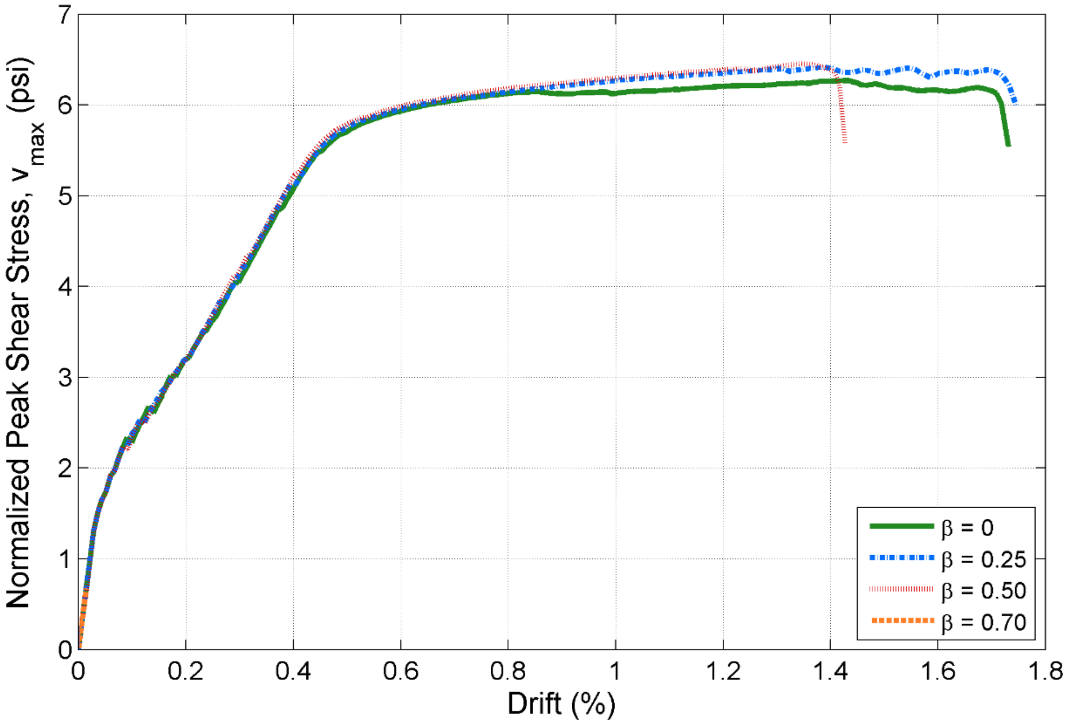

Figure 3.14 – Specimen RW2 Normalized Peak Shear Stress vs. Drift for Varied β

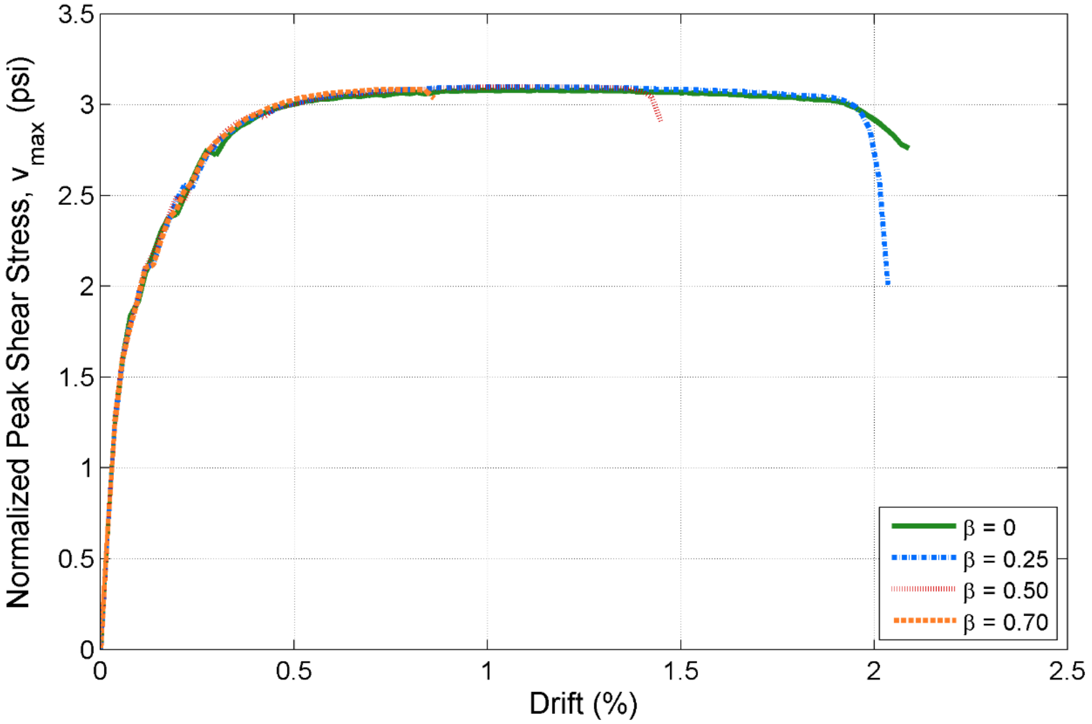

Figure 3.15 – Specimen WR0 Normalized Peak Shear Stress vs. Drift for Varied β

3.3.3 Shear Factor Coefficient, S_F

The Shear Factor Coefficient, S_F, defines the relationship between stiffness normal to the crack surface and parallel to the crack stiffness. Characterizing the shear strength of cracked concrete is complicated and based on a variety of parameters (Vecchio and Nieto 1991, Stevens et al. 1991). In the NC2 concrete model, the shear stiffness parallel to the crack surface, K_s, is defined equal to a multiple of the tensile stiffness normal to the crack surface as shown in Figure 3.16.

$$K_s = S_F * K_t \qquad \textit{(Eq. 3.10)}$$

The ATENA user's manual recommends an S_F range from 20 to 200. For the current study, the S_F parameter was selected on the basis of simulated response data for S6, RW2, and WR0 specimens, as noted in Section 3.3. These are presented in Figures 3.21-3.23.

The selection of an S_F value is based on the criteria outlined above:

- The load-displacement figures show that the impact of the shear factor on response is consistent from $S_F = 50$ to 100.
- The lower value of $S_F = 20$ leads to premature sliding failure in the case of WR0. Response at $S_F = 50$ and above does not significantly alter wall behavior and avoids sliding failures that are not indicative of experimentally-observed wall response.
- Response is stable up to $S_F = 100$.

These lead to the use of $S_F = 50$. System response is relatively insensitive to the parameter in this range, and it avoids the sliding failures posed by $S_F = 20$ and numerical instability of $S_F = 200$.

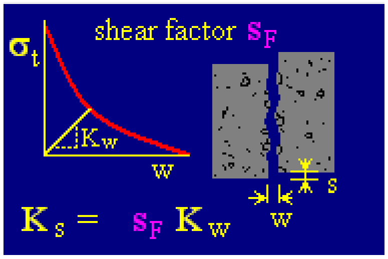

Figure 3.16 – ATENA Documentation for Shear Retention Factor (Cervenka et al. 2013

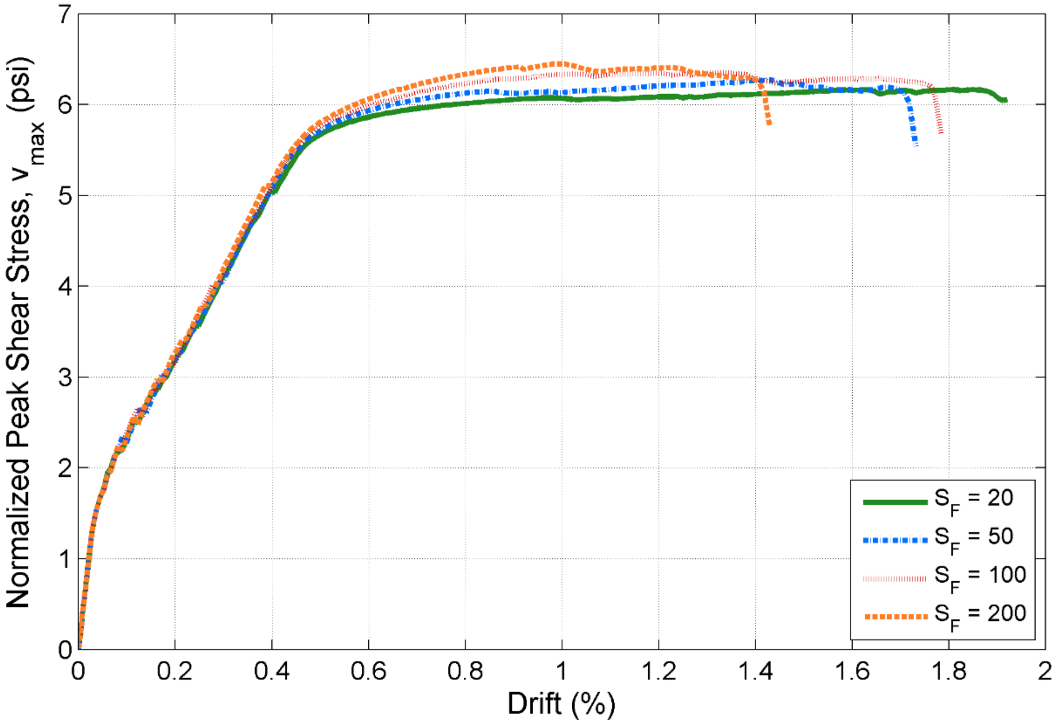

Figure 3.17 – Specimen S6 Normalized Peak Shear Stress vs. Drift for Varied S_F

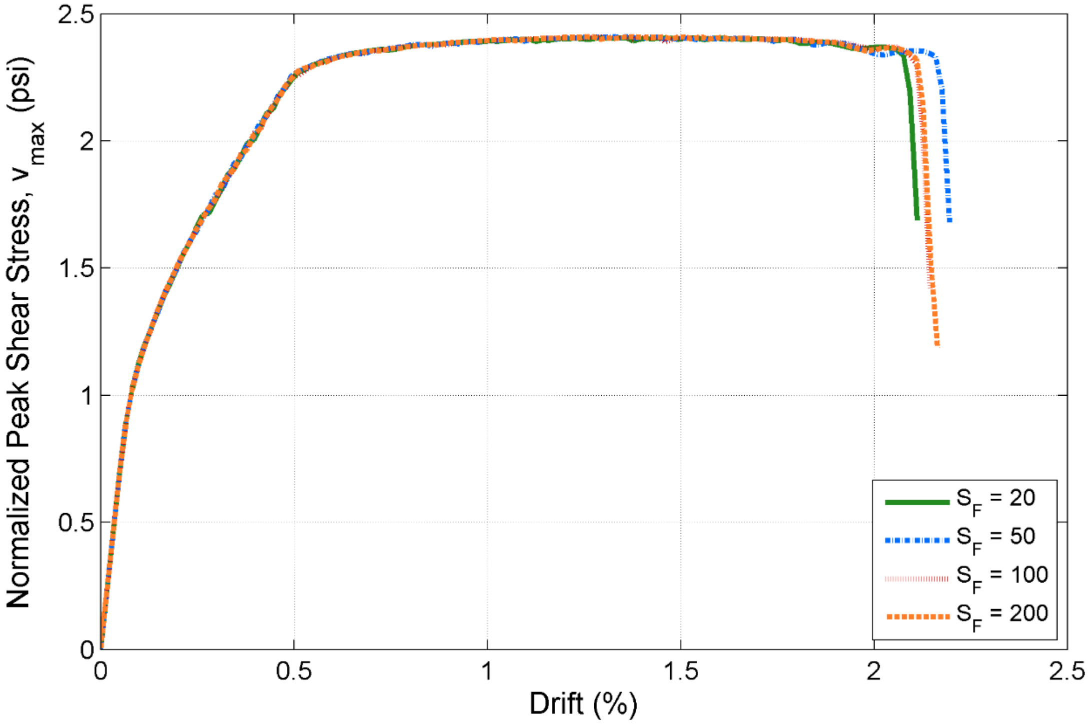

Figure 3.18 – Specimen RW2 Normalized Peak Shear Stress vs. Drift for Varied S_F

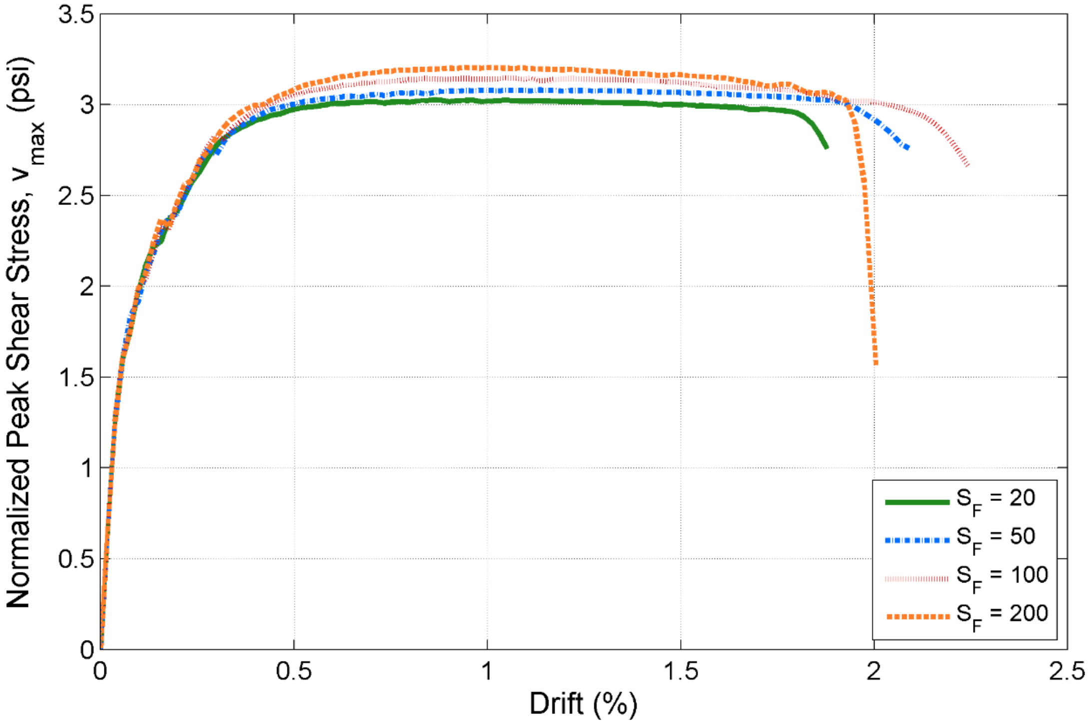

Figure 3.19 – Specimen WR0 Normalized Peak Shear Stress vs. Drift for Varied S_F

3.3.4 Tension Stiffening

Tension stiffening refers to the non-zero residual tensile strength that is introduced into a concrete tension response model to represent the stiffness and strength provide by the volume of uncracked concrete that exists between cracks (Cervenka et al. 2013). Including tension stiffening could be expected to increase the strength and stiffness of the model as tensile stress normal to a crack surface does not decay to zero at large strain demands. Including tension stiffening could also be expected to enhance numerical stability as concrete maintains some strength and stiffness normal to crack surfaces at large strain demands.

The NC2 concrete model in ATENA employs a tensile stress versus strain response model, normal to a crack surface, that deteriorates either exponential or linearly with increasing strain to the residual tensile strength. Figure 3.20 shows the exponential curve decaying to the residual strength; in this figure:

- f_t is the concrete tensile strength, which is considered to be a fundamental material property and may be determined from laboratory testing of plain concrete or estimated per CEB-FIP Model Code 1990.
- G_f is the concrete fracture energy, which is considered to be a fundamental material property and may be determined from laboratory testing of plain concrete beams or estimated per Vos et al. (1983).
- L_t is a mesh dependent characteristic length, which is computed for each element using the approach described in Section 3.2.3.
- $c_{ts}f_t$ is the residual tensile strength for the concrete; based on the work of Cervenka et al. (2013), the ATENA documentation recommends that $0.00 < c_{ts} < 0.05$.

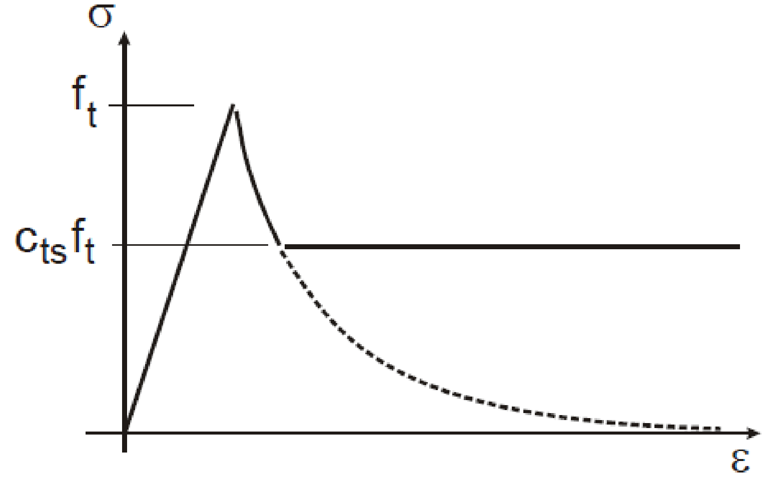

Figure 3.20 – ATENA Documentation for Tension Stiffening Parameter

To investigate the impact of tension stiffening on simulated response, a parameter study was conducted for wall specimens S6, RW2, and WR0. The simulated base shear versus drift curves for the specimens are presented in Figures 3.21-3.23. The data in these figures and observation of simulation results indicate

- The use of tension stiffening values greater than 1% typically results in significantly greater strength and deformation capacity than is observed for the case of zero tension stiffening.
- The use of a tension stiffening value of 1% can increase deformation capacity and may slightly increase strength.
- Model stability can be improved by the use of 1% tension stiffening.

Given the results above, all wall analyses were initial run with zero tension stiffening. If numerical instability was observed, tension stiffening was increased to 1% in an effort to improve numerical stability.

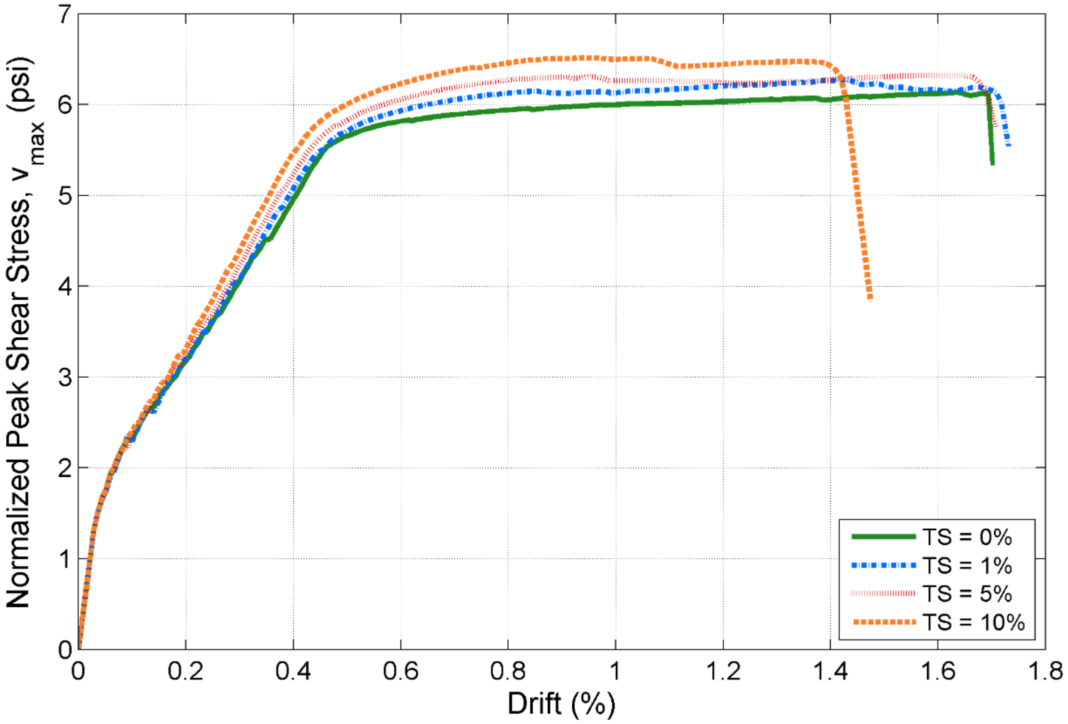

Figure 3.21 – Specimen S6 Normalized Peak Shear Stress vs. Drift for Varied Tension Stiffening

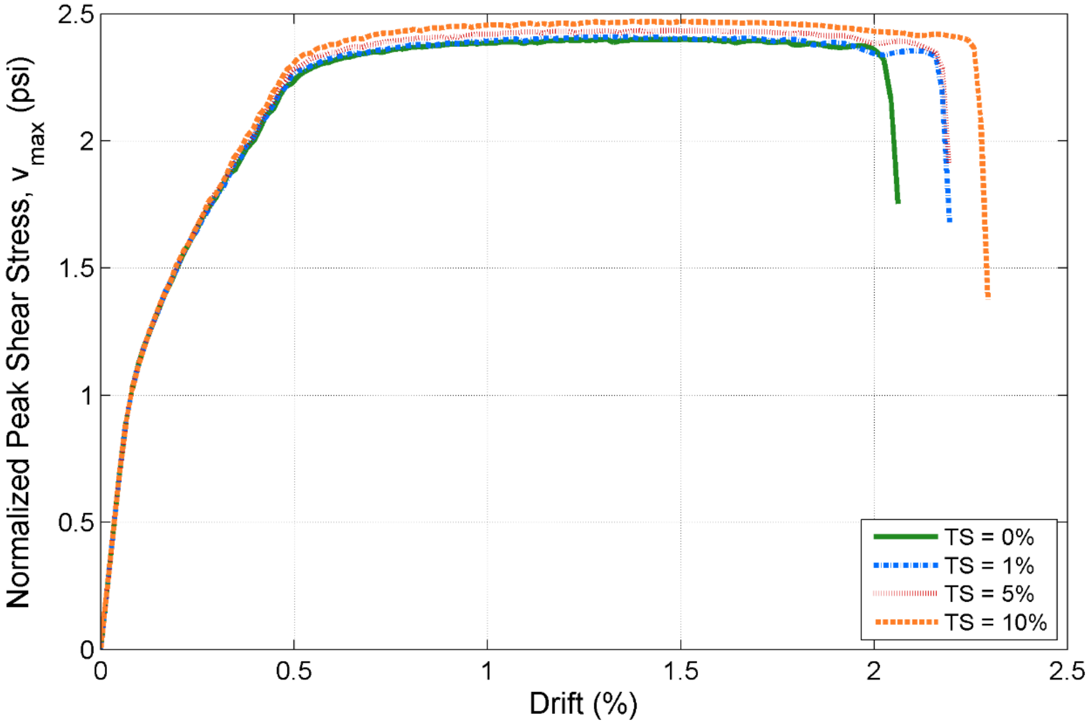

Figure 3.22 – Specimen RW2 Normalized Peak Shear Stress vs. Drift for Varied Tension Stiffening

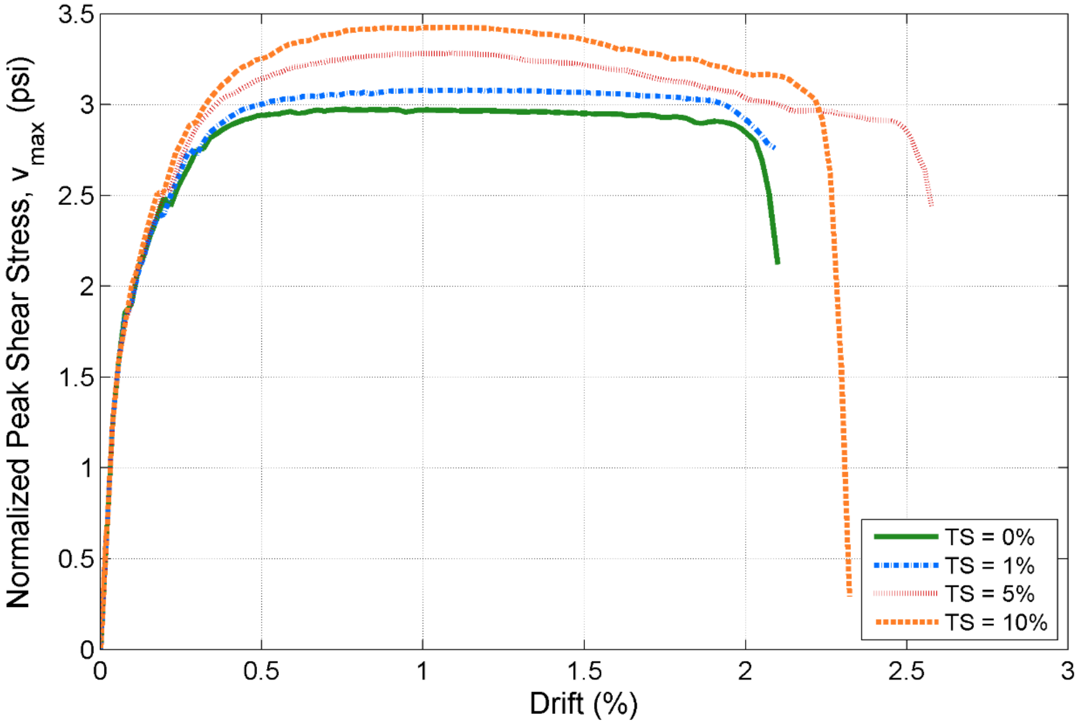

Figure 3.23 – Specimen WR0 Normalized Peak Shear Stress vs. Drift for Varied Tension Stiffening

3.3.5 Smeared Reinforcement

ATENA supports modeling of steel reinforcing bars as discrete axial (i.e. truss) elements that are embedded in concrete elements and as smeared reinforcement within a concrete element. Discrete reinforcement provides a slightly more accurate representation of the true wall configuration, as reinforcement strains are computed and reinforcement forces act at the true location of the steel. However, the use of smeared reinforcement has the potential to reduce model building time and computational demand as well as provide numerical stability as each concrete element is stiffened by the addition of some reinforcing steel.

Smeared reinforcement is calculated in ATENA as the percentage of the concrete element area that is replaced by reinforcement. A 1% value ($c_{ts} = 0.01$) for smeared reinforcement in ATENA replaces 1% of the selected 2-dimensional concrete surface with the specified reinforcement material model. The calculation for this is:

$$A_{s,sm} = A_{c,proj}\rho_{sm} \qquad \textit{(Eq. 3.11)}$$

Where $A_{s,sm}$ is the area of reinforcement crossing the concrete surface, $A_{c,proj}$ is the concrete surface on which the reinforcement is smeared, and ρ_{sm} = smeared reinforcement ratio.

The majority of boundary element reinforcement was modeled as discrete bars, as accurate representation of the location of these bars could be expected to affect simulated response. However, web region reinforcement was typically smeared as the reinforcement area was small and smearing the reinforcement reduced computational demand without affecting simulation results. In some cases, web reinforcement was modeled discretely as this was found to improve numerical instability; this is discussed in Section 3.6.

Boundary element reinforcement in this model includes both discrete and smeared reinforcement. This is added to the model as it provides additional model stability. In the case of purely discrete boundary element reinforcement, there exist plain concrete elements which do not contain any steel, and these elements often exhibit numerical instability when subjected to large strain demands. By providing a small portion of smeared reinforcement, it is possible to avoid the stability issues associated with these elements while not affecting the model result.

Smeared Longitudinal Reinforcement

To investigate the impact of smeared versus discrete longitudinal boundary element reinforcement on predicted response, for each of the study walls, four analyses were conducted in which 5% to 25% of the vertical boundary element reinforcement was smeared across the boundary element with the remaining 95% to 75% of the vertical boundary element reinforcement modeled using discrete bars. Figures 3.24-3.26 show the results of these analyses. The data in these figures support the following observations:

- Smearing less than 25% of the longitudinal boundary element reinforcement has no effect on simulated stiffness or strength.
- With a portion (5% to 25%) of the boundary element longitudinal reinforcement represented as smeared reinforcement rather than discrete bars, it is possible to see a slight increase in deformation capacity; however, values of 5-10% typically produce consistent prediction of specimen deformation.
- Models are most stable with 5-15% of longitudinal boundary element reinforcement represented by smeared reinforcement in place of discrete bars. Models with no smeared reinforcement are

often unstable, and those with 15-25% smeared also have potential for numerical error (Figure 3.25).

On the basis of these observations it was decided that 10% of the longitudinal boundary element reinforcement be represented by smeared reinforcement. This small amount of smeared longitudinal reinforcement allows for a greater level of model stability without affecting system response.

Smeared Confining Reinforcement

To investigate the impact of smeared versus discrete confining reinforcement on predicted response, for the study walls which utilize confining reinforcement (i.e., RW2 and S6), analyses were conducted in which 10% to 50% of the confining boundary element reinforcement was smeared across the boundary element with the remaining 90% to 50% of the confining boundary element reinforcement modeled using discrete bars. Figures 3.27-3.28 show the results of these analyses. The data in these figures support the following observations:

- Smearing less than 30% of the boundary element confining reinforcement has no effect on simulated stiffness, strength or deformation capacity.
- Representing more than 30% of the confining boundary element reinforcement as smeared reinforcement increases the deformation capacity of the wall specimens, as shown in Figures 3.27-3.28. The smeared portion of confining reinforcement has a significant and predictable impact on deformation capacity.
- Gross smeared reinforcement ratios greater than 0.20% may also increase the deformation capacity of the wall specimens. This occurs with the “Horiz 30%” case shown in Figure 3.27. It is recommended that gross smeared reinforcement ratios be limited to a maximum of 0.20%.
- It is possible to achieve numerical stability by representing 10-25% of the confining boundary element reinforcement as smeared reinforcement, with the most stable behavior occurring in models which have 25% of confining reinforcement represented by smeared reinforcement.

On the basis of these observations it was decided that 25% of the boundary element confining reinforcement be represented by smeared reinforcement, with ρ_{sm} not to exceed 0.20%. This application of smeared confining reinforcement allows for a greater level of model stability without affecting system response.

The application of reinforcement in this model is summarized in Table 3.6.

Table 3.6 – Summary of Reinforcement Configuration in ATENA

Wall Region	**Horiz./Conf.**		**Longitudinal**	
	Discrete	**Smeared**	**Discrete**	**Smeared**
Upper boundary element	90%	10%	0%	100%
Lower boundary element	90%	10%	75%	25%
Web	0%	1000%	0%	100%

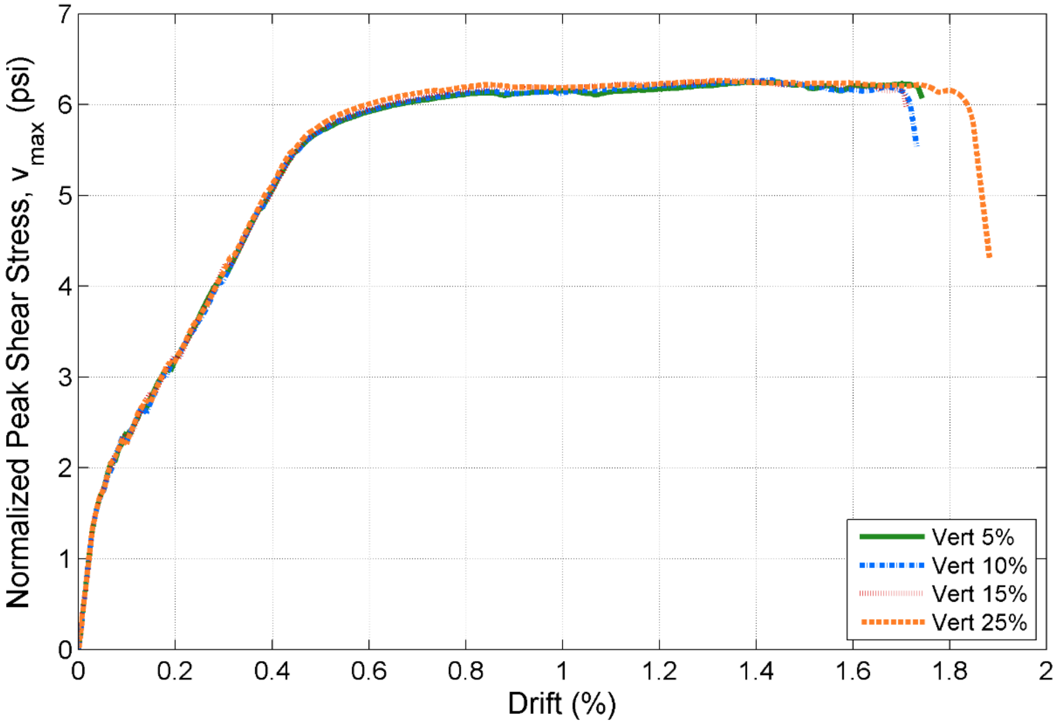

Figure 3.24 – Specimen S6 Normalized Peak Shear Stress vs. Drift for Varied Smeared Longitudinal Reinf.

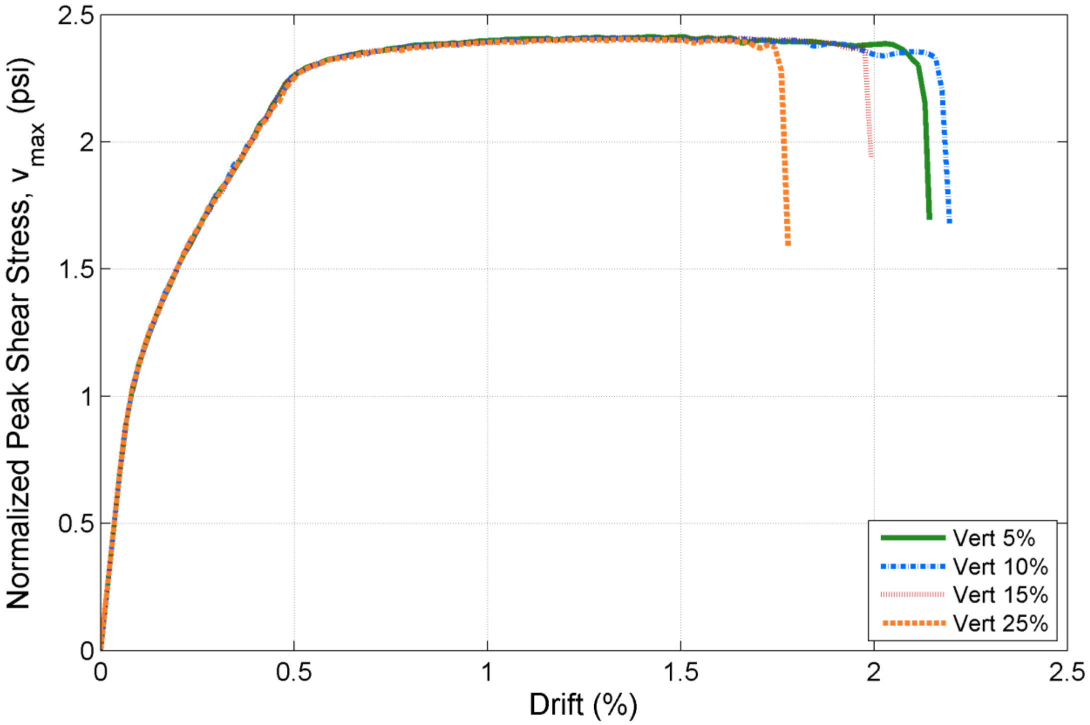

Figure 3.25 – Specimen RW2 Normalized Peak Shear Stress vs. Drift for Varied Smeared Longitudinal Reinf.

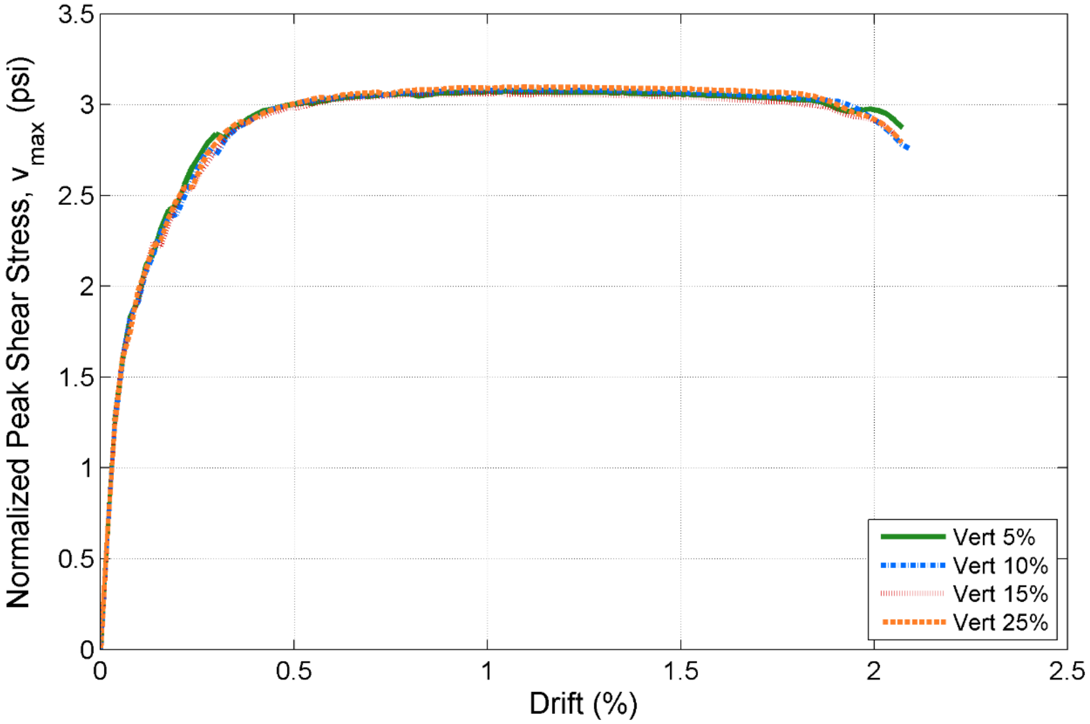

Figure 3.26 – Specimen WR0 Normalized Peak Shear Stress vs. Drift for Varied Smeared Longitudinal Reinf.

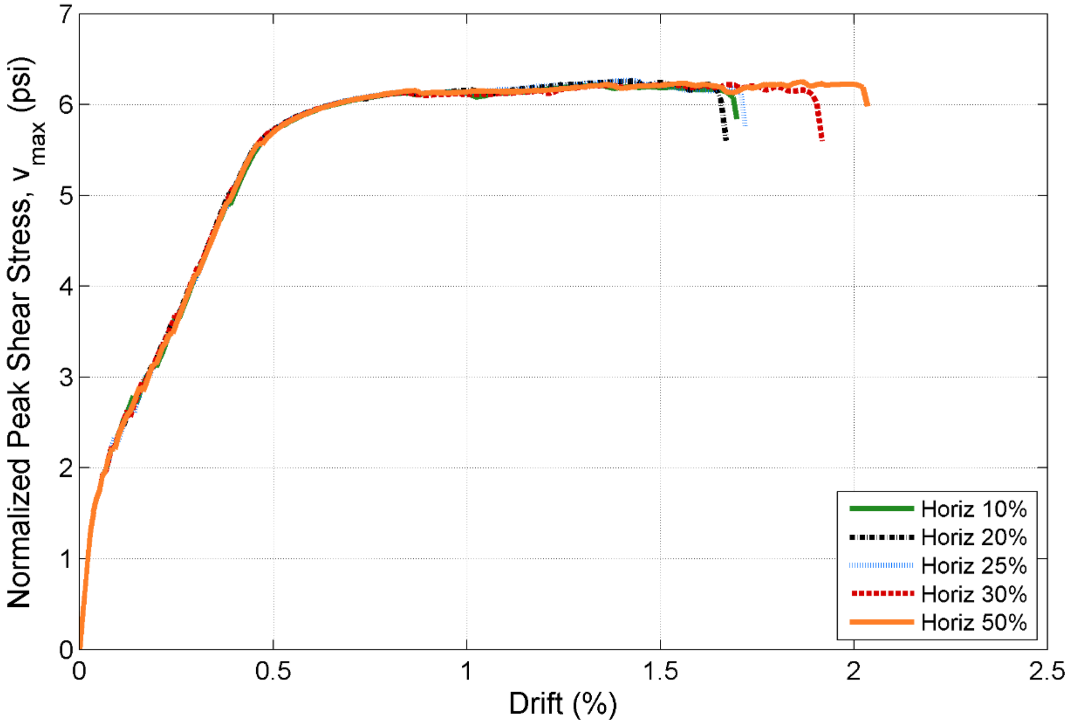

Figure 3.27 – Specimen S6 Normalized Peak Shear Stress vs. Drift for Varied Smeared Conf. Reinf.

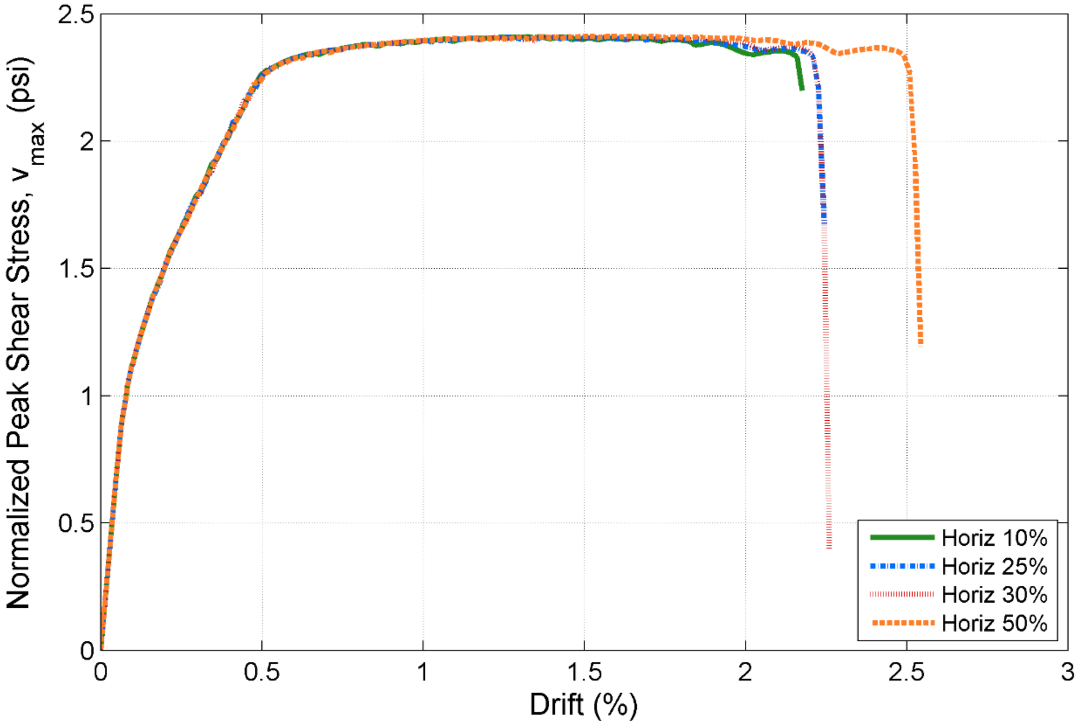

Figure 3.28 – Specimen RW2 Normalized Peak Shear Stress vs. Drift for Varied Smeared Conf. Reinf.

3.4 DETERMINATION OF A CB VERSUS A BR FAILURE

Accurate simulation of the mechanism that determines loss of lateral load carrying capacity is an objective of this model calibration effort. Previous work by others (Pugh 2012) suggests that for flexure-controlled planar rectangular walls, significant loss of lateral load carrying capacity typically results from either compression-buckling (CB) failure, characterized by simultaneous crushing of boundary element concrete and buckling of boundary element longitudinal reinforcement, or buckling-rupture (BR) characterized by rupture of previously buckled longitudinal reinforcement. Using ATENA, CB versus BR failure may be determined on the basis of the tensile strain in the boundary element reinforcement and the compressive stress in the opposite boundary element.

Determining when reinforcing steel will exhibit significant compressive strength loss due to buckling is complicated, and buckling is not captured by the ATENA reinforcing steel model. Thus, determining if a wall exhibits strength loss due to a buckling-rupture failure can only be accomplished by post-processing ATENA simulation data. To establish criteria for determining the onset of strength loss due to buckling rupture, the models that represent BR failures do not experience failure at the experimentally recorded value because ATENA does not have a buckling model for reinforcement elements. To observe the experimental behavior, the analysis of each BR wall model is stopped after reaching the drift at which it failed in the lab. This experimental failure point then yields data which can be used to calibrate a buckling-rupture post-processing method which can identify these failures in ATENA.

Ten walls from the dataset were used to calibrate the buckling-rupture post-processing method; these walls met the following requirements:

- Reinforcing steel is not spliced at the base of the wall where moment demand is greatest and inelastic action is expected.
- Reinforcing steel has a ductility typical of modern construction, where the fracture strain of the longitudinal reinforcement ($\varepsilon_{u,BE}$) is greater than 0.10 in/in.
- The envelope to the measured response history is accurately represented by the numerical simulation up to the point of strength loss in the laboratory.
- Reinforcing configuration is typical of modern construction.
- The BR failure mode is clearly observed in the laboratory.

Table 3.7 shows the tensile strain in the longitudinal boundary element reinforcement (ε_t) in each of the ten qualifying wall specimens at failure. Table 3.8 shows the three walls with low-ductility steel that failed to qualify for this calibration study.

Table 3.7 – Tensile Strains Observed in Wall Simulations at Failure

Specimen	**Failure Mode**	ε_t	$\varepsilon_{u,BE}$	$\varepsilon_t/\varepsilon_{u,BE}$
--	--	In/in	In/in	%
RW2	CB	0.031	0.10	30.9
S6	CB	0.028	0.15	18.7
WR0	CB	0.041	0.15	27.3
RW-A20-P10-S38	CB	0.057	0.19	30.0
RW-A20-P10-S63	CB	0.054	0.19	28.4
RW-A15-P10-S51	CB	0.056	0.19	29.5
RW-A15-P10-S78	CB	0.048	0.19	25.3
R1	BR	0.055	0.18	30.6
R2	BR	0.059	0.18	32.8
RW1	BR	0.033	0.10	33.2

Table 3.8 – Tensile Strains Observed in Wall Simulations at Failure w/ Low Ductility Steel

Specimen	**Failure**	ε_t	$\varepsilon_{u,BE}$	$\varepsilon_t/\varepsilon_{u,BE}$
--	--	In/in	In/in	%
WSH2	BR	0.030	0.08	37.9
WSH3	BR	0.033	0.08	41.3
WSH5	BR	0.037	0.08	46.5

There are three eligible BR failures accounted for in this data set, with the values for Specimens R1, R2, and RW1 all falling in a tight margin between 30.6% and 33.2%. The average $\varepsilon_t/\varepsilon_{u,BE}$ value of these three walls is 32.2%. For ease of calculation, a limit of $\varepsilon_t/\varepsilon_{u,BE}$ = 33% (i.e., one-third) is defined for the rupture-buckle reinforcement model. Note that all CB failures presented in Table 3.1 exhibit values less than this 33% limit, correctly predicting the compression-buckling behavior observed experimentally, as shown in Figure 3.29. Note that this figure plots the 13 specimens included above, with the x-axis representing BR failures as specimens 1 through 6 and CB failures as specimens 7 through 13.

It is notable that the three specimens with low ductility (Table 3.8) all reach strains of 3% prior to failure. For this reason, it is recommended that the buckle-rupture failure model include a lower limit such that the strain at failure is the greater of {0.03 (in/in), $0.33\varepsilon_{u,BE}$ (in/in)}.

Figure 3.29 also shows that there are buckle/rupture failures which occur slightly below the defined tension limit, reaching the same normalized tensile strains at failure as are observed in some CB failures. This is evidence of the similar behavior observed walls which exhibit BR and CB failure modes. As discussed in Chapters 4-5, BR and CB failures exhibit similar deformation capacities and are not practically different from a design perspective.

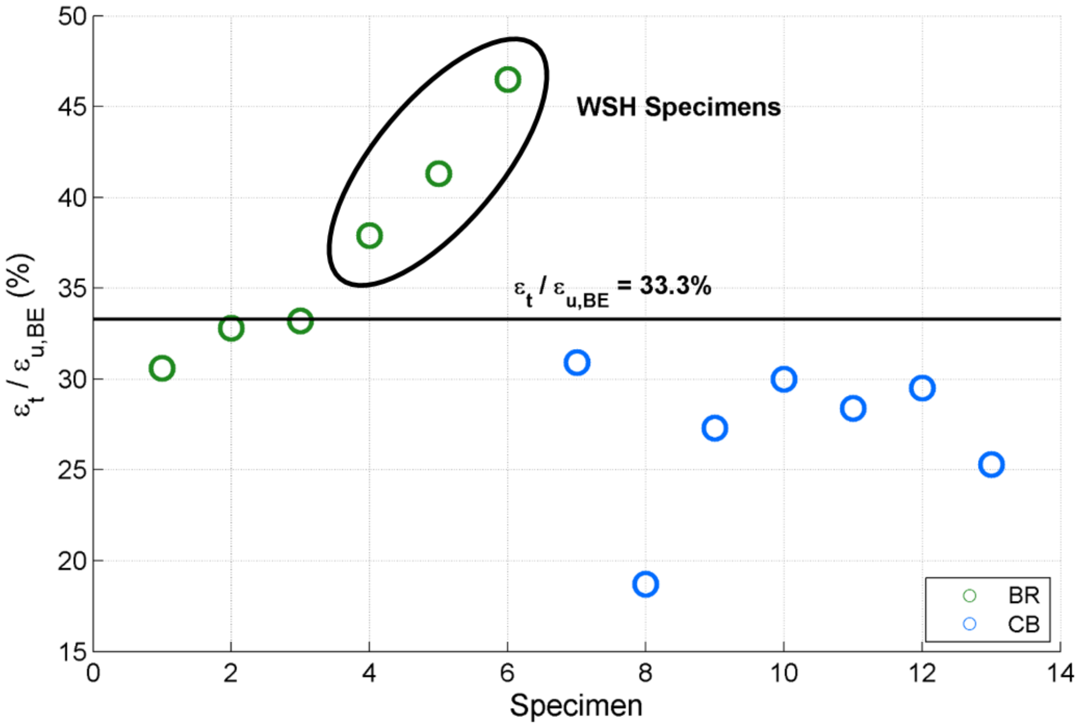

Figure 3.29 – Normalized Tensile Strain at Failure for Wall Specimens

An ideal model would include information about BR and CB failures in the reinforcement models. Specifically, the reinforcement material model would include the one-third tensile limit as well as a limit on compression defined by the strength of the concrete to which it is bonded. However, as numerical instability is a significant concern in this analysis, it was not possible to employ these limits, creating the need to post-process results to determine failure mode.

3.5 POST-PROCESSING AND DETERMINING FAILURE MODE IN ATENA

Given the need for post-processing to determine the onset of a buckling-rupture failure as well as the potential for analyses to fail to converge due to numerical instability, it is necessary to establish criteria for identifying the onset of failure. These criteria are listed below. Note that concrete is determined to have crushed when compressive stress diminishes to 30% of peak strength.

Case 1: Failure determined by simulated strength loss in excess of 20% of maximum strength:

- If the concrete has crushed (i.e., diminished to 30% of peak strength) and $\varepsilon_t/\varepsilon_{u,BE}$ is less than 33%, failure is classified as a CB failure.
- If the concrete has crushed and $\varepsilon_t/\varepsilon_{u,BE}$ is greater than 33%, it is necessary to consider the solution step at which $\varepsilon_t/\varepsilon_{u,BE}$ equaled 33%. If the concrete was crushed at that point, failure is classified as a CB failure. If the concrete had not crushed, failure is classified as a BR failure.

Case 2: ATENA reports a numerical error (i.e., zero pivot error).

- If $\varepsilon_t/\varepsilon_{u,BE}$ is greater than 33% and the concrete has not crushed, then failure is classified as a BR failure.
- If $\varepsilon_t/\varepsilon_{u,BE}$ is less than 33% and the concrete has not crushed (i.e., declined to a 30% residual of its peak strength), the numerical instability has caused termination of the analysis and the numerical stability of the model must be improved to enable simulation of response out to failure.
- If $\varepsilon_t/\varepsilon_{u,BE}$ is greater than 33% and the concrete has crushed, the rules for Case 1 apply.

Case 3: ATENA does not fail. The load protocol completed successfully.

- If $\varepsilon_t/\varepsilon_{u,BE}$ is greater than 33% and concrete has not crushed, a BR failure has occurred.
- If the concrete crushed at an earlier point and load transferred into the compression reinforcement, go back to that point and apply rules from Case 1. This phenomenon is characterized by the load-displacement curve exhibiting a large strength loss that is regained upon activation of the longitudinal reinforcement in compression
- If $\varepsilon_t/\varepsilon_{u,BE}$ is less than 33% and concrete has not crushed, the load protocol must be extended for the specimen to reach failure.

3.6 NUMERICAL INSTABILITY

Issues with numerical instability are common to wall analyses in ATENA, most generally when concrete elements crack under tensile loading and experience a dramatic loss of stiffness. Frequently, this arises at system yield in walls which have heavy longitudinal boundary element reinforcement and a lightly-reinforced longitudinal web region. It is also a significant concern in walls which are not subjected to axial loading. Numerical errors are generally reported as a "zero pivot" in ATENA.

The issue of instability is the biggest problem associated with this software package and is not resolved for 3 of 23 experimental wall specimens. The following approaches were taken to improve model stability:

Mesh Scheme: Numerical instability may be eliminated by introducing a biased mesh scheme. This modifies the mesh scheme described in 3.2.3 by introducing a coarse mesh in the web as well as the boundary element subjected to tension. The issues with numerical instability which arise due to the yielding of reinforcement are mitigated by the presence of larger concrete elements in the tension region. An example of this biased mesh scheme is shown in Figure 3.30.

This was not often utilized in modeling as it is preferable to have a fine and consistent mesh across the bottom of the wall. It also restricts analysis to the use of a strictly monotonic load protocol as the mesh is designed to resolve instability on only the coarsely-meshed end of the specimen.

Tension Stiffening: In some cases, model convergence is aided by the addition of tension stiffening. This provides the concrete elements with a small residual strength, which prevents concrete elements that have cracked from having zero tensile stiffness. This parameter is discussed in greater detail in 3.3.4.

Numerical Solver and Solution Algorithm: It is possible to achieve greater numerical stability by altering the numerical solver and solution algorithm:

- Numerical solver: use whichever of "LU decomposition" or "PARDISO" offers more stable results. It is recommended that "PARDISO" be used where possible as it is a more computationally efficient solver.
- Solution algorithm: It is recommended that the Full Newton-Raphson (FNR) Method be used as a default as it provides greater computational efficiency than does the Modified Newton-Raphson (MNR). The MNR is recommended if there are stability issues encountered with the FNR.

Discrete Web Reinforcement: It is possible to gain more stable response by defining web reinforcement with discrete bars rather than the smeared reinforcement recommended in Section 3.2.1. The discrete bars are more computationally expensive but may offer a greater level of stability at the point where web reinforcement yields. The use of fully-smeared reinforcement in the web concrete elements can result in a sudden loss of stiffness when the reinforcement yields. This results in numerical instability as the elements undergo large deformations, as shown in Figure 3.31.

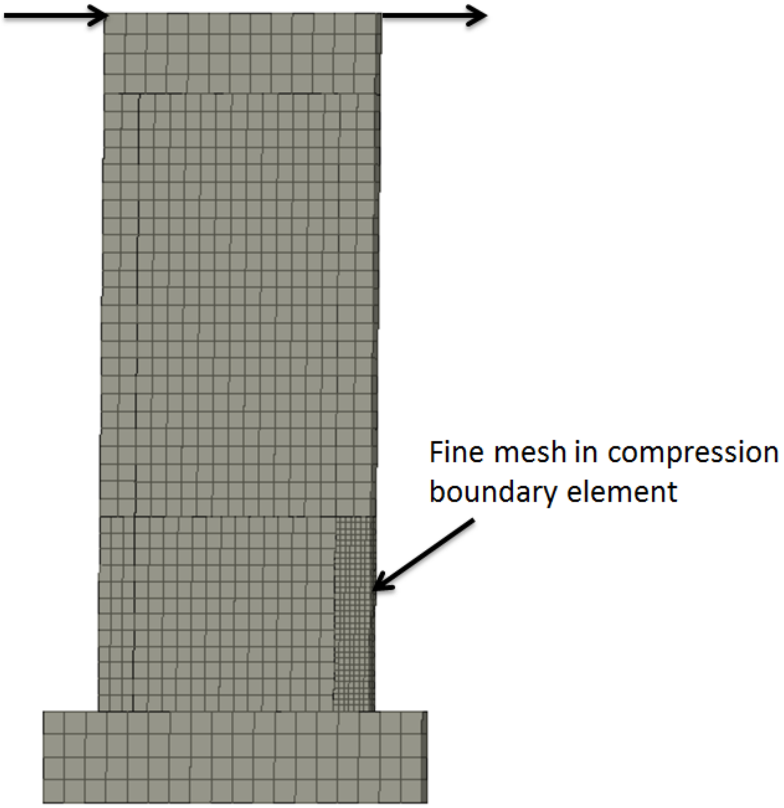

Figure 3.30 – Layout of Biased Meshing Scheme

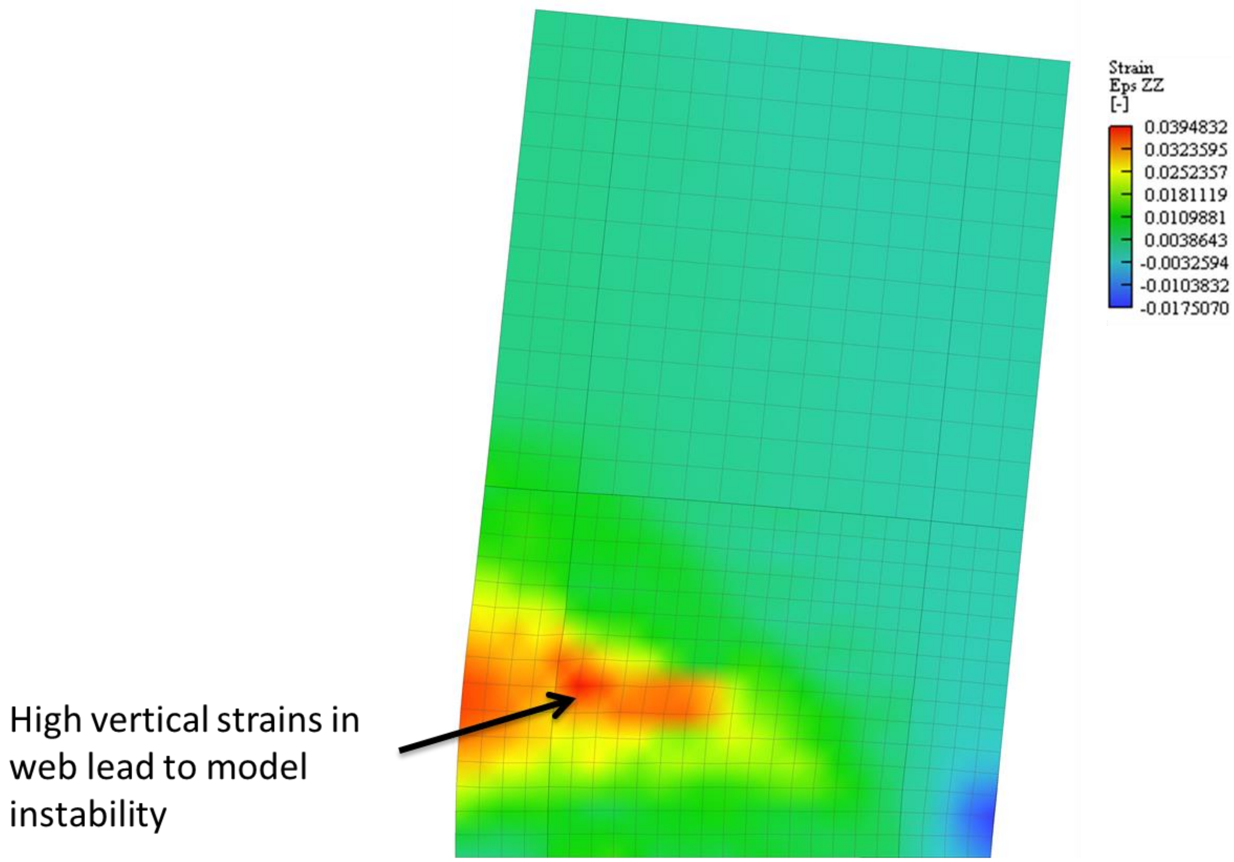

High vertical strains in web lead to model instability

Figure 3.31 – Typical Vertical Strain Contour Plot Associated with Instability

3.7 Results for Simulations of Experimental Specimens

Listed below are experimental results and simulation errors for the 19 experimental test specimens for which it was possible to complete simulation of response through to failure. For three wall test specimens (WR20, WSH1, RW-A15-P2.5-S64) numerical instability resulted in premature termination of the analysis.

Simulation results are evaluated on the basis of the accuracy with which the strength, stiffness, deformation capacity, and failure mode are simulated as described below. Note that simulated peak strength (V_{max}), stiffness to yield (Δ_y) and deformation capacity (Δ_u) are compared with quantities determined from the envelope to the measured cyclic load-displacement history for the specimen.

Table 3.9 – Simulation Accuracy for Full Experimental Wall Database

Specimen	**Stiffness**		**Strength**		**Deformation**		**Failure Mode**
	Exp. Δ_y	Sim./ Exp.	Exp. V_{max}	Sim./ Exp.	Exp. Δ_u	Sim./ Exp.	
	%	--	kips	--	%	--	--
WSH2	0.38	0.90	81.1	0.98	1.75	1.00	BR
WSH3	0.41	0.96	102.4	0.97	2.07	0.91	BR
WSH4	0.36	0.89	99.0	1.03	1.60	1.10	CB

Specimen	Stiffness		Strength		Deformation		Failure Mode
	Exp. Δ_y	Sim./ Exp.	Exp. V_{max}	Sim./ Exp.	Exp. Δ_u	Sim./ Exp.	
WSH5	0.25	0.91	97.4	0.99	1.52	0.86	BR
WSH6	0.36	0.91	135.4	0.99	2.04	0.98	CB
W1	0.52	0.92	58.8	1.06	2.98	0.96	CB
W2	0.49	0.94	62.1	1.06	2.91	1.13	BR
PW4	0.41	0.76	218.0	1.08	1.01	1.87[T]	CB
RW1	0.37	0.98	33.4	0.98	2.26	1.01	BR
RW2	0.35	0.94	35.7	0.91	2.35	0.93	CB
S6	0.41	0.93	194.3	0.98	1.65	0.96	CB
WR10	0.47*	0.56	96.7	1.04	2.82	0.98	CB
WR0	0.52*	0.50	95.4	1.04	2.14	0.99	CB
R1	0.15	1.81	27.4	0.93	2.52	1.12	BR
R2	0.34	0.95	50.4	0.92	3.25	1.01	BR
RW-A20-P10-S38	0.14	0.90	108.0	0.93	3.14	0.99	CB
RW-A20-P10-S63	0.55	0.88	166.9	0.97	3.00	1.09	CB
RW-A15-P10-S51	0.34	0.61	135.5	0.99	3.31	0.96	CB
RW-A15-P10-S78	0.40	0.87	193.2	1.05	3.00	0.92	CB

		Stiffness	Strength	Deformation
Total	Median	0.91	0.99	0.98
	COV	0.29	0.05	0.06
BR	Median	0.95	0.98	1.01
	COV	0.31	0.05	0.10
CB	Median	0.89	1.01	0.98
	COV	0.20	0.05	0.07

*Note that the yield displacement for specimens in this experimental program is discussed below.

[T] Note that experimental issues associated with Specimen PW4 are discussed below. This specimen is an outlier per Pierce's criterion as outlined in ATC-58 (2012) and thus not included in the COV calculation.

3.7.1 Load-Displacement Response Typical of Model Accuracy

Figures 3.32-3.34 show simulated and measured base shear versus drift histories for are a representative set of the walls in the dataset. These five representative walls are discussed in greater detail in Chapter 4. Plots for all specimens are included in Appendix A.

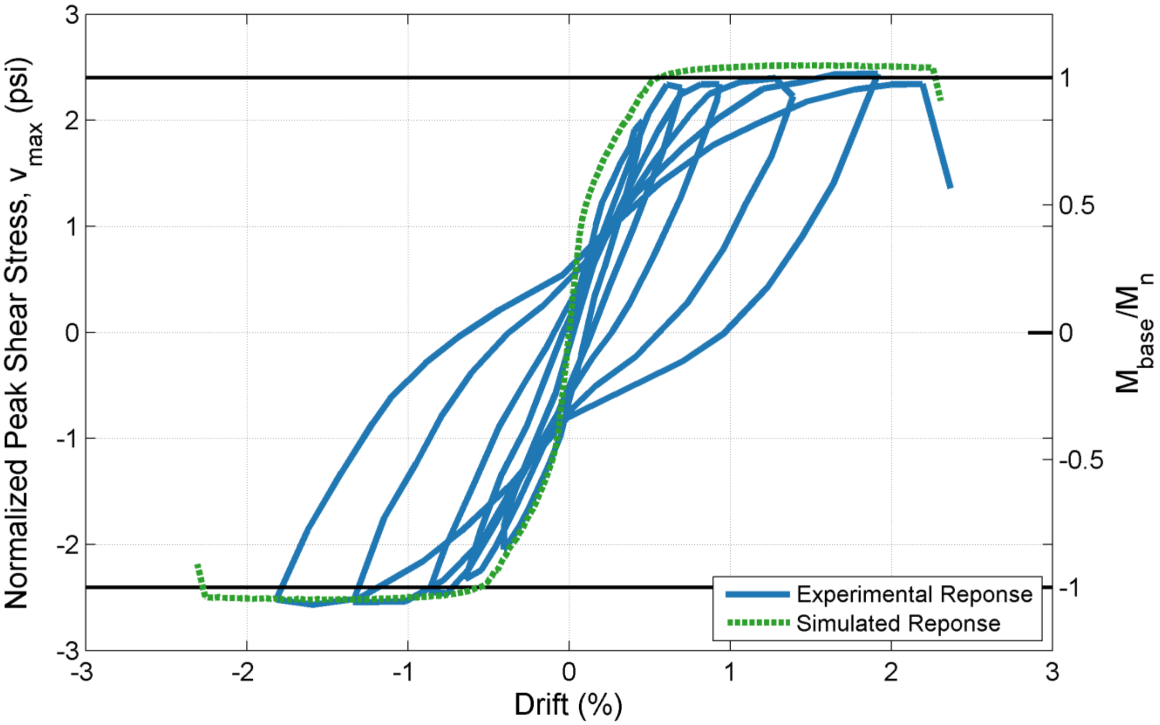

Figure 3.32 – Specimen RW1 Normalized Peak Shear Stress vs. Drift

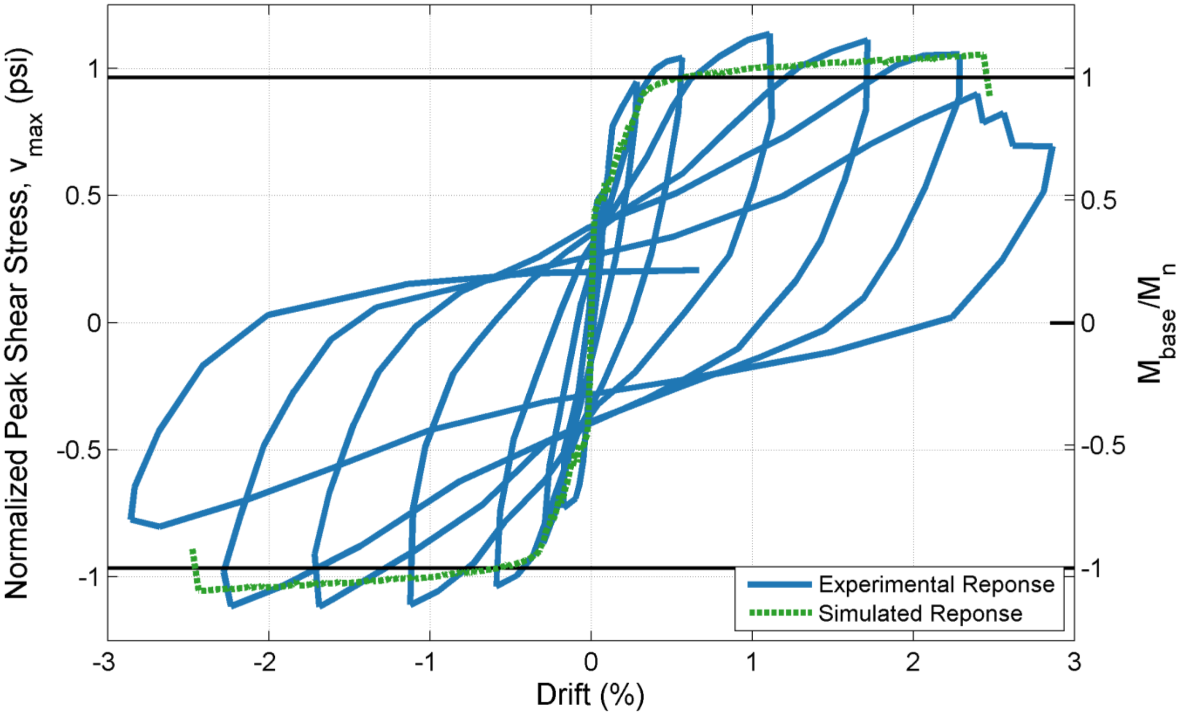

Figure 3.33 – Specimen R1 Normalized Peak Shear Stress vs. Drift

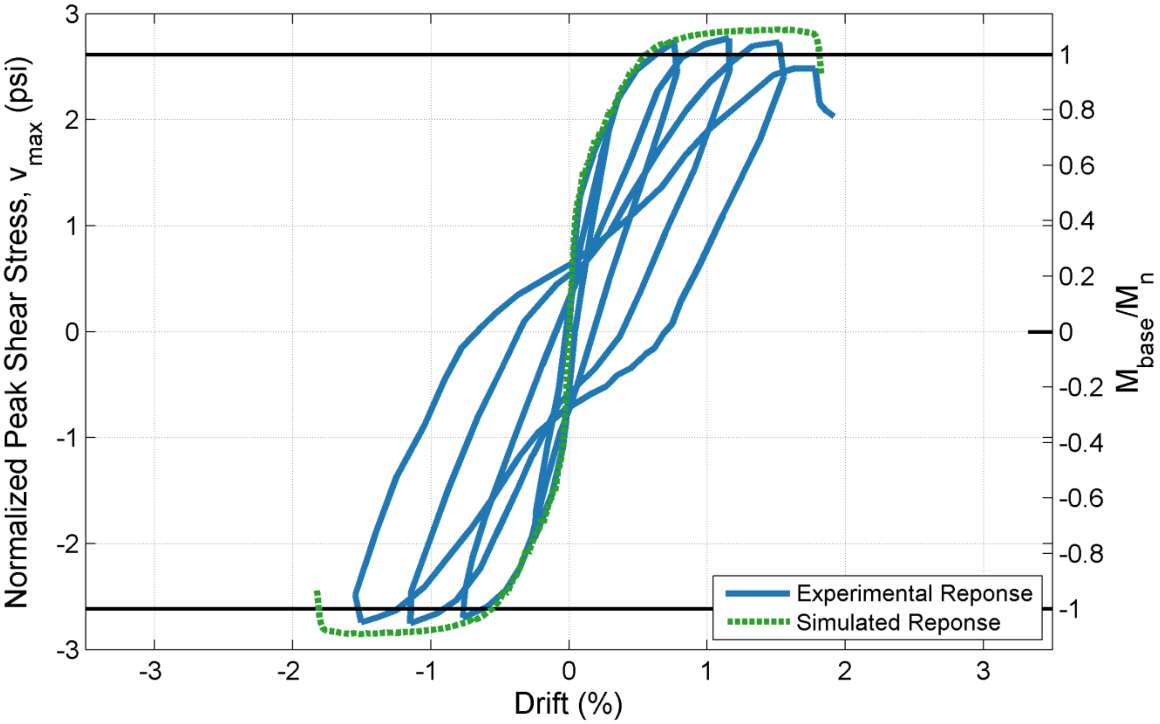

Figure 3.34 – Specimen WSH4 Normalized Peak Shear Stress vs. Drift

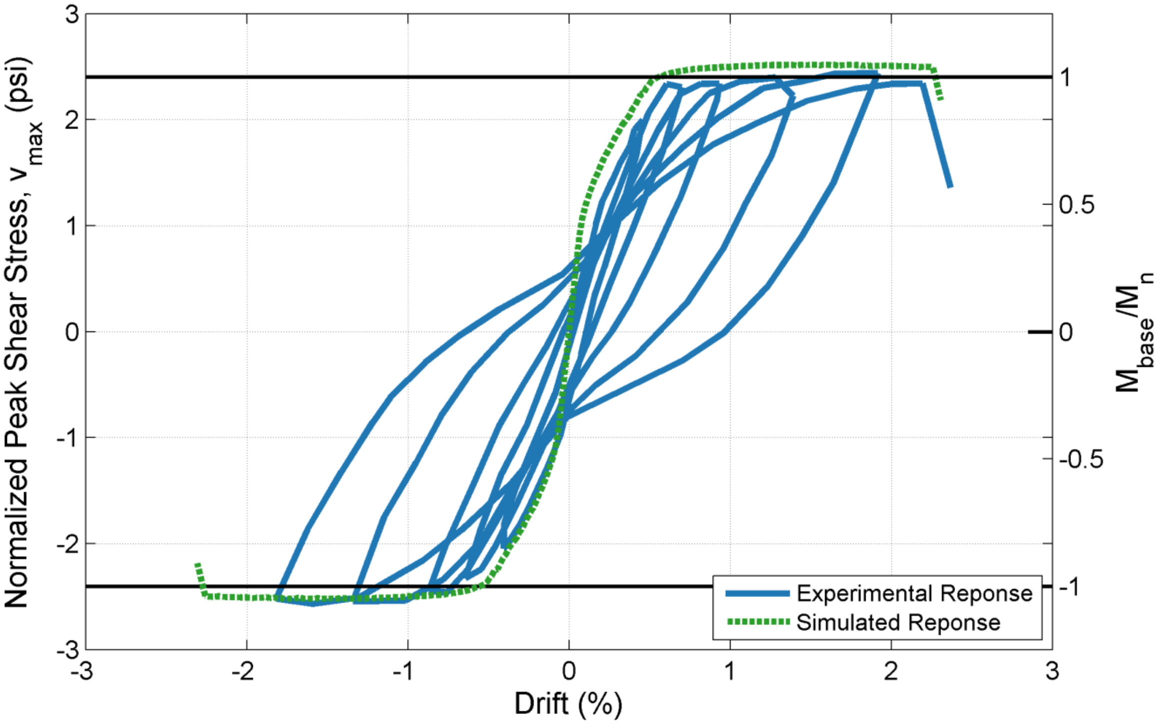

Figure 3.35 – Specimen S6 Normalized Peak Shear Stress vs. Drift

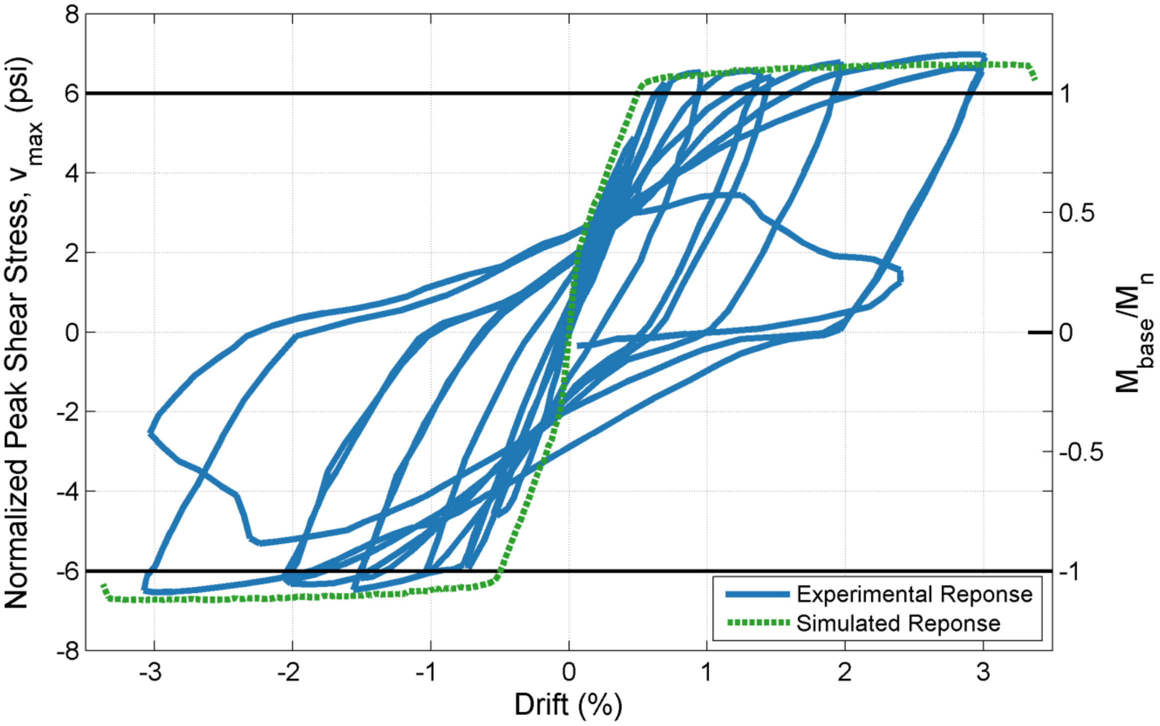

Figure 3.36 – Specimen RW-A20-P10-S63 Normalized Peak Shear Stress vs. Drift

3.7.2 Average Accuracy and Precision of Wall Simulations

The general model results and accuracy detailed in Section 3.7 are discussed below for each of the primary response parameters used in this chapter: stiffness, strength, and deformation capacity.

General Comments

- Only 19 of 22 unique walls in the database were modeled successfully. Specimens WSH1, WR20, and RW-A15-P2.5-S64 did not achieve the required numerical stability to reach failure in the ATENA model.
- 1 of the 23 total walls was not considered. Specimens S5 and S6 present the same section with different loading protocols. As the ATENA model is only capable of monotonic loading, only S6 was considered in analysis, as noted in Section 3.7.3.
- Specimen PW4 exhibits greater stiffness, strength, and deformation capacity in the simulation than is observed experimentally. This is consistent with the results of other simulation efforts (Birely 2012 and Pugh 2012). Birely (2012) attributes this to poor consolidation of boundary element concrete. As there is likely an issue with the experimental testing, experimental results for this specimen are not included in the studies of Chapter 4 and 5. This specimen is removed from the data set as an outlier using Pierce’s criterion as outlined in ATC-58 (2012).

Comments on Stiffness Prediction Accuracy

- The model does not provide and precise simulation of the secant stiffness at yield for the specimens with a mean error of -9.1% and coefficient of variation of 0.29. Note that a large portion of the uncertainty comes for Specimen R1; considering only the other 18 specimens, the coefficient of variation drops to 0.17.

- The yield stiffness is not accurately simulated for Specimens WR0 and WR10, with the model predicting much greater initial stiffness than is reported experimentally.
    - Specimens WR0 and WR10 possess the same geometry as that of WR20, which has a significantly smaller yield drift. It would be expected that the walls exhibit similar yield drifts given the similarities in longitudinal boundary element reinforcement, configuration, and geometry.
    - The model stiffness prediction is much closer to that of Specimen WR20 than that of Specimens WR0 and WR10, and the disparity is likely due to excessive shrinkage occurring in the latter specimens. Because of this, the yield value for Specimen WR20 is considered for Specimens WR0 and WR10.
- For 18 of 19 specimens, simulated stiffness is greater than the measured stiffness. As discussed above, this is attributed to the ATENA simulations not accounting for the impact of shrinkage cracking on wall stiffness, which could be expected to reduce yield drift (Pugh 2012)
- Predictions fall within a consistent window (0% to -15% error) for 17 of the 22 specimens. The model could be adjusted to account for the impact of shrinkage cracking, but the extent of this effect is difficult to quantify in the laboratory and typically not provided by the researchers. This shrinkage parameter could be calibrated to provide accurate prediction of secant stiffness to yield.
- Specimen R1 presents the only model in the data set for which the simulated stiffness is greater than that exhibited experimentally.

Comments on Strength Prediction Accuracy

- The model provides accurate and precise simulation of maximum strength, with an average error of -0.9%, coefficient of variation of 0.05, and maximum error of less than 10%.
- For specimens PW3, RW2, and RW-A20-P10-S38, strength is under-predicted with errors greater than 6%. These wall specimens exhibit significant hardening up to the point of the simultaneous concrete crushing and reinforcement buckling associated with a compression-buckling failure mode. This hardening is not captured by the ATENA analyses.
- Specimen WR10 exhibits different strength capacity in each loading direction. This is not atypical behavior for the specimens the experimental dataset, with the ATENA analyses typically consistent with the stronger of the two strength capacities. This is likely the result of poor concrete consolidation local to one end of the specimen.

Comments on Deformation Prediction Accuracy

- Wall drift capacity is accurate and precisely simulated, with an average error of -1.3% and a coefficient of variation of 0.07. With the exception of wall specimen PW4, the maximum error for all CB failures is 10%. The maximum error for all BR failures is 14.2%.
- The prediction for wall specimen PW4 has 87% error. As discussed earlier, this is attributed to poor consolidation of boundary element concrete (Birely 2012). If this wall is considered in the data set, the coefficient of variation in deformation prediction accuracy is 0.21.

3.7.3 Accuracy, Precision and Robustness of Simulations for Individual Specimens

Included below are brief discussions of the success and model parameters for each of the 23 experimental specimens. These are grouped by experimental program.

- Dazio, et al, WSH1-WSH6:
    - The web reinforcement for Specimen WSH1 has a fracture strain of 0.02 in/in. This low-ductility web reinforcement fails before significant deformation occurs in the boundary

  element. Continuing the simulation beyond the point at which the web reinforcement fractures results in numerical instability. Thus, the response of Specimen WSH1 is not successfully simulated to the point of strength loss due to buckling-rupture or compression-buckling failure of the boundary elements. In the laboratory WSHI is observed to exhibit a BR failure mode.
  - Specimens WSH2, WSH3, WSH5, and WSH6 are all stable and were modeled using the reference model parameters.
  - Specimen WSH4 was modeled with fully-smeared horizontal reinforcement in both the web and boundary element regions. This is because the specimen does not include confining reinforcement and horizontal reinforcement provided in the web is extended to the boundary element.
- Liu, W1-W2:
  - Specimens W1 and W2 are stable and modeled using typical parameters.
- Birely, PW4
  - Specimen PW4 is stable and modeled using typical parameters.
- Thomsen et al., RW1-RW2:
  - Specimens RW1 and RW2 are stable and modeled using typical parameters.
- Vallenas et al., S5-S6:
  - Specimens S5 and S6 mainly differ in load protocol and produce similar envelopes. As the ATENA model developed in this chapter is only capable of monotonic loading, only Specimen S6 is modeled.
  - Specimens S6 is stable and modeled using typical parameters.
- Oh et al., WR0-WR20:
  - Specimens WR0 and WR10 are stable. Specimen WR10 was analyzed with a biased mesh scheme (Section 3.6). Specimen WR0 used the LU decomposition solver rather than the default solver (PARDSIO).
  - As with Specimen WSH4, Specimen WR0 does not have defined boundary element confining reinforcement. All horizontal reinforcement in the wall and boundary element regions is thus modeled as smeared reinforcement.
  - Specimen WR20 did not achieve sufficient numerical stability to successfully run to the point of specimen failure.
- Oesterle et al., R1-R2:
  - Specimens R1 and R2 are stable and modeled using typical parameters.
- Tran, RW-A20-P10-S38, RW-A20-P10-S63, RW-A15-P10-S51, RW-A15-P10-S78, RW-A15-P2.5-S64:
  - Specimens RW-A20-P10-S38, RW-A20-P10-S63, RW-A20-P10-S51, and RW-A15-P10-S78 are stable after making several changes to the typical model. All are modeled in full (i.e., no symmetry boundary condition) use discrete reinforcing bars in the web. All use a Modified Newton-Raphson solution algorithm.
  - Specimens RW-A15-P2.5-S64 is not modeled successfully in this analysis. This is another example of ATENA exhibiting numerical instability at low axial load ratios as this wall (ALR < 2%) differed mainly in ALR from the other four walls in the experimental program.

3.8 CONCLUSIONS

Numerical instability was the primary issue associated with the development of this model. It was particularly difficult to achieve numerical stability when modeling walls without axial load or with heavily-reinforced boundary elements and lightly-reinforced web regions. No specimens were successfully subjected to a cyclic load protocol that progressed to failure. The application of smeared reinforcement, tensioning stiffening, and different solution algorithms, along with the monotonic load protocol, allowed for the successful modeling of 19 of 22 unique specimens.

It is possible to accurately assess the stiffness, strength, deformation capacity, and failure mode of experimental specimens with the model calibrated in this chapter , as seen in the statistics in Table 3.10. The calibration of the concrete deformation capacity and buckle/rupture reinforcement model allowed for accuracy and precision in the prediction of deformation capacity. Strength for both failure modes was accurately and precisely predicted, but the model exhibited less precision in predicting stiffness, with outliers present for both BR (Specimen R1) and CB (Specimens WR0 and WR10) failures. With the exception of these outliers, it would be possible to calibrate a shrinkage model to correctly predict the stiffness of BR and CB failures with both accuracy and precision.

Table 3.10 – Ratios of Simulated/Experimental and Coefficients of Variation for Experimental Wall Simulations (Grouped by Failure Mode)

	Stiffness		**Strength**		**Deformation**	
	BR	CB	BR	CB	BR	CB
Mean	0.95	0.89	0.98	1.01	1.01	0.98
COV	0.31	0.20	0.05	0.05	0.10	0.07

4 NUMERICAL INVESTIGATION OF WALL BEHAVIOR

In Chapter 3, a nonlinear finite element analysis method is presented, calibrated and validated using a dataset of 23 rectangular reinforced concrete walls subjected to axial and lateral loading. The experimental dataset included tests with a wide range of shear stress demands, axial load ratios, confinement details, and reinforcement ratios. In addition, the walls exhibited different failure modes, including bar fracture (tension) and boundary element crushing (compression). The evaluation of analysis results shows that the modeling approach provides accurate simulation of initial stiffness, strength, deformation capacity and failure mode.

In this chapter, the simulated response of a set of five *reference* walls from the wall database is investigated in more depth.

Section 4.1.1 introduces the reference walls, detailing the unique characteristics offered by each wall that merit inclusion in the reference set. This is followed in Sections 4.1.2-4.1.6 by a discussion of simulated response, presenting the load-displacement response and stress and strain contour plots for each reference wall. These results are then used in Section 4.2 to compare the behavior of different failures, ultimately leading to a summary of behavior observed in each failure mode (Section 4.3).

4.1 FINITE ELEMENT ANALYSIS OF REFERENCE WALLS

The FE approach was evaluated using the full set of walls, as presented in Chapter 3. A subset of five reference walls were selected to provide a detailed look at different behaviors and failure modes; the detailed results include the study of graphical stress and strain contour plots for each wall, information which is then used to provide a greater understanding of wall failure.

The walls were selected to study the accuracy of the model for variation in loading (shear and axial) and geometry (wall length to thickness ratio) where accuracy is judged using the global parameters of peak strength and drift at the onset of strength loss. Table 4.1 presents the selected walls.

The stress and strain contour plots for each wall are presented at three points corresponding to: (1) the nominal moment strength, M_n, (2) initial strength degradation, and (3) midpoint between the peak and initial strength degradation. Simulated wall stiffness is also computed. While the strength, deformation capacity, and failure mode are key behavioral aspects which reflect the ultimate performance of the wall specimens, the stiffness is ultimately less influential in behavior. The wall stiffness is also influenced by shrinkage resulting in a section that is more flexible than predicted by the FE model.

Section 4.1.1 provides all necessary information to model and evaluate each reference wall, including wall geometry, loading, material properties, reinforcing details, and a detailed brhnnheakdown of ACI 318-14 compliance for the confinement detailing of each specimen boundary element. Sections 4.1.2 to 4.1.6 present the simulated response of each reference wall, including the load-displacement curve, accuracy of predicted response relative to experimental data, and contour plots for both stress and strain.

4.1.1 Overview of Reference Walls

To summarize the model's capability, a set of reference walls were chosen. These walls span all critical parameters and failure modes. Table 4.1 presents a short description of each wall. Table 4.2 presents the parameters relevant to demand and geometry.

New parameters listed in Tables 4.1-4.4 are defined as follows:

- h_{eff}: effective wall height, defined as the constant ratio between the base moment and base shear.
- $f_{y,BE}$: yield strength of longitudinal boundary element reinforcing steel.
- $E_{s,BE}$: Elastic modulus of longitudinal boundary element reinforcing steel.
- $f_{u,BE}$: ultimate strength of longitudinal boundary element reinforcing steel.
- $\varepsilon_{u,BE}$: rupture strain of longitudinal boundary element reinforcing steel.
- $f_{y,v}$: yield strength of longitudinal web reinforcing steel.
- $E_{s,v}$: Elastic modulus of longitudinal web reinforcing steel.
- $f_{u,v}$: ultimate strength of longitudinal web reinforcing steel.
- $\varepsilon_{u,v}$: rupture strain of longitudinal web reinforcing steel.
- $\rho_{vert,BE}$: longitudinal reinforcement ratio for wall end region.
- $\rho_{vert,web}$: longitudinal reinforcement ratio for wall web.
- ρ_{gross}: total gross longitudinal reinforcement ratio.
- $\rho_{t,web}$: transverse reinforcement ratio for wall web.
- ρ_{vol}: volumetric reinforcement ratio for wall end region.
- $\rho_{vert,BE}$: longitudinal reinforcement ratio for wall end region.
- h_x: horizontal spacing of vertical reinforcement for wall end region.
- s_{vert}: longitudinal spacing of confining reinforcement for wall end region.
- d_b: diameter of longitudinal reinforcement for wall end region.

Table 4.1 – Description of Key Reference Wall Parameters

Specimen	**Author**	**Axial Load Ratio**	**Peak Shear Stress**	**CSAR**	**Failure Mode**
RW1	Thomsen et al. (1995)	High	Moderate	Moderate	BR
R1	Oesterle et al. (1975)	None	Low	High	BR
WSH4	Dazio et al. (2009)	Moderate	Moderate	Moderate	CB
S6	Vallenas et al. (1979)	Low	High	High	CB
RW-A20-P10-S63	Tran (2012)	Moderate	High	Low	CB

Table 4.2 – Summary of Reference Wall Demands and Failure Modes

Specimen	**Geometry**					**Loading**		**Results**			
	l_w	**t**	**H**	h_{eff}	**CSAR**	**Shear Span**	**ALR**	$V_{max}/A_{cv}f'_c{}^{0.5}$	V_b/V_n	Δ_u	**Failure Mode**
	in.	in.	in.	in.	--	--	%	psi	--	%	--
RW1	48	4	144	150	12.0	3.1	10.5	2.57	0.50	2.3	BR
R1	75	4	176	180	18.8	2.4	0.0	1.10	0.23	2.5	BR
WSH4	79.	5.9	159	180.	13.3	2.3	6.3	2.77	0.62	1.6	CB
S6	95	4.5	120	152.	21.1	1.6	4.8	6.42	0.83	1.7	CB
RW-A20-P10-S63	48	6	96	96	8.0	2.0	7.3	6.10	0.91	3.0	CB

Table 4.3 – Summary of Reference Wall Material Parameters

Specimen	**Materials**								
	$\mathbf{f'_c}$	$\mathbf{f_{y,be}}$	$\mathbf{E_{s,be}}$	$\mathbf{f_{u,be}}$	$\boldsymbol{\varepsilon_{u,be}}$	$\mathbf{f_{y,v}}$	$\mathbf{E_{s,v}}$	$\mathbf{f_{u,v}}$	$\boldsymbol{\varepsilon_{u,v}}$
	psi	ksi	ksi	ksi	in/in	ksi	ksi	ksi	in/in
RW1	4580	63	29000	93	0.1	65	29000	85	0.08
R1	6490	74.2	29000	111	0.18	75.7	29000	101.5	0.18
WSH4	5932	83.5	29000	97.9	0.07	84.7	29000	103.6	0.08
S6	5033	69.9	29000	99.6	0.15	73.5	29000	105.9	0.12
RW-A20-P10-S63	7050	68.4	29000	88.9	0.19	61.4	29000	71.3	0.071

The specimens were selected to provide variation in failure mode, axial load ratio, shear stress demand, and cross-sectional aspect ratio. The following provides a description of the variation in these parameters. A description of the variation in the three key parameters identified in Chapter 2 (CSAR, ALR, and shear demand) and various secondary parameters is presented below.

- Cross-Sectional Aspect Ratio: Spanned from an aspect ratio of 8.0 to 21.1. CSAR was identified as a key parameter in Chapter 2.
- Axial Load Ratio: Spanned from no applied axial loading (R1) to a specimen subjected to an axial load of 10.51%.
- Peak Shear Stress: Peak shear stress was identified as a key parameter in Chapter 2, so reference specimens were selected such that there were varying peak shear stresses for different failure modes in the data set. To this end, there are BR failures with $1.10\sqrt{f'c}$ psi ($0.09\sqrt{f'c}$ MPa) and $2.57\sqrt{f'c}$ psi ($0.21\sqrt{f'c}$ MPa) and CB failures spanning from $2.77\sqrt{f'c}$ psi ($0.23\sqrt{f'c}$ MPa) to $6.42\sqrt{f'c}$ psi ($0.53\sqrt{f'c}$ MPa). Note that low peak shear stresses are those below $2.5\sqrt{f'c}$ psi ($0.21\sqrt{f'c}$ MPa) and high shear stresses are those above $6\sqrt{f'c}$ psi ($0.50\sqrt{f'c}$ MPa).
- Shear Span: Spanned from 1.60 to 3.13. Slender shear walls are typically loaded with a shear span ratio of 1.50 or greater.
- V_b/V_n: specimens were selected such that there are specimens ranging from 0.23 to slightly greater than 1.0.
- $\rho_{vert,BE}$: Spanned from vertical reinforcement present in boundary elements varies from 1.47% to 7.11%.
- ACI 318-14 Boundary Element Classification: Include specimens that exhibit CB failures that both do and do meet special boundary element confinement criteria. Note that for the selected wall set the walls exhibiting BR failures do not meet the special boundary element criteria, but confinement is less critical for this failure mode.
- Failure mode: Include BR, CB, and CS failure modes.

Reinforcing Details

Table 4.4 presents the confining reinforcement details and Table 4.5 summarizes ACI 318-14 boundary element code compliance for each reference wall. The details used to confine the individual test boundary elements are provided in Figure 4.1.

Table 4.4 – Summary of Reference Wall Geometry and Reinforcement

ID	**Reinforcing Steel**					**Confinement**				
	$\rho_{vert,BE}$	$\rho_{vert,web}$	ρ_{gross}	$\rho_{t,web}$	ρ_{vol}	h_x	s_{vert}	s_{vert}/d_b	h_x/s	ACI BE
	%	%	%	%	%	in	--	--	--	--
RW1	2.95	0.33	1.12	0.33	0.78	2.00	3.00	8.00	0.67	NBE
R1	1.47	0.28	0.47	0.31	0.80	5.50	4.00	10.67	1.38	NBE
WSH4	1.74	0.54	0.82	0.25	0.00	--	--	--	--	NBE
S6	5.66	0.55	1.75	0.55	0.84	2.70	1.34	2.14	2.02	SBE
RW-A20-P10-S63	7.11	0.61	2.84	0.61	2.23	2.00	2.00	2.67	1.00	SBE

Table 4.5 – Summary of Reference Wall Boundary Element Compliance to ACI 318-14

Specimen	**ACI BE Classification**	**SBE Criteria Met**	**SBE Criteria Failed**
RW1	NBE	BE length c/l_w Horizontal spacing Min. wall thickness.	Vertical spacing Min. volumetric reinf. ratio.
R1	NBE	c/l_w Min. wall thickness.	BE length. Vertical spacing Horizontal spacing Min. volumetric reinf. ratio
WSH4	NBE	N/A	No boundary element
S6	SBE	All	None
RW-A20-P10-S63	SBE	All	None

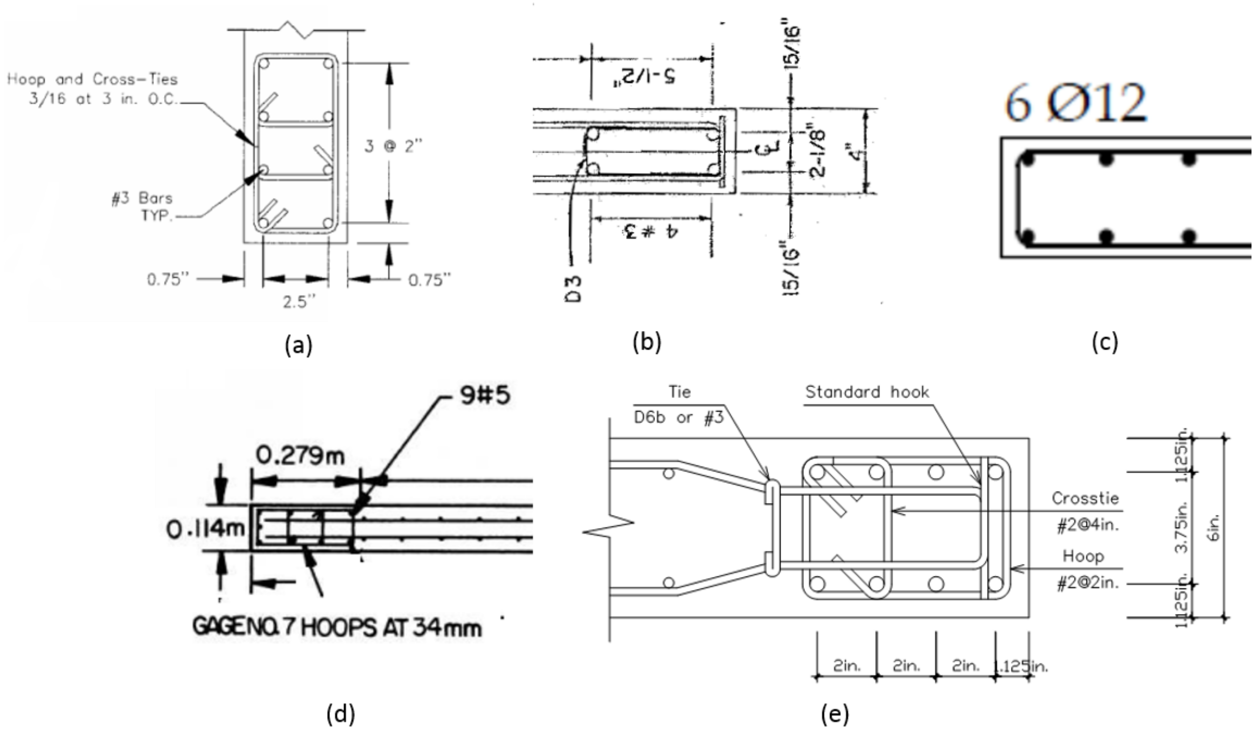

(a) (b) (c)

(d) (e)

Figure 4.1 – Base View of Reference Wall Boundary Elements, (a)-(e)

<u>Evaluation Criteria</u>

Specimens are evaluated in strength, stiffness, and deformation as described in Section 3.7.

4.1.2 Simulated Response of Specimen RW1 (High Axial Load/Low Shear)

Specimen RW1 was subjected to a high axial load ratio and a low-to-moderate shear stress. Table 4.6 summarizes the model parameters and Figures 4.2-4.3 show the wall elevation and cross-section.

Specimen RW1 has a cross-sectional aspect ratio of 12.0 (48 in. (1.22 m) wall length, 4 in. (0.10 m) wall thickness) and a shear span of 3; this wall geometry is utilized in parameter studies detailed in Chapter 5. The specimen is subjected to high axial load and a moderate level of peak shear stress and exhibited a BR failure. The load-displacement is provided in Figure 4.4.

Table 4.6 – Specimen RW1 Key Parameters

	Geometry		Loading			Results		
	CSAR	**Shear Span**	**ALR**	**$V_{max}/A_{cv}f'_c{}^{0.5}$**	**V_b/V_n**	**$\Delta_{y,exp}$**	**$\Delta_{u,exp}$**	**Failure Mode**
	--	--	%	psi	--	%	%	--
RW1	12	3.13	10.5	2.57	0.50	0.48	2.26	BR

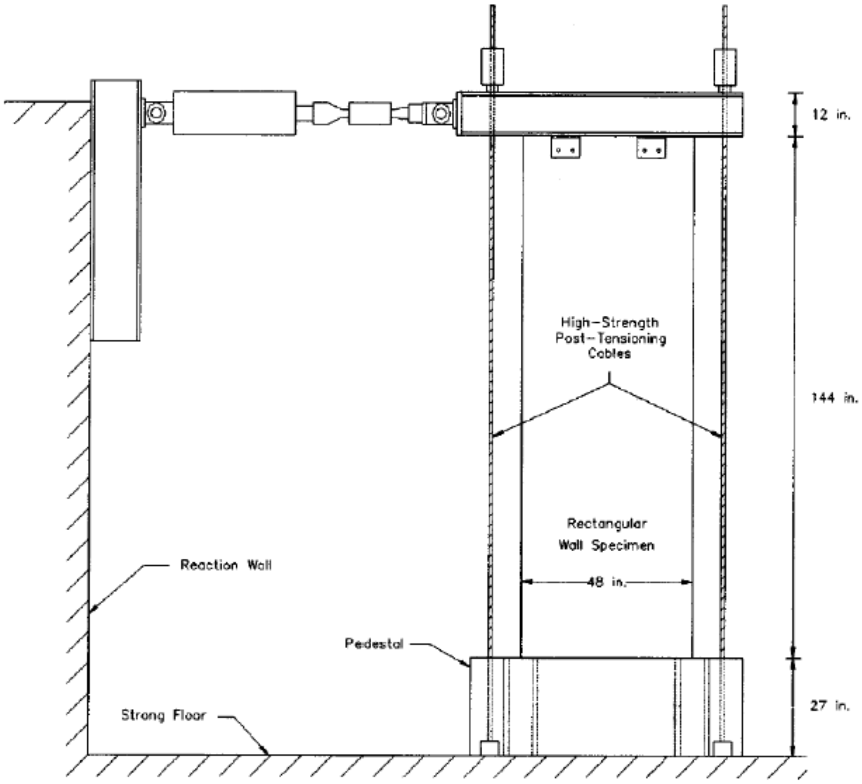

Figure 4.2 – Specimen RW1 Elevation View

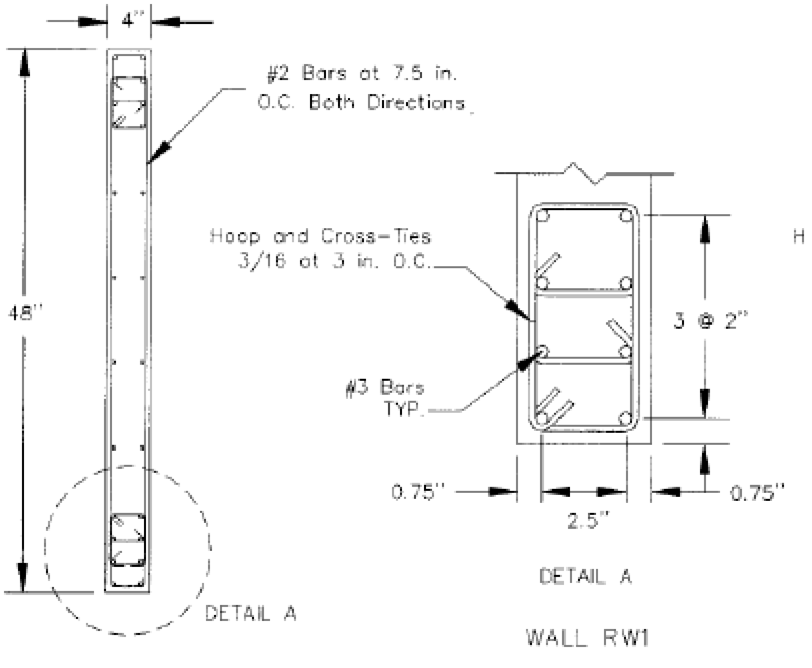

Figure 4.3 – Specimen RW1 Cross-Section at Specimen Base

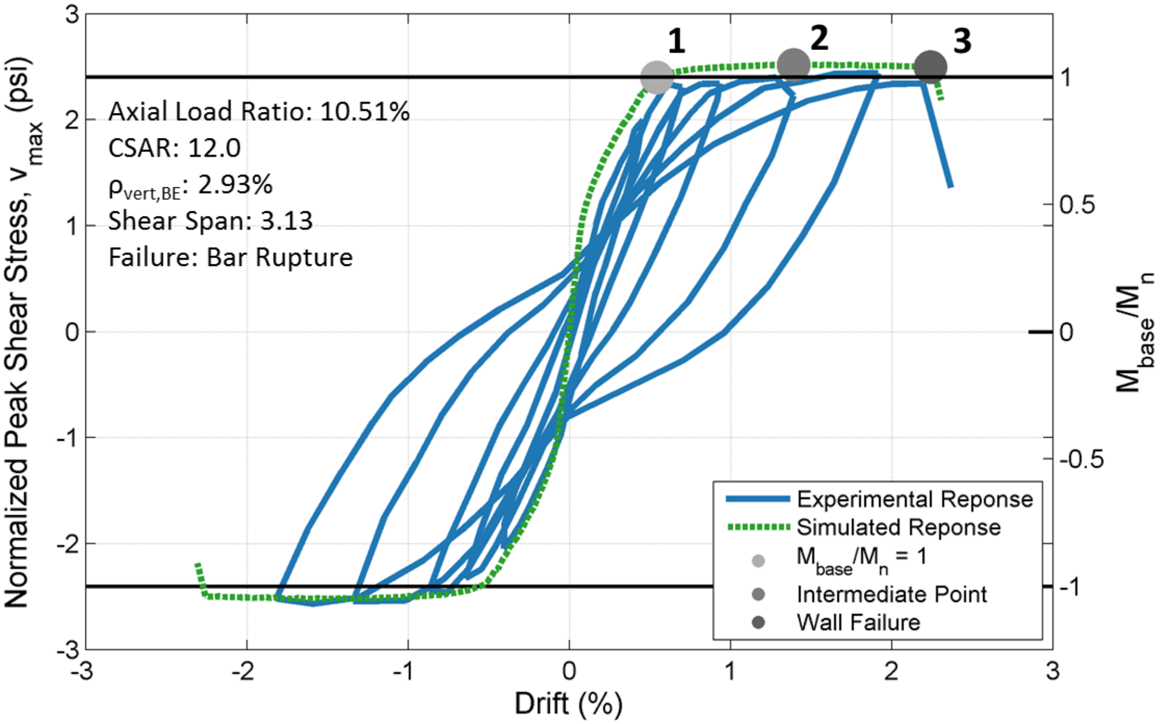

Figure 4.4 – Specimen RW1 Normalized Peak Shear Stress vs. Drift

Table 4.7 – Comparison of Simulated and Experimental Results for Specimen RW1

Strength			Stiffness			Deformation			
Exp. V_{max}	**Sim. V_{max}**	**Error**	**Exp. Δ_y**	**Sim. Δ_y**	**Error**	**Exp. Δ_u**	**Sim. Δ_u**	**Error**	**Failure Mode**
kips	kips	%	%	%	%	%	%	%	--
33.4	32.7	-1.9	0.37	0.36	-2.0	2.28	2.26	0.7	BR

The following provides an overview of the modeling accuracy.

- Specimen RW1 is well-modeled in all regards, with predictions of wall strength, stiffness, and failure mode closely matching those observed experimentally
- As observed in Figure 4.4 and Table 4.7, the simulation is able to model the yield displacement of the specimen with a high level of accuracy (2.0% error).
- Specimen peak strength is modeled with -1.9% error.
- Specimen deformation capacity is modeled with 0.7% error and the failure mode is correctly predicted.

Figures 4.5-4.10 show the development of the relevant stresses and strains in Specimen RW1, starting from the point at which the wall reaches the shear force corresponding to M_n (point 1 in Figure 4.4) and ending at the failure point (Point 3 on Figure 4.4).

Specimen RW1 exhibits a BR failure. The characteristics of a BR failure observed in the contour plots are as follows:

- There is limited strength degradation observed in both Figure 4.5 and Figure 4.7. Though strength does begin to decline at the outermost fiber of the concrete core, there is not significant strength loss observed at failure in this specimen.
- The shear stresses observed in Figure 4.6 are small in magnitude relative to other walls in the data set. There is no significant diagonal shear strut and the shear stress in the boundary element does not result in significant strength loss.
- The minimum principal strains shown in Figure 4.10 do not extend beyond the boundary element. The web does not experience significant minimum principal strains in this test specimen.
- All of these combine to show that shear demand is not influential in the behavior of Specimen RW1.

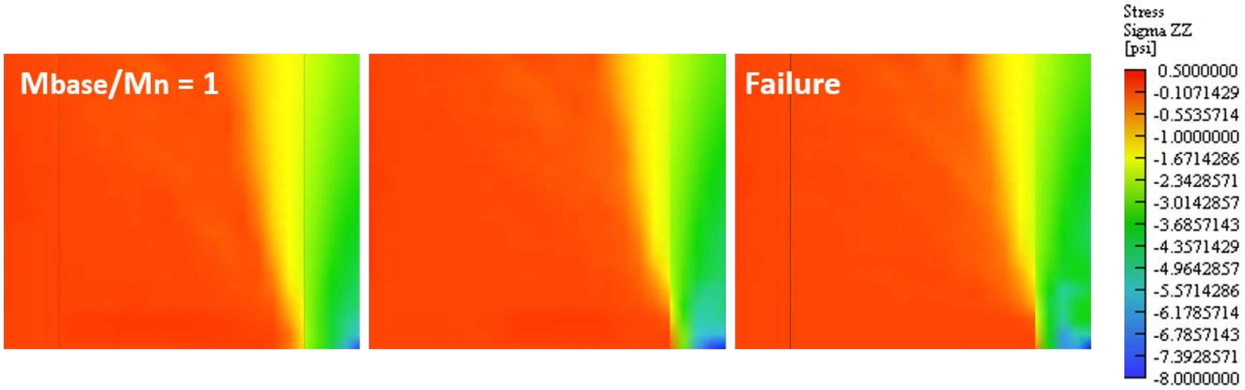

Figure 4.5 – Specimen RW1 Vertical Stress Contour Plots (Showing Bottom of Wall at 28% of h_w and 100% of l_w)

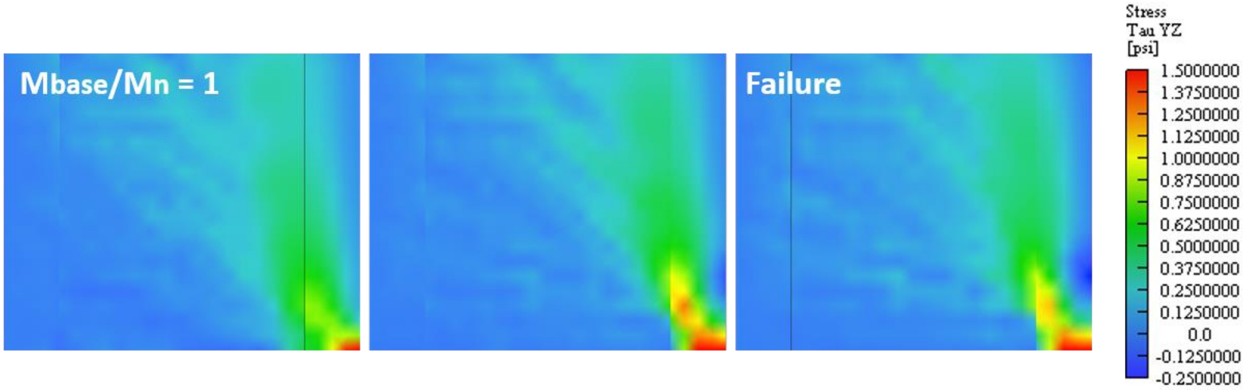

Figure 4.6 – Specimen RW1 In-Plane Stress Contour Plots (Showing Bottom of Wall at 28% of h_w and 100% of l_w)

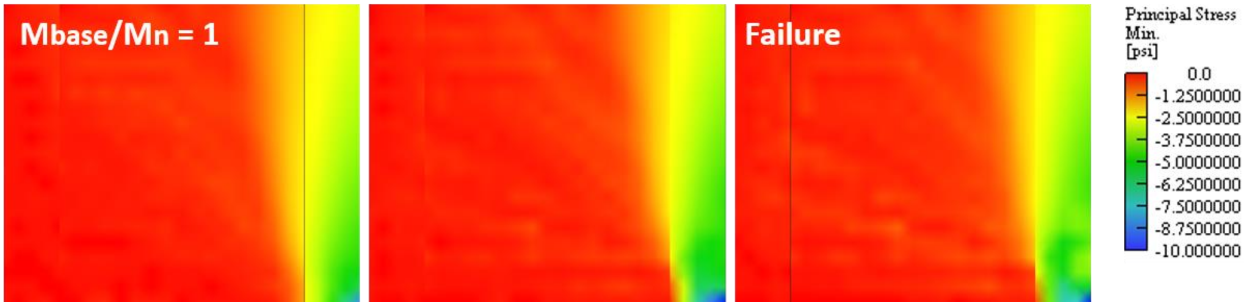

Figure 4.7 – Specimen RW1 Min. Principal Stress Contour Plots (Showing Bottom of Wall at 28% of h_w and 100% of l_w)

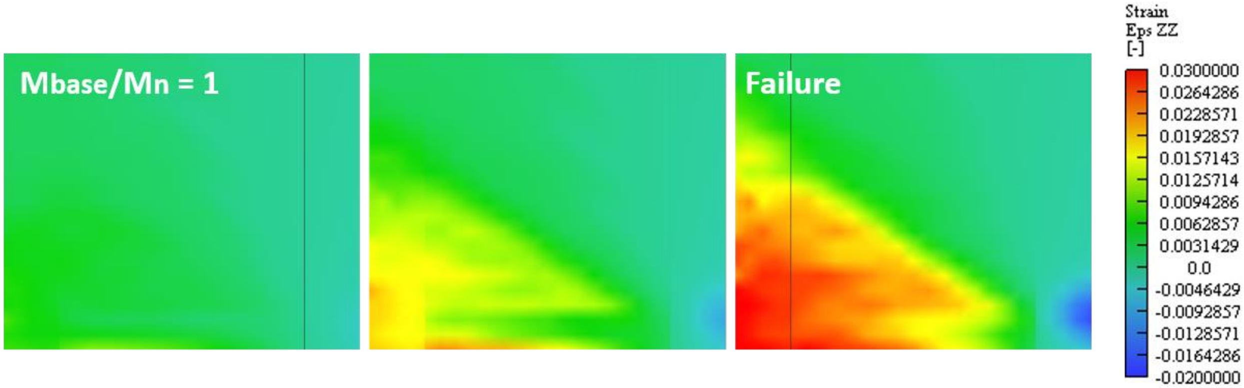

Figure 4.8 – Specimen RW1 Vertical Strain Contour Plots (Showing Bottom of Wall at 28% of h_w and 100% of l_w)

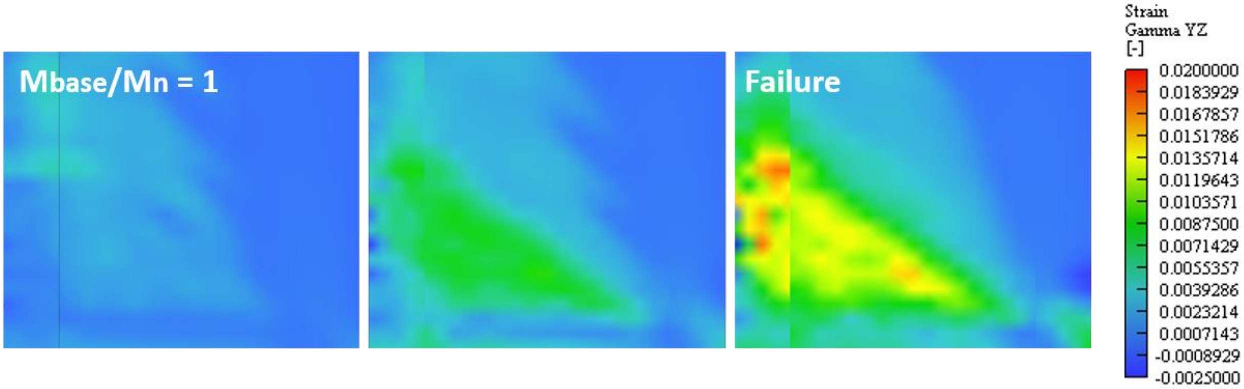

Figure 4.9 – Specimen RW1 In-Plane Shear Strain Contour Plots (Showing Bottom of Wall at 28% of h_w and 100% of l_w)

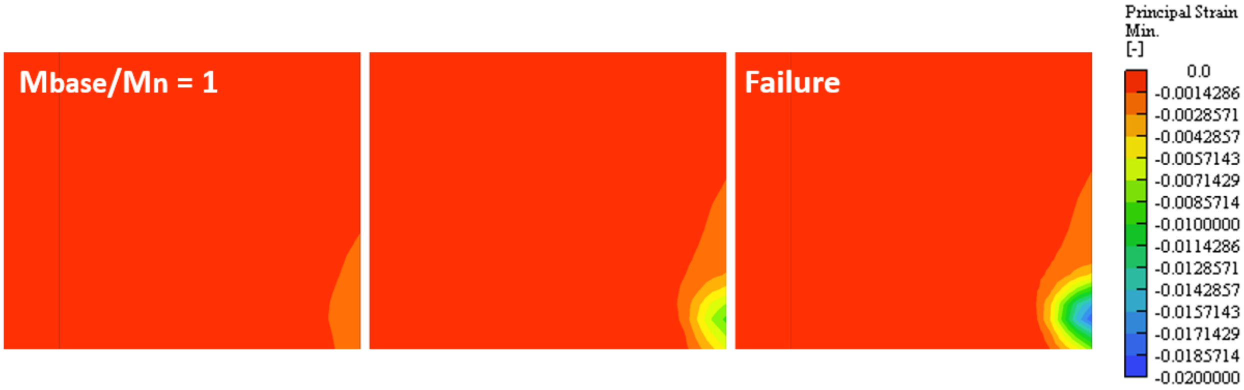

Figure 4.10 – Specimen RW1 Min. Principal Strain Contour Plots (Showing Bottom of Wall at 28% of h_w and 100% of l_w)

4.1.3 Simulated Response of Specimen R1 (Low Axial Load/Low Shear Stress)

Specimen R1 represents a BR failure with no applied axial load, low shear stress, and a large cross-sectional aspect ratio. The low shear and low axial load result in a hardening section, the behavior of which significantly differs from other experimental specimens in the data set. Along with R2, this wall is used in Chapter 3 to calibrate the model for bar-rupture failure prediction. Table 4.8 summarizes the model parameters and Figures 4.11-4.12 show the wall in both elevation and section. The load-displacement is provided in Figure 4.13.

Table 4.8 – Specimen R1 Parameter Statistics

	Geometry		**Loading**		**Results**			
	CSAR	**Shear Span**	**ALR**	**$V_{max}/A_{cv}f'_c{}^{0.5}$**	**V_b/V_n**	**$\Delta_{y,exp}$**	**$\Delta_{u,exp}$**	**Failure Mode**
	--	--	%	psi	--	%	%	--
R1	18.75	2.40	0.0	1.10	0.23	0.17	2.52	BR

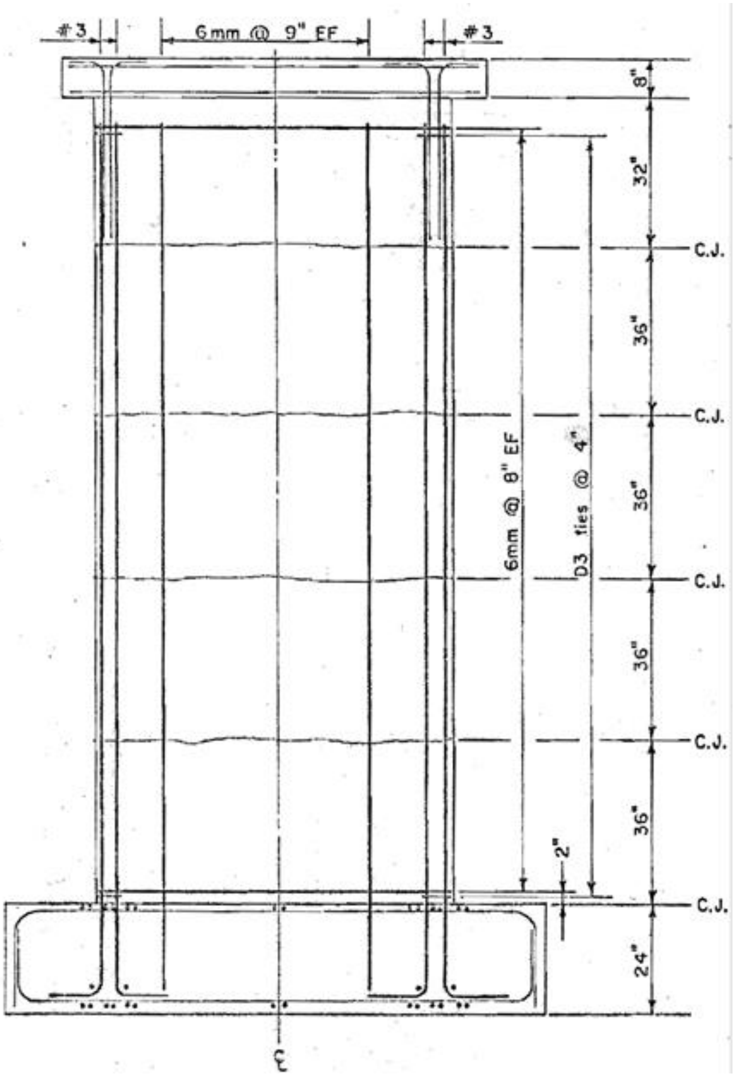

Figure 4.11 – Specimen R1 Elevation View

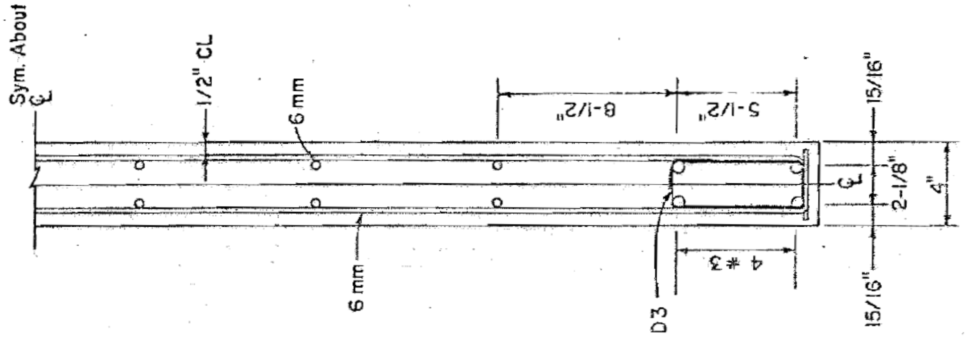

Figure 4.12 – Specimen R1 Base Section

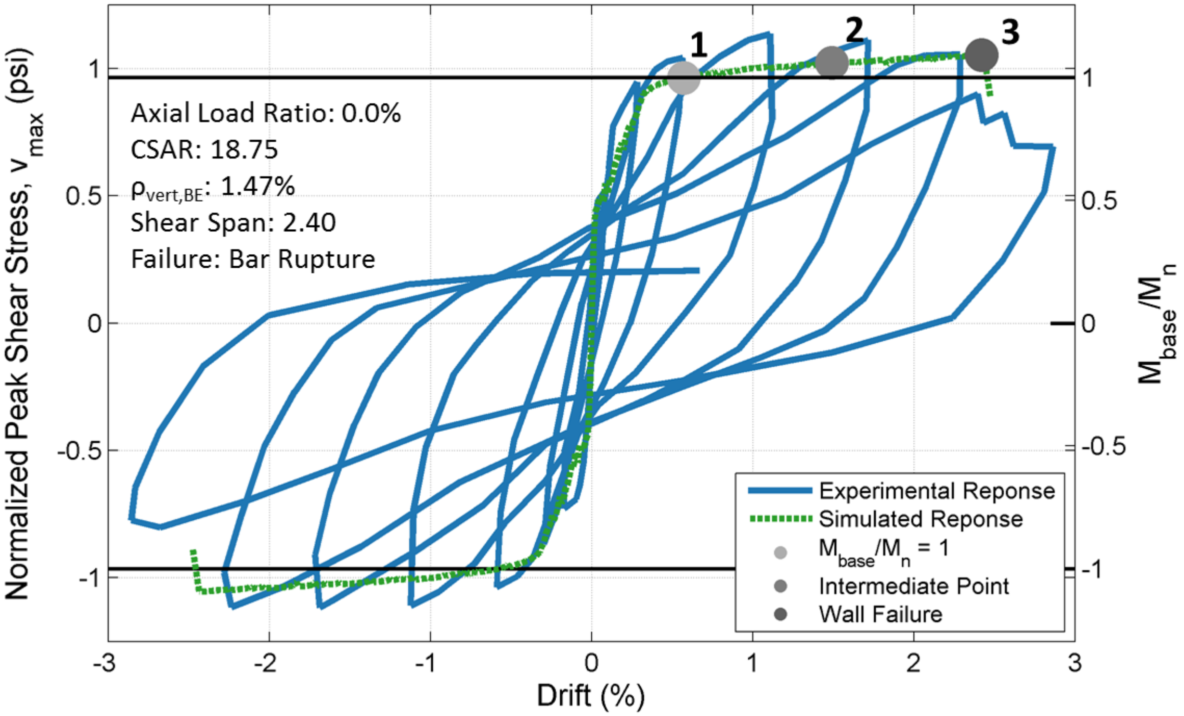

Figure 4.13 – Specimen R1 Normalized Peak Shear Stress vs. Drift

Table 4.9 – Comparison of Simulated and Experimental Results for Specimen R1

Strength			**Stiffness**			**Deformation**			
Exp. V_{max}	**Sim. V_{max}**	**Error**	**Exp. Δ_y**	**Sim. Δ_y**	**Error**	**Exp. Δ_u**	**Sim. Δ_u**	**Error**	**Failure Mode**
kips	kips	%	%	%	%	%	%	%	--
27.4	25.5	-7.1	0.15	0.27	81.0	2.82	2.52	11.9	BR

The following provides an overview of the modeling accuracy.

- Specimen R1 is simulated well in failure mode and ultimate behavior, but is less accurate early in the load protocol. This wall is the only one in the reference wall set with no applied axial load, and this condition is not handled well by ATENA. The program appears to prematurely predict cracking and loss of stiffness in the model.
- As observed in Figure 4.13 and Table 4.9, the simulation is unable to model the specimen stiffness. The initial tangent is correct, but the simulation is significantly more flexible at the point of section yield. The stiffness is modeled with 81% error.
- Specimen strength matches the experimental data at the end of the load protocol, but it is unable to closely predict the strength at intermediate drift levels. The experimental specimen gains strength more quickly than in the ATENA simulation. Peak strength is modeled with 7.1% error.
- The deformation capacity is modeled with 11.9% error. This is slightly above the 10% error criteria but still acceptable.

Figures 4.14-4.19 show the development of the relevant stresses and strains in Specimen R1, starting from the point at which the wall reaches the shear force corresponding to M_n (point 1 in Figure 4.13) and ending at the failure point (Point 3 in Figure 4.13).

Specimen R1 exhibits a BR failure. The characteristics of a BR failure observed in the contour plots are as follows:

- There is no strength loss observed in either Figure 4.14 or Figure 4.16. This is expected as the section is still hardening at the point of failure.
- The shear stresses observed in Figure 4.15 show that there is no significant diagonal shear strut. There is no evidence of shear influence on wall response.
- The minimum principal strains observed in Figure 4.19 show that a significant portion of the boundary element has a positive minimum principal strain. The compression region is smaller than the boundary element.

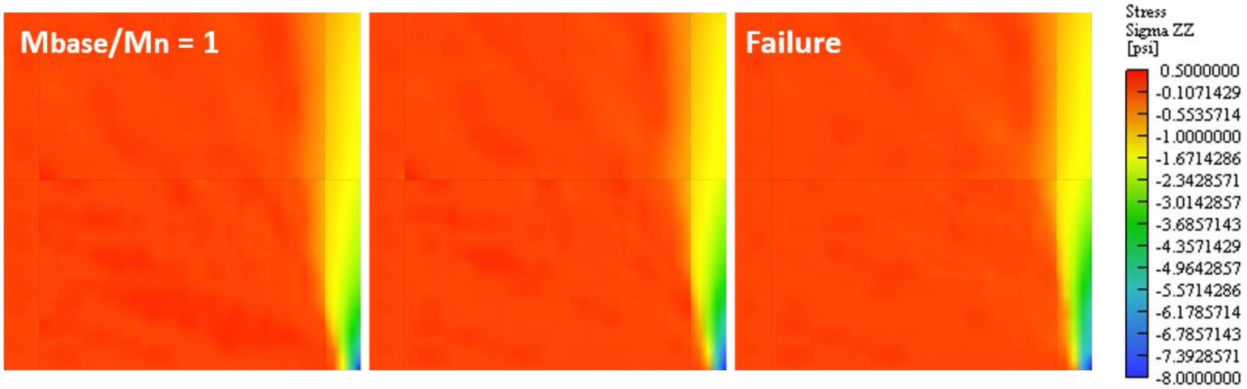

Figure 4.14 – Specimen R1 Vertical Stress Contour Plots (Showing Bottom of Wall at 43% of h_w and 100% of l_w)

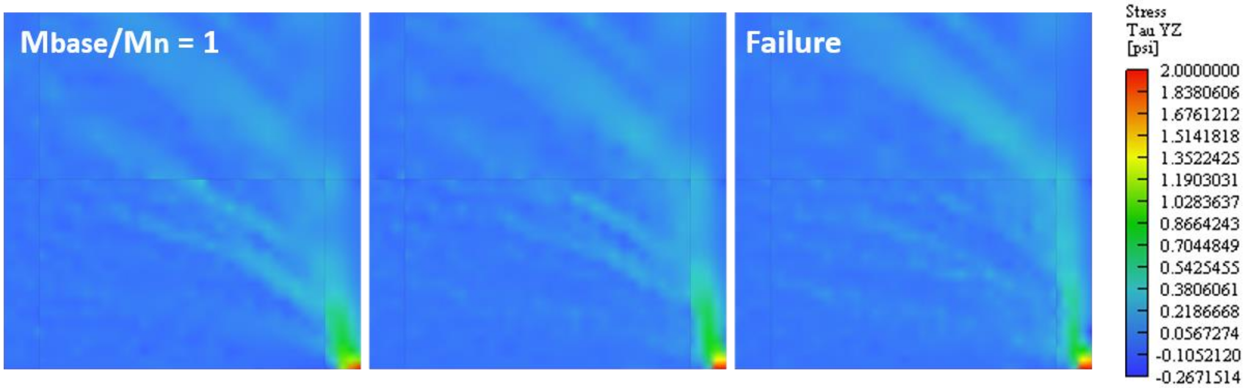

Figure 4.15 – Specimen R1 In-Plane Shear Stress Contour Plots (Showing Bottom of Wall at 43% of h_w and 100% of l_w)

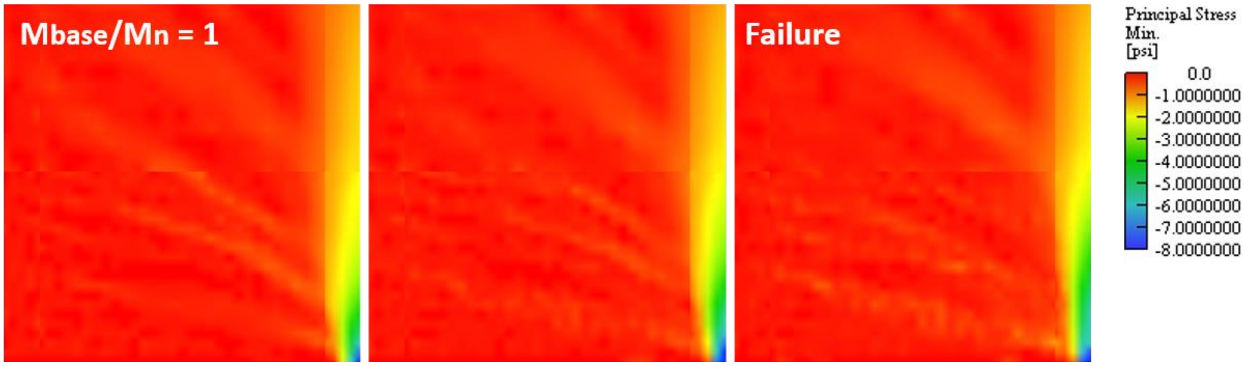

Figure 4.16 – Specimen R1 Min. Principal Stress Contour Plots (Showing Bottom of Wall at 43% of h_w and 100% of l_w)

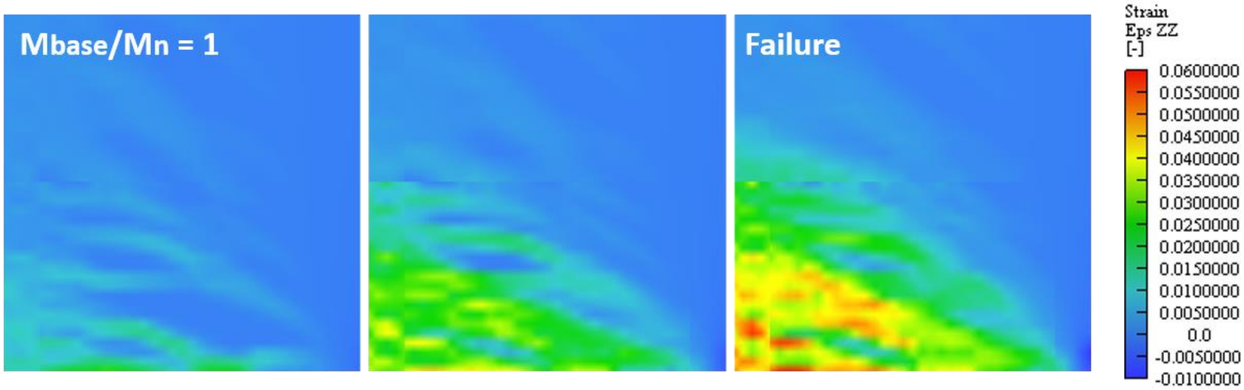

Figure 4.17 – Specimen R1 Vertical Strain Contour Plots (Showing Bottom of Wall at 43% of h_w and 100% of l_w)

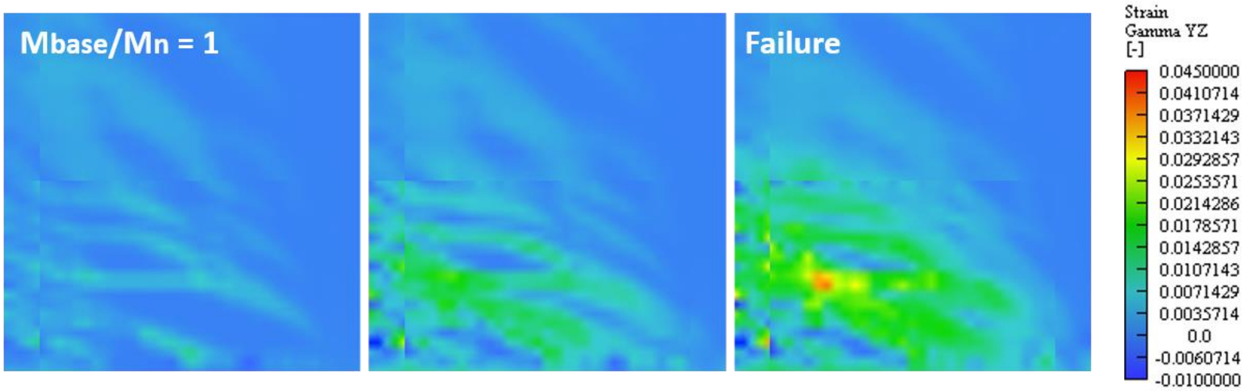

Figure 4.18 – Specimen R1 In-Plane Shear Strain Contour Plots (Showing Bottom of Wall at 43% of h_w and 100% of l_w)

Figure 4.19 – Specimen R1 Min. Principal Strain Contour Plots (Showing Bottom-Right of Wall at 17% of h_w and 36% of l_w)

4.1.4 Simulated Response of Specimen WSH4 (Moderate Axial Load/Low Shear)

Specimen WSH4 represents a CB failure with a low axial load ratio, low shear stress, and a moderate cross-sectional aspect ratio. This specimen is included in the data set as it does not have a defined boundary element, with horizontal reinforcement instead only provided through large hoops which bound the length of the cross-section. This lack of detailed confinement is what causes the specimen to fail in compression, as the wall most resembles BR failures in most other parameters. Table 4.10 summarizes the model parameters and Figures 4.20-4.21 show the wall in both elevation and section. The load-displacement response is provided in Figure 4.22.

Table 4.10 – Specimen WSH4 Parameter Statistics

	Geometry		**Loading**		**Results**			
	CSAR	**Shear Span**	**ALR**	**$V_{max}/A_{cv}f'_c{}^{0.5}$**	**V_b/V_n**	**$\Delta_{y,exp}$**	**$\Delta_{u,exp}$**	**Failure Mode**
	--	--	%	psi	--	%	%	--
WSH4	13.35	2.28	6.28	2.77	0.62	0.29	1.60	CB

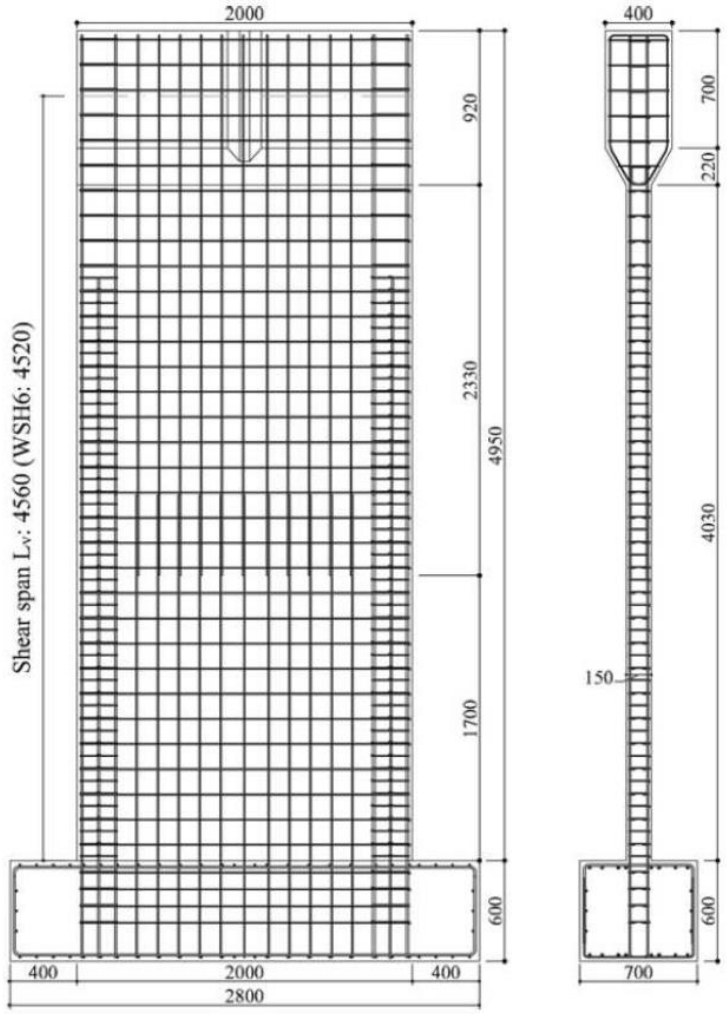

Figure 4.20 – Specimen WSH4 Elevation View

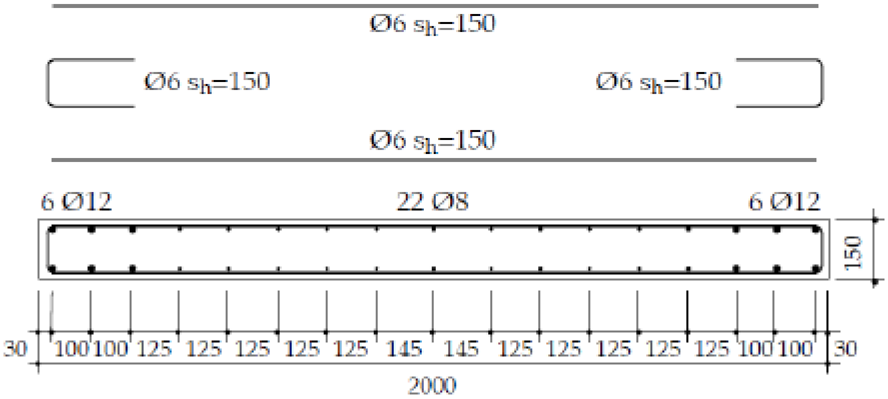

Figure 4.21 – Specimen WSH4 Base Section

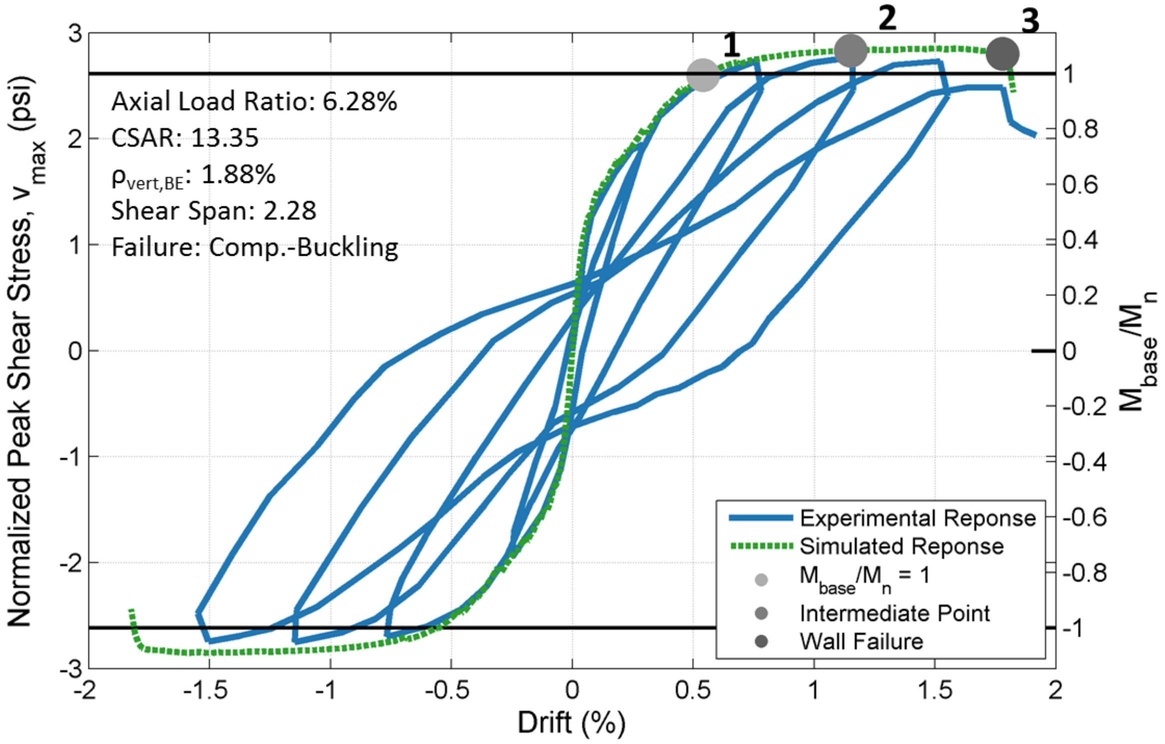

Figure 4.22 – Specimen WSH4 Normalized Peak Shear Stress vs. Drift

Table 4.11 – Comparison of Simulated and Experimental Results for Specimen WSH4

Strength			**Stiffness**			**Deformation**			
Exp. V_{max}	**Sim. V_{max}**	**Error**	**Exp. Δ_y**	**Sim. Δ_y**	**Error**	**Exp. Δ_u**	**Sim. Δ_u**	**Error**	**Failure Mode**
kips	kips	%	%	%	%	%	%	%	--
99.0	102.1	3.1	0.36	0.32	-10.6	1.60	1.76	10.0	CB

The following provides an overview of the modeling accuracy.

- Specimen WSH4 is well-modeled in all regards, with predictions of wall strength, degradation, and deformation capacity closely matching those observed experimentally. The crushing failure observed experimentally is also correctly predicted by the simulation.
- As observed in Figure 4.22 and Table 4.11, the simulation models the specimen stiffness within criteria. The error in predicted stiffness is 11.1%.
- Specimen strength is well-modeled, though the experimental test does see slightly more strength degradation at cycles which reached 0.75% and 1.20% drift. Even with this behavior, the simulated model prediction error for peak strength is only 3.1%.
- The model predicts degradation at a drift level of 1.65% before a full loss of strength at 1.79%. The experimental specimen lost significant strength after a drift cycle that reached 1.55% drift, finally failing at 1.78% drift on the following cycle. Deformation capacity is modeled with only 0.7% error.

Figures 4.23-4.28 show the development of the relevant stresses and strains in Specimen WSH4, starting from the point at which the wall reaches the shear force corresponding to M_n (point 1 in Figure 4.22) and ending at the failure point (Point 3 in Figure 4.22).

Specimen WSH4 exhibits a CB failure. The characteristics of a CB failure observed in the contour plots are as follows:

- Concrete strength declines in the concrete core at failure, as shown in Figure 4.23 and Figure 4.25.
- Though the shear stresses observed in Figure 4.24 are larger than those seen in reference wall BR failures (R1 and RW1), diagonal shear is limited and does not cause significant strength loss. This is expected as Specimen WSH4 is only subjected to a peak shear stress of $2.77\sqrt{f'c}$ psi ($0.23\sqrt{f'c}$ MPa).
- The minimum principal strains shown in Figure 4.28 reveal that significant strains are experienced across all elements in the boundary element region; the full length of the boundary element is in compression. The strain profile shows that the largest strains are those observed at the outermost fiber of the section.

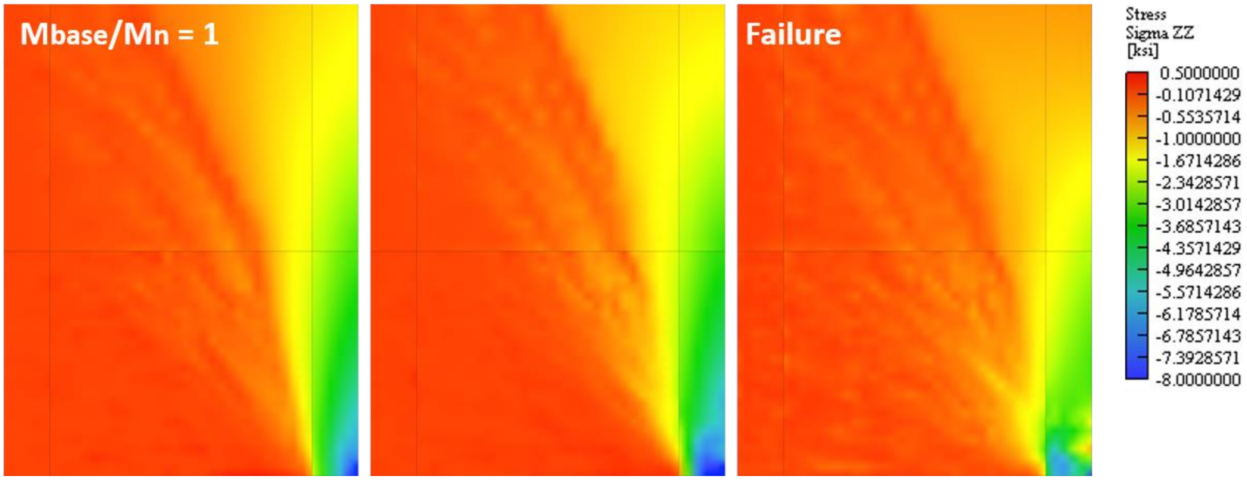

Figure 4.23 – Specimen WSH4 Vertical Stress Contour Plots

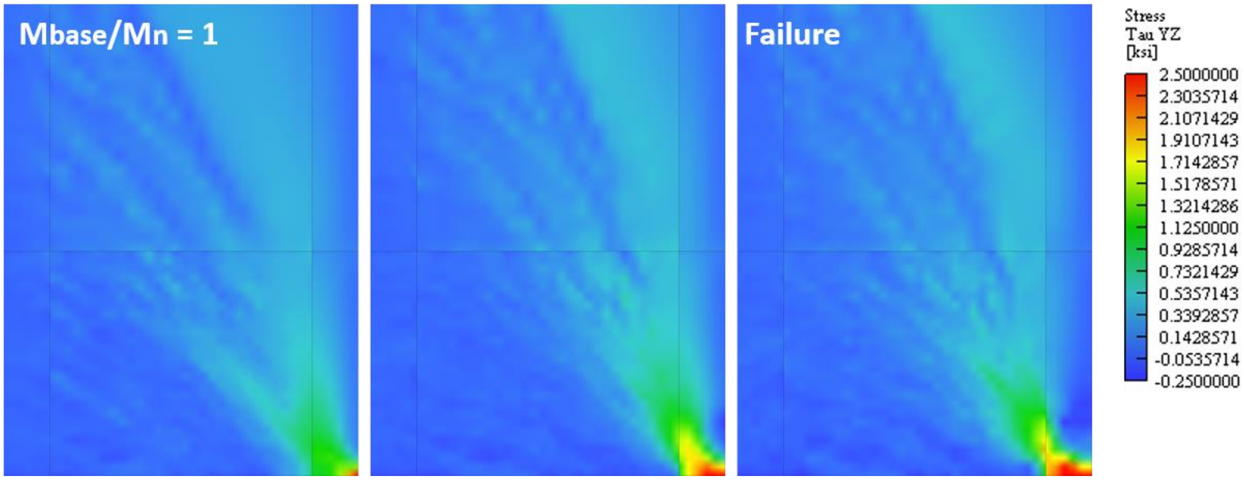

Figure 4.24 – Specimen WSH4 In-Plane Stress Contour Plots

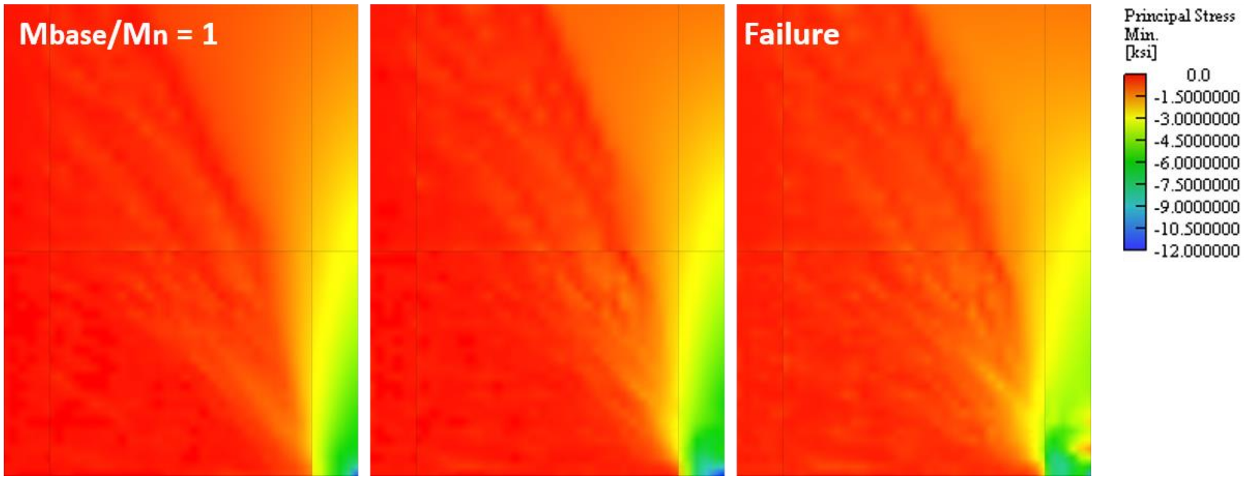

Figure 4.25 – Specimen WSH4 Min. Principal Stress Contour Plots

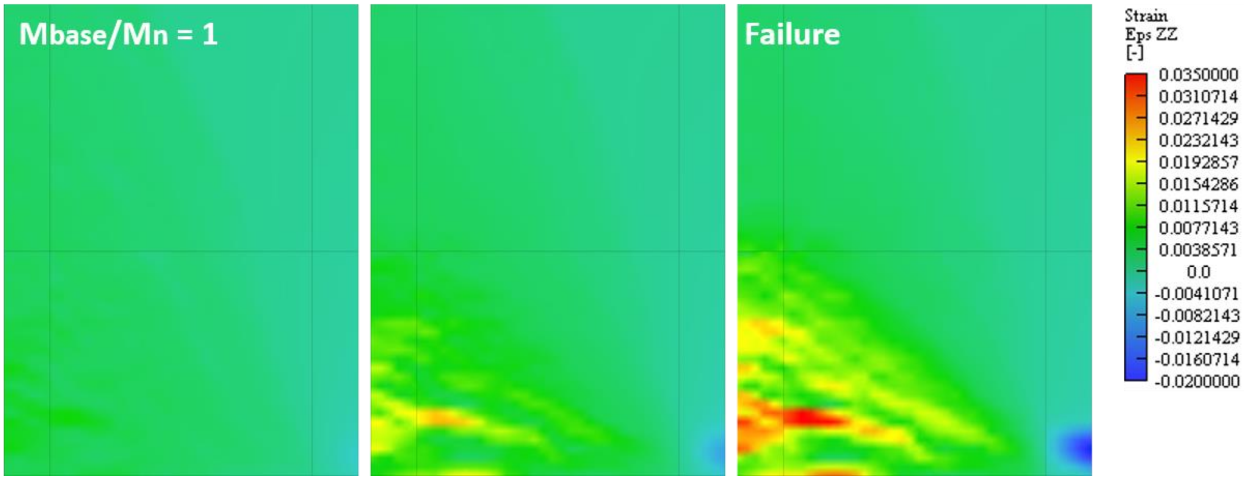

Figure 4.26 – Specimen WSH4 Vertical Strain Contour Plots

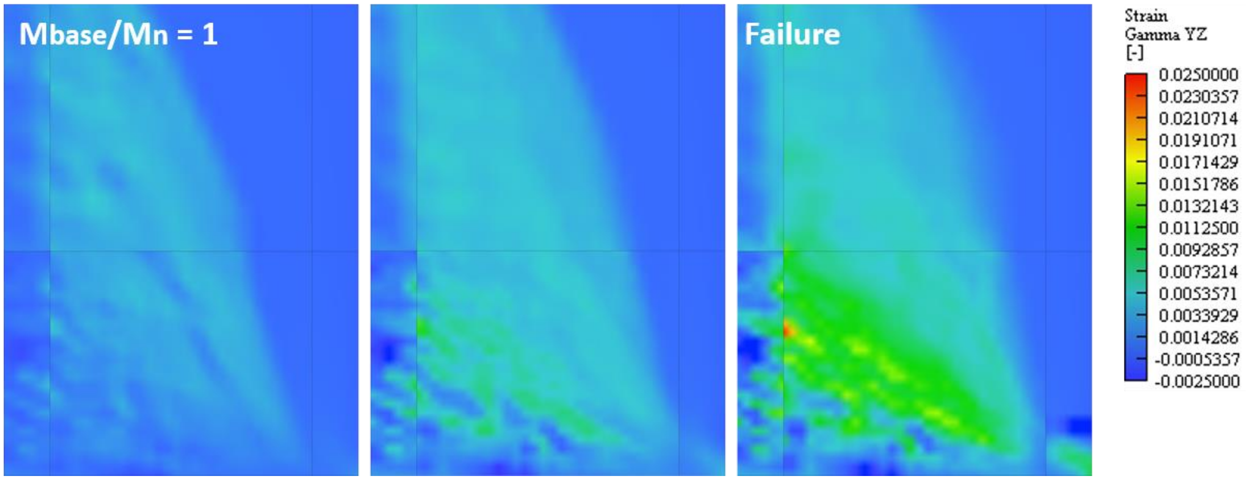

Figure 4.27 – Specimen WSH4 In-Plane Shear Strain Contour Plots

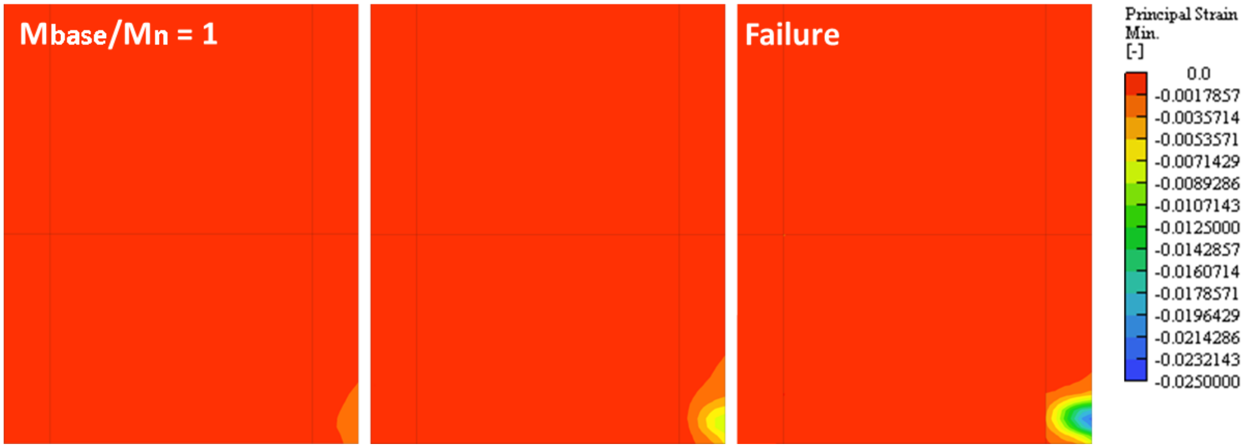

Figure 4.28 – Specimen WSH4 Min. Principal Strain Contour Plots

4.1.5 Simulated Response of Specimen S6 (Low Axial Load/High Shear)

Specimen S6 represents a compression failure with low axial load ratio, high shear stresses, and a large cross-sectional aspect ratio. The amount of confinement and vertical reinforcement provided is comparable to Specimen RW-A20-P10-S63, with the key difference being the specimen shape. Specimen S6 has a cross-sectional aspect ratio of 21.1 (95 in. (2.41 m) wall length, 4.5 in. (0.11 m) wall thickness) where Specimen RW-A20-P10-S63 has a cross-sectional aspect ratio of 8.0 (48 in. (1.22 m) wall length, 4 in. (1.52 m) thickness). This wall is included as it provides an example of a wall subjected to high shear stress that fails at a small ultimate deformation. Table 4.12 summarizes the model parameters and Figures 4.29-4.30 show the wall in both elevation and section. The load-displacement response is provided in Figure 4.31.

Table 4.12 – Specimen S6 Parameter Statistics

	Geometry	**Loading**			**Results**			
	CSAR	**Shear Span**	**ALR**	**$V_{max}/A_{cv}f'_c{}^{0.5}$**	**V_b/V_n**	**$\Delta_{y,exp}$**	**$\Delta_{u,exp}$**	**Failure Mode**
	--	--	%	psi	--	%	%	--
S6	21.1	1.60	4.80	6.42	0.83	0.32	1.65	CS

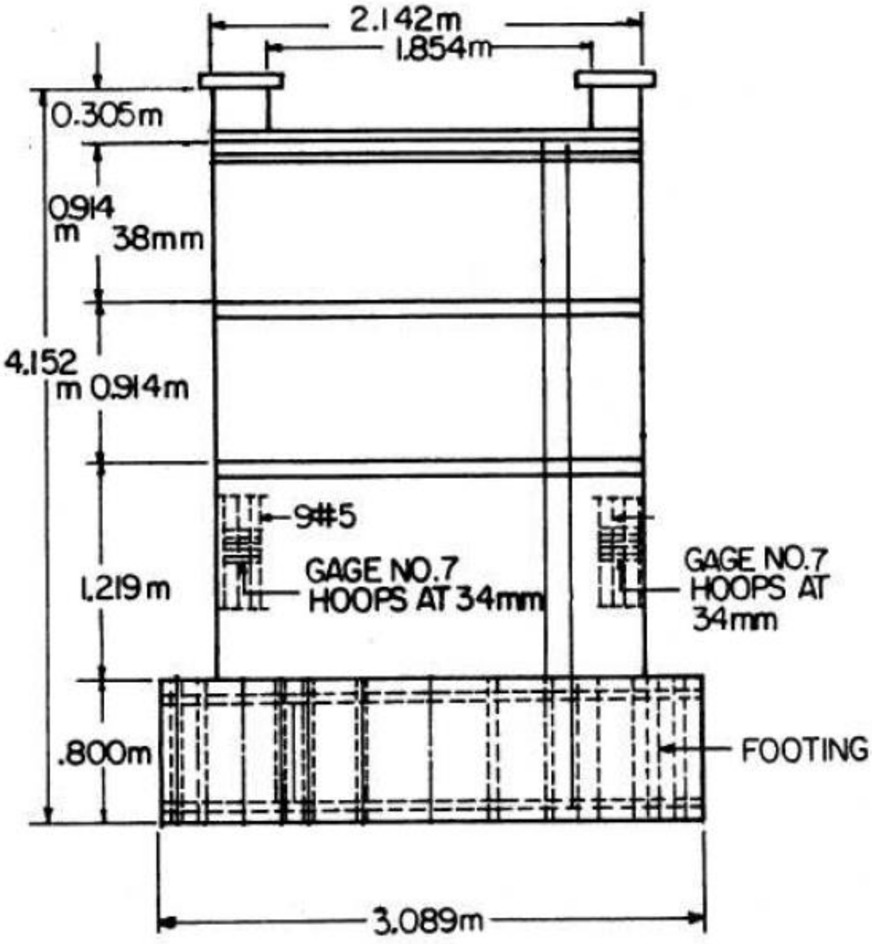

Figure 4.29 – Specimen S6 Elevation View

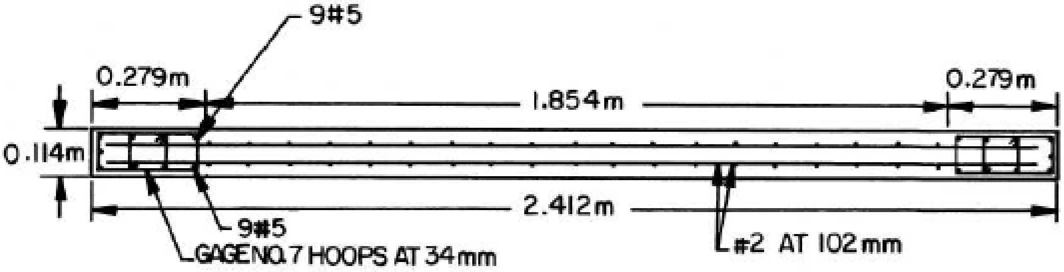

Figure 4.30 – Specimen S6 Base Section

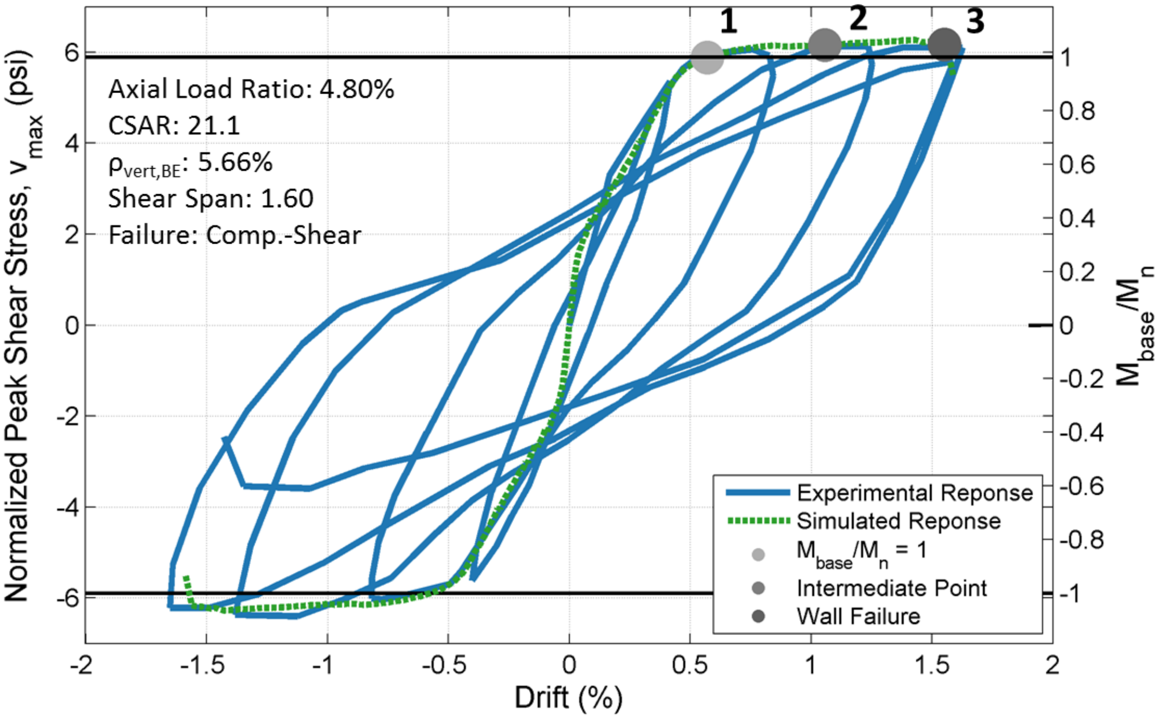

Figure 4.31 – Specimen S6 Normalized Peak Shear Stress vs. Drift

Table 4.13 – Comparison of Simulated and Experimental Results for Specimen S6

Strength			**Stiffness**			**Deformation**			
Exp. V_{max}	**Sim. V_{max}**	**Error**	**Exp. Δ_y**	**Sim. Δ_y**	**Error**	**Exp. Δ_u**	**Sim. Δ_u**	**Error**	**Failure Mode**
kips	kips	%	%	%	%	%	%	%	--
194.3	190.1	-2.2	0.41	0.38	-7.3	1.65	1.58	-4.4	CB

The following provides an overview of the modeling accuracy.

- Specimen S6 is well-modeled in all regards, with predictions of wall strength, degradation, and deformation capacity closely matching those observed experimentally. The crushing failure observed experimentally is also correctly predicted by the simulation.
- As observed in Figure 4.31 and Table 4.13, the simulation is able to model the stiffness of the specimen. The initial stiffness is slightly greater than observed experimentally, but the two curves quickly converge above a peak shear stress of $3\sqrt{f'c}$ psi ($0.25\sqrt{f'c}$ MPa). The stiffness prediction error is 7.3%.
- Specimen strength is modeled with only 2.2% error, closely the maximum observed experimental strength.
- The model predicts degradation at a drift level of 1.50% before a full loss of strength at 1.58%. It was observed experimentally that this behavior would occur at a drift of 1.65%. The simulated drift error is only 4.4%.

Figures 4.32-4.37 show the development of the relevant stresses and strains in Specimen S6, starting from the point at which the wall reaches the shear force corresponding to M_n (point 1 in Figure 4.31) and ending at the failure point (Point 3 in Figure 4.31).

Specimen S6 exhibits a CS failure. The characteristics of a CS failure observed in the contour plots are as follows:

- As shown in Figure 4.32 and Figure 4.34, strength loss in the concrete first occurs at the web/boundary element interface and not the outermost fiber of the boundary element, as was observed in the WSH4 CB failure.
- The shear stresses observed in Figure 4.33 are larger in magnitude relative to the three previous reference walls examined. There is a significant diagonal shear strut which results in the loss of strength in concrete near the web/boundary element interface.
- The minimum principal strains shown in Figure 4.37 extend beyond the boundary element, with large strains occurring across the length of the boundary element and not focused at the outermost fiber. The web is subjected to compression prior to failure.
- In a CB failure, the outermost fibers diminish in strength first, with the inner fibers of the boundary element providing a reserve capacity which allows for greater global deformation capacity. In this failure, strength loss occurs at both the web/boundary element interface and boundary element outermost fiber; the lack of reserve capacity results in lesser deformation capacity relative to that exhibited in a CB failures.

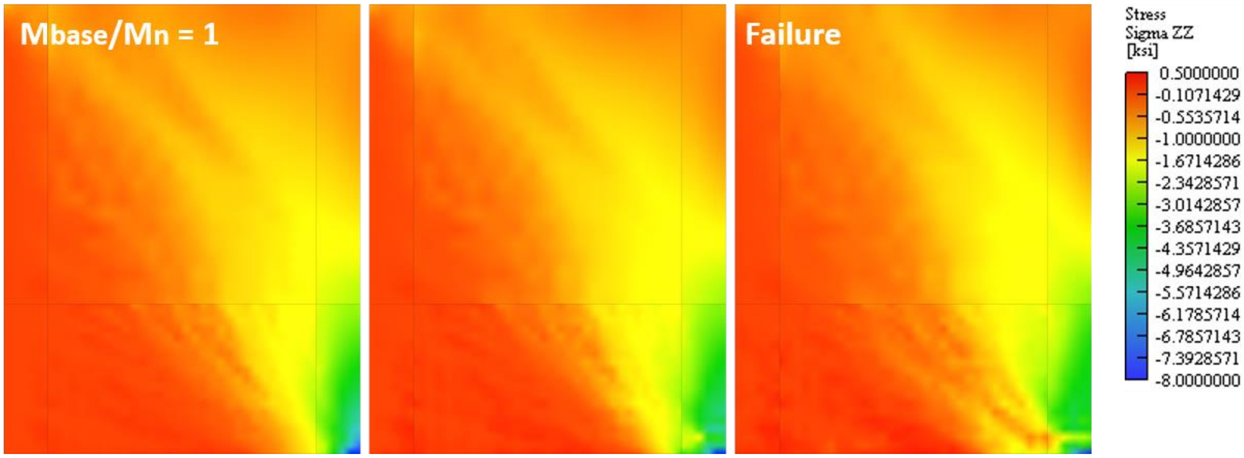

Figure 4.32 – Specimen S6 Vertical Stress Contour Plots

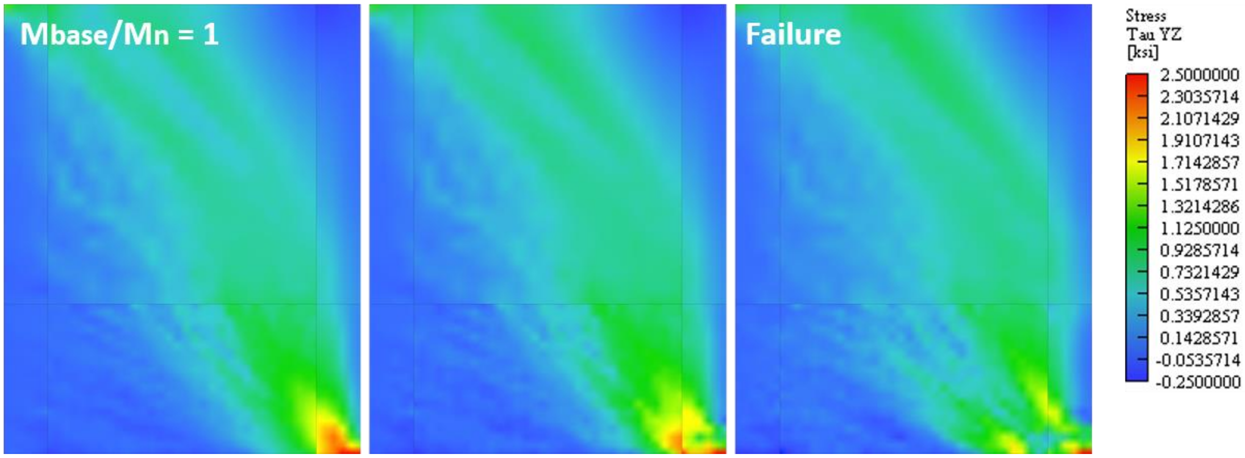

Figure 4.33 – Specimen S6 In-Plane Stress Contour Plots

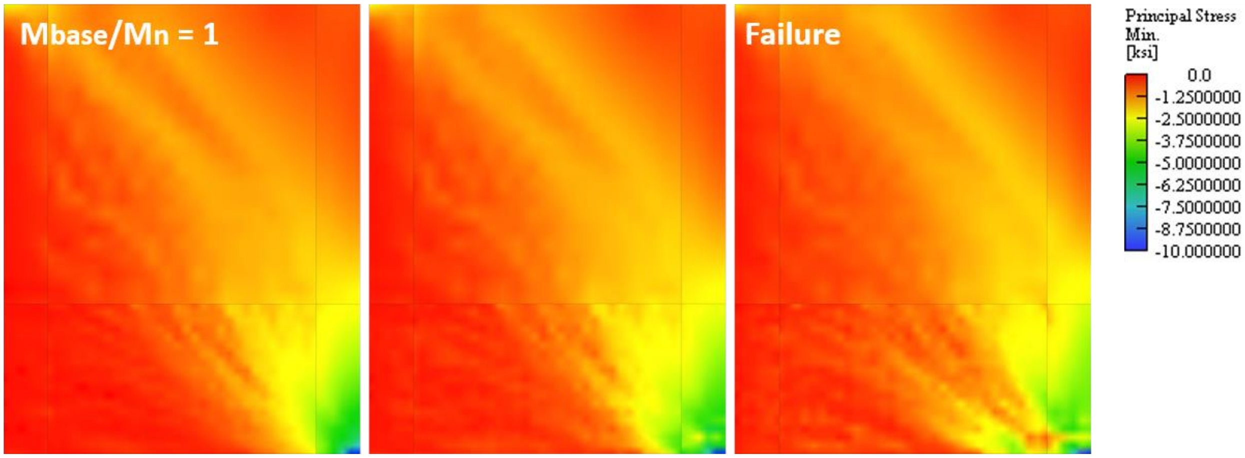

Figure 4.34 – Specimen S6 Min. Principal Stress Contour Plots

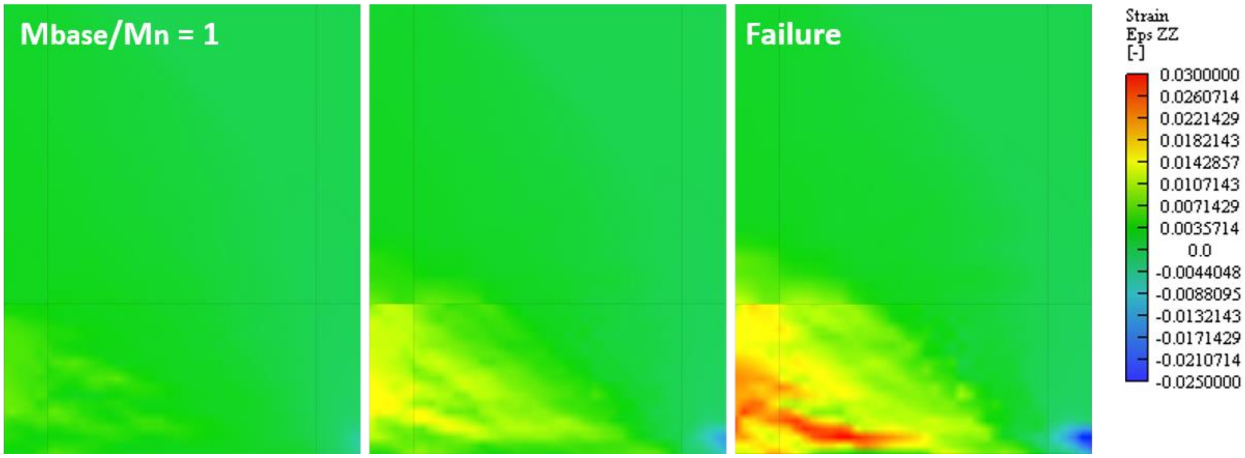

Figure 4.35 – Specimen S6 Vertical Strain Contour Plots

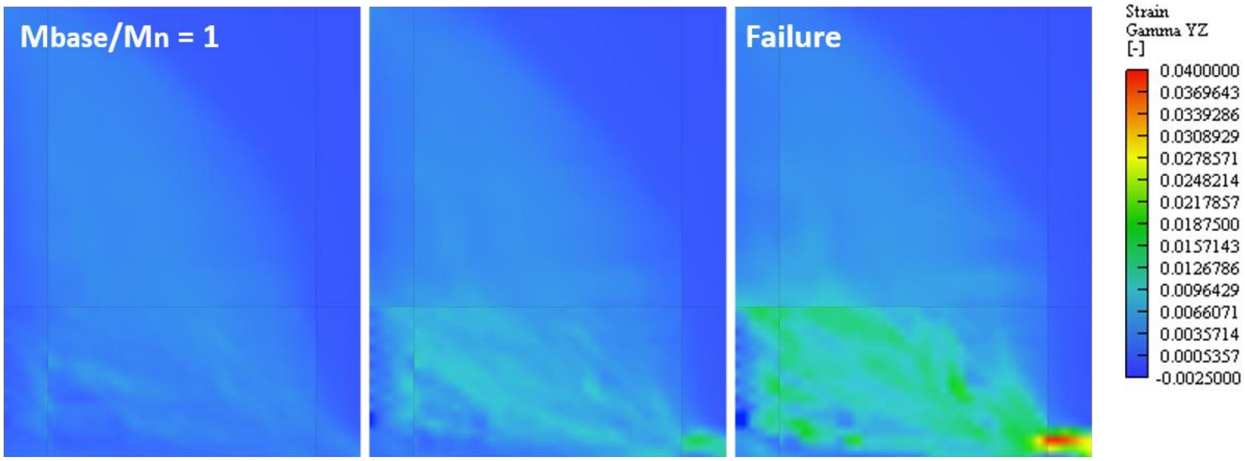

Figure 4.36 – Specimen S6 In-Plane Shear Strain Contour Plots

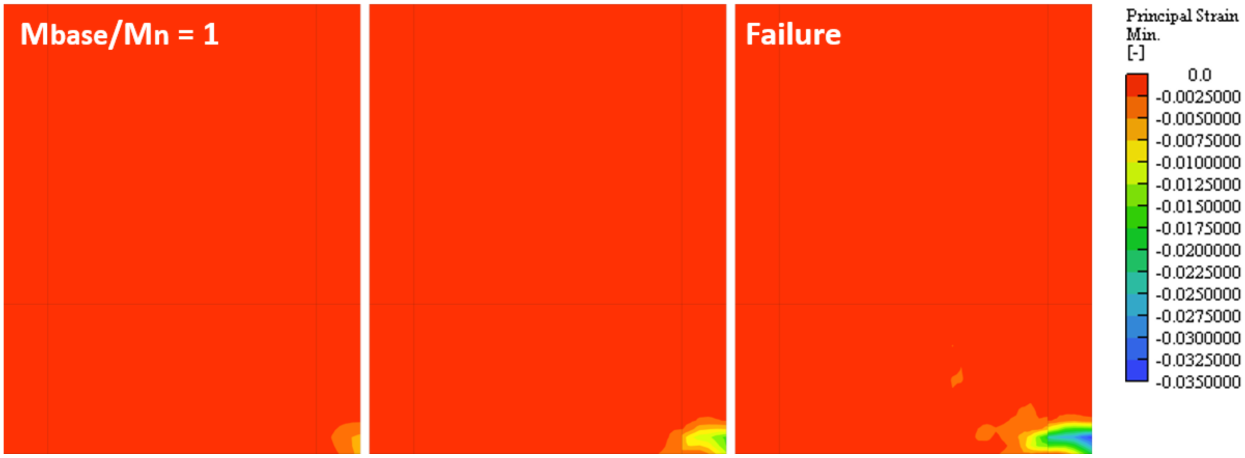

Figure 4.37 – Specimen S6 Min. Principal Strain Contour Plots

4.1.6 Simulated Response of Specimen RW-A20-P10-S63 (Moderate Axial Load/High Shear)

Specimen RW-A20-P10-S63 represents a compression failure with a moderate axial load ratio, high shear stresses, and a small cross-sectional aspect ratio. As noted previously, the amount of confinement and vertical reinforcement provided is comparable to Specimen S6, with the two walls differing mainly in cross-sectional aspect ratio. This wall is included as it provides an example of a wall subjected to high shear stress that is able to reach a large ultimate deformation. Table 4.14 summarizes the key model parameters and Figures 4.38-4.39 show the wall in both elevation and section. The load-displacement response is provided in Figure 4.40.

Table 4.14 – Specimen RW-A20-P10-S63 Parameter Statistics

	Geometry		**Loading**			**Results**		
	CSAR	**Shear Span**	**ALR**	**$V_{max}/A_{cv}f'_c{}^{0.5}$**	**V_b/V_n**	**$\Delta_{y,exp}$**	**$\Delta_{u,exp}$**	**Failure Mode**
	--	--	%	psi	--	%	%	--
RW-A20-P10-S63	8.0	2.0	7.29	6.10	0.91	0.66	3.00	CB

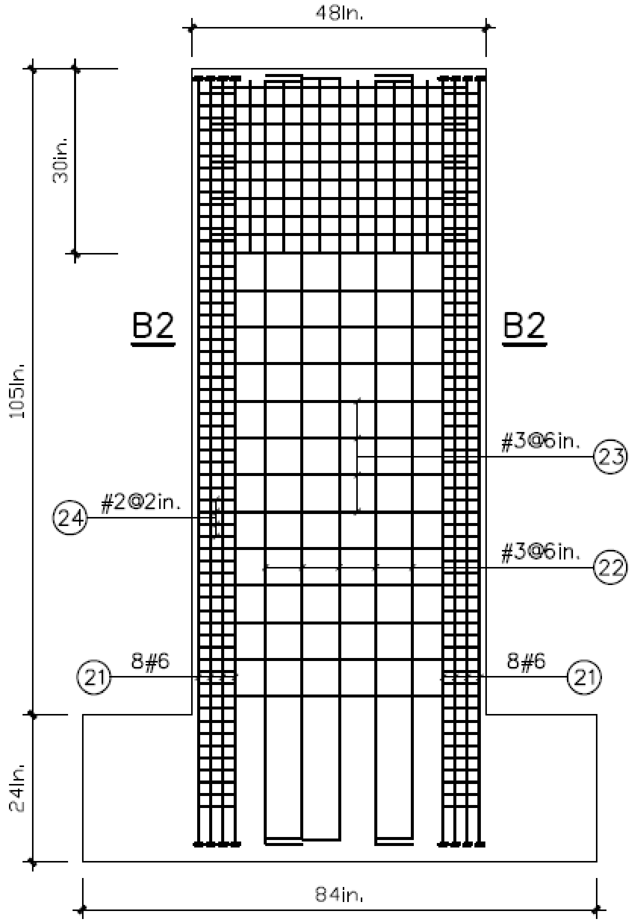

Figure 4.38 – Specimen RW-A20-P10-S63 Elevation View

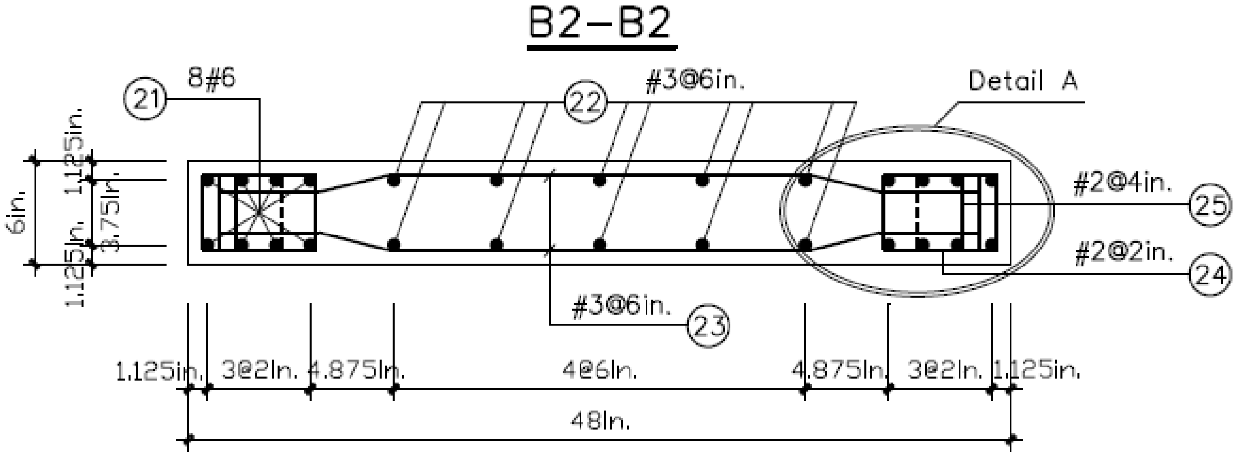

Figure 4.39 – Specimen RW-A20-P10-S63 Base Section

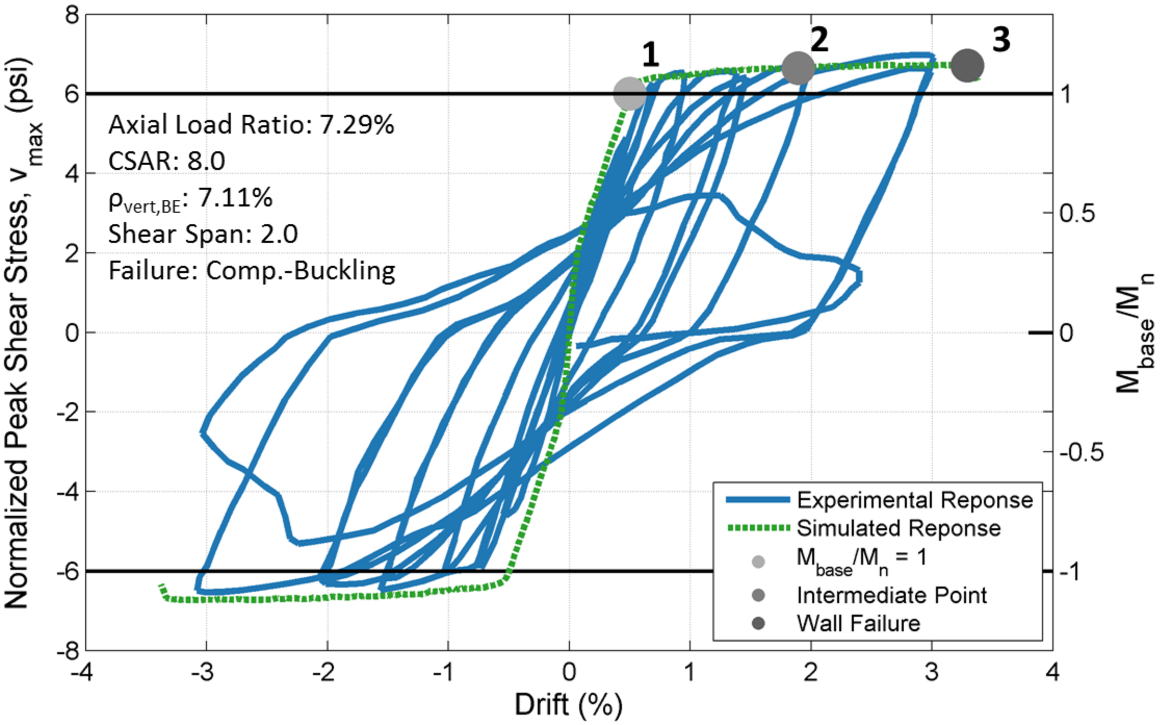

Figure 4.40 – Specimen RW-A20-P10-S63 Normalized Peak Shear Stress vs. Drift

Table 4.15 – Comparison of Simulated and Experimental Results for Specimen RW-A20-P10-S63

Strength			Stiffness			Deformation			
Exp. V_{max}	**Sim. V_{max}**	**Error**	**Exp. Δ_y**	**Sim. Δ_y**	**Error**	**Exp. Δ_u**	**Sim. Δ_u**	**Error**	**Failure Mode**
kips	kips	%	%	%	%	%	%	%	--
166.9	162.7	-2.5	0.55	0.48	-12.1	3.00	3.27	9.1	CB

The following provides an overview of the modeling accuracy.

- Despite a slight over-estimation of ultimate drift, specimen RW-A20-P10-S63 is well-modeled, with predictions of wall strength and degradation closely matching those observed experimentally. The crushing failure observed experimentally is also correctly predicted by the simulation.
- As observed in Figure 4.40 and Table 4.15, the simulation over-predicts the specimen stiffness by 11%.
- Specimen strength is well-modeled, with the experimental and simulated values only diverging at the end of the load protocol, where the experimental specimen gains a small amount of strength. The simulation under-predicts the strength by 2.5%.
- The model predicts degradation at a drift level of 3.05% before failing at 3.27%. The experimental specimen was subjected to a loading of 3% drift and then failed while loading in the

other direction. As the simulation is monotonic, it is unable to capture this behavior. The error in prediction of deformation capacity is 9.1%.

Figures 4.41-4.46 show the development of the relevant stresses and strains in Specimen RW-A20-P10-S63, starting from the point at which the wall reaches the shear force corresponding to M_n (point 1 In Figure 4.40) and ending at the failure point (Point 3 in Figure 4.40).

Specimen RW-A20-P10-S63 exhibits a CB failure. The characteristics of a CB failure observed in the contour plots are as follows:

- As shown in Figure 4.41 and Figure 4.43, strength loss in the concrete first occurs in the boundary element core.
- The shear stresses observed in Figure 4.33 are larger in magnitude relative to Specimens R1, RW1, and WSH4 but are similar in magnitude to those present in Specimen S6. There is a significant diagonal shear strut, but it does not cause concrete crushing prior to specimen failure.
- The minimum principal strains shown in Figure 4.37 extend beyond the boundary element, but significant minimum principal strains do not occur in the web. The largest strains occur at the outermost fibers of the boundary element.
- The specimen thus loses strength first at the outermost fiber of the boundary element, with reserve capacity still available in the inner fibers of the boundary element. There is thus lateral load-carrying capacity which still remains after initial crushing, allowing for the large deformation capacity (Δ_u = 3.0%). This global deformation capacity is greater than that exhibited in Specimen WSH4 as the confinement provided meets ACI SBE criteria, which allows the concrete to exhibit greater deformation capacity. Confinement has a significant influence in the ductility of specimens exhibiting CB failure.

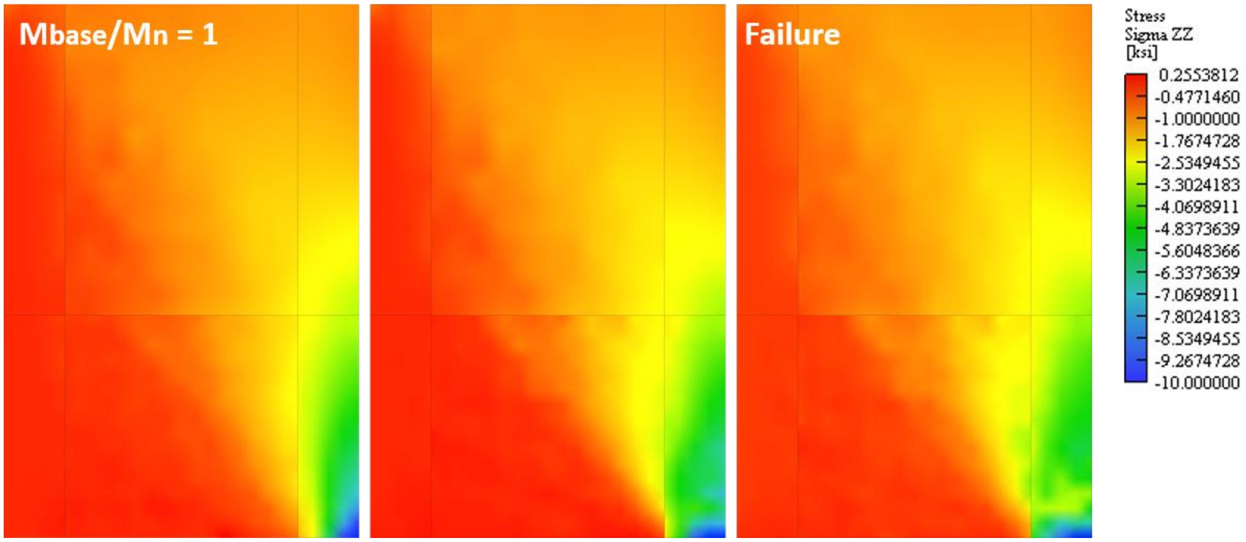

Figure 4.41 – Specimen RW-A20-P10-S63 Vertical Stress Contour Plots

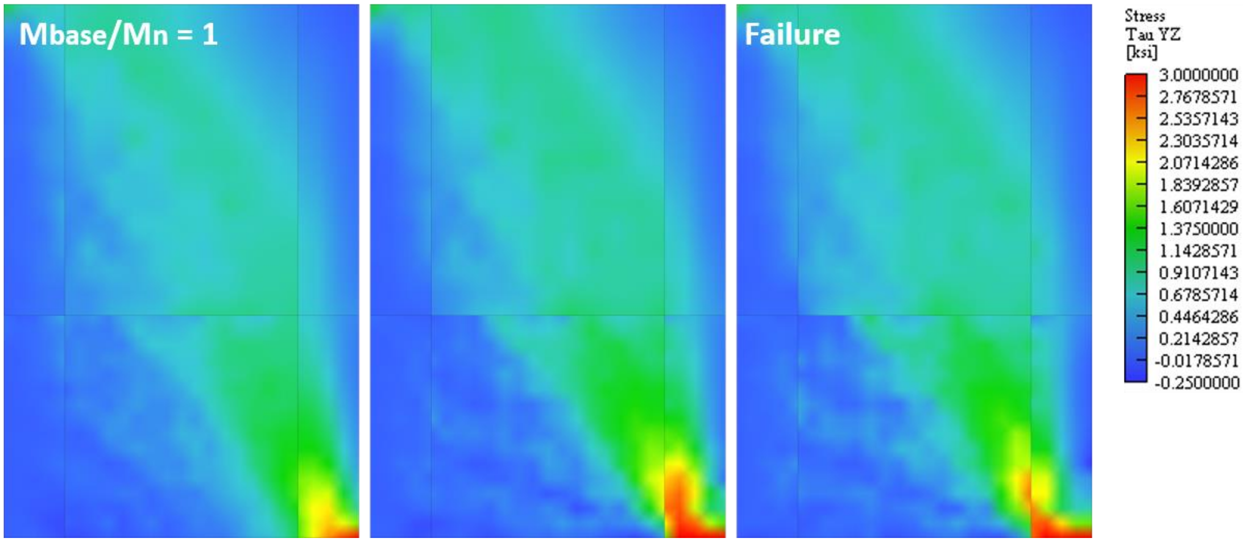

Figure 4.42 – Specimen RW-A20-P10-S63 In-Plane Shear Stress Contour Plots

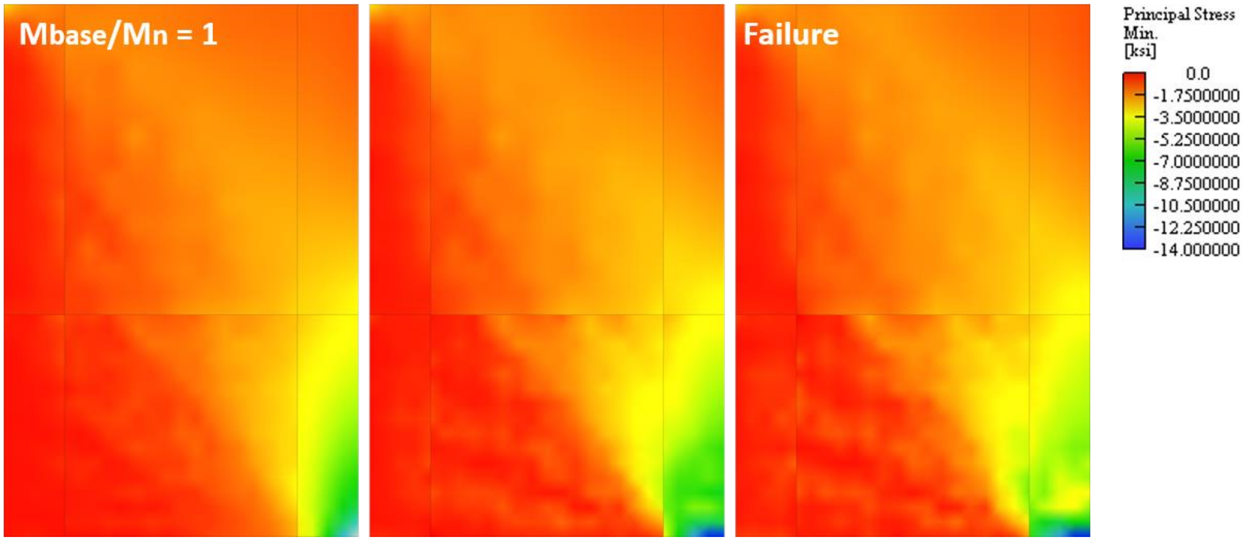

Figure 4.43 – Specimen RW-A20-P10-S63 Min. Principal Stress Contour Plots

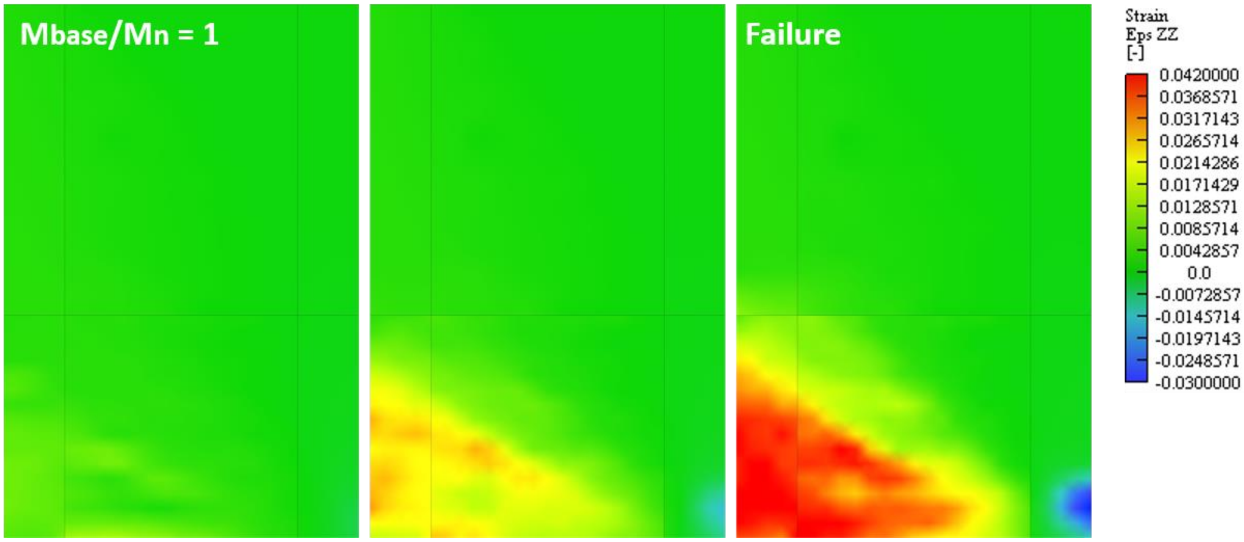

Figure 4.44 – Specimen RW-A20-P10-S63 Vertical Strain Contour Plots

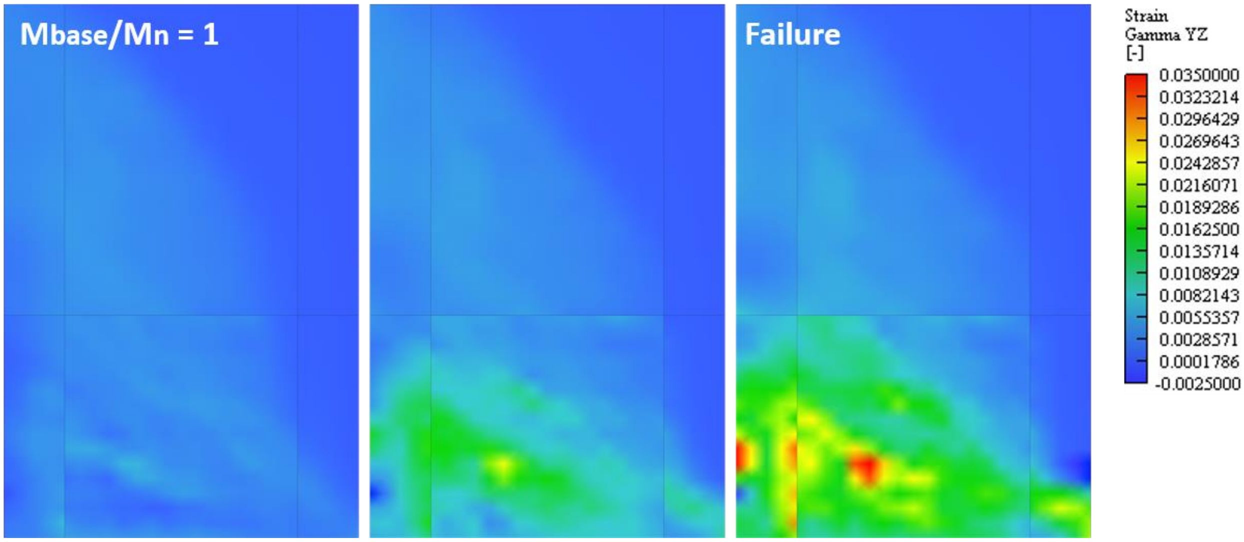

Figure 4.45 – Specimen RW-A20-P10-S63 In-Plane Shear Strain Contour Plots

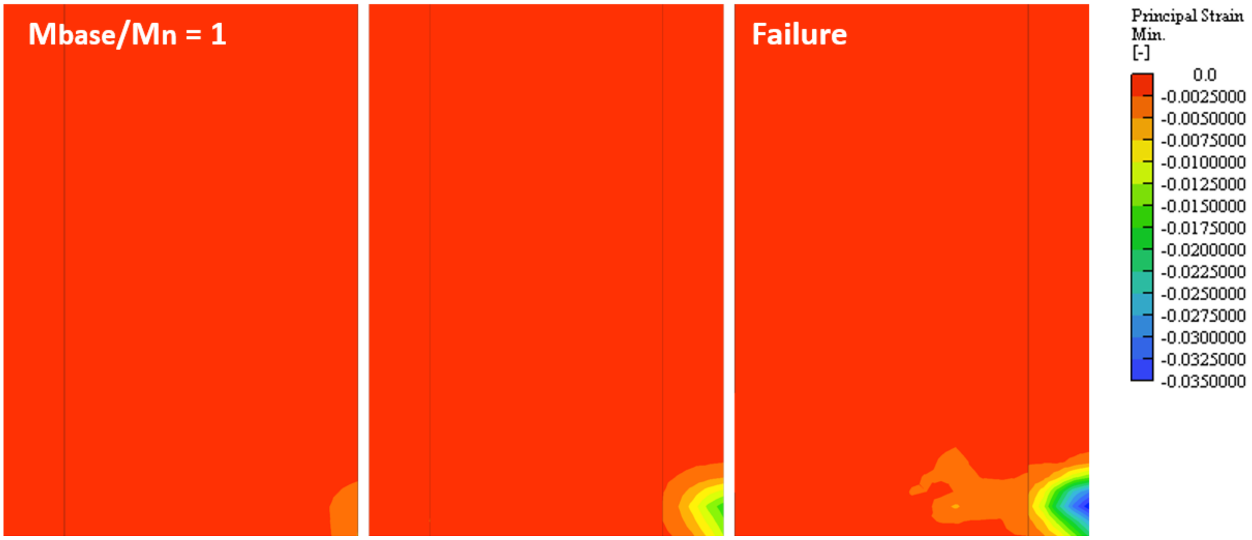

Figure 4.46 – Specimen RW-A20-P10-S63 Min. Principal Strain Contour Plots

4.2 Comparison of Stress Contour Plots for Different Failure Modes

The stress contour plots show that behavioral response varies for the reference walls across the different failure modes. To better understand how these failures are differentiated, sets of each type of stress and strain contour plots are compared.

For simplicity, only one specimen is presented for each failure mode in Section 4.2.1. The main behavioral response that is exhibited in the two BR (RW1 and R1) and two CB (WSH4 and RW-A20-P10-S63) is consistent for each failure mode. Failure modes are thus studied by directly comparing one set of contour plots from each of the three failure mechanisms.

Compression failures are studied in Sections 4.2.2-4.2.4, and the relative performance of Specimens RW-A20-P10-S63 and S6 is particularly notable and worthy of investigation. These specimens are subjected to similar peak shear stresses and axial load ratios, but Specimen S6 exhibits little more than half of the deformation capacity observed in Specimen RW-A20-P10-S63. The main difference between these two walls is the cross-sectional aspect ratio, with Specimen RW-A20-P10-S63 possessing a CSAR of 8 and Specimen S6 a CSAR of 21.1. The high-fidelity stress and strain data available in the model simulations is used in the following sections to determine how CSAR and shear demand affect response.

4.2.1 Vertical Stress Contour Plots for BR and CB Failures

The following stress contour plots are used to illustrate the difference between BR (Specimen RW1), CB (Specimen WSH4) and CS (Specimen S6) failure modes.

BR: The vertical stress contour plots for Specimen RW1 are shown in Figure 4.47. The specimen retains strength in the compressive boundary element. The stress along the height of the specimen is vertically-oriented, without an obvious diagonal shear strut forming. There is no significant compressive strength loss in the concrete at specimen failure.

CB: The vertical stress contour plots for Specimen WSH4 show a loss of compressive strength in the boundary element (Figure 4.48). As with BR failure RW1, there is no significant diagonal shear present. Failure occurs because of strength loss in the boundary element core which causes a loss of specimen lateral load-carrying capacity. This wall exhibits limited deformation capacity due to the lack of defined boundary element reinforcement, which results in concrete with limited deformation capacity.

CS: The vertical stress contour plots for Specimen S6 are shown in Figure 4.49. This specimen exhibits a compression failure that is influenced by the larger shear stress demand, denoted as a CS failure. This failure is characterized by strength loss which first occurs at the web/boundary element interface. Specimen failure occurs due to strength loss at both the web/boundary element interface and concrete crushing in the boundary element core. The shear stresses at the web/boundary element interface result in a loss of reserve capacity for the specimen; when concrete begins to experience crushing in the boundary element core, strength loss has already occurred toward the inner fiber of the boundary element and the specimen loses lateral load-carrying capacity. The deformation capacity observed in CS failures is limited as these two concrete regions lose strength simultaneously, rather than the gradual strength loss observed in a CB failure.

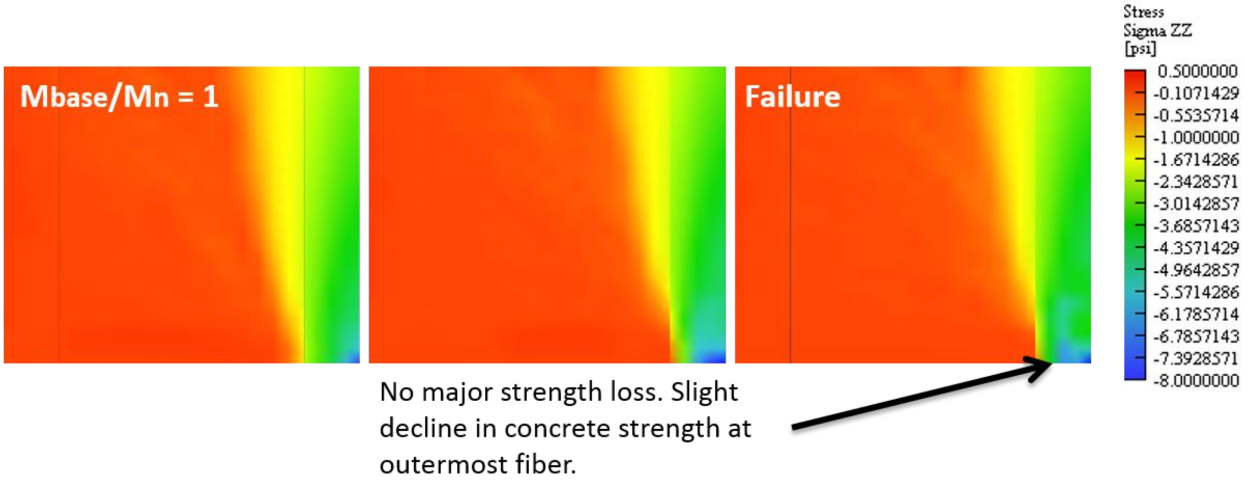

No major strength loss. Slight decline in concrete strength at outermost fiber.

Figure 4.47 – Specimen RW1 Vertical Stress Contour Plots ($v_{max} = 2.52\sqrt{f'c}$ psi ($0.21\sqrt{f'c}$ MPa) and CSAR = 12.0, Zoomed to Bottom of Wall with 28% of h_w and 100% of l_w Shown)

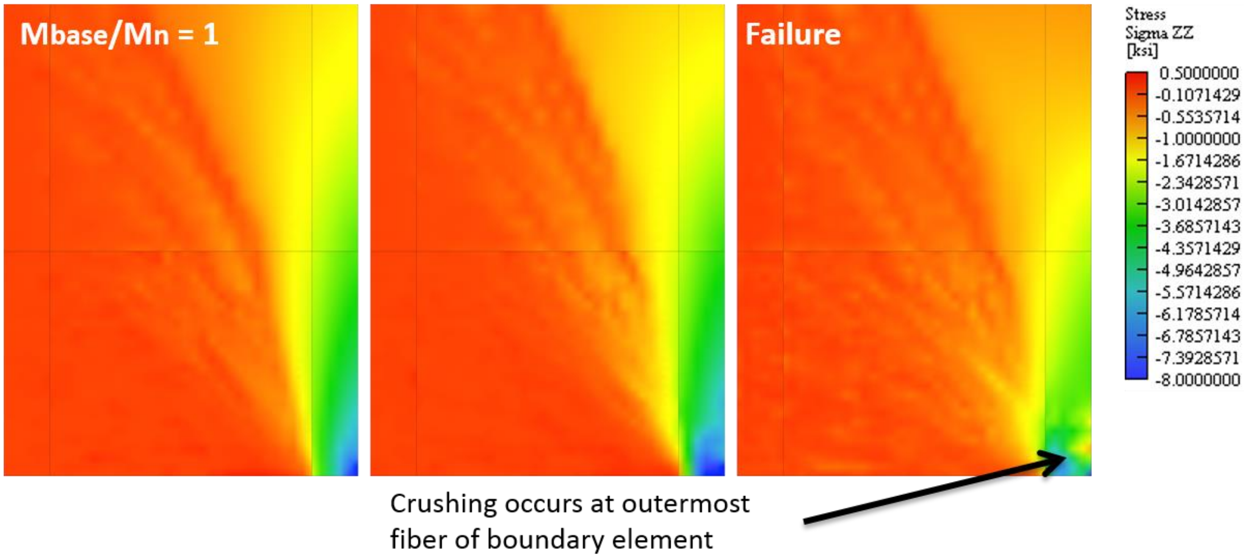

Crushing occurs at outermost fiber of boundary element

Figure 4.48 – Specimen WSH4 Vertical Stress Contour Plots ($v_{max} = 2.85\sqrt{f'c}$ psi ($0.24\sqrt{f'c}$ MPa) and CSAR = 13.35)

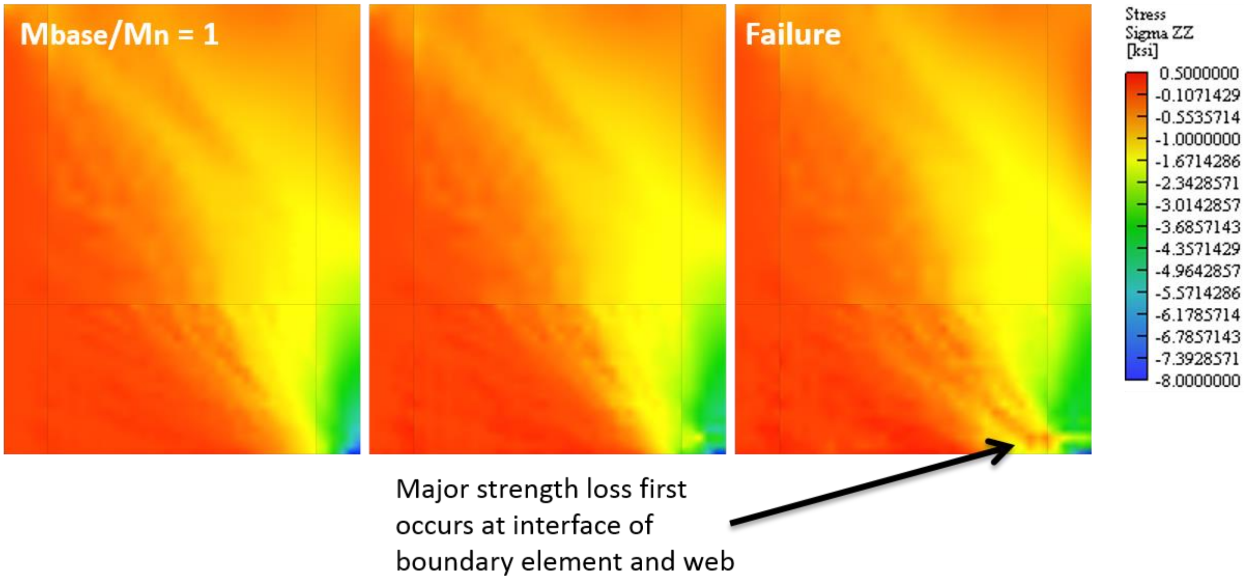

Major strength loss first occurs at interface of boundary element and web

Figure 4.49 – Specimen S6 Vertical Stress Contour Plots ($v_{max} = 6.27\sqrt{f'c}$ psi ($0.52\sqrt{f'c}$ MPa) and CSAR = 21.1)

4.2.2 Shear Stress Contour Plots for CB Failures

It is clear from the vertical stress contour plots that the BR failure occurs when the longitudinal boundary element reinforcement reaches the buckle/rupture limit prior to concrete crushing. The differentiation of the compression failure modes (CB and CS) is more subtle and worthy of further inspection. For this reason, the plots presented for the rest of this section will only focus on the three reference walls exhibiting compression failure: WSH4, RW-A20-P10-S63, and S6. Note that the shear stress demands for these three specimens were $2.85\sqrt{f'c}$ psi ($0.24\sqrt{f'c}$ MPa), $6.73\sqrt{f'c}$ psi ($0.56\sqrt{f'c}$ MPa) and $6.27\sqrt{f'c}$ psi ($0.52\sqrt{f'c}$ MPa), respectively.

CB: Specimens RW-A20-P10-S63 and WSH4 do not exhibit significant strength loss at the web/boundary element interface prior to failure. Though high shear stresses are observed in RW-A20-P10-S63, the shear is carried through one primary shear strut.

CS: Specimen S6 shows high shear stresses between M_n and failure, leading to the loss of strength at the web/boundary element interface. As the initial shear strut begins to cause strength loss at this interface, a second shear strut develops below. The development of multiple shear struts near the interface is typical of CS failure.

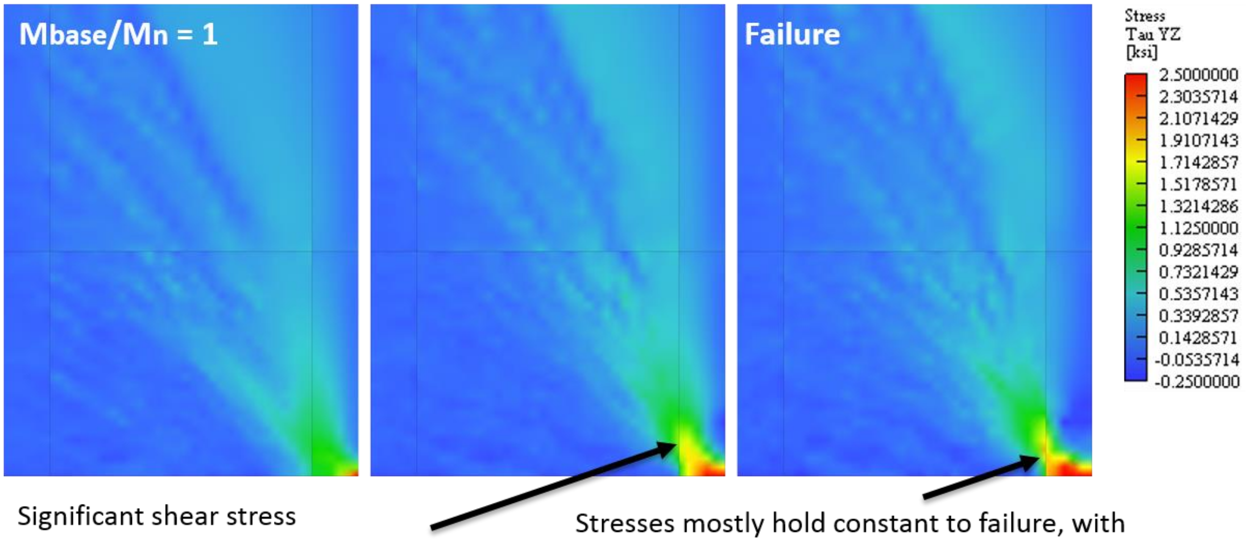

Significant shear stress develops across the boundary element region

Stresses mostly hold constant to failure, with no significant loss of capacity due to shear. Interface between BE and web is intact.

Figure 4.50 – Specimen WSH4 In-Plane Shear Stress Contour Plots ($v_{max} = 2.85\sqrt{f'c}$ psi ($0.24\sqrt{f'c}$ MPa), CSAR = 13.35)

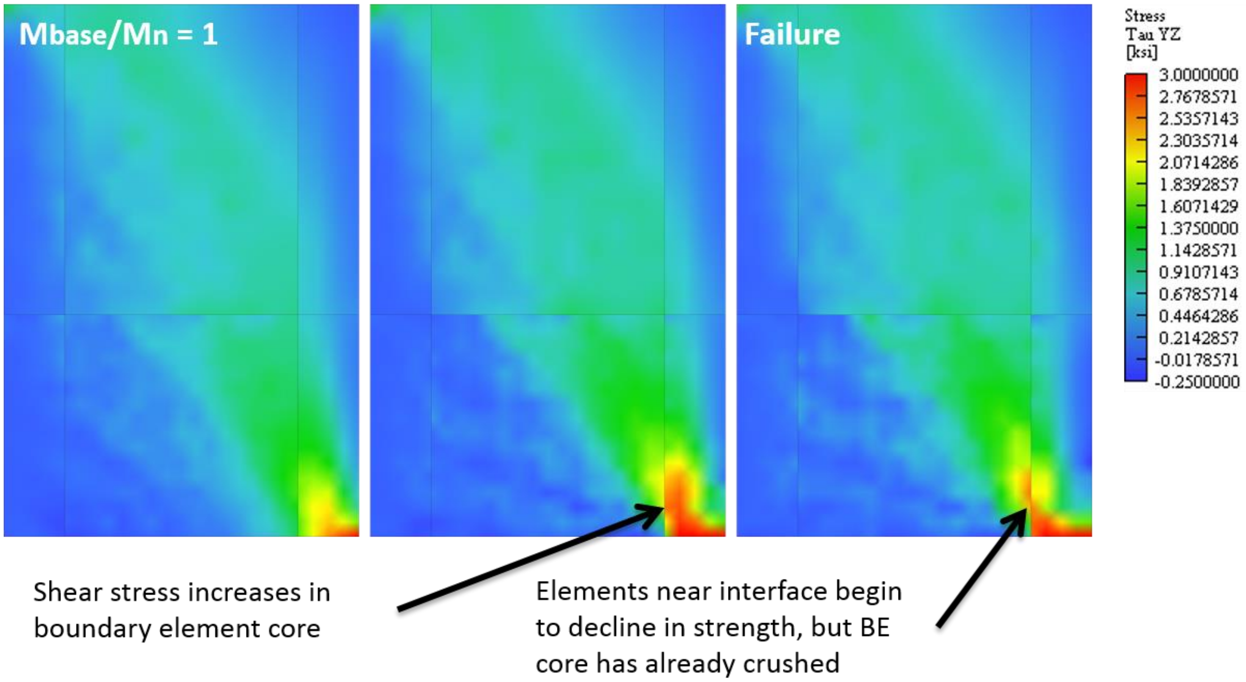

Shear stress increases in boundary element core

Elements near interface begin to decline in strength, but BE core has already crushed

Figure 4.51 – Specimen RW-A20-P10-S63 In-Plane Shear Stress Contour Plots ($v_{max} = 6.73\sqrt{f'c}$ psi ($0.56\sqrt{f'c}$ MPa), CSAR = 8.0)

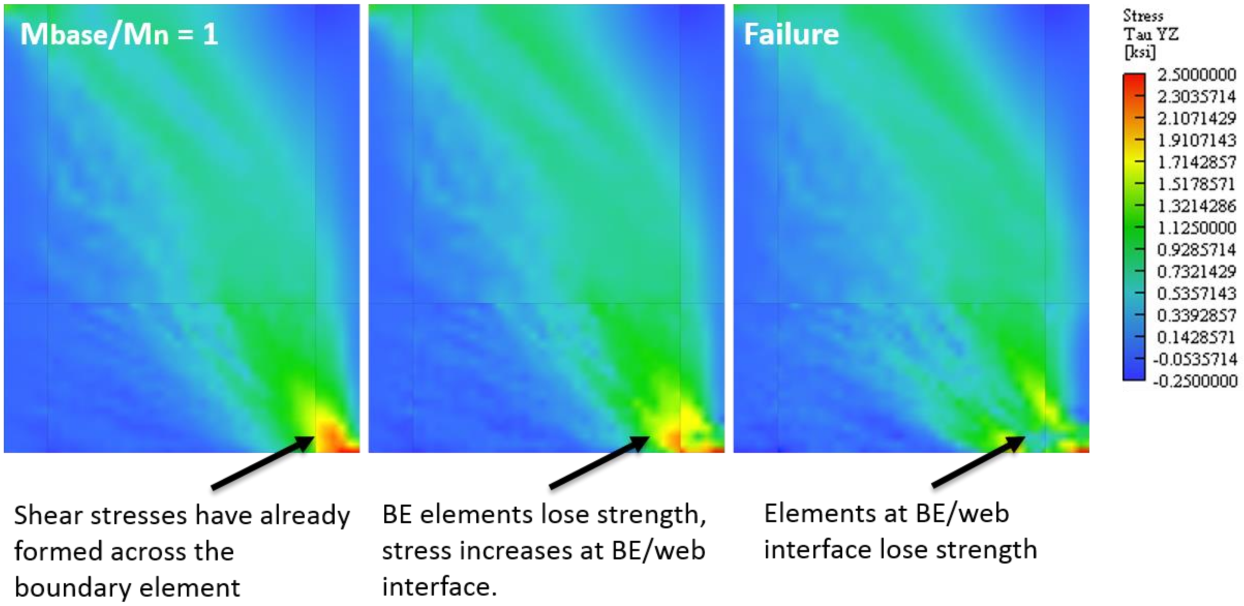

Shear stresses have already formed across the boundary element

BE elements lose strength, stress increases at BE/web interface.

Elements at BE/web interface lose strength

Figure 4.52 – Specimen S6 In-Plane Shear Stress Contour Plots ($v_{max} = 6.27\sqrt{f'c}$ ps ($0.52\sqrt{f'c}$ MPa)i, CSAR = 21.1)

4.2.3 Minimum Principal Stress Contour Plots for CB Failures

The minimum principal stress contour plots for the three reference walls exhibiting compression-buckling failures are shown in Figure 4.53-Figure 4.55.

CB: As seen in the vertical and shear stress plots above, the CB failures do not exhibit significant strength loss at the web/boundary element interface prior to failure. CB failures are characterized by crushing at the outermost fibers of the boundary element core, with reserve capacity available toward the inner portion of the boundary element. While Specimen RW-A20-P10-S63 exhibits much more deformation capacity than that observed in Specimen WSH4, this is attributable to the lack of confining boundary element reinforcement in Specimen WSH4. For CB failures, deformation capacity is significantly affected by the detailing of confining reinforcement in the boundary element.

CS: Specimen S6 shows a loss of strength near the web/boundary element interface and the development of multiple diagonal shear struts prior to failure. These two behaviors are primary indicators of CS failure. The specimen loses strength across the length of the boundary element, rather than the gradual progression of crushing observed in CB failures.

Impact of CSAR: It is possible to gain further insight into the role of CSAR in CS failure by investigating these minimum principal strain plots. Take note of the contour plots for Specimens S6 and RW-A20-P10-S63 at M_n, the first contour plot in the sequence. In Specimen RW-A20-P10-S63 (CSAR = 8), the primary shear strut terminates in the boundary element well above the critical region, which results in significant compression and tension loads being concentrated in the boundary element at the critical section. This is different from Specimen S6 (CSAR = 21.1), where several shear struts terminate near the bottom of the wall, resulting in significant compression demands at the interface. For cross-sectionally stout walls, the concentration of tension and compression demands in the boundary element result in a stress field more consistent with that of a typical beam.

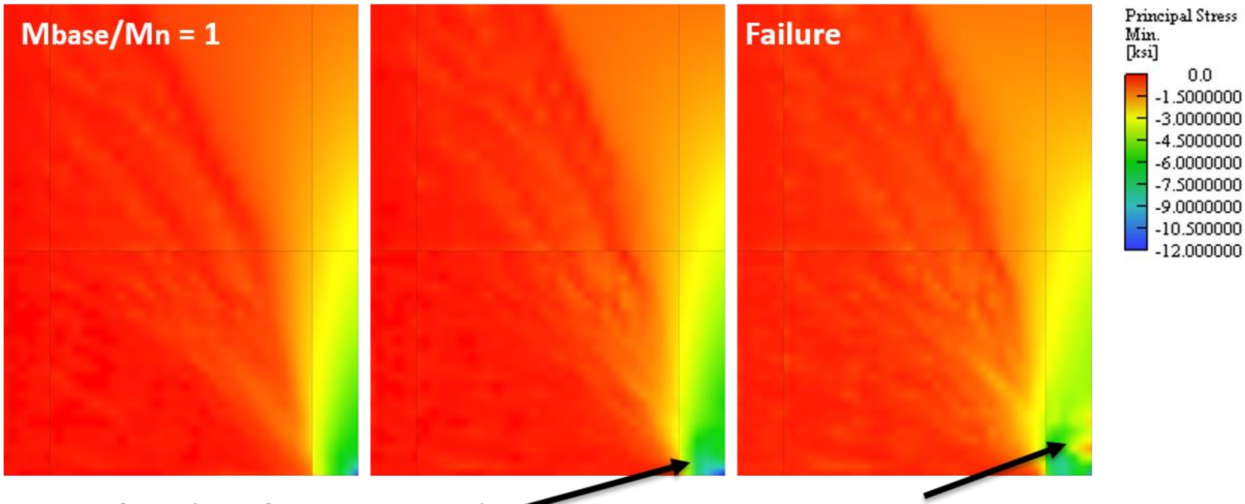

No significant loss of concrete strength. Stresses are almost all vertically-oriented, with no evidence of meaningful shear impact.

Strength loss occurs at extreme outer fiber of boundary element core and not at web/BE interface.

Figure 4.53 – Specimen WSH4 Min. Principal Stress Contour Plots ($v_{max} = 2.85\sqrt{f'c}$ psi ($0.24\sqrt{f'c}$ MPa), CSAR = 13.4)

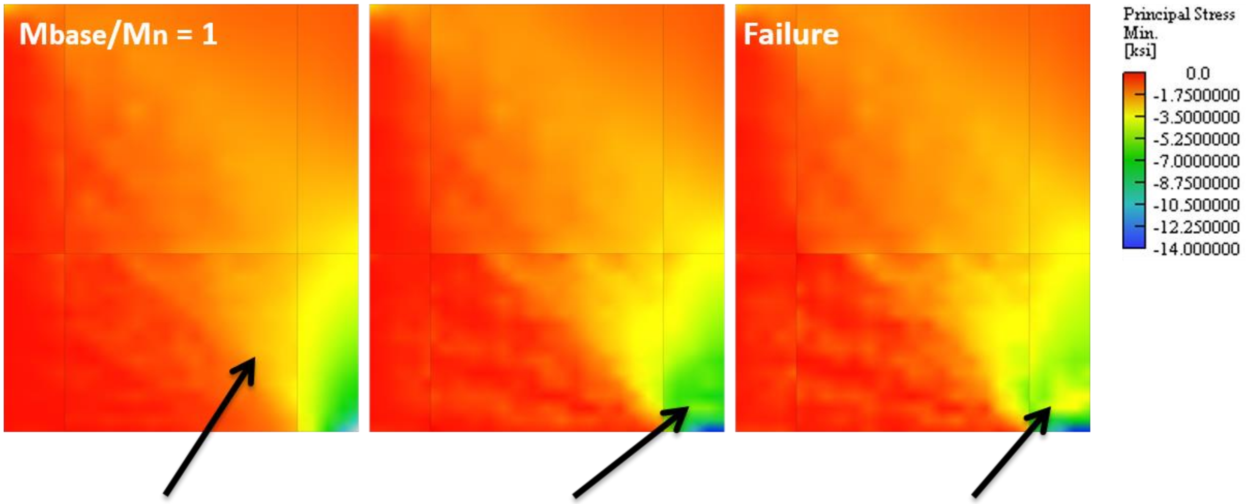

Diagonal shear strut magnitude relatively low

Concrete declines in strength in the core region of the boundary element.

Failure occurs due to crushing in the core region of the boundary element.

Figure 4.54 – Specimen RW-A20-P10-S63 Min. Principal Stress Contour Plots ($v_{max} = 6.73\sqrt{f'c}$ psi ($0.56\sqrt{f'c}$ MPa), CSAR = 8.0)

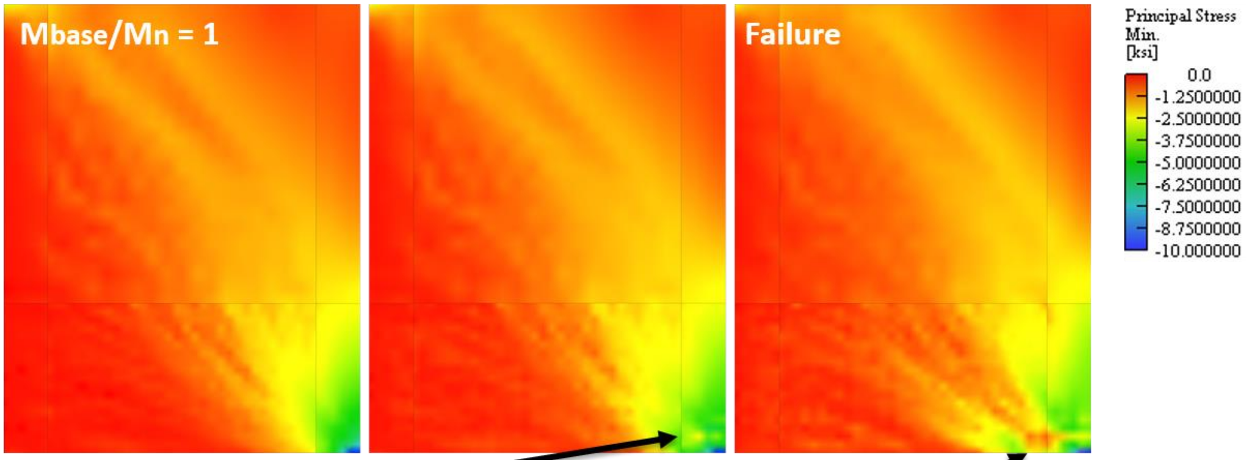

Strength loss occurs near BE/web interface, stresses increase at interface

Elements at BE/web interface lose strength, leading to wall failure

Figure 4.55 – Specimen S6 Min. Principal Stress Contour Plots ($v_{max} = 6.27\sqrt{f'c}$ psi ($0.52\sqrt{f'c}$ MPa), CSAR = 21.1)

4.2.4 Minimum Principal Strain Contour Plots for CB Failures

The minimum principal strain contour plots for Specimens WSH4, RW-A20-P10-S63, and S6 at failure are shown in Figures 4.56-4.58. These two plots provide a method for differentiating the two failure modes: CB and CS.

CB: In both CB failures, the minimum principal strains are largest at the outermost fiber and increase toward the web. For Specimen WSH4, which does not have a defined boundary element, the wall fails as soon as the full boundary element is subjected to compressive strain, and this occurs at a low deformation capacity. For Specimen RW-A20-P10-S63, the specimen retains lateral load-carrying capacity until significant strains are present in the web and the full boundary element core has crushed.

CS: There are significant minimum principal strains present across the length of the boundary element. These do not increase gradually from the outer fiber of the boundary element as observed in the two CB failures. The loss of strength that occurs at the web/boundary element interface is a result of the high strains shown in this plot; this flat strain distribution also explains the lack of reserve capacity observed in CS specimens, as the full length of the boundary element is subjected to crushing due to the interaction of shear and flexural demand.

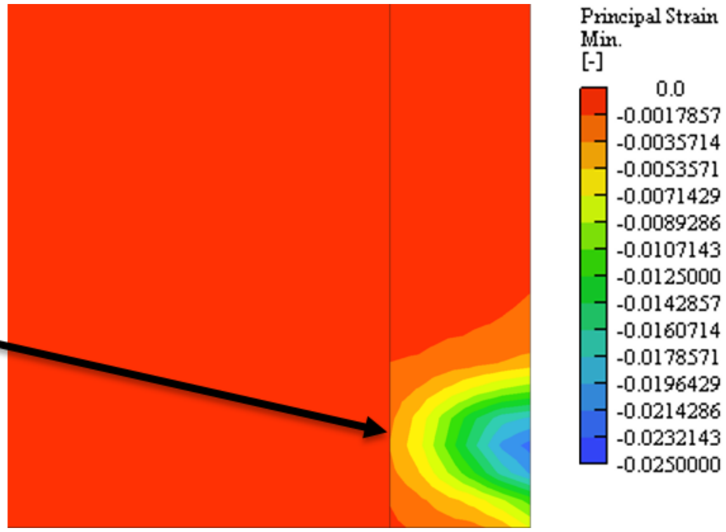

Largest principal strains at extreme fiber. Strains decrease towards BE/web interface. Strains in web are zero.

Figure 4.56 – Specimen WSH4 Min. Principal Strain Contour Plot at Failure ($v_{max} = 2.85\sqrt{f'c}$ psi ($0.24\sqrt{f'c}$ MPa) and CSAR = 13.4, Showing Bottom-Right of Wall at 36% of h_w and 49% of l_w)

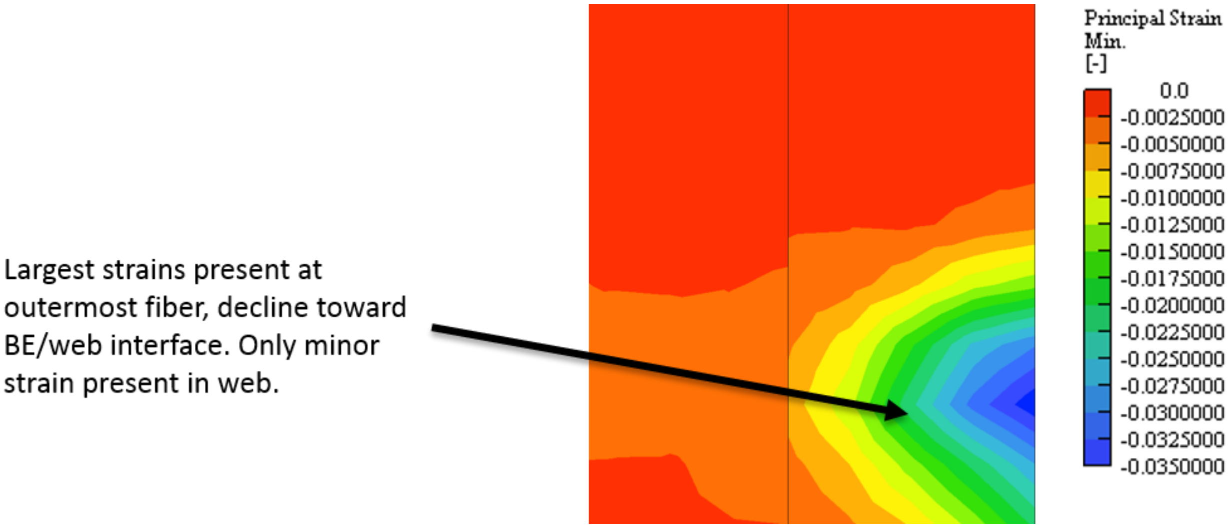
Largest strains present at outermost fiber, decline toward BE/web interface. Only minor strain present in web.

Figure 4.57 – Specimen RW-A20-P10-S63 Min. Principal Strain Contour Plot at Failure ($v_{max} = 6.73\sqrt{f'c}$ psi ($0.56\sqrt{f'c}$ MPa) and CSAR = 8.0, Showing Bottom-Right of Wall at 24% of h_w and 31% of l_w)

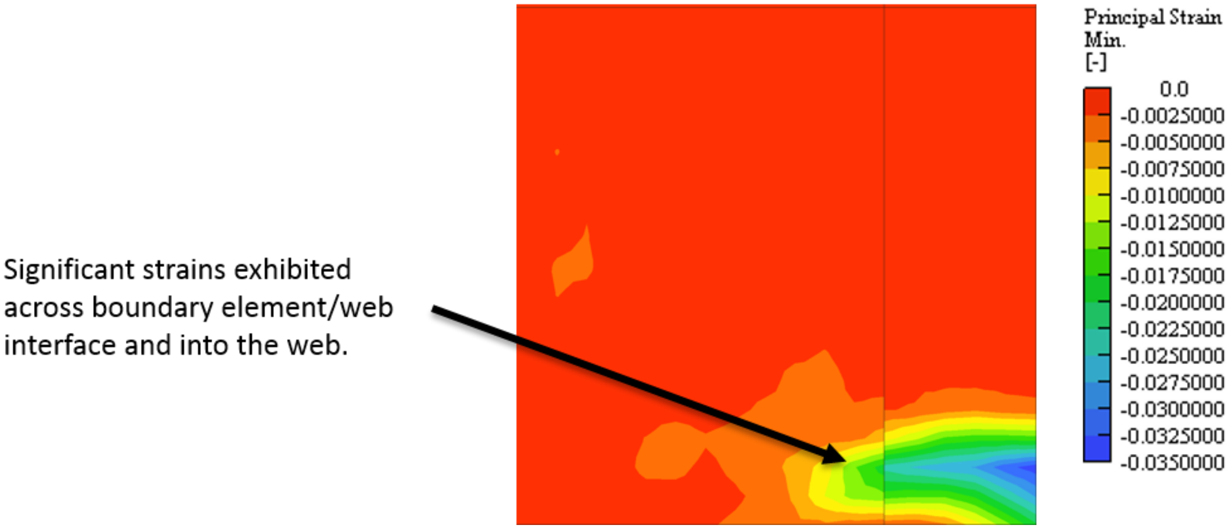
Significant strains exhibited across boundary element/web interface and into the web.

Figure 4.58 – Specimen S6 Min. Principal Strain Contour Plot at Failure ($v_{max} = 6.27\sqrt{f'c}$ psi ($0.52\sqrt{f'c}$ MPa) and CSAR = 21.1, Showing Bottom-Right of Wall at 34% of h_w and 42% of l_w)

4.3 CONCLUSIONS

The reference wall results suggest that the modeling approach is accurate and a parametric study using the modeling approach to more thoroughly assess the impact of the salient parameters is justified.

The characteristics of the three failure modes were defined by investigation of the stress and strain contour plots for the reference walls. The following represent the key behaviors of each failure mode.

BR: Behavior is characterized by limited concrete crushing at the point where the longitudinal boundary element reinforcement reaches the buckle/rupture limit defined in Section 3.4. There is limited shear influence.

CB: Behavior is characterized by concrete crushing in the boundary element core which occurs prior to the longitudinal reinforcement reaching the buckle/rupture limit defined in Section 3.4. There may be significant diagonal shear stresses, but CB failures do not exhibit significant strength loss due to shear demand prior to crushing of the boundary element core. Crushing first occurs at the outermost fiber of the boundary element and progresses through the boundary element core and toward the web/boundary element interface. With adequate confining reinforcement, the wall maintains lateral-load carrying capacity as the neutral axis progresses toward the web/boundary element interface. This allows for greater plastic deformation than is observed in CS failures.

CS: Behavior is characterized by concrete crushing across the length of the boundary element, which occurs prior to the longitudinal reinforcement reaching the buckle/rupture limit defined in Section 3.4. There are significant diagonal shear stresses, and these result in the loss of strength at the web/boundary element interface. Initial crushing occurs at both the web/boundary element interface and the outermost fiber of the boundary element core, and the specimen loses lateral-load carrying capacity as crushing occurs across the length of the boundary element. Significant minimum principal strains are present across the length of the boundary element and into the web.

5 PARAMETER STUDY

The response of reinforced concrete structural walls has been the subject of numerous experimental studies, as quantified and qualified by Birely (2012). There is a need to quantify the impact of salient parameters on the response of walls. However, because of financial and laboratory-capacity limitations, systematic evaluation of walls that both represent the characteristics of modern building construction (e.g., high CSAR, presence of an axial load and higher shear stress demands) and study key parameters is difficult. The analytical model developed in Chapter 3 and evaluated in Chapter 4 provides a means of investigating these key parameters; this model is not affected by equipment, specimen size, loading, or funding issues that limit experimental testing. The model also provides insight into wall behavior that cannot be gleaned from experimental tests, such as high-fidelity compressive strain field data.

Discussed in Chapters 2 and 4 is the idea that wall configuration (CSAR), axial load ratio, and shear demand are key parameters in the development of compression-shear failure. The influence of CSAR is particularly notable in the response of Specimen S6 (CS) relative to that of Specimen RW-A20-P10-S63 (CB), where the walls are of similar reinforcement configuration, loading, and peak shear stress, but differ in CSAR and exhibit significantly different deformation capacities. It is necessary to extend analysis beyond that which has been tested experimentally to better isolate the key study parameters.

In particular this study would systematically: (1) evaluate a range of walls with different CSARs, (2) further investigate the compression-shear failure observed in Specimen S6, and (3) study the relative performance of compression-shear failures vs. specimens which undergo either compression-buckling or bar rupture failures.

To achieve this, an extensive modeling parameter study was developed and executed. First, several reference wall specimens were selected from the experimental dataset that span the range of cross-section geometries (i.e. CSAR) found within the dataset. Then, for each of these reference walls, axial load ratio, shear span, and vertical boundary element reinforcement ratio were varied to achieve different simulated peak shear stress demands and failure modes for the walls.

The parameter study is presented in this chapter as follows. Section 5.1 presents definitions for all relevant parameters and introduces the simulation model matrix. Results are then presented in Sections 5.2, including an investigation of all relationships between the main input parameters (e.g., axial load ratio, cross-sectional aspect ratio) and defined output parameters (e.g., story drift, hinge rotation). These findings lead into a discussion (Section 5.2.4-5.2.5) of the impact of cross-sectional aspect ratio on specimen failure and the development of CS failures. Finally, Section 5.3 provides a discussion of the deformation capacity for all failure modes.

5.1 PARAMETER STUDY OUTLINE

The parametric study is structured as follows. First, three base specimens from the experimental matrix are defined. The input parameters are then defined and their range of values in the study quantified.

5.1.1 Selection of Base Specimens

Experimental specimens RW1, PW4, and RW-A20-P10-S63 are selected to ensure variation in the cross-sectional aspect ratio (CSAR), from 8.0 to 20.0, which are the rough bounds of the full data set.

To further expand the range of CSAR values tested in this study, modified models of both RW1 and PW4 are utilized. In both cases, the thickness of the specimen was increased to decrease the CSAR of the original specimen. The thickness of RW1 and PW4 were increased to 4.8 in. (122 mm) and 7.5 in. (191 mm), respectively, resulting in CSAR values of 10.0 and 16.0. The selected base specimens are

Table 5.1 – List of Parameter Study Base Specimens

Base Specimen	Reference	CSAR	Simulation of Base Specimen
PW4	Birely (2012)	20	PW4
PW16	--	16	None
RW1	Thomsen et. al (1995)	12	RW1
RW10	--	10	None
RW-A20-P10-S63	Tran (2012)	8	RW-A20-P10-S63

The information for all base specimens is shown in Tables 5.2-5.5. Base views of sections and boundary element details are presented in Figures 5.1-5.3.

Table 5.2 – Properties of Parameter Study Base Specimens

Specimen	Geometry				Loading			Results		
	l_w	t_w	h	CSAR	Shear Span	ALR	$V_{max}/A_{cv}f'_c{}^{0.5}$	V_{max}/V_n	Δ_{ult}	Failure Mode
	in.	in.	in.	--	--	%	psi	--	%	--
PW4	120	6	144	20.0	2.00	12.2	4.63	0.88	1.01	CB
PW16	120	7.5	144	16.0	--	--	--	--	--	--
RW1	48	4	144	12.0	3.13	10.5	2.57	0.50	2.26	BR
RW10	48	4.8	144	10.0	--	--	--	--	--	--
RW-A20-P10-S63	48	6	96	8.0	2.00	7.3	6.10	0.91	3.00	CB

Table 5.3 – Material Properties of Parameter Study Base Specimens

Specimen	Materials								
	f'_c	$f_{y,be}$	$E_{s,be}$	$f_{u,be}$	$\varepsilon_{u,be}$	$f_{y,v}$	$E_{s,v}$	$f_{u,v}$	$\varepsilon_{u,v}$
	psi	ksi	ksi	ksi	in/in	ksi	ksi	ksi	in/in
PW4	4272	67.1	29000	109.5	0.12	75.7	29000	77.0	0.06
PW16	4272	67.1	29000	109.5	0.12	75.7	29000	77.0	0.06
RW1	4580	63.0	29000	93.0	0.10	65.0	29000	85.0	0.08
RW10	4580	63.0	29000	93.0	0.10	65.0	29000	85.0	0.08
RW-A20-P10-S63	7050	68.4	29000	88.9	0.19	61.4	29000	71.3	0.071

Table 5.4 – Reinforcing Properties of Parameter Study Base Specimens

Specimen	Reinforcing Steel					Confinement				
	$\rho_{vert,BE}$	$\rho_{vert,web}$	ρ_{gross}	$\rho_{t,web}$	ρ_{vol}	h_x	s_{vert}	s_{vert}/d_b	h_x/s	ACI BE
	%	%	%	%	%	in.	in.	--	--	--
PW4	3.50	0.28	1.32	0.28	1.24	3.00	2.00	4.00	1.50	SBE
PW16	3.50	0.28	1.32	0.28	1.24	4.50	2.00	4.00	2.25	SBE
RW1	2.95	0.33	1.12	0.33	0.78	2.00	3.00	8.00	0.67	NBE
RW10	2.95	0.33	1.12	0.33	0.78	2.80	3.00	8.00	0.93	NBE
RW-A20-P10-S63	7.11	0.61	2.84	0.61	2.23	2.00	2.00	2.67	1.00	SBE

Table 5.5 – Summary of ACI 318-14 BE Compliance for Parameter Study Base Specimens

Specimen	ACI BE Classification	SBE Criteria Met	SBE Criteria Failed
PW4	OBE	BE length c/l_w Horizontal spacing Min. wall thickness. Min. volumetric reinf. ratio	Vertical Spacing
PW16	OBE	BE length c/l_w Horizontal spacing Min. wall thickness. Min. volumetric reinf. ratio	Vertical Spacing
RW1	NBE	BE length c/l_w Horizontal spacing Min. wall thickness.	Vertical spacing Min. volumetric reinf. ratio.
RW10	NBE	BE length c/l_w Horizontal spacing Min. wall thickness.	Vertical spacing Min. volumetric reinf. ratio.
RW-A20-P10-S63	SBE	All	None

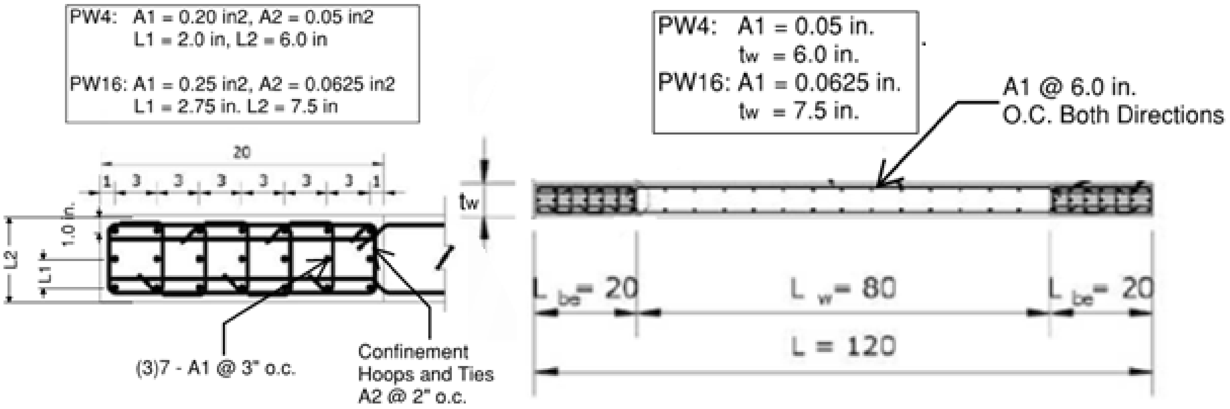

Figure 5.1 – Base View of Section and Boundary Element Detail for Specimen PW4/PW16 (Birely 2012)

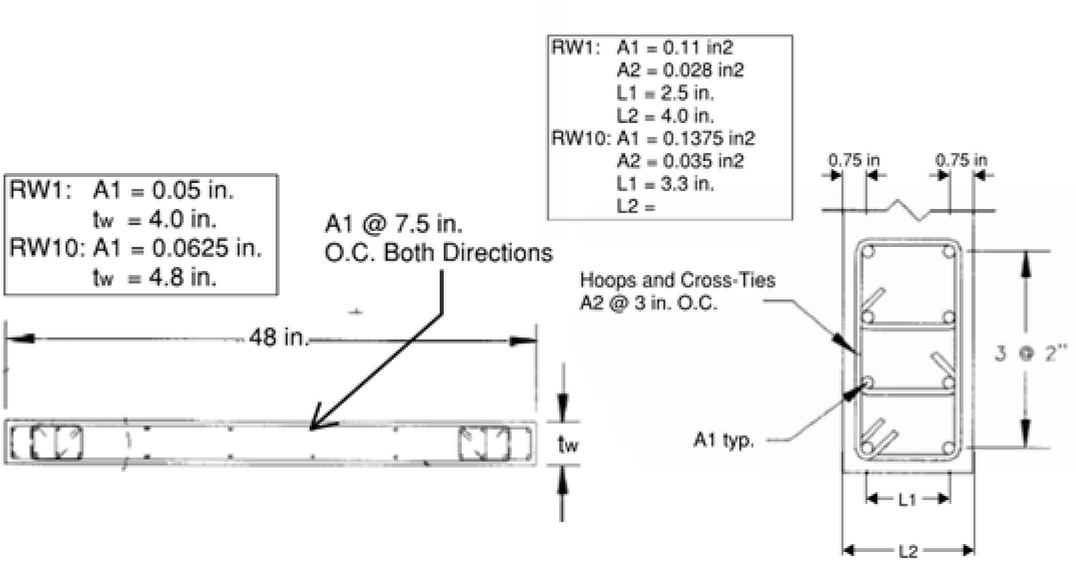

Figure 5.2 – Base View of Section and Boundary Element Detail for Specimen RW1/RW10 (Thomsen et al. 1995)

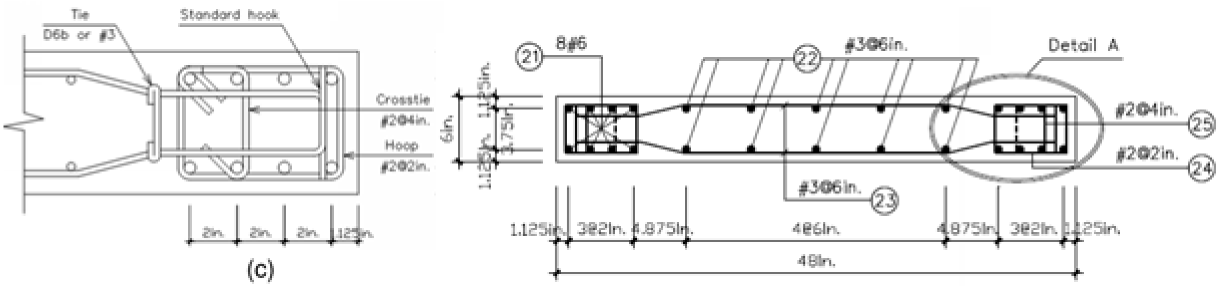

Figure 5.3 – Base View of Section and Boundary Element Detail for Specimen RW-A20-P10-S63 (Tran 2012)

5.1.2 Study Parameters

The design and loading of each of the base specimens was varied to study the impact of the following parameters for different CSARs. Note that only the loading and vertical reinforcement was varied; the confinement and geometry were not varied from the base specimen definition.

- Normalized peak shear stress (v_{max}), $V_{max}/f'_c A_{cv}^{0.5}$: peak shear stress was determined to be a key factor in the failure of Specimen S6 in Chapter 4 and is thus a key parameter for study. The normalized peak shear stress was varied from $2\sqrt{f'c}$ to $10\sqrt{f'c}$ psi ($0.17\sqrt{f'c}$-$0.83\sqrt{f'c}$ MPa) in this study.
- Axial Load Ratio (ALR): the base models were subjected to axial load ratios between 2.5% and 15%. The lower bound of 2.5% is necessary for model stability, as there are issues with convergence when less than 2.5% ALR is applied. The upper bound of 15% is also an upper bound for the experimental data set, for which the highest ALR is 13.7%. When discussing the results, the term “Low axial load ratio” refers to ratios below 5% and “high axial load ratio” refers to ratios 10% or greater. It is noted that changing the axial load ratio will also change the shear stress demand for a given geometry.

The axial load ratio and shear span were the primary parameters used to achieve different shear stress demands for the same CSAR; the longitudinal boundary element reinforcement was also increased for some walls to achieve different shear stress demands. The targeted range of peak shear stress demands for each base specimen was achieved by varying the parameters across the following ranges:

- ALR: the primary mechanism by which the peak shear stress was altered was the axial load ratio. For the PW4-C20 and RW1-C12 model series, a wide range of ALRs were considered; however, the RW-C8 and RW1-C10 simulations exhibited behavioral change at a higher peak shear stress than in the base specimens with a lower CSAR. These walls were thus run exclusively with ALRs of 10% or greater.
- Shear span: as with the ALR, this was varied widely for the RW1-C12 and PW4-C20 series. For the low-CSAR specimens, which required a greater level of peak shear stress to reach a CS failure mode, the shear spans were kept to values no greater than 2.0.
- $f_{y,BE}$ and $\rho_{vert,BE}$: in many cases, it was necessary to increase the effective reinforcement area in the boundary element as the shear span and axial load ratio were insufficient to drive the peak shear stress to the required level.

The study was constructed to examine the effect of shear stress demand on wall behavior when grouped by CSAR. While axial load was also studied across a wide range of values, problems with numerical stability limited the number of low-ALR models run in the study, particularly at low CSARs. Further study is also required to more comprehensively understand the impact of the shear span and vertical reinforcement ratio on wall behavior, as these parameters were not varied systematically.

Note that the $\rho_{t,web}$ was modified for some models with a high peak shear stress. This was to increase the nominal shear capacity of the section and produce a V_{max}/V_n ratio of less than 1.0.

5.1.3 Simulation Model Matrix

Tables 5.6-5.10 present all of the simulation models used for this study. Each model is defined by: (1) the base specimen, (2) the cross sectional aspect ratio (CSAR) and (3) an identification number that is unique within the series. For example, Model PW4-C20-1 uses experimental Specimen PW4 as its base, has a cross-sectional aspect ratio of 20, and specimen 1 of 13 within the PW4-C20-* series (Table 5.6).

Table 5.6 – List of Simulated Models in PW4-C20 Series

Specimen	**Shear Span**	**ALR**	**f_y**	**$\rho_{vert,BE}$**	**$\rho_{t,web}$**
	--	%	ksi	%	%
PW4-C20-1	1.50	5.0	67	3.44	0.27
PW4-C20-2	1.50	7.5	67	3.44	0.27
PW4-C20-3	1.50	10.0	67	3.44	0.35
PW4-C20-4	1.50	15.0	67	3.44	0.45
PW4-C20-5	2.25	5.0	67	3.44	0.27
PW4-C20-6	2.25	7.5	67	3.44	0.27
PW4-C20-7	2.25	10.0	67	3.44	0.27
PW4-C20-8	2.25	15.0	67	3.44	0.27
PW4-C20-9	3.00	5.0	67	3.44	0.27
PW4-C20-10	3.00	7.5	67	3.44	0.27
PW4-C20-11	3.00	15.0	67	3.44	0.27
PW4-C20-12	1.50	10.0	67	1.87	0.27
PW4-C20-13	1.50	10.0	67	2.66	0.35

Table 5.7 – List of Simulated Models in RW1-C12 Series

Specimen	**Shear Span**	**ALR**	$f_{y,BE}$	$\rho_{vert,BE}$	ρ_h
	--	%	ksi	%	%
RW1-C12-1	1.75	2.5	63	2.93	0.33
RW1-C12-2	1.75	5.0	63	2.93	0.33
RW1-C12-3	1.75	7.5	63	2.93	0.33
RW1-C12-4	1.75	10.0	63	2.93	0.33
RW1-C12-5	1.75	15.0	63	2.93	0.33
RW1-C12-6	2.50	2.5	63	2.93	0.33
RW1-C12-7	2.50	5.0	63	2.93	0.33
RW1-C12-8	2.50	7.5	63	2.93	0.33
RW1-C12-9	2.50	10.0	63	2.93	0.33
RW1-C12-10	2.50	15.0	63	2.93	0.33
RW1-C12-11	3.13	2.5	63	2.93	0.33
RW1-C12-12	3.13	5.0	63	2.93	0.33
RW1-C12-13	3.13	7.5	63	2.93	0.33
RW1-C12-14	3.13	10.0	63	2.93	0.33
RW1-C12-15	3.13	15.0	63	2.93	0.33
RW1-C12-16	1.75	2.5	90	2.93	0.33
RW1-C12-17	1.75	5.0	90	2.93	0.33
RW1-C12-18	1.75	7.5	90	2.93	0.33
RW1-C12-19	1.75	10.0	90	2.93	0.33
RW1-C12-20	1.75	15.0	90	2.93	0.42

Table 5.8 – List of Simulated Models in RW-C8 Series

Specimen	**Shear Span**	**ALR**	$f_{y,BE}$	$\rho_{vert,BE}$	ρ_h
	--	%	ksi	%	%
RW-C8-1	2.0	15.0	68	7.07	0.75
RW-C8-2	2.0	15.0	80	7.07	0.90
RW-C8-3	2.0	15.0	86	7.07	0.95
RW-C8-4	2.0	15.0	95	7.07	0.95
RW-C8-5	2.0	15.0	100	7.07	1.01
RW-C8-6	2.0	10.0	68	3.53	0.63
RW-C8-7	2.0	10.0	68	7.07	0.70
RW-C8-8	2.0	10.0	130	3.53	0.63
RW-C8-9	2.0	5.0	90	7.7	1.00

Table 5.9 – List of Simulated Models in RW10-C10 Series

Specimen	**Shear Span**	**ALR**	$f_{y,BE}$	$\rho_{vert,BE}$	ρ_h
	--	%	ksi	%	%
RW10-C10-1	1.5	10.0	63	2.93	0.33
RW10-C10-2	1.5	12.5	63	2.93	0.33
RW10-C10-3	1.5	15.0	63	2.93	0.40

Specimen	Shear Span	ALR	$f_{y,BE}$	$\rho_{vert,BE}$	ρ_h
	--	%	ksi	%	%
RW10-C10-4	2.0	10.0	63	2.93	0.33
RW10-C10-5	2.0	12.5	63	2.93	0.33
RW10-C10-6	2.0	15.0	63	2.93	0.33
RW10-C10-7	1.5	15.0	85	2.93	0.50
RW10-C10-8	1.5	15.0	85	3.66	0.55
RW10-C10-9	1.5	15.0	85	4.40	0.70

Table 5.10 – List of Simulated Models in PW16-C16 Series

Specimen	Shear Span	ALR	$f_{y,BE}$	$\rho_{vert,BE}$	ρ_h
	--	%	ksi	%	%
PW16-C16-1	1.5	10.0	67	3.44	0.27
PW16-C16-2	2.0	9.0	67	3.44	0.27
PW16-C16-3	2.0	15.0	80	3.44	0.35
PW16-C16-4	2.0	15.0	85	3.70	0.35
PW16-C16-5	2.0	12.5	85	3.70	0.35
PW16-C16-6	2.0	10.0	85	3.70	0.35

5.2 RESULTS

Simulation models for the walls presented in Section 5.1 were constructed and analyzed using the methods developed in Chapter 3. Failure mode was determined using the processes presented in Sections 3.4 and 4.3; drift and rotation capacities were computed using the methods presented below.

5.2.1 Computed Response Quantities

The objectives of the study were to determine the impact of the response parameters on failure mode and deformation capacity. Thus, for each model, the following quantities were determined or computed from the simulation results.

- Failure mode: The results were used to determine if lateral strength loss was due to bar rupture (BR), compression-buckling (CB), or compression-shear (CS).
- $V_{max}/A_{cv}f'_c{}^{0.5}$: the peak shear strength in terms of maximum base shear strength achieved, normalized by the gross concrete section and concrete compressive strength. Note that $A_{cv} = A_g$ for planar walls.
- Deformation capacity: The deformation parameters of interest are the story drift and hinge rotation; these were calculated for each model. The deformation capacity is compared to the failure mode and used to compile fragility functions for each.
  - Story Drift: defined as the drift level at failure. The drift is recorded at a distance of one story height above the base of each specimen.
  - Hinge Rotation: defined as the hinge rotation at failure, where the hinge length is assumed to be $l_w/2$. Vertical displacements were computed at each end of the wall at a distance $l_w/2$ above the specimen base, which is assumed to be the critical section of the wall. The rotation was then calculated as:

$$\text{Hinge Rotation (rad)} = (\Delta_{\text{vert,left}} - \Delta_{\text{vert,right}})/\text{l}_\text{w} \qquad \textit{(Eq. 5.1)}$$

5.2.2 Tabular Results

Tables 5.11-5.15 present the results of each analysis including story drift, hinge rotation, and failure mode.

Table 5.11 – List of Results for Simulated Models in the PW4-C20 Series

Specimen	ALR	Shear Span	$V_{max}/A_{cv}f'_c{}^{0.5}$	V_b/V_n	Story Drift	Hinge Rotation	Failure Mode
	%	--	psi	--	%	rad	--
PW4-C20-1	5.0	1.50	5.37	0.88	1.19	0.0073	CS
PW4-C20-2	7.5	1.50	5.84	0.95	1.28	0.0083	CS
PW4-C20-3	10.0	1.50	6.23	0.88	1.14	0.0073	CS
PW4-C20-4	15.0	1.50	6.97	0.97	1.02	0.0068	CS
PW4-C20-5	5.0	2.25	3.83	0.74	2.19	0.0171	BR
PW4-C20-6	7.5	2.25	4.05	0.79	2.04	0.0157	CB
PW4-C20-7	10.0	2.25	4.28	0.83	1.95	0.0152	CB
PW4-C20-8	15.0	2.25	4.70	0.91	1.73	0.0133	CB
PW4-C20-9	5.5	3.00	2.83	0.46	2.07	0.0153	CB
PW4-C20-10	7.5	3.00	2.95	0.48	1.90	0.0148	CB
PW4-C20-11	15.0	3.00	3.46	0.67	1.94	0.0159	CB
PW4-C20-12	15.0	1.50	4.75	0.92	1.93	0.0138	CB
PW4-C20-13	15.0	1.50	5.52	0.91	1.55	0.0102	CS

Table 5.12 – List of Results for Simulated Models in the RW1-C12 Series

Specimen	ALR	Shear Span	$V_{max}/A_{cv}f'_c{}^{0.5}$	V_b/V_n	Story Drift	Hinge Rotation	Failure Mode
	%	--	psi	--	%	rad	--
RW1-C12-1	2.5	1.75	3.96	0.70	2.33	0.0204	BR
RW1-C12-2	5.0	1.75	4.29	0.75	2.36	0.0206	BR
RW1-C12-3	7.5	1.75	4.56	0.80	2.17	0.0189	BR
RW1-C12-4	10.0	1.75	4.84	0.85	2.07	0.0182	CB
RW1-C12-5	15.0	1.75	5.48	0.96	1.42	0.0127	CS
RW1-C12-6	2.5	2.50	2.57	0.50	1.98	0.0173	BR
RW1-C12-7	5.0	2.50	2.81	0.54	2.48	0.0223	BR
RW1-C12-8	7.5	2.50	2.99	0.58	2.43	0.0225	BR
RW1-C12-9	10.0	2.50	3.18	0.61	2.35	0.0214	CB
RW1-C12-10	15.0	2.50	3.53	0.68	1.78	0.0170	CB
RW1-C12-11	2.5	3.13	2.19	0.42	2.30	0.0215	BR
RW1-C12-12	5.0	3.13	2.34	0.45	2.30	0.0204	BR
RW1-C12-13	7.5	3.13	2.52	0.48	2.38	0.0211	BR
RW1-C12-14	10.0	3.13	2.70	0.52	2.23	0.0209	CB
RW1-C12-15	15.0	3.13	2.98	0.57	1.78	0.0171	CB
RW1-C12-16	2.5	1.75	4.66	0.81	2.08	0.0184	BR
RW1-C12-17	5.0	1.75	4.96	0.87	2.19	0.0191	CB
RW1-C12-18	7.5	1.75	5.28	0.93	2.08	0.0179	CB
RW1-C12-19	10.0	1.75	5.64	0.99	1.61	0.0138	CS
RW1-C12-20	15.0	1.75	6.32	0.96	1.28	0.0110	CS

Table 5.13 – List of Results for Simulated Models in the RW-C8 Series

Specimen	ALR	Shear Span	$V_{max}/A_{cv}f'_c{}^{0.5}$	V_b/V_n	Story Drift	Hinge Rotation	Failure Mode
	%	--	psi	--	%	rad	--
RW-C8-1	15.0	2.0	7.70	1.03	2.42	0.0218	CB
RW-C8-2	15.0	2.0	8.47	0.99	2.48	0.0225	CB
RW-C8-3	15.0	2.0	8.87	0.99	2.13	0.0181	CB
RW-C8-4	15.0	2.0	9.37	1.04	1.54	0.0123	CS
RW-C8-5	15.0	2.0	9.89	1.05	1.56	0.0071	CS
RW-C8-6	10.0	2.0	5.12	0.77	2.90	0.0285	CB
RW-C8-7	10.0	2.0	7.08	0.99	2.79	0.0237	CB
RW-C8-8	10.0	2.0	5.97	0.90	2.64	0.0243	CB
RW-C8-9	5.0	2.0	8.64	0.93	1.31	0.0079	CS

Table 5.14 – List of Results for Simulated Models in the RW10-C10 Series

Specimen	ALR	Shear Span	$V_{max}/A_{cv}f'_c{}^{0.5}$	V_b/V_n	Story Drift	Hinge Rotation	Failure Mode
	%	--	psi	--	%	rad	--
RW10-C10-1	10.0	1.5	5.77	0.93	2.04	0.0175	CB
RW10-C10-2	12.5	1.5	6.15	0.99	2.00	0.0172	CB
RW10-C10-3	15.0	1.5	6.53	0.95	1.65	0.0143	CB
RW10-C10-4	10.0	2.0	4.37	0.84	2.44	0.0221	CB
RW10-C10-5	12.5	2.0	4.62	0.89	2.07	0.0191	CB
RW10-C10-6	15.0	2.0	4.90	0.94	1.94	0.0182	CB
RW10-C10-7	15.0	1.5	7.38	0.94	1.51	0.0121	CS
RW10-C10-8	15.0	1.5	8.18	0.98	1.53	0.0119	CS
RW10-C10-9	15.0	1.5	8.99	0.92	1.36	0.0101	CS

Table 5.15 – List of Results for Simulated Models in the PW16-C16 Series

Specimen	ALR	Shear Span	$V_{max}/A_{cv}f'_c{}^{0.5}$	V_b/V_n	Story Drift	Hinge Rotation	Failure Mode
	%	--	psi	--	%	rad	--
PW16-C16-1	10.0	1.5	6.16	1.00	0.94	0.0062	CS
PW16-C16-2	9.0	2.0	4.67	0.91	1.70	0.0133	CB
PW16-C16-3	15.0	2.0	5.83	0.96	1.22	0.0097	CS
PW16-C16-4	15.0	2.0	6.07	1.00	1.11	0.0087	CS
PW16-C16-5	12.5	2.0	5.77	0.95	1.13	0.0087	CS
PW16-C16-6	10.0	2.0	5.20	0.86	1.17	0.0089	CS

5.2.3 Results

Each of the three key inputs is plotted against the output parameters to evaluate the impact on (1) deformation capacity and (2) failure mode. There are two plots presented for each input, one vs. story drift and another vs. hinge rotation. Failure mode is presented in each plot with red scatter points representing CS failures, blue indicating CB failures, and green indicating BR failures.

The plots present simulations both for the experimental test specimens (database in Appendix A) and the parameter study designs (Tables 5.11-5.15). Per Birely et al. (2011), walls not subjected to axial load behave differently than specimens which are subjected to axial loads. For this reason, Specimens R1 and R2 are not included in the results presented below.

Axial Load Ratio

The influence of axial load ratio (ALR) on the hinge rotation and story drift of the simulated models is shown in Figures 5.4-5.5. Table 5.16 shows ALR distribution statistics for all simulated results. The data in the figures and table shows:

- The experimental test specimens span the range of ALR values considered, as noted in Section 5.1.2.
- ALR correlation: $R^2 = 0.14$ for story drift and $R^2 = 0.08$ for hinge rotation.
- There is very little correlation between axial load ratio and either story drift or hinge rotation capacity for low ALRs.
- For higher ALRs (> 7%) drift and rotation capacity decrease with increasing ALR; however, the correlation is still weak ($R^2 = 0.23$ for drift and $R^2 = 0.16$ for hinge rotation).
- Axial load ratio is influential in the determination of failure mode. CS and CB failures tend to occur for moderate to large axial load ratios (>7.5%); BR failures typically occur in specimens subjected to low to moderate axial load ratios (<7.5%).

Table 5.16 – Distribution Statistics for Axial Load Ratio of Simulated Models

Study Parameter	**Basic Statistics**			**Quartiles**				
	Mean	Median	StDev	Min	Q1	Q2	Q3	Max
ALR	9.8	10.0	3.9	2.5	7.3	10.0	14.4	15.0

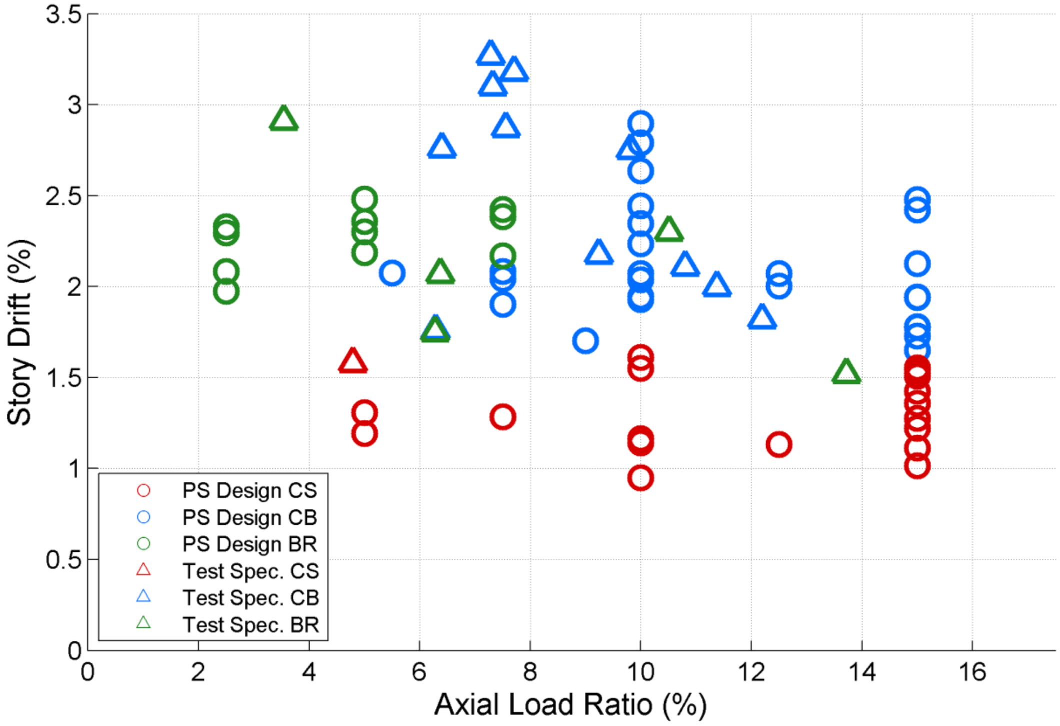

Figure 5.4 – Relationship Between Story Drift and Axial Load Ratio for All Simulated Models

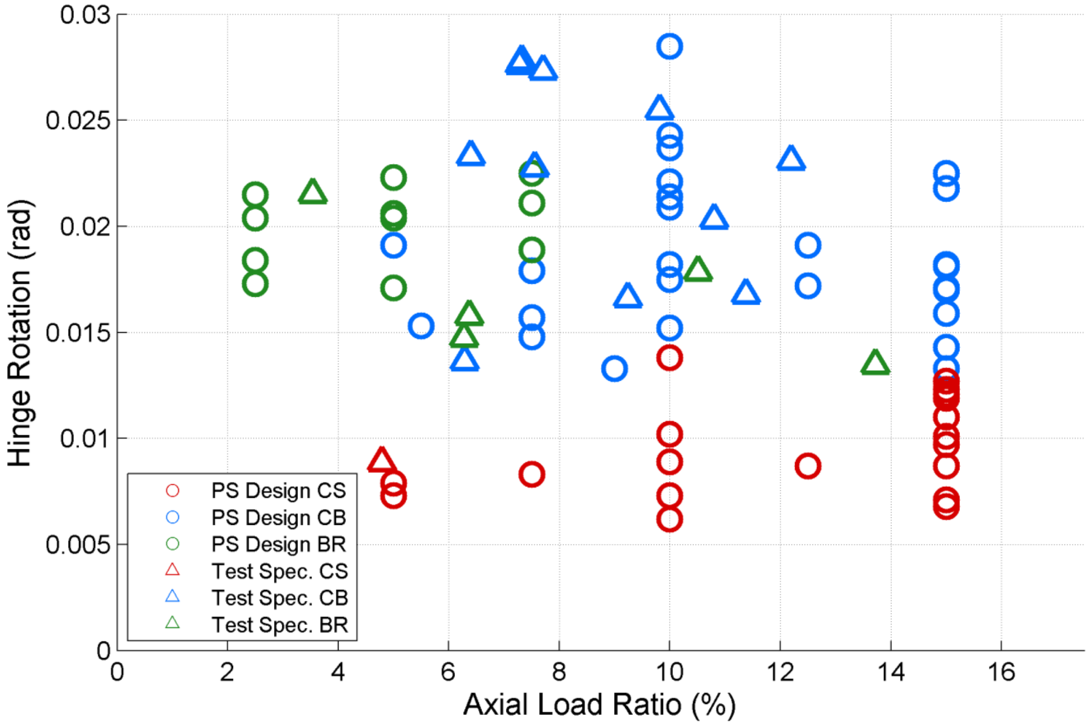

Figure 5.5 – Relationship Between Hinge Rotation and Axial Load Ratio for All Simulated Models

Cross-Sectional Aspect Ratio

Figures 5.6-5.7 show the impact of cross-sectional aspect ratio on story drift and hinge rotation. Table 5.17 shows CSAR distribution statistics for all simulated results.

- CSAR correlation: $R^2 = 0.31$ for drift and $R^2 = 0.36$ for hinge rotation.
- There is a clear trend between these two parameters, with the cross-sectionally slender (CSAR > 12) walls exhibiting less deformation capacity than those with a thicker cross-section.
- The relationship between CSAR and deformation capacity appears to hold true by failure mode, with low-CSAR failures exhibiting more deformation capacity than high-CSAR walls exhibiting the same failure mode.
- There are few experimental test specimens with a CSAR greater than 14.

Table 5.17 – Distribution Statistics for CSAR of Simulated Models

Study Parameter	**Basic Statistics**			**Quartiles**				
	Mean	Median	StDev	Min	Q1	Q2	Q3	Max
CSAR	12.9	12.0	4.4	6.0	10.0	12.0	16.0	21.1

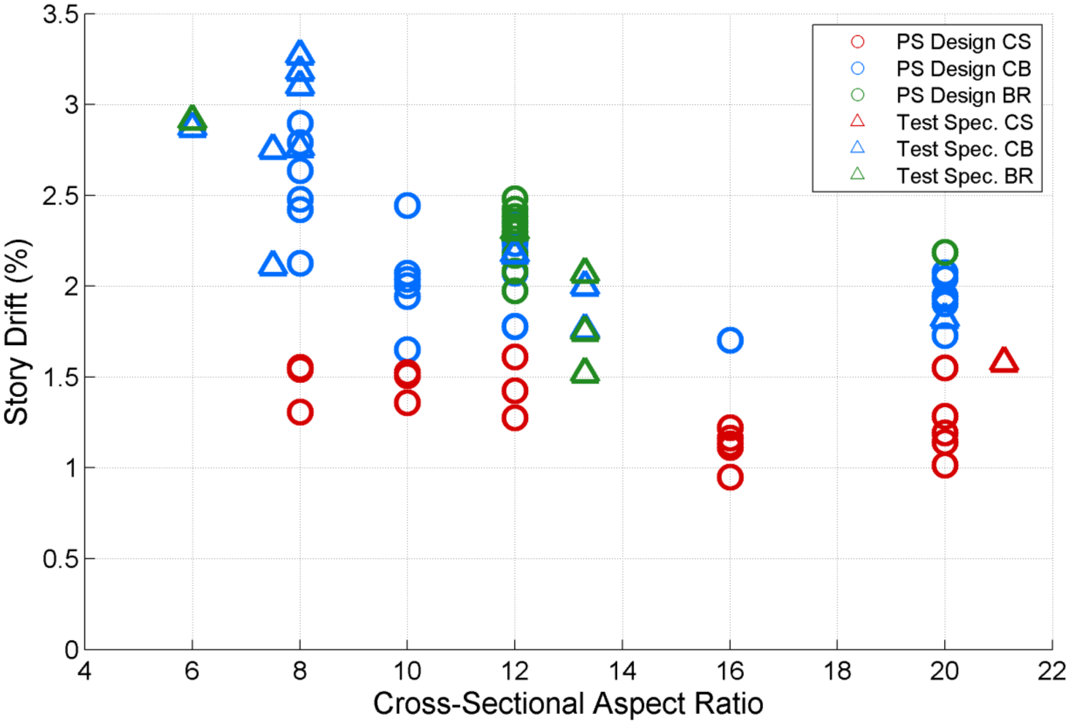

Figure 5.6 – Relationship Between Story Drift and CSAR for All Simulated Models

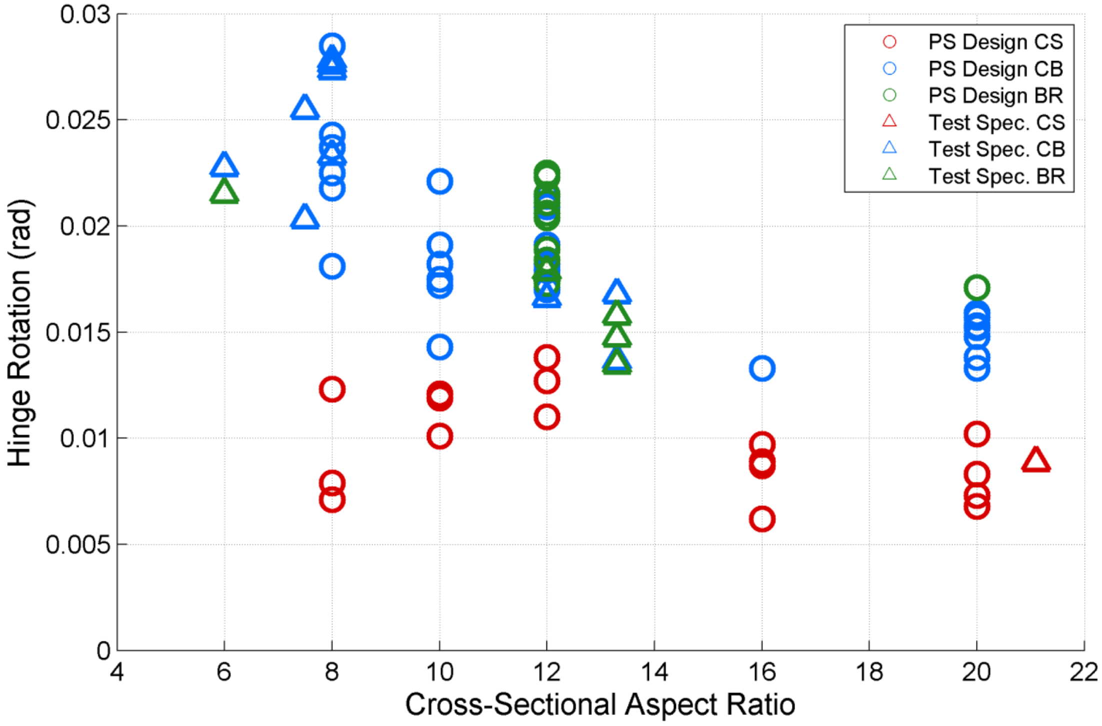

Figure 5.7 – Relationship Between Hinge Rotation and CSAR for All Simulated Models

Normalized Peak Shear Stress

The peak shear stress sustained by each wall specimen was also studied. The influence of peak shear stress on the story drift and hinge rotation capacity of the simulated models is shown in Figures 5.8-5.9.

- Peak shear stress correlation: $R^2 = 0.09$ for drift and $R^2 = 0.11$ for hinge rotation.
- The correlation coefficients are small, but most of this arises from the models with a CSAR of 8, as indicated in Figure 5.8. The correlation coefficients when excluding those CSAR = 8 models are much larger: $R^2 = 0.40$ for drift and $R^2 = 0.38$ for hinge rotation. The relationship between CSAR and peak shear stress is studied in Section 5.2.4.
- The CS failure mode occurs only for walls with a shear stress demand greater than $5\sqrt{f'c}$ psi ($0.42\sqrt{f'c}$ MPa).
- Fewer experimental test specimens have shear stresses demands greater than $5\sqrt{f'c}$ psi ($0.42\sqrt{f'c}$ MPa); thus, there are fewer opportunities to observed CS failures in the laboratory.

Table 5.18 – Distribution Statistics for Peak Shear Stress of Simulated Models

Study Parameter	**Basic Statistics**			**Quartiles**				
	Mean	Median	StDev	Min	Q1	Q2	Q3	Max
Peak Shear Stress, $V_{max}/A_{cv}f'_c{}^{0.5}$ (psi)	4.92	4.75	1.98	1.74	3.04	4.75	6.11	9.89

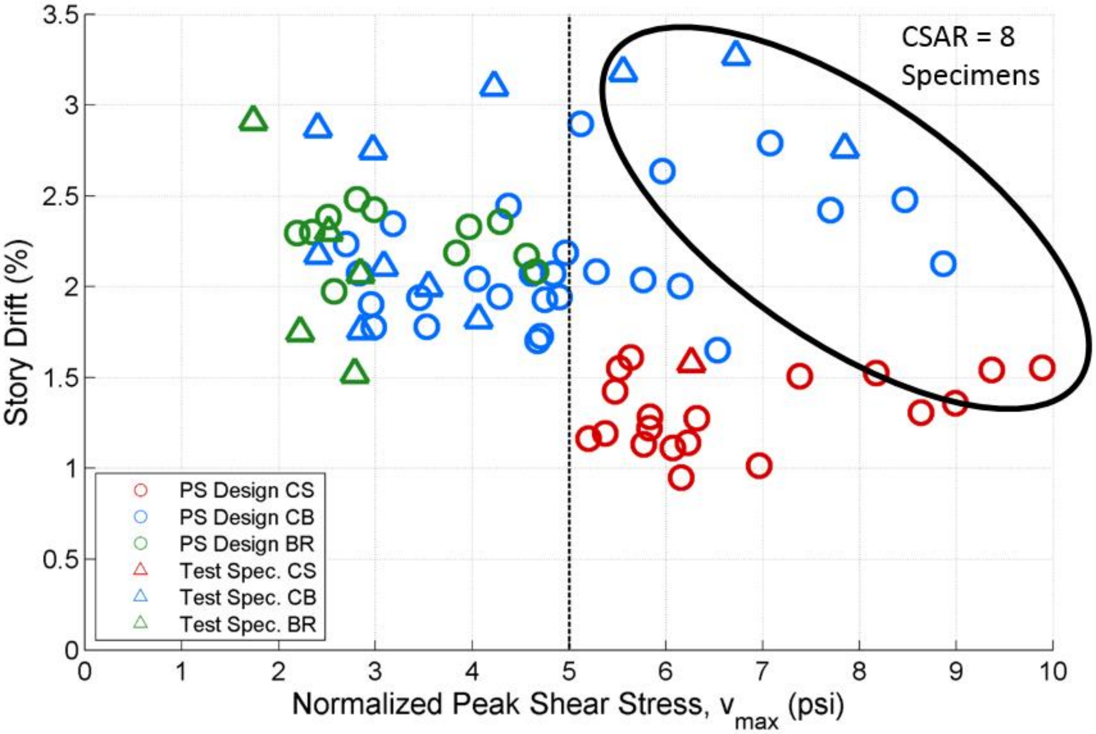

Figure 5.8 – Relationship Between Story Drift and Peak Shear Stress (v_{max}) for All Simulated Models

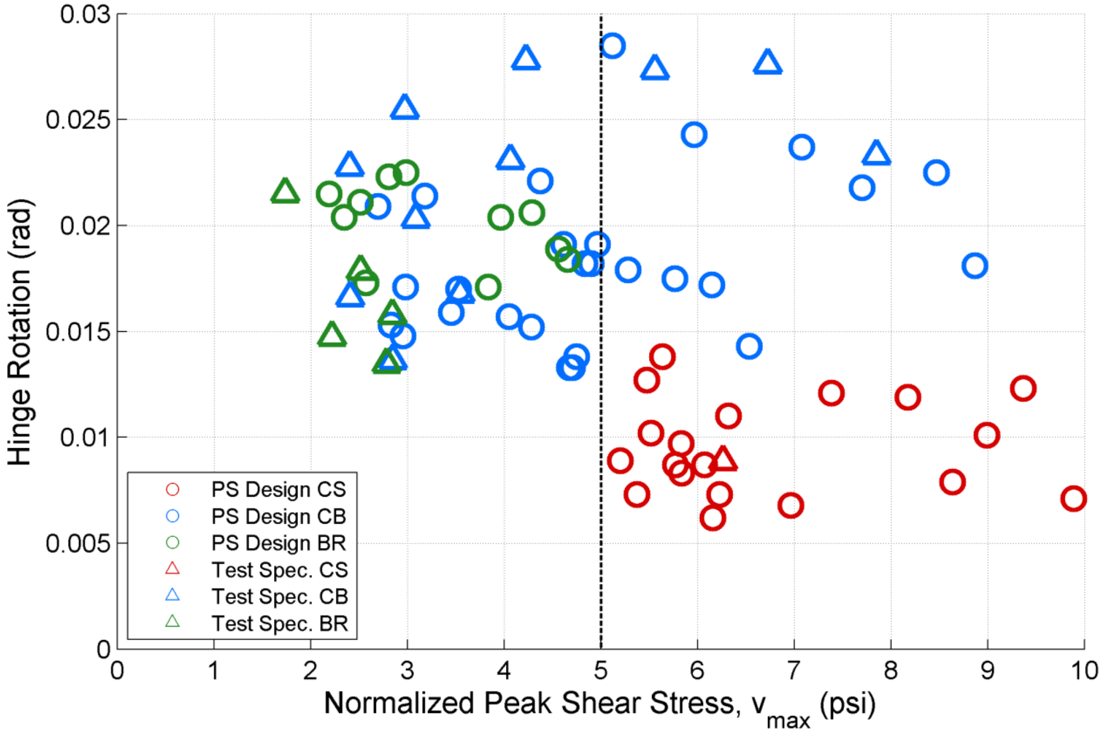

Figure 5.9 – Relationship Between Hinge Rotation and Peak Shear Stress (v_{max}) for All Simulated Models

5.2.4 Influence of Cross-Sectional Aspect Ratio on Failure Mode

Deformation Capacity

The data presented above show that cross-sectional aspect ratio (CSAR) and shear stress demand influence failure mode and deformation capacity. To further investigate the impact of these parameters on response, plots of drift and rotation capacity versus shear stress demand were created with data subdivided on the basis of CSAR (Figures 5.10-5.11). By grouping the data, a significant relationship is revealed between shear demand and deformation capacity; this is detailed in Table 5.19.

Table 5.19 – Correlation of Peak Shear Stress to Deformation Capacity (Grouped by CSAR)

Output Parameter	CSAR	#	R^2
Story Drift (%)	8	13	0.66
	12	22	0.41
	16	6	0.77
	20	14	0.61
Hinge Rotation (rad)	8	13	0.70
	12	22	0.41
	16	6	0.71
	20	14	0.71

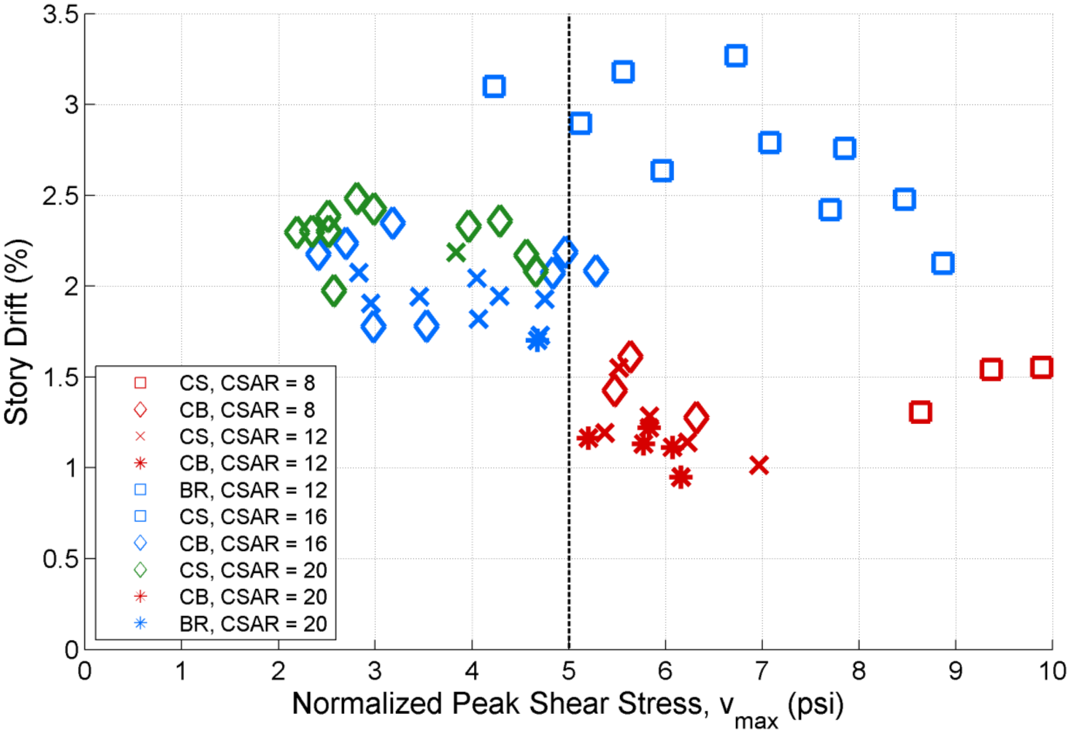

Figure 5.10 – Relationship Between Story Drift and Peak Shear Stress (Grouped by CSAR)

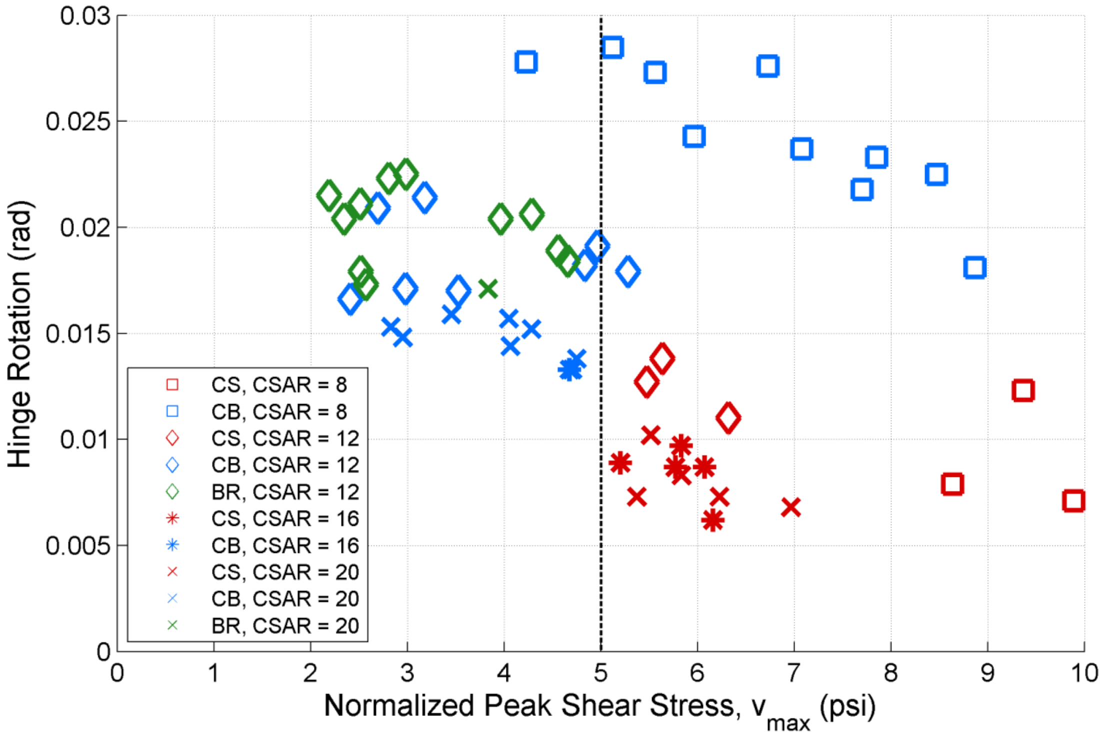

Figure 5.11 – Relationship Between Hinge Rotation and vs. Peak Shear Stress (Grouped by CSAR)

<u>Failure Mode</u>

CSAR also affects failure mode. This is clearly shown in Figure 5.12, which shows CSAR versus peak shear stress with failure mode identified. The data in Figure 5.12 show that walls with smaller CSARs can sustain a larger shear stress demands without incurring a CS failure. In contrast, walls with higher CSAR values sustain CS failures at lower shear stress demands. As a CS failure results in a lower deformation capacity, the data in Figure 5.12 show that walls with higher CSAR values exhibit require lower shear stress demands to sustain the same deformation capacity as walls with lower CSAR values.

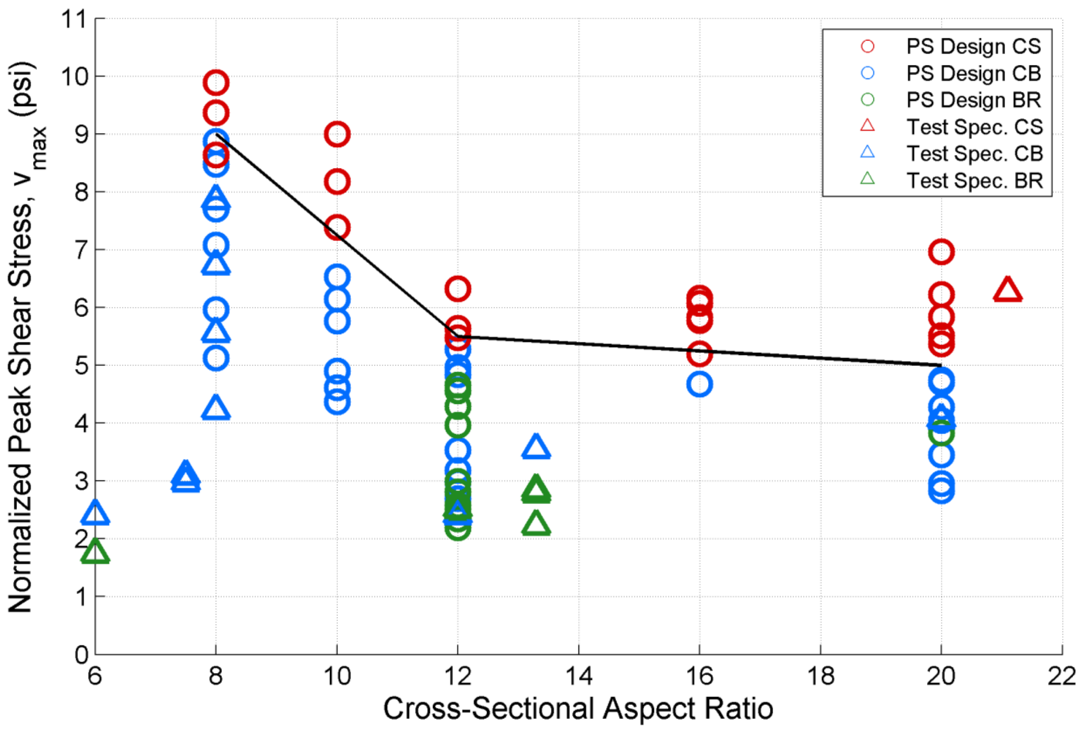

Figure 5.12 – Relationship Between Peak Shear Stress (v_{max}) vs. CSAR for All Simulated Models

These data help to improve understanding of compression-shear failure and why this failure is not commonly observed in the laboratory. Note that the majority of experimental planar wall specimens have a peak shear stress less than $5\sqrt{f'c}$ psi ($0.42\sqrt{f'c}$ MPa), and CS failures do not occur below this limit. Outlier examples are the tests by Tran (2012), which sustain a peak shear stress greater than $5\sqrt{f'c}$ psi ($0.42\sqrt{f'c}$ MPa) (between $5.5\sqrt{f'c}$ and $7.8\sqrt{f'c}$ psi ($0.46\sqrt{f'c}$-$0.65\sqrt{f'c}$ MPa)), but have a CSAR of 8 and therefore do not exhibit compression-shear failure. In contrast, Specimen S6 had a high CSAR and a high peak shear stress. As described in Chapter 4, this specimen sustained a lower drift capacity than a comparable wall tested by Tran. These specimens are noted in Figure 5.13.

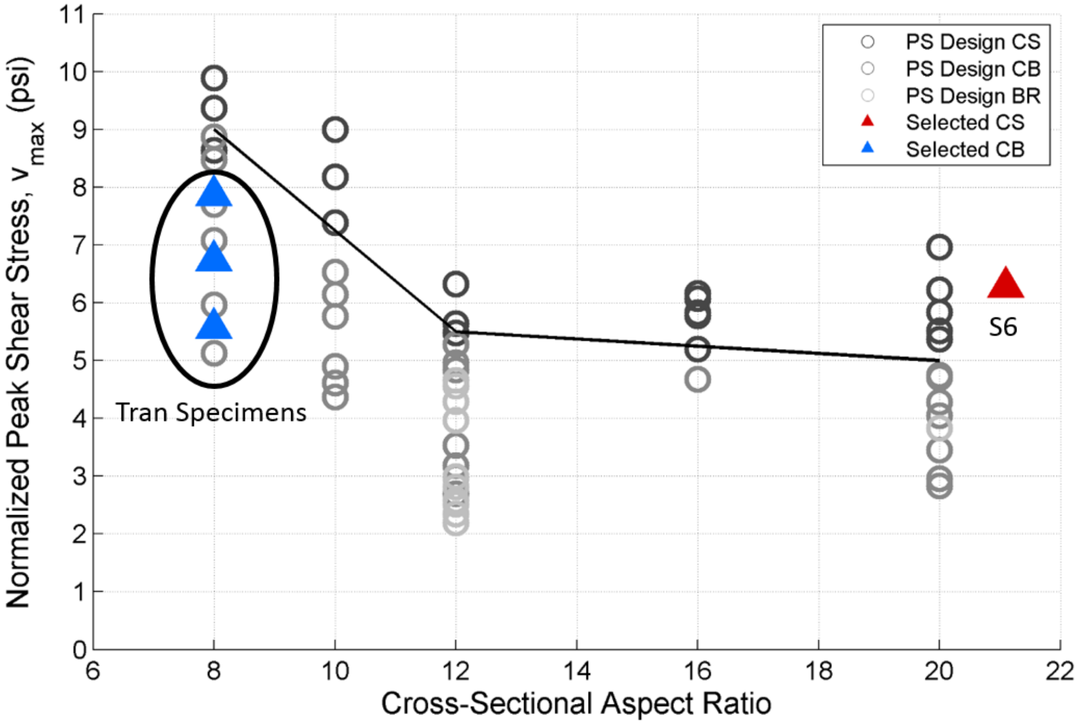

Figure 5.13 – Relationship Between Peak Shear Stress (v_{max}) vs. CSAR w/ Selected Walls Highlighted

5.2.5 Use of Stress Contour Plots to Identify Differences in CB and CS Failure Modes

The different failure modes are captured well by minimum principal stress and strain contour plots. Three different wall simulations are presented below to show the impact of cross-sectional aspect ratio on the two compression-based failure modes: crushing (CB) and compression-shear (CS). The relevant parameters are listed in Table 5.20. Results are presented in Table 5.21.

The walls were selected such that they would span cross-sectional aspect ratios while keeping the peak normalized shear stress approximately constant. Figure 5.14 shows the selected wall subset on a plot of peak shear stress vs. cross-sectional aspect ratio.

Table 5.20 – Summary of Wall Parameters for Selected Simulation Models

Specimen	**Shear Span**	**ALR**	**f_y**	**$\rho_{vert,BE}$**	**ρ_h**
	--	%	ksi	%	%
RW1-C12-18	1.75	7.5	90	2.93	0.33
RW-C8-8	2.0	10.0	130	3.53	0.63
PW4-C20-1	1.50	5.0	67	3.44	0.27

Table 5.21 – Summary of Simulation Results for Selected Simulation Models

Specimen	ALR	$V_{max}/A_{cv}f'_c{}^{0.5}$	V_b/V_n	Story Drift	Hinge Rotation	Failure Mode
	--	%		%	Rad	--
RW1-C12-18	7.5	5.28	0.93	2.08	0.0179	CB
RW-C8-8	10.0	5.97	0.90	2.64	0.0119	CB
PW4-C20-1	5.0	5.37	0.88	1.19	0.0073	CS

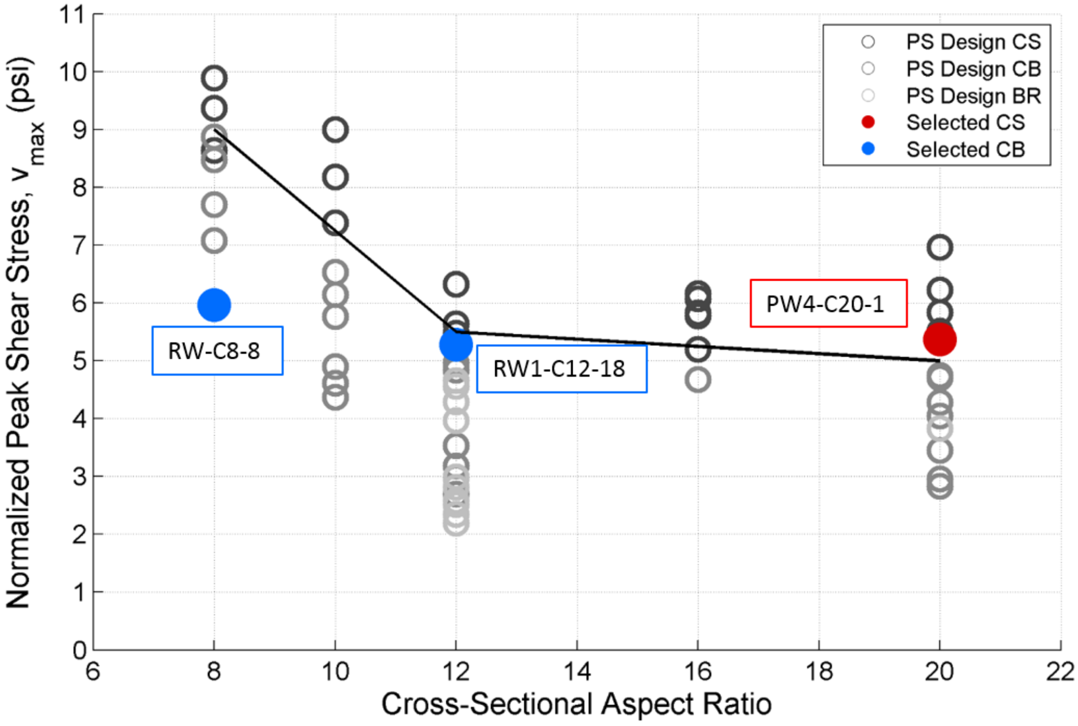

Figure 5.14 – Relationship Between Peak Shear Stress (v_{max}) vs. CSAR vs. w/ Selected Models

Model RW-C8-8 sustained a peak shear stress demand of $5.97\sqrt{f'c}$ psi ($0.50\sqrt{f'c}$ MPa) and exhibited a CB failure. Figure 5.15 and Figure 5.18 show the development of stress contours for this model, at the three selected points of interest.

Model RW1-C12-18 sustained a peak shear stress demand of $5.28\sqrt{f'c}$ psi ($0.44\sqrt{f'c}$ MPa) and exhibited a CB failure. This is the highest shear demand sustained by a wall with this CSAR without a CS failure. Figure 5.16 and Figure 5.19 show the development of stress distributions at the three points for interest for Model RW-C8-8.

Model PW4-C20-1 was subjected to a peak shear stress demand of $5.37\sqrt{f'c}$ psi ($0.45\sqrt{f'c}$ MPa) and exhibited a CS failure. Figure 5.17 and Figure 5.20 show the development of the stress distributions for Simulation Model RW-C8-8.

Note that in the figures below, CB and CS failures show the following characteristics:

- For a CS failure, concrete compressive strength loss occurs first as a result of diagonal shear stress. Strength loss is observed across the entire boundary element, including at the web/boundary element interface. For a CB failure, concrete compressive strength loss occurs fist in the core of the boundary element concrete at the extreme fiber.

- For a CS failure, large minimum principal strains occur across the length of the boundary element, showing a flat contour profile. For a CB failure, the minimum principal strain plots show that the highest strains occur at the outermost fiber of the section and gradually decrease toward the web/boundary element interface.

These behaviors result in CS failures exhibiting a loss of strength across the full boundary element, leaving no strength capacity. CB failures first see strength loss at the outermost fiber and have reserve capacity available in the boundary element. These three different damage progressions present the stark difference in failure between compression-shear and compression-buckling failures, and all three occur at similar levels of applied shear. The geometry of the wall cross-section causes a significant loss of deformation capacity in PW4-C20-1.

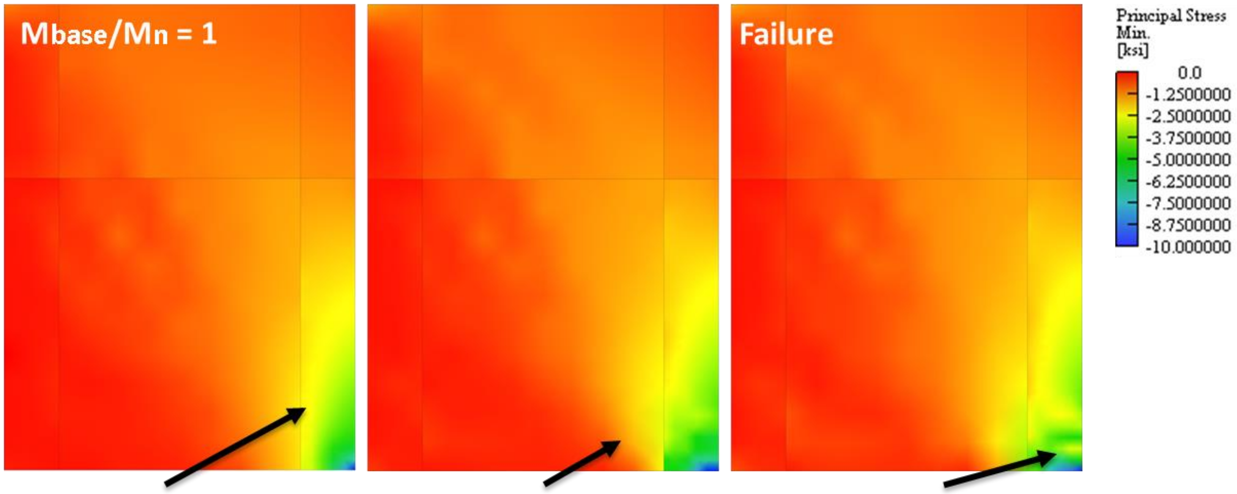

Stress contours are vertically-oriented and not driven by a diagonal shear strut.

Some diagonal shear does form, but does not cause a decline in strength at the web/BE interface.

Specimen sees crushing in located at boundary element core.

Figure 5.15 – Specimen RW-C8-8 Min. Principal Stress Contour Plots ($v_{max} = 5.97\sqrt{f'c}$ *psi* ($0.50\sqrt{f'c}$ *MPa) and CSAR = 8.0)*

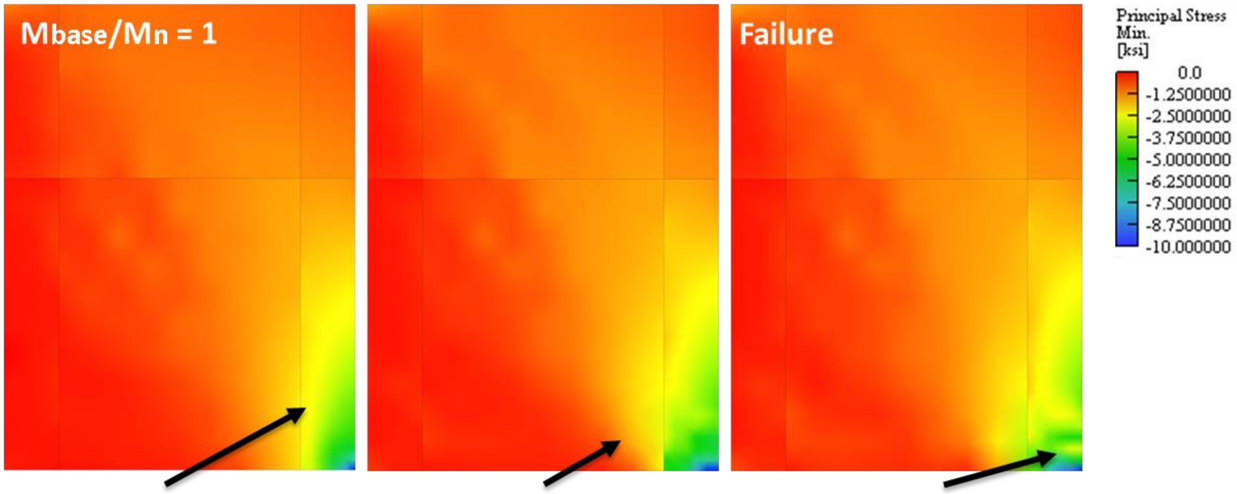

Stress contours are vertically-oriented and not driven by a diagonal shear strut.

Some diagonal shear does form, but does not cause a decline in strength at the web/BE interface.

Specimen sees crushing in located at boundary element core.

Figure 5.16 – Specimen RW1-C12-18 Min. Principal Stress Contour Plots ($v_{max} = 5.28\sqrt{f'c}$ psi ($0.48\sqrt{f'c}$ MPa) and CSAR = 8.0)

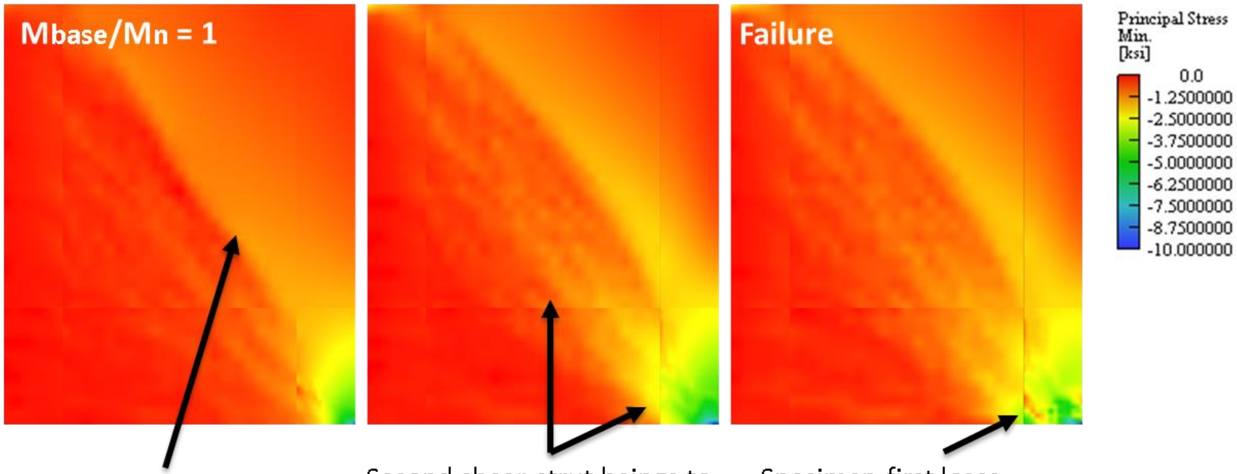

One major diagonal shear strut

Second shear strut beings to form, sending stress into interface of boundary element and web.

Specimen first loses significant strength near the web

Figure 5.17 – Specimen PW4-C20-1 Min. Principal Stress Contour Plots ($v_{max} = 5.37\sqrt{f'c}$ psi ($0.45\sqrt{f'c}$ MPa) and CSAR = 20.0)

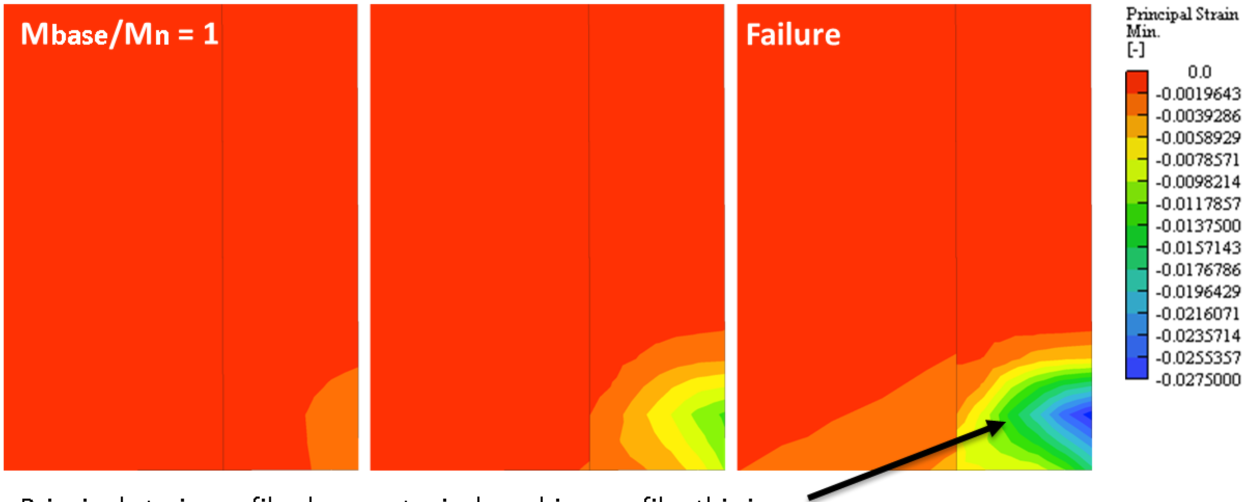

Principal strain profile shows a typical crushing profile; this is characterized by smooth, more concentric contours increasing gradually outward.

Figure 5.18 – Specimen RW-C8-8 Min. Principal Strain Contour Plots ($v_{max} = 5.97\sqrt{f'c}$ psi ($0.50\sqrt{f'c}$ MPa) and CSAR = 8.0, Showing Bottom-Right of Wall at 33% of h_w and 36% of l_w)

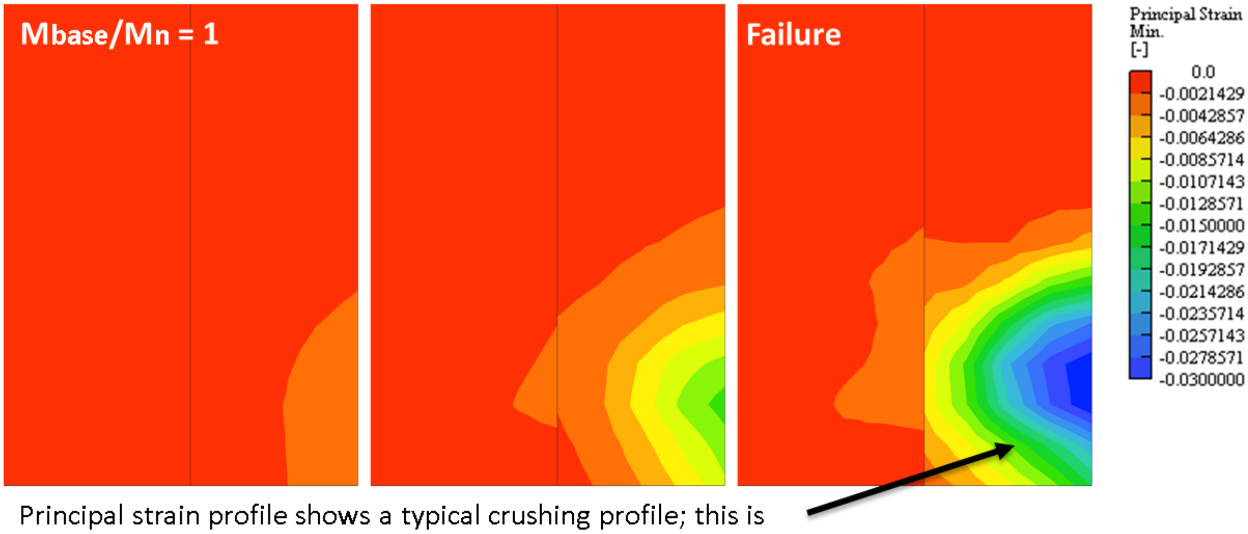

Principal strain profile shows a typical crushing profile; this is characterized by smooth, more concentric contours increasing gradually outward.

Figure 5.19 – Specimen RW1-C12-18 Min. Principal Strain Contour Plots ($v_{max} = 5.28\sqrt{f'c}$ psi ($0.44\sqrt{f'c}$ MPa) and CSAR = 12.0, Showing Bottom-Right of Wall at 40% of h_w and 41% of l_w)

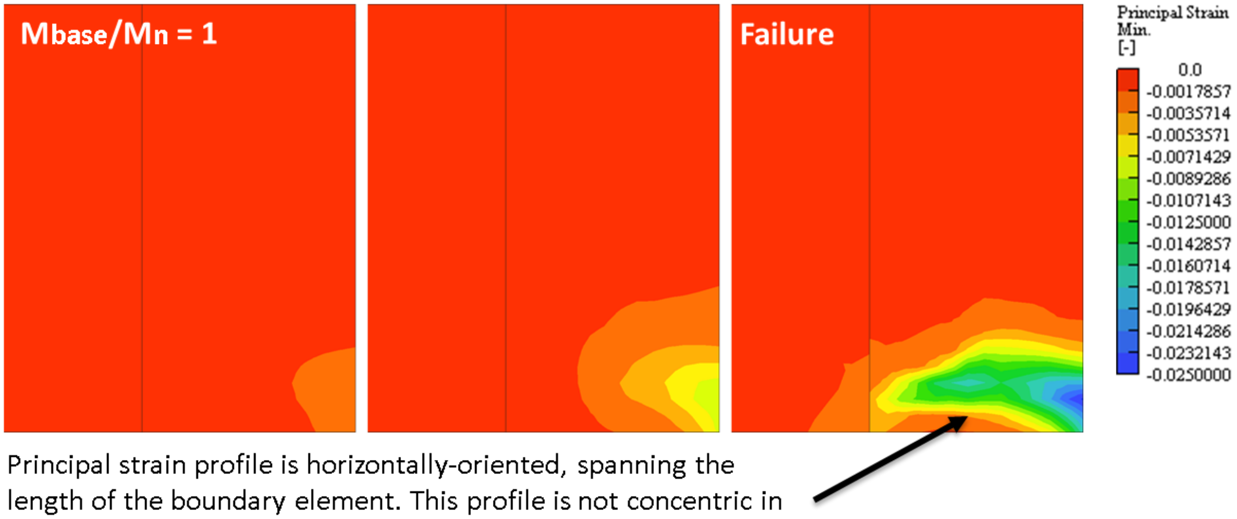

Principal strain profile is horizontally-oriented, spanning the length of the boundary element. This profile is not concentric in nature, which is typically observed in crushing-buckling failures.

Figure 5.20 – Specimen PW4-C20-1 Min. Principal Strain Contour Plots ($v_{max} = 5.37\sqrt{f'c}$ psi ($0.45\sqrt{f'c}$ MPa) and CSAR = 20.0, Showing Bottom-Right of Wall at 28% of h_w and 27% of l_w)

5.3 DISCUSSION OF DEFORMATION CAPACITY FOR FAILURE MODES

Failure modes are clearly defined by both Section 5.2.5 and 4.3, and the ability to predict CS failure is clear from Figure 5.12. With failure mode identified, it is now necessary to determine the influence of failure mode on deformation capacity. As noted in Chapter 2, Birely et al. (2011) did not find that there was a relationship between failure mode and deformation capacity; however, that analysis did not consider specimens which undergo CS failure.

It is determined in this chapter that BR and CB failures do exhibit similar deformation capacities. CS failures, however, exhibit less deformation capacity, and this finding is summarized in the fragility curves of Section 5.3.1. These data support the idea presented by Birely that failure mode is not relevant to the design process except in that CS failures have significantly lower deformation capacity than the BR and CB failures.

The influence of key parameters on the deformation capacity of CB failures is discussed in Section 5.3.2.

5.3.1 Fragility Curves per Failure Mode

The discussion of failure mode is supplemented by providing fragility curves that clearly show how the CS, CB, and BR failures relate in deformation capacity.

The fragility functions in Figure 5.21 and Figure 5.22 define the likelihood of a wall exhibiting failure, characterized by significant loss in lateral load carrying capacity, given maximum story drift demand (Δ_j) or maximum hinge rotation demand (θ_j). The figures include empirical fragility functions (thin lines) for which

$$P\left(x \middle| \Delta_{story} = \Delta_j\right)_{observed} = \frac{\text{number of failures when } \Delta_{story} = \Delta_j}{\text{number of total specimens}} \qquad \textit{(Eq. 5.2)}$$

$$P(x|\theta_{hinge} = \theta_j)_{observed} = \frac{\text{number of failures when } \theta_{hinge} = \theta_j}{\text{number of total specimens}}$$

(Eq. 5.3)

Where Δ_{story} is the story drift and θ_{hinge} is the hinge rotation, calculated as defined in Section 5.2.1.

The figures include also functional fragilities for which P is defined by the lognormal cumulative probability:

$$P = F(x|\mu, \sigma) = \frac{1}{\sigma\sqrt{2\pi}} \int_0^x \frac{e^{-\frac{(\ln(t)-\mu)^2}{2\sigma^2}}}{t} dt$$

(Eq. 5.4)

Where the sample mean equals $e^{\mu+\frac{\sigma^2}{2}}$ and sample median equals e^{μ}.

The fragility curves in Figure 5.21 and Figure 5.22 and the data in Tables 5.22-5.23 shows that:

- Walls exhibiting CS failure have much lower deformation capacity than do walls exhibiting CB or BR failure, such that for a given drift or rotation demand the probability of failure for a wall exhibiting a CS failure is much larger than that of a wall exhibiting a CB or BR failure.
- Walls exhibiting either CB or BR failure have similar deformation capacities such that for a given drift or rotation demand, the probability of a failure for a wall exhibiting either a CB or BR failure mode is similar.
- The uncertainty in failure prediction (i.e. dispersion in the data) is approximately the same for all failure modes; though, the uncertainty associated with prediction of CB failure is greatest.

Additional fragility curves considering only CS failures are presented in Figures 5.23-5.24; these are grouped by CSAR rather than failure mode. These curves reinforce the idea that CSAR has a secondary impact on wall deformation capacity. High-CSAR walls exhibit less deformation capacity than equivalent low-CSAR walls. CSAR-specific fragility curves for CB failures are presented in Section 5.3.2.

Table 5.22 – Medians and Coefficients of Variation for Failure Modes of Planar Walls

Output Parameter	**Failure Mode**	**#**	**Median**	**COV**
Story Drift (%)	BR	18	2.30	0.17
	CB	38	2.08	0.21
	CS	20	1.30	0.15
Hinge Rotation (rad)	BR	18	0.0204	0.17
	CB	38	0.0181	0.24
	CS	20	0.0089	0.23

Table 5.23 – Medians and Coefficients of Variation for Failure Modes of Planar Walls (Grouped by CSAR)

Output Parameter	**Failure Mode**	**CSAR ≤ 12**			**CSAR > 12**		
		#	**Median**	**COV**	**#**	**Median**	**COV**
Story Drift (%)	BR	12	2.32	0.10	6	2.13	0.27
	CB	27	2.23	0.19	11	1.93	0.13
	CS	9	1.51	0.08	11	1.17	0.16
Hinge Rotation (rad)	BR	12	0.021	0.09	6	0.016	0.29
	CB	27	0.021	0.19	11	0.015	0.13
	CS	9	0.012	0.20	11	0.009	0.15

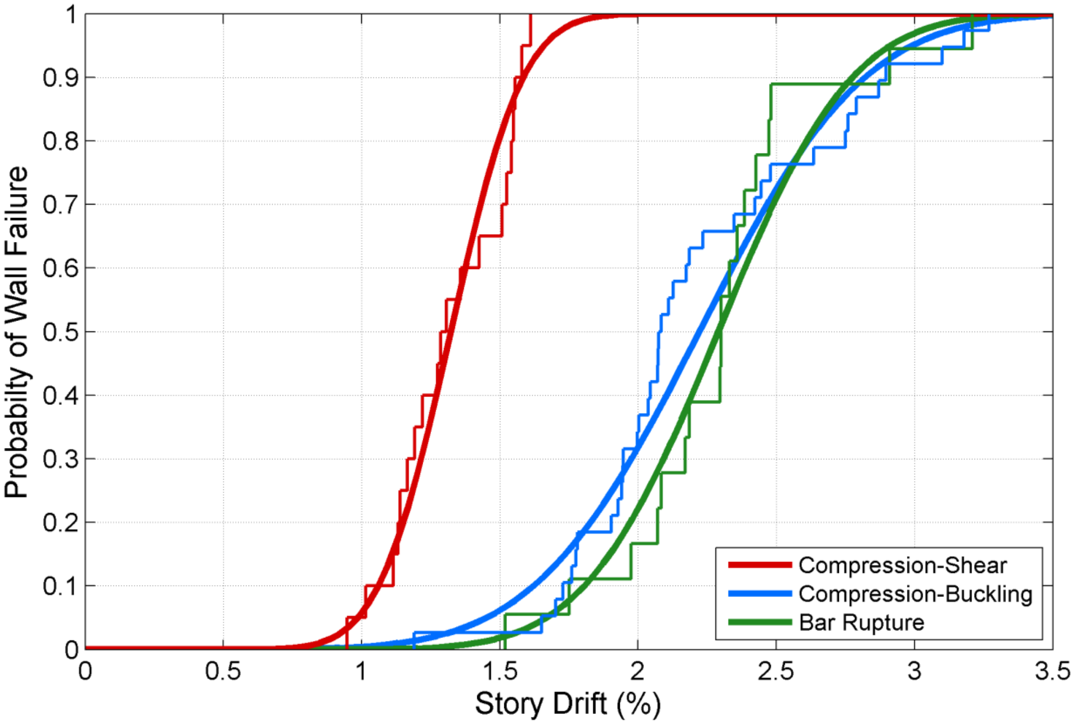

Figure 5.21 – Fragility Curves for Planar Wall Failure Modes, Story Drift (All Simulated Models)

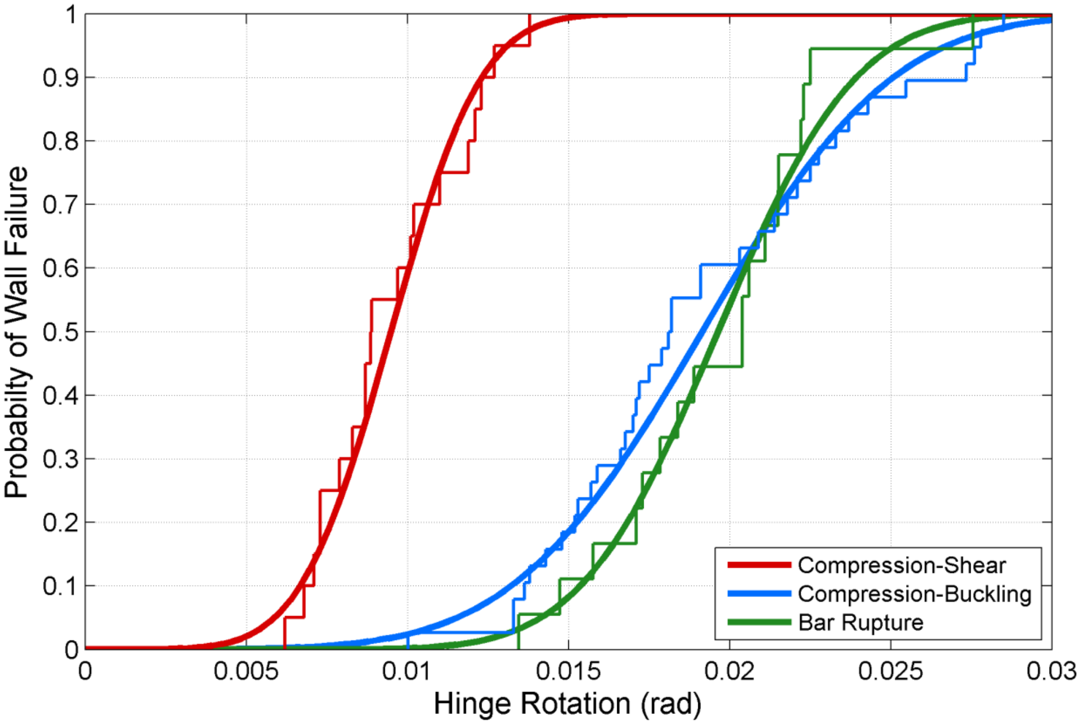

Figure 5.22 – Fragility Curves for Planar Wall Failure Modes, Hinge Rotation (All Simulated Models)

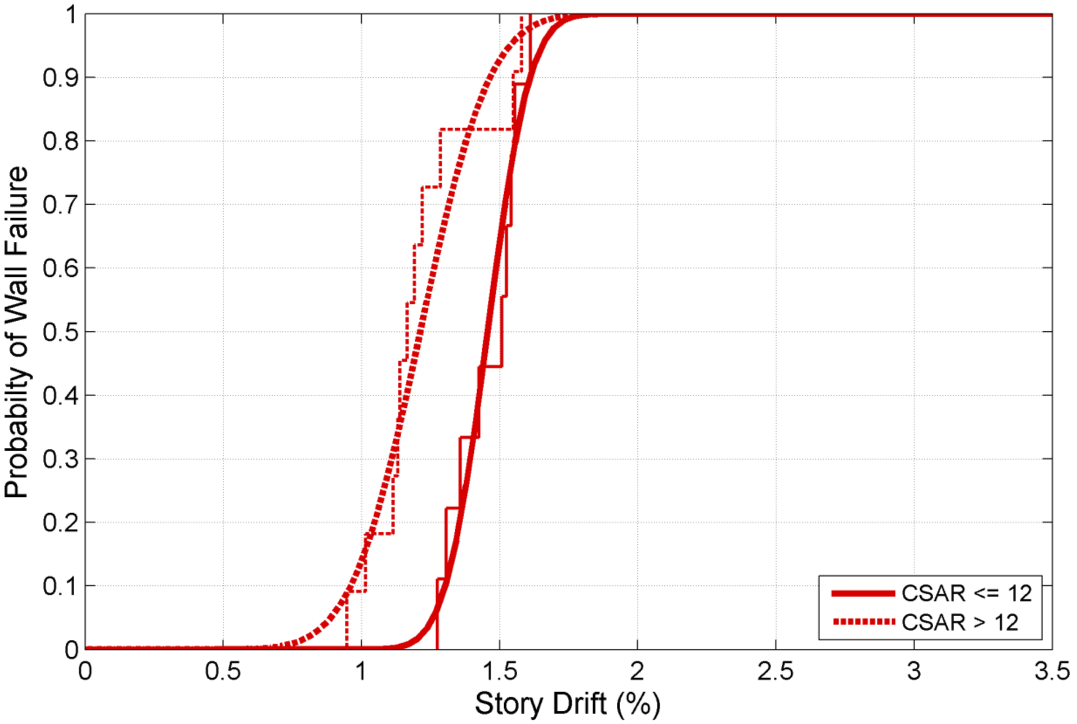

Figure 5.23 – Fragility Curves for CS Planar Wall Failures, Story Drift

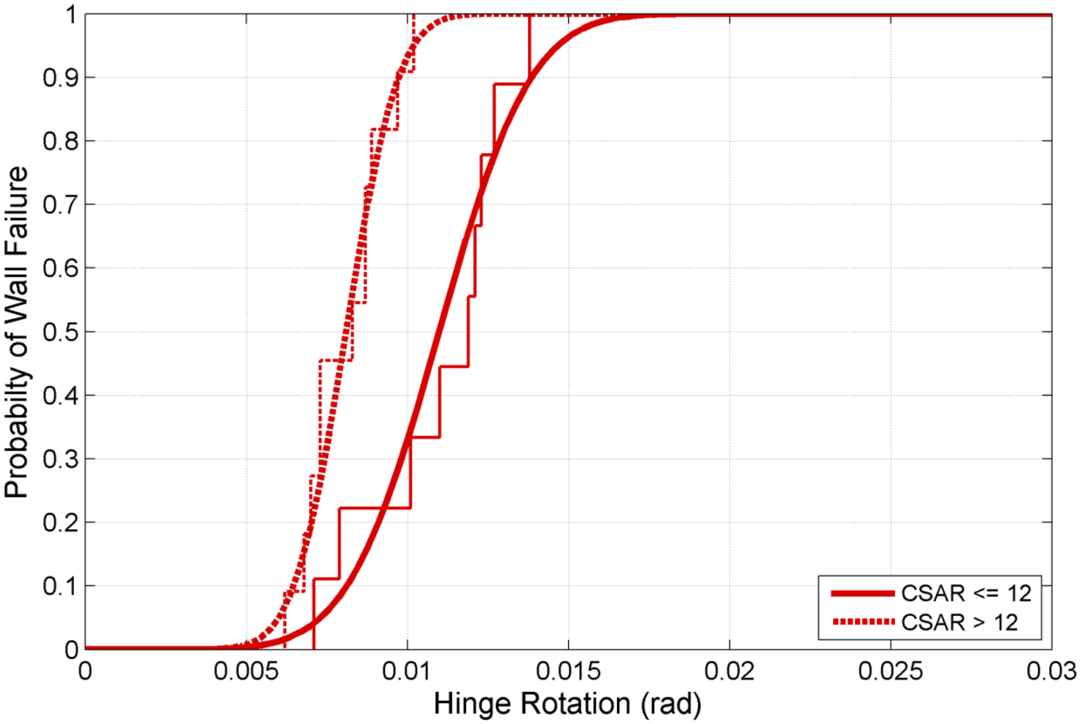

Figure 5.24 – Fragility Curves for CS Planar Wall Failures, Hinge Rotation

5.3.2 Deformation Capacity of Compression-Buckling Failures

The data in Figures 5.21-5.22 show greater dispersion and less accuracy in predicting the onset of a CB failure, than BR and CS failure, given rotation demand or drift demand. There is the potential that this dispersion can be reduced by defining the onset of failure on the basis of deformation demand as well as other design and load parameters. This section investigates the impact of other design and load parameters on the deformation capacity of walls exhibiting CB failure. Figures 5.25-5.30 show drift capacity and hinge rotation capacity plotted versus axial load ratio, CSAR, aspect ratio and shear stress demand. Note that the confining reinforcement in the boundary element affects the deformation capacity of CB failures, but this was not varied in the parameter study.

The data in Figures 5.25-5.30 support the following observations regarding deformation capacity of CB walls.

1. Axial load ratio has minimal impact on deformation capacity on hinge rotation and a slight impact on story drift ($R^2 = 0.12$, $R^2 = 0.04$ for rotation).
2. CSAR (Figures 5.27-5.28) has a signficant impact on deformation capacity ($R^2 = 0.43$ for drift, $R^2 = 0.58$ for rotation).Walls with larger CSARs have smaller drift and hinge rotation capacities; while, walls with smaller CSARs have larger drift and hinge rotation capacities. This suggests that as CSAR increases, walls exhibiting CB failure move towards CS failure.
3. Peak shear stress affects deformation capacity for walls with a low CSAR. For walls with CSAR of 8, increased shear stress demand results in reduced deformation capacity. For walls with CSAR of 12 or 20, there is no correlation between shear demand and deformation capacity ($R^2 = 0.02$ for drift, $R^2 = 0.02$ for rotation).

Based on the data in Figures 5.29-5.30, fragility functions were created for walls exhibiting CB failure in which the onset of failure is a function of both drift demand (or hinge rotation demand) and CSAR. The fragility curves are shown in Figure 5.31-5.32 and data is presented in Table 5.24.

Table 5.24 – Medians and Coefficients of Variation for CB Failures

Output Parameter	CSAR	#	Median	COV
Story Drift (%)	8	6	2.56	0.11
	12	7	2.08	0.11
	20	8	1.94	0.07
Hinge Rotation (rad)	8	6	0.0231	0.15
	12	7	0.0182	0.09
	20	8	0.0150	0.07

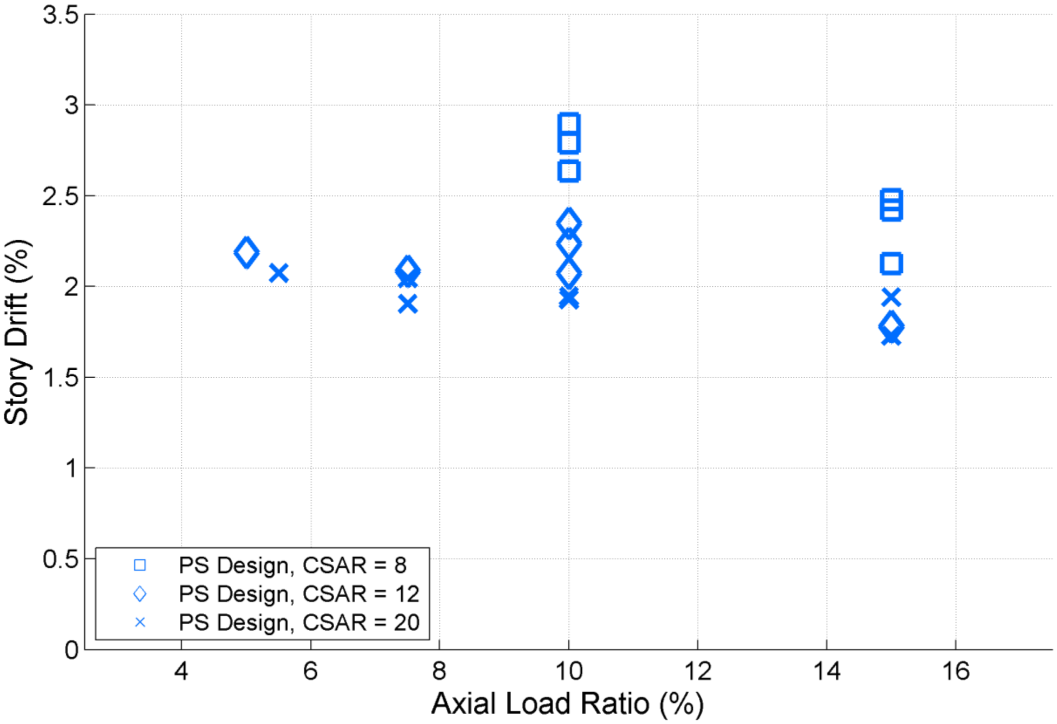

Figure 5.25 – Story Drift vs. Axial Load Ratio for Simulated CB Failures, Grouped by CSAR

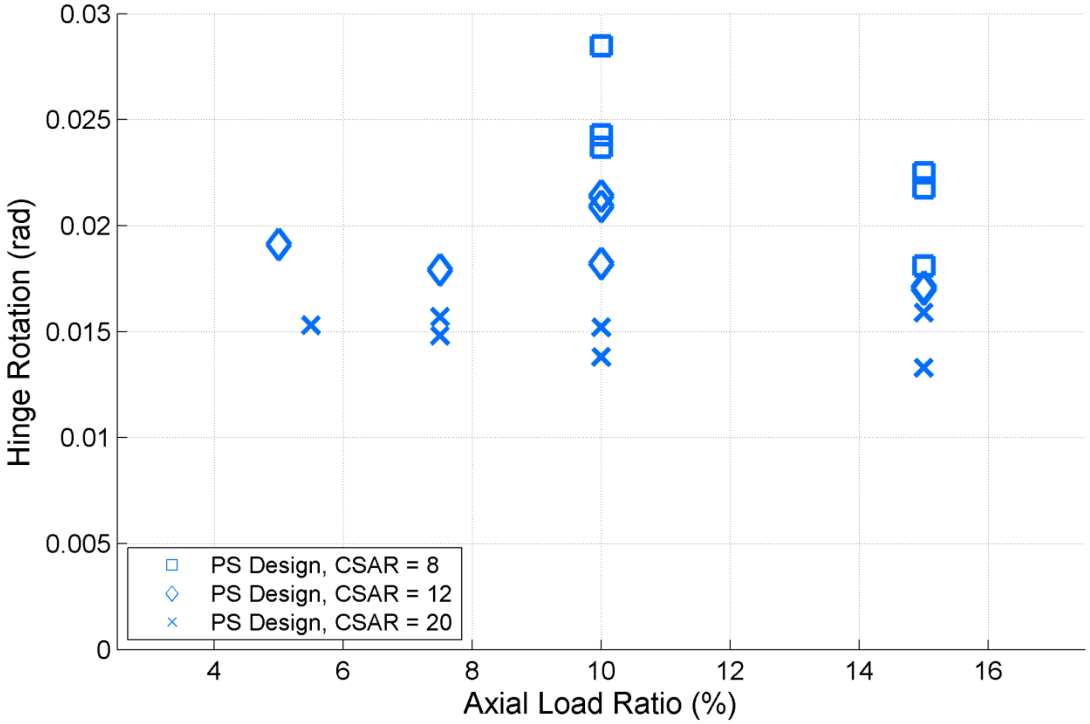

Figure 5.26 – Hinge Rotation vs. Axial Load Ratio for Simulated CB Failures, Grouped by CSAR

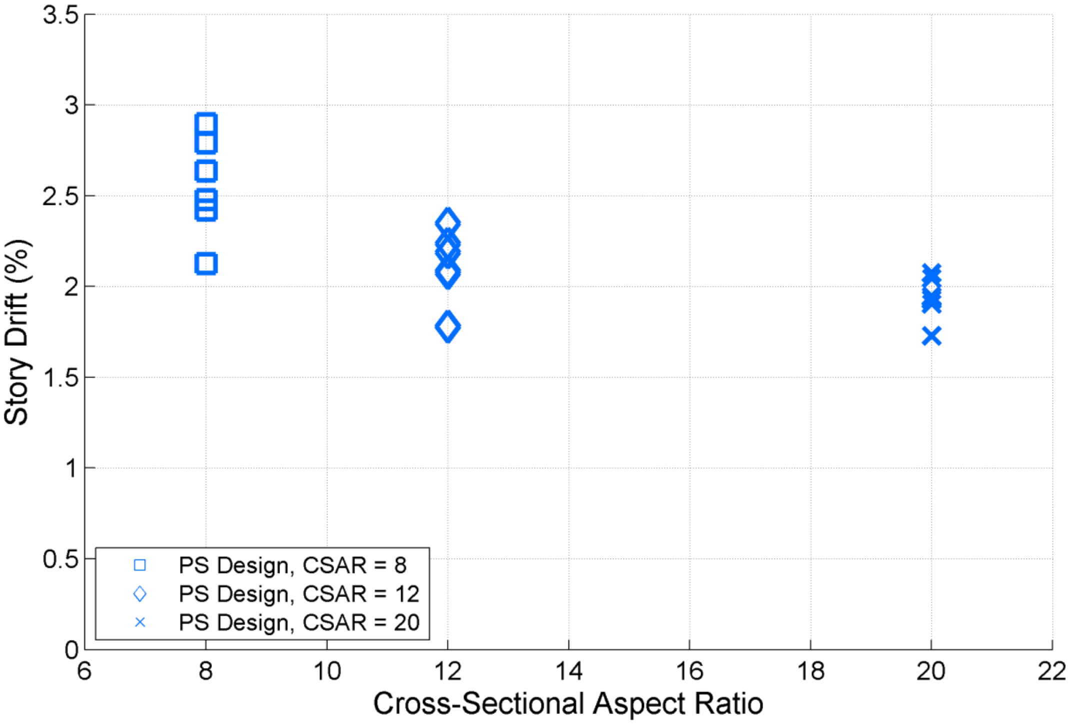

Figure 5.27 – Story Drift vs. CSAR for Simulated CB Failures, Grouped by CSAR

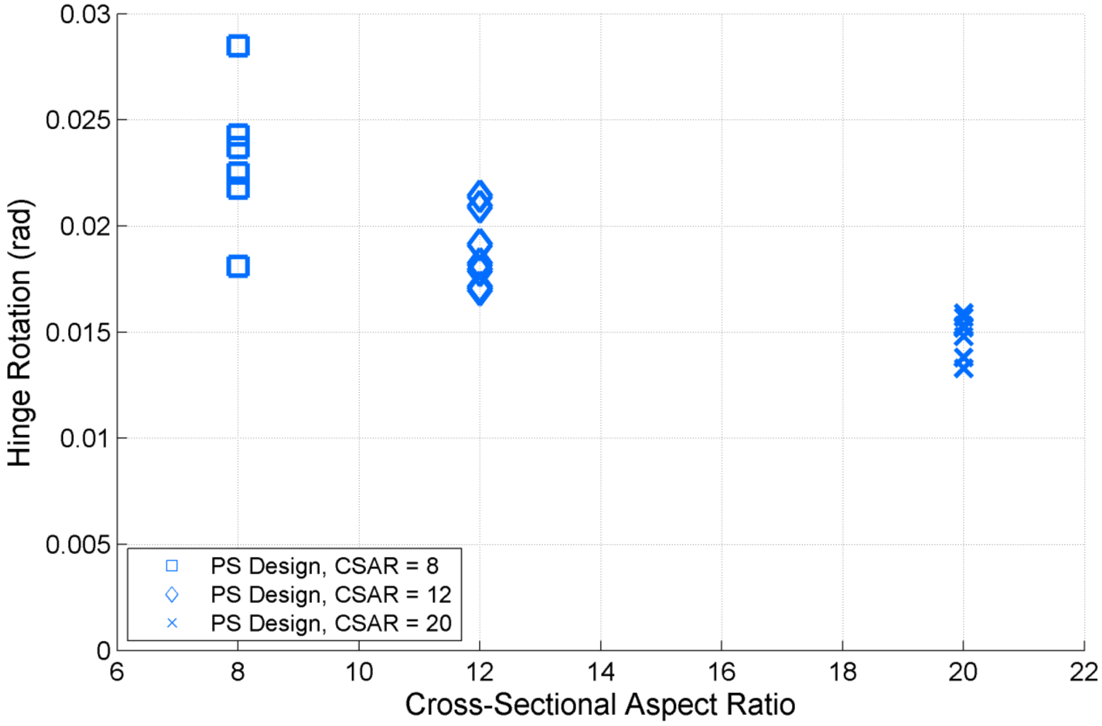

Figure 5.28 – Hinge Rotation vs. CSAR for Simulated CB Failures, Grouped by CSAR

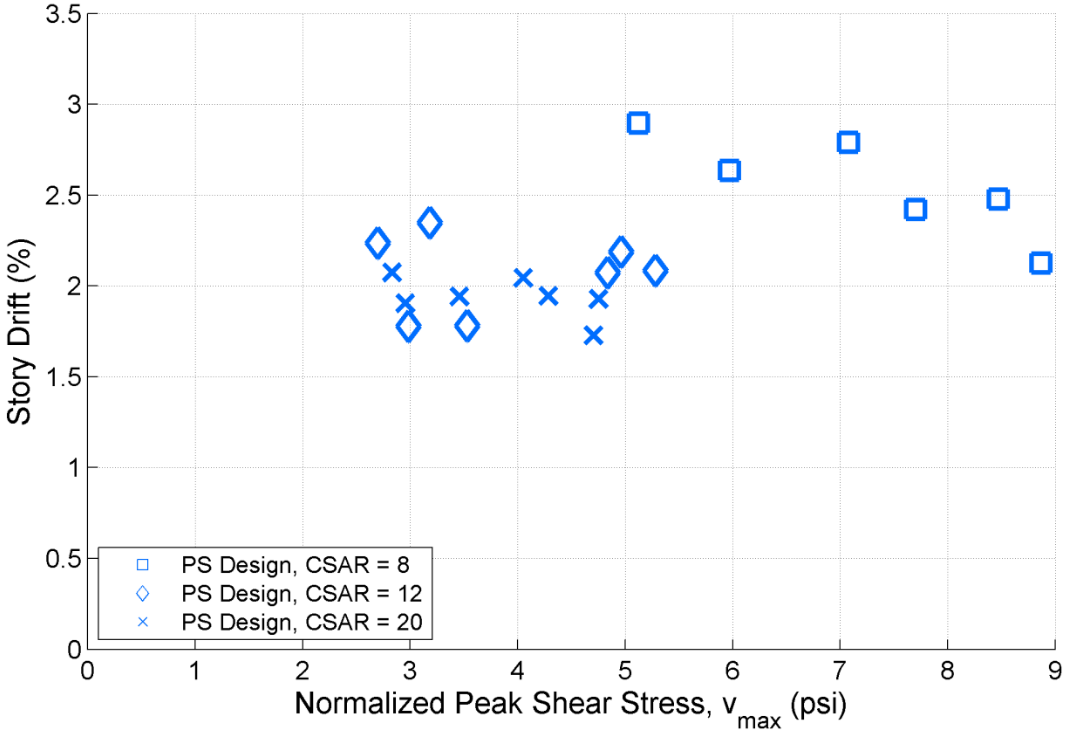

Figure 5.29 – Story Drift vs. Peak Shear Stress for Simulated CB Failures, Grouped by CSAR

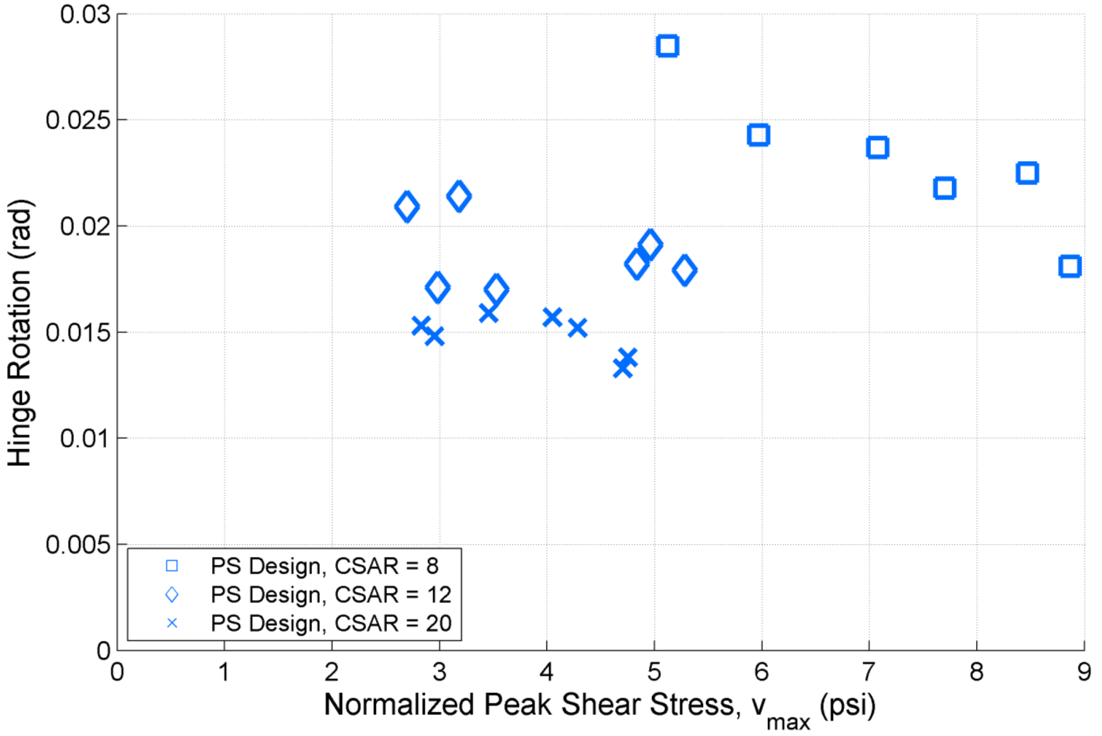

Figure 5.30 – Hinge Rotation vs. Peak Shear Stress for Simulated CB Failures, Grouped by CSAR

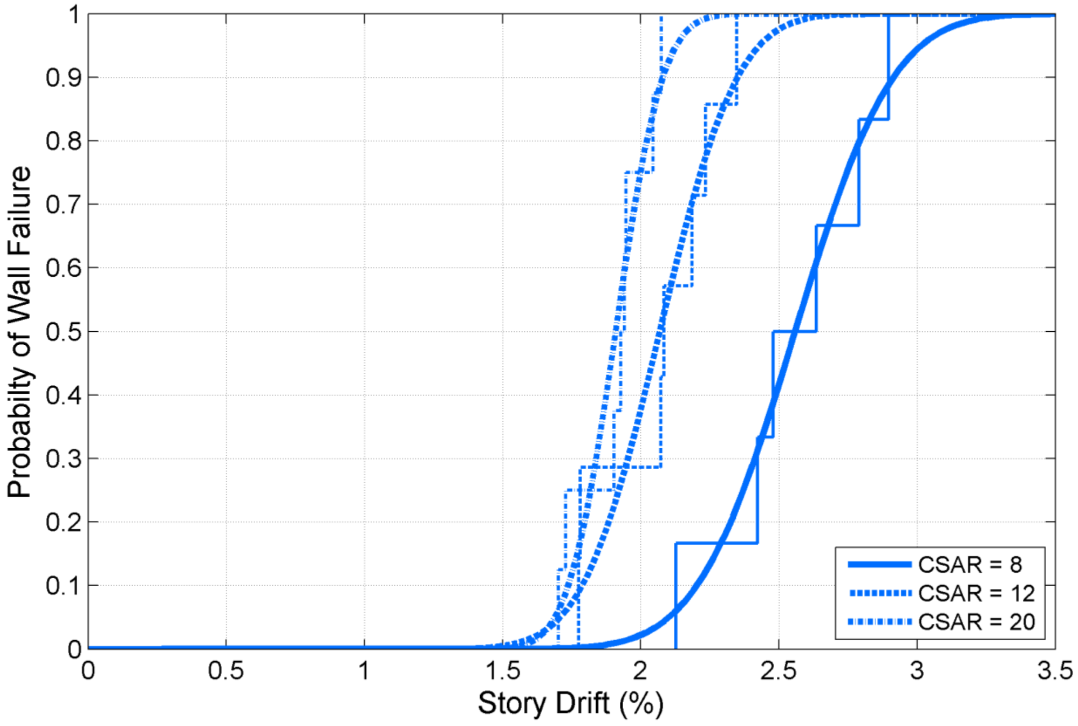

Figure 5.31 – Fragility Curves for CB Failures, Story Drift (Grouped by CSAR)

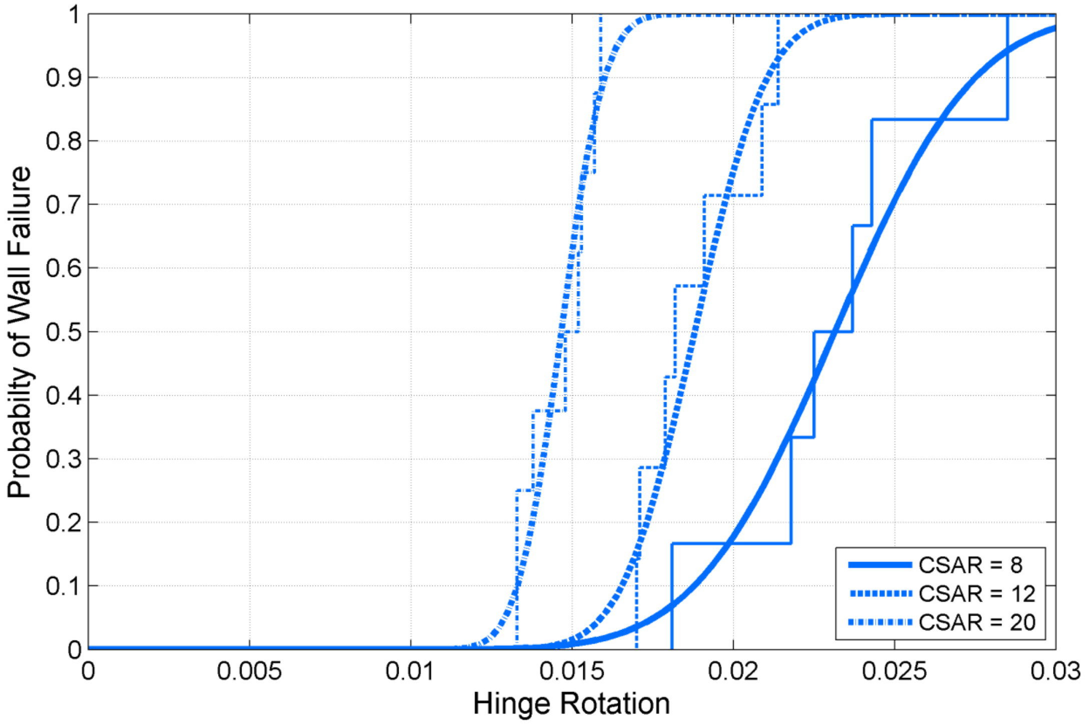

Figure 5.32 – Fragility Curves for CB Failures, Hinge Rotation (Grouped by CSAR)

5.4 CONCLUSIONS

The key result of this chapter is that CS failure can be predicted with by wall CSAR and shear demand. For the three primary variables identified in Chapter 2, the findings are:

<u>CSAR:</u> This parameter is strongly correlated in determination of failure and deformation capacity. Walls of a low-CSAR are able to resist larger shear demands before exhibiting CS failure than equivalent high-CSAR walls.

<u>Shear demand:</u> The shear demand is highly correlated with determination of failure mode between CB/BR and CS. There is not a strong correlation between shear demand and deformation capacity when considered independent of failure mode. This parameter does not appear to be influential in determining whether non-CS walls fail in CB or BR.

<u>ALR:</u> The axial load ratio impacts the determination of failure mode. BR failures more frequently occur at low ALRs (<7.5%) and CB and CS failures occur at higher ALRs. However, this parameter does not have a strong correlation with deformation capacity.

The fragility curves in Section 5.3 show that CB and BR failures exhibit similar deformation capacity. Failure mode is an important consideration in design as CS failure and the inherent loss of deformation capacity should be avoided; however, CB and BR failures are not much different from a practical design perspective.

6 DESIGN TO PREVENT COMPRESSION-SHEAR FAILURE

The research results presented in Chapter 5 show that walls with a cross-sectional aspect ratio (CSAR) greater than 10 are susceptible to compression-shear failure at lower levels of normalized shear stress demand than walls with higher CSARs and that walls exhibiting a compression-shear failure have significantly lower deformation capacity than walls exhibiting compression-buckling or buckling-rupture failure. This research presented in this chapter seeks to (1) provide further understanding of the CS failure mechanism and (2) develop design recommendations to prevent CS failure.

It was determined in Chapter 4 that CS failure originates at the web/boundary element interface, and it may thus be possible to prevent this failure mechanism by improving concrete response through an extension of confining reinforcement. Current ACI requirements for the BE confinement length are based on neutral axis depth, and plane-sections-remain-plane (PSRP) analysis does not yield an accurate estimate of the neutral axis for specimens subjected to high shear demand levels (i.e., the specimens that are at risk for CS failure). The accuracy of PSRP analysis is evaluated to determine if it possible use a PSRP-defined neutral axis in design.

Section 6.1 evaluates the accuracy of PSRP analysis. An additional parameter study is conducted in Section 6.2, analyzing the neutral axis and boundary element data for all simulations. A proposed design process for prevention of CS failure is then detailed in Section 6.3.

6.1 VERTICAL STRAIN DISTRIBUTIONS

ACI 318-14 requires that the confined boundary element extend to half the neutral axis depth. For design purposes, the neutral axis depth is determined based on section analysis and the assumption that plane sections remain plane and perpendicular to the neutral axis. Here, the neutral axis depths computed using a PSRP section analysis and as computed using 3D continuum analysis are compared.

Several ATENA models were selected representing a range of peak shear stress demands and CSARs. For each model, the vertical strain distribution along the length of the wall was recorded at the crushing height (i.e., where the boundary element core crushing localized, typically located 2-4 elements up from the specimen base) and center of the wall thickness at a moment demand equal to the nominal flexural strength, M_n, which is defined as the moment at a concrete compressive strain of -0.003 in/in. The strain distribution was defined by an isometric contour map, the contours of which were calculated by interpolation of strain values provided at nearby quadrature points; approximately 15 points along the length of the wall define the vertical strain distribution. These results are compared with the strain distribution for a “plane-sections-remain-plane (PSRP) and perpendicular to the neutral axis” section analysis at the nominal flexural strength, M_n; again the nominal flexural strength was defined by a maximum concrete compressive stress of -0.003 in/in.

Figure 6.1 shows the two strain distributions for RW1-C12-19, a wall design from the parameter study that is subjected to a peak shear stress of $5.64\sqrt{f'c}$ psi ($0.47\sqrt{f'c}$ MPa) and has a CSAR of 12. The data in Figure 6.1 show

- Significant nonlinearity in the vertical strain distribution when the continuum model is employed and a nonlinear shear strain distribution along the wall length included in the analysis.
- There is significant inaccuracy in the plane-sections-remain-plane analysis prediction of both (1) the maximum tensile strain in the reinforcing steel and (2) the location of the neutral axis.

Figure 6.2 shows vertical strain distributions for nine wall designs from the parameter study with varying CSAR and shear stress demands. In Figure 6.2, each row represents a different cross-sectional aspect ratio, with CSAR increasing as one moves down the figure; columns represent low, medium, and high levels of shear stress demand. Data in this figure show:

- Specimens with a high CSAR tend to under-predict by a greater margin the tensile strain distribution but are more accurate in predicting the location of the neutral axis.
- Specimens with a high peak shear stress tend to be less accurate in predicting the location of the neutral axis.

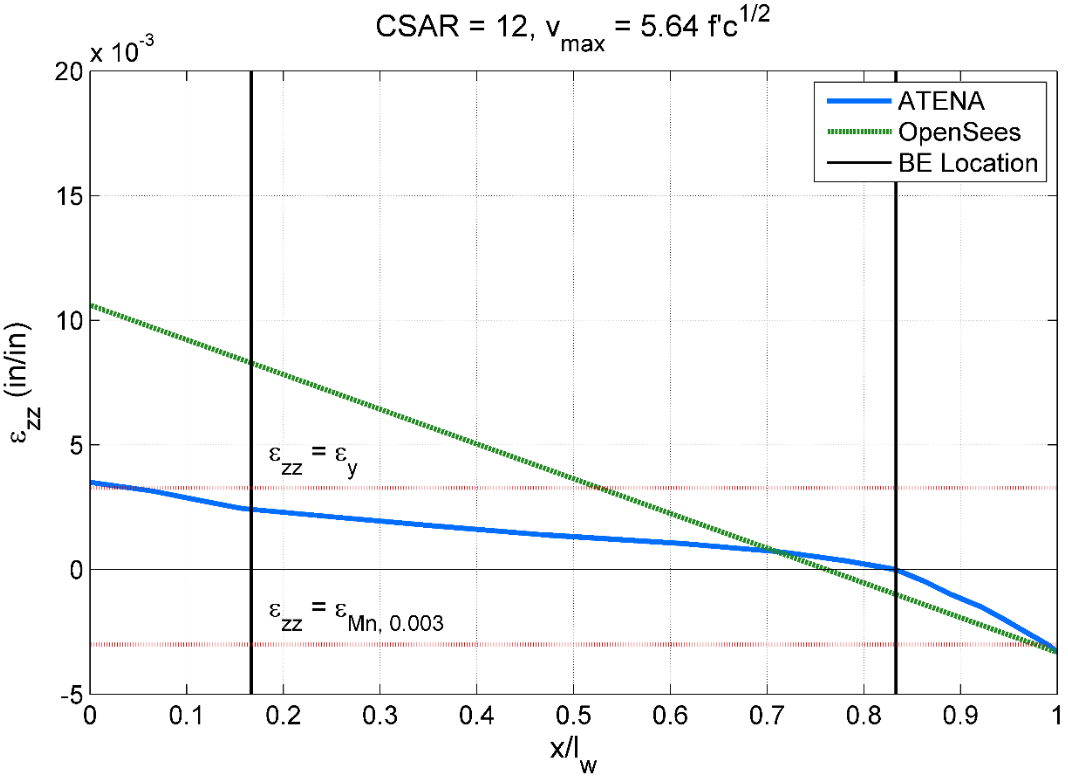

Figure 6.1 – RW1-C12-19 Vertical Strain Distribution at M_n

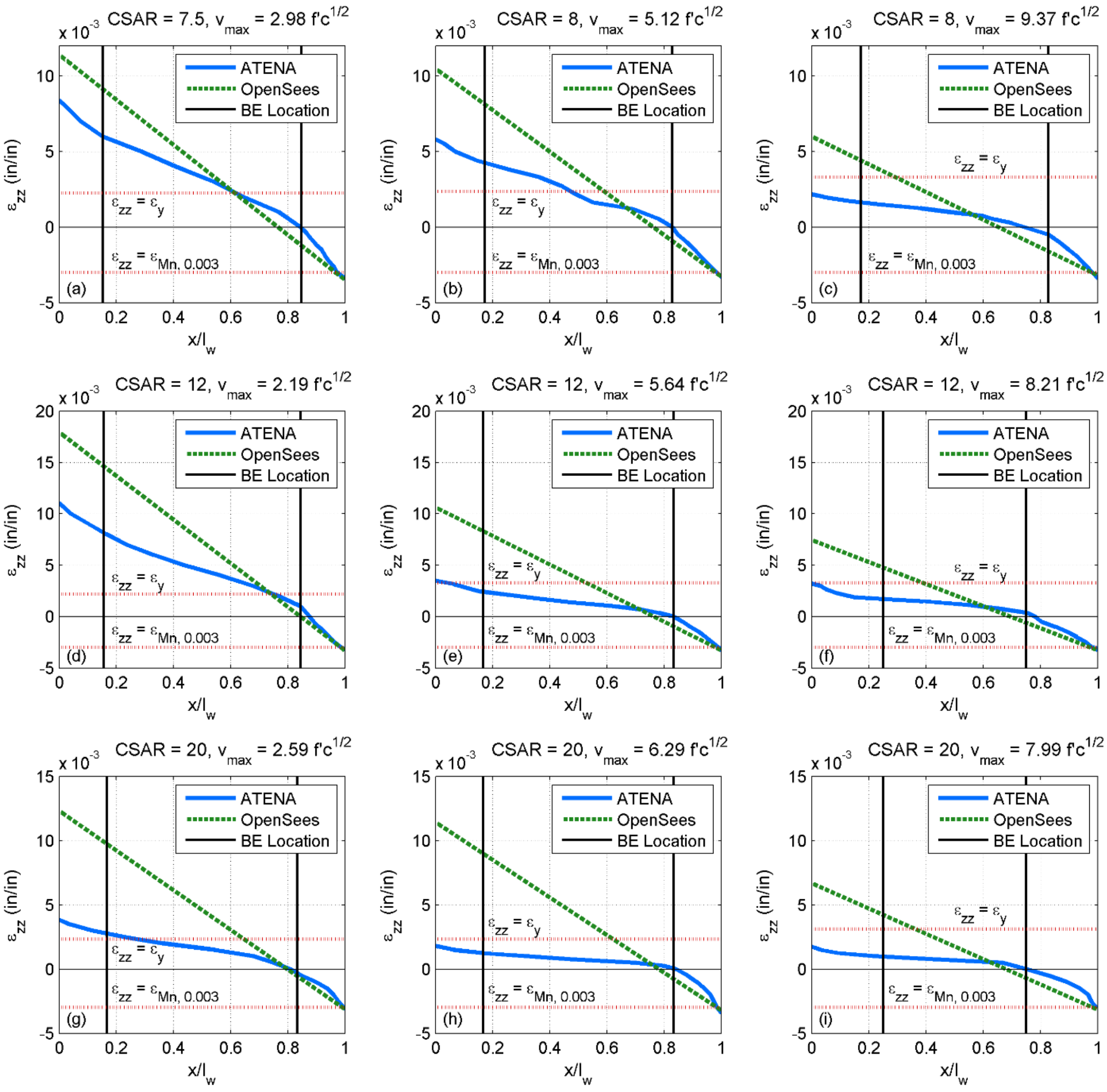

Figure 6.2 – Vertical Strain Distributions at M_n for Varied CSAR and Peak Shear Stresses

New parameters are defined as follows:

- $\varepsilon_{t,ATENA}/\varepsilon_{t,PSRP}$ = where $\varepsilon_{t,ATENA}$ is the extreme tensile strain observed at M_n in the ATENA simulation and $\varepsilon_{t,PSRP}$ is the extreme tensile strain at M_n in a PSRP analysis.
- c_{ATENA}/c_{PSRP} = where c_{ATENA} is the location of the neutral axis from the extreme compressive fiber and in the ATENA simulation and c_{PSRP} is the location of the neutral axis from the extreme compressive fiber assumed in a PSRP analysis.

Figures 6.3-6.6 show the impact of axial load ratio, shear span, CSAR, and the peak shear stress on c_{ATENA}/c_{PSRP}, and Figures 6.7-6.10 show the relationships between the same parameters and $\varepsilon_{t,ATENA}/\varepsilon_{t,PSRP}$. The key takeaways are as follows:

- The strain at failure in tension is much lower than is estimated in PSRP analysis, and particularly in walls with a high CSAR. This means that specimens designed to fail by tensile rupture of longitudinal reinforcement may instead fail in a CB mode.
- Design by ACI 318-14 requires confinement to the greater of $c_{PSRPI}/2$ and $c - 0.1l_w$. For walls of a small CSAR, this estimation is conservative, as the actual compression region is smaller than predicted by PSRP. This is not the case in high-CSAR walls, where the ATENA and PSRP predictions of the neutral axis are similar. This means that the confinement length is greater relative to the neutral axis for less-critical low-CSAR walls. The shear-critical high-CSAR walls are effectively required to confine less of the actual neutral axis.

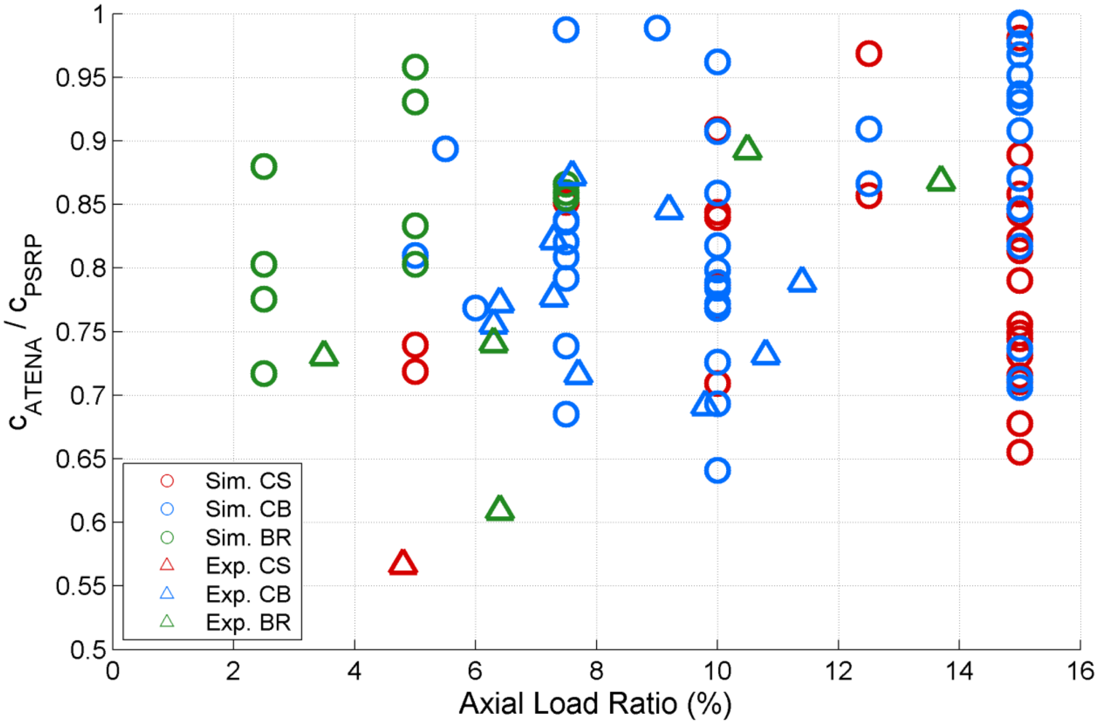

Figure 6.3 – Relationship Between c_{ATENA}/c_{PSRP} and Axial Load Ratio

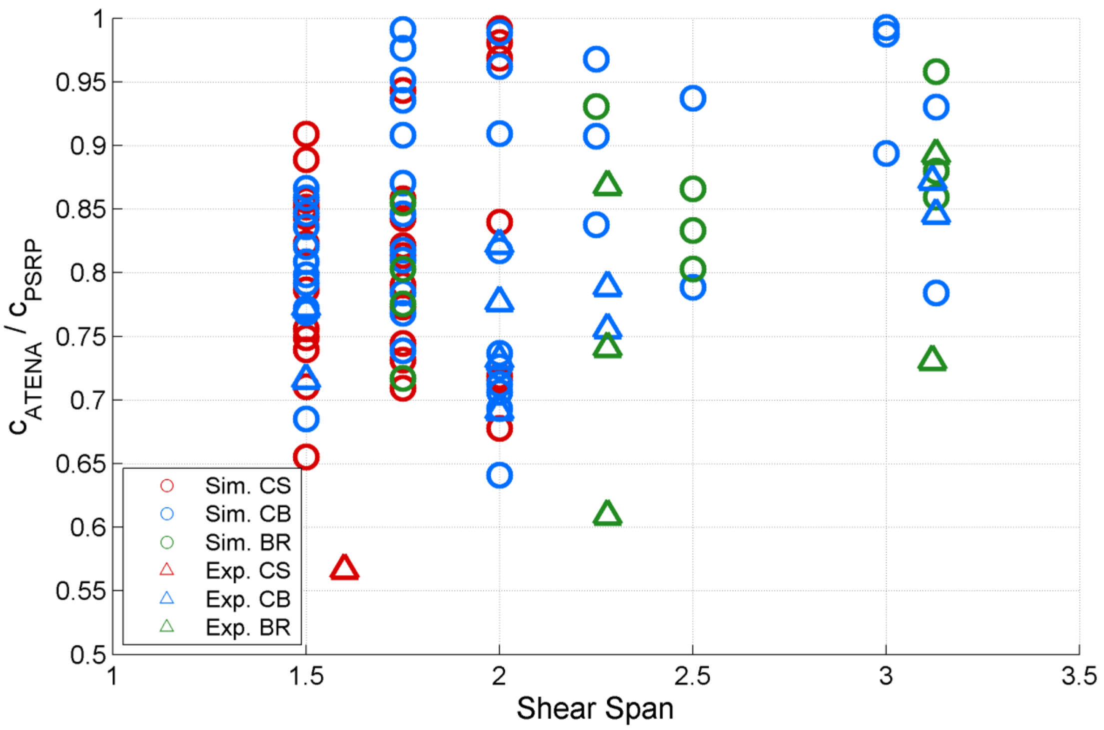

Figure 6.4 – Relationship Between c_{ATENA}/c_{PSRP} and Shear Span

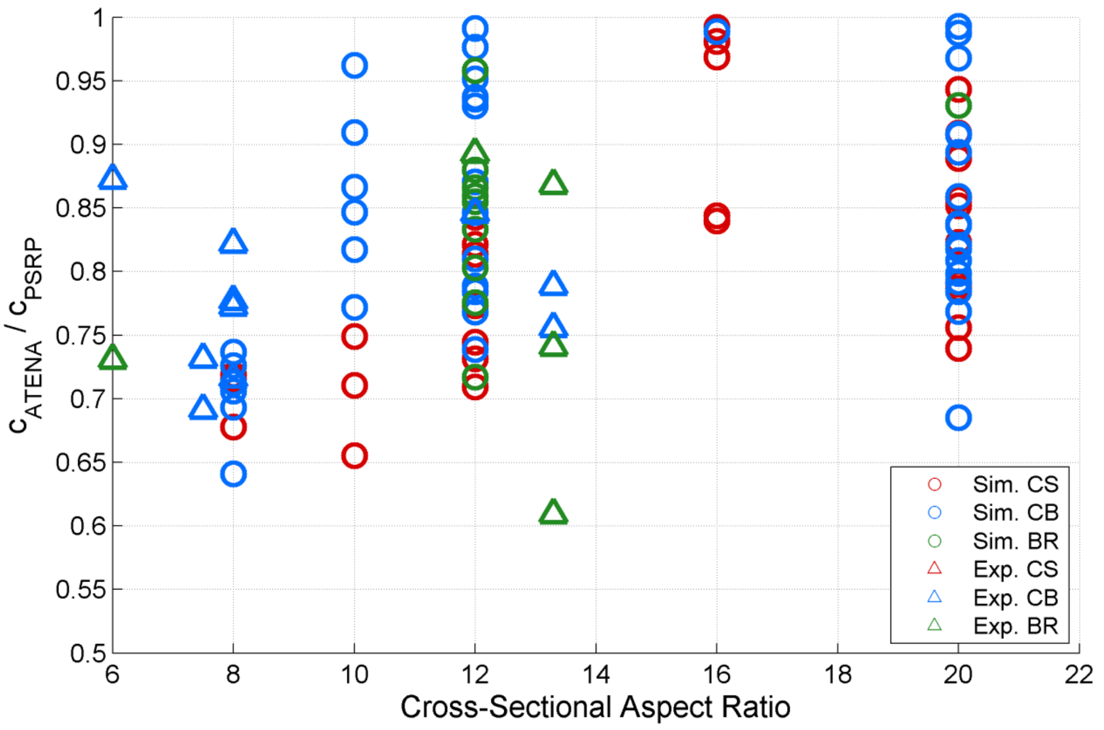

Figure 6.5 – Relationship Between c_{ATENA}/c_{PSRP} and CSAR

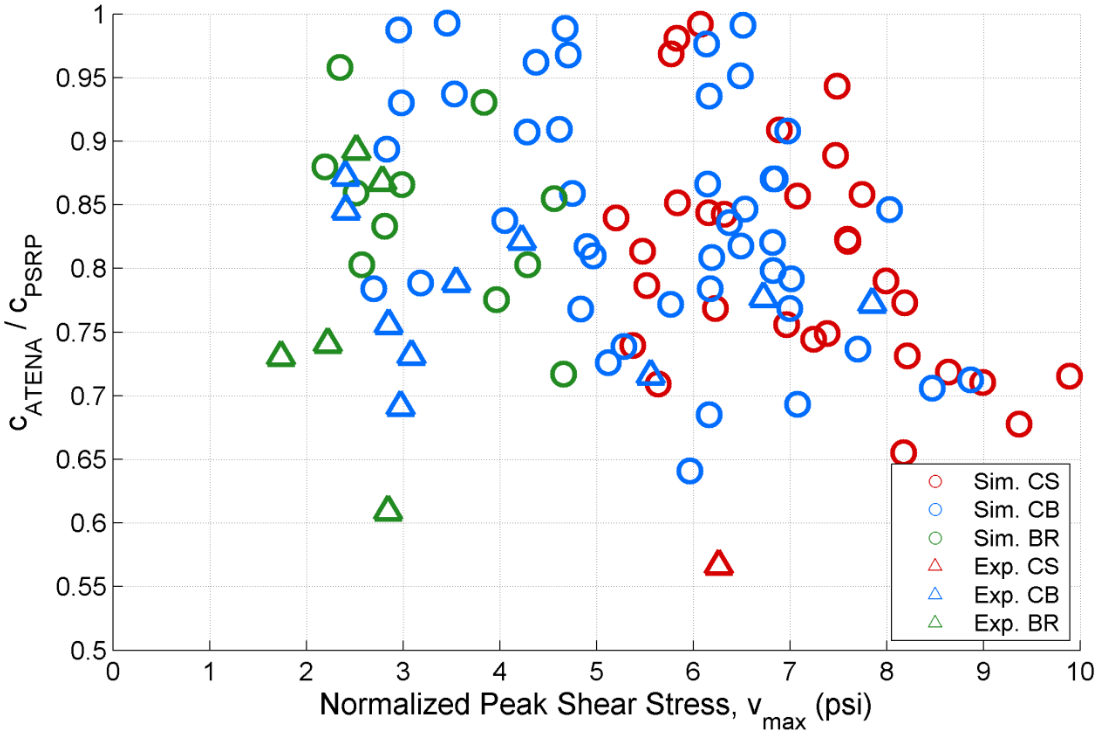

Figure 6.6 – Relationship Between c_{ATENA}/c_{PSRP} and Peak Shear Stress

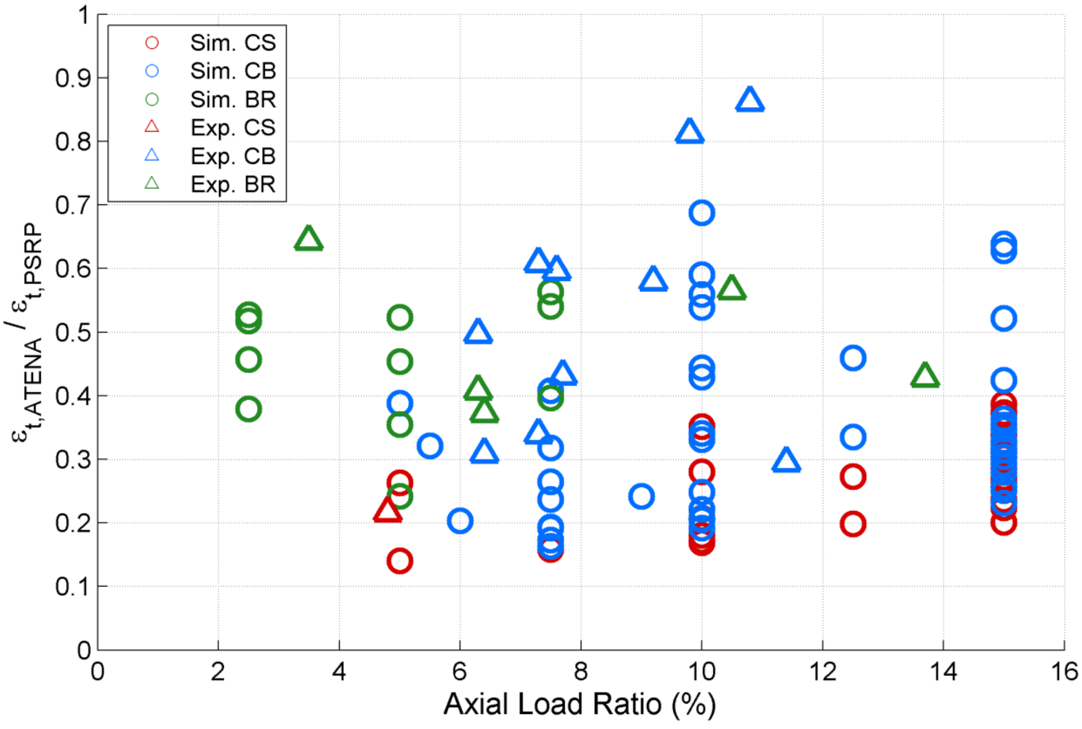

Figure 6.7 – Relationship Between $\varepsilon_{t,ATENA}/\varepsilon_{t,PSRP}$ vs. Axial Load Ratio

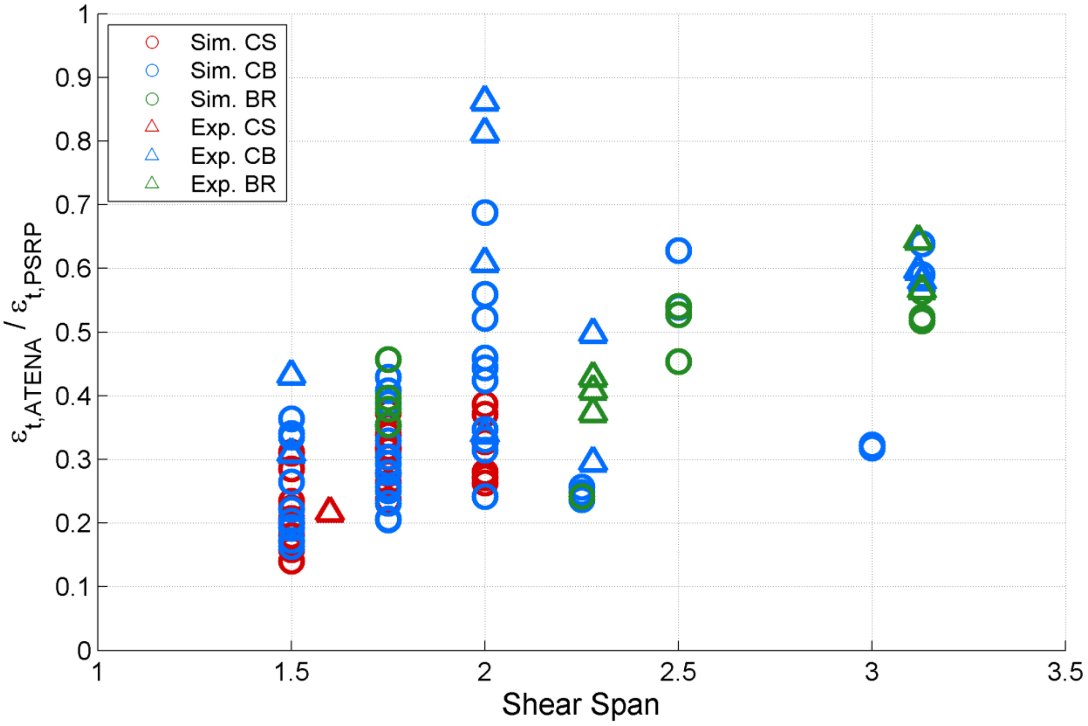

Figure 6.8 – Relationship Between $\varepsilon_{t,ATENA}/\varepsilon_{t,PSRP}$ and CSAR

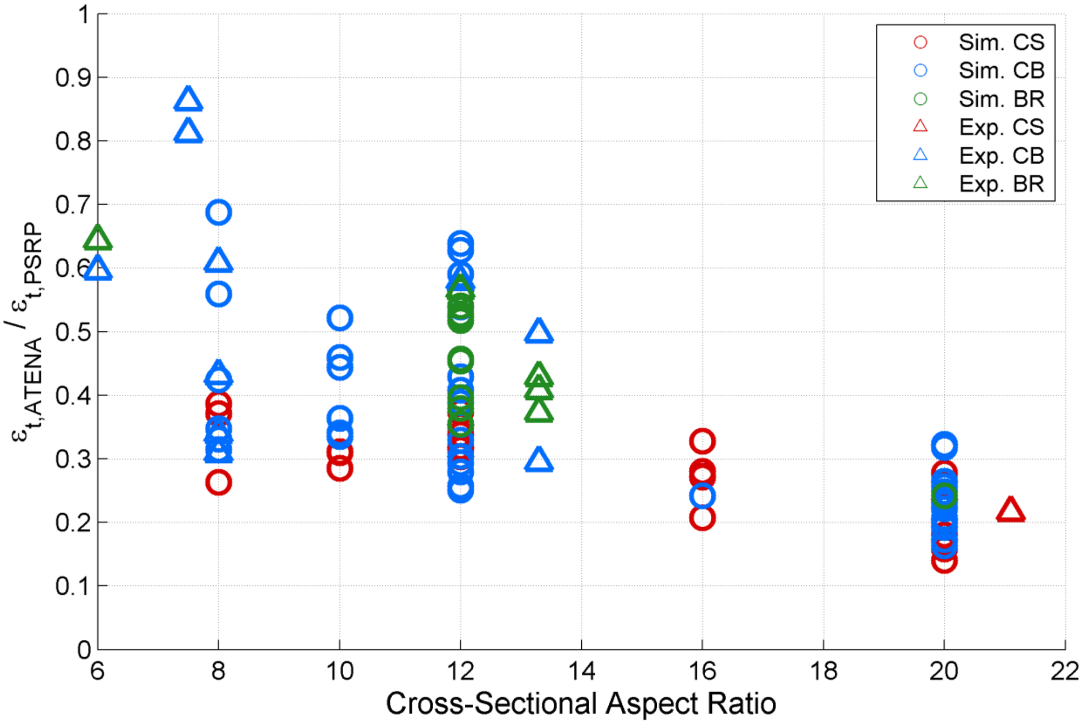

Figure 6.9 – Relationship Between $\varepsilon_{t,ATENA}/\varepsilon_{t,PSRP}$ and CSAR

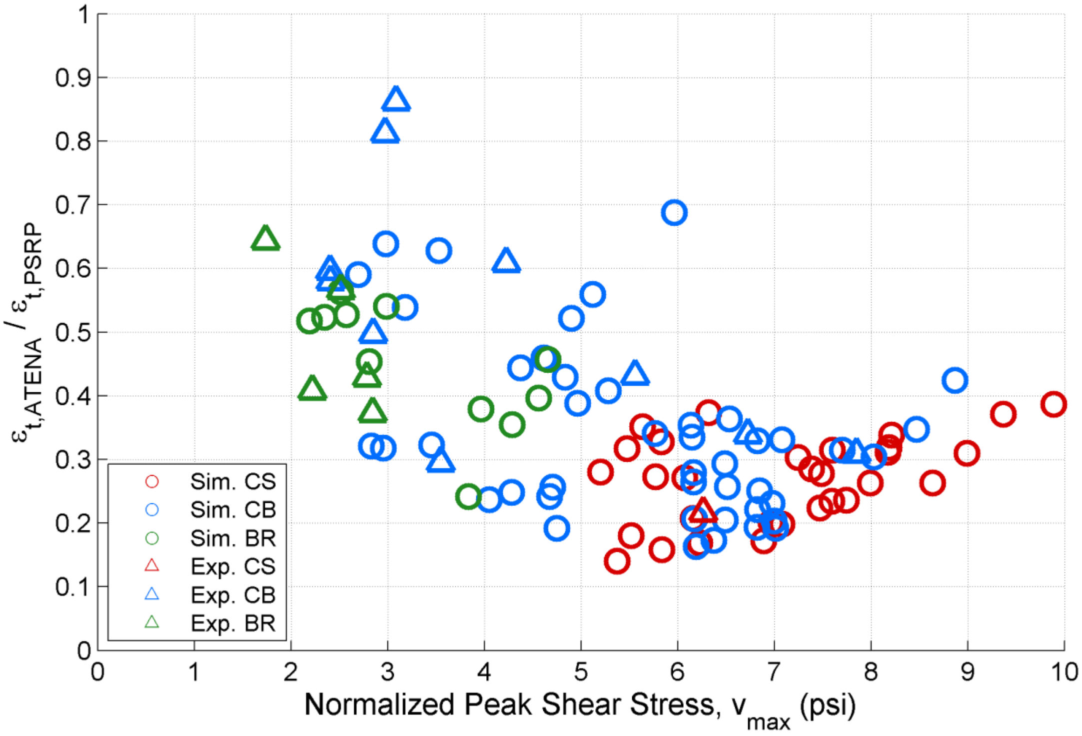

Figure 6.10 – Relationship Between $\varepsilon_{t,ATENA}/\varepsilon_{t,PSRP}$ *and Peak Shear Stress*

6.2 BOUNDARY ELEMENT LENGTH

This section investigates the relationship between the length of BE confining reinforcement relative to the neutral axis and wall failure mode; compression-shear failures tend to develop near the web-boundary element interface and behavior can be improved by locating this interface in a region which is not subjected to significant compression demands. The goal is to determine the necessary location of the web/boundary element interface relative to the neutral axis to prevent the development of compression-shear failure.

The methodology for examination of boundary element length is as follows:

1. Walls were simulated in ATENA, establishing a neutral axis depth.
2. The same model was analyzed in a PSRP analysis to establish the neutral axis used in design.
3. If CS failure resulted at a given peak shear stress, the boundary element length was extended and analysis was repeated.

6.2.1 Extended Boundary Element Models

This section defines an additional parameter study to that conducted in Chapter 5, systematically varying the confinement length to determine if this measure can prevent CS failure. The models in Chapter 5 with CSARs greater than 12 exhibited CS failure at much lower shear stresses than walls with CSARs below 12. This parameter study will thus focus on walls with CSARs greater than 12, using two base specimens: RW1 (CSAR = 12) and PW4 (CSAR = 20).

The new RW1 and PW4 model series vary the geometry by changing the boundary element length. The RW1-C12-BE and PW4-C20-BE series only differ from the original specimen geometries in boundary element length. The specifics of each parameter study design are shown in Table 6.1.

Table 6.1 – List of Model Series with CSAR of 12 and 20

Base Specimen	**CSAR**	l_{BE}/l_w
RW1-C12	12	0.16
RW1-C12-BE	12	0.21 to 0.25
PW4-C20	20	0.17
PW4-C20-BE	20	0.21 to 0.25

Table 6.2 lists all simulated models in the RW1-C12-BE series. Also included are all parameters which may change from the original RW1 specimen. The same information is presented for the PW4-C20-BE series in Table 6.3. All wall models are constructed and analyzed using the methods developed in Chapters 3-5. Tables 6.4-6.5 present the results of each analysis including story drift, hinge rotation, and failure mode.

Table 6.2 – List of Simulated Models in RW1-C12-BE Series

Specimen	**Shear Span**	**ALR**	$f_{y,BE}$	$\rho_{vert,BE}$	$\rho_{t,web}$	l_{BE}	l_{BE}/l_w
	--	%	ksi	%	%	in	--
RW1-C12-BE-1	1.75	15.0	63	2.93	0.50	10	0.21
RW1-C12-BE-2	1.75	15.0	73	2.93	0.50	10	0.21
RW1-C12-BE-3	1.75	15.0	83	2.93	0.50	10	0.21
RW1-C12-BE-4	1.75	15.0	95	2.93	0.50	10	0.21
RW1-C12-BE-5	1.75	20.0	83	2.93	0.50	10	0.21
RW1-C12-BE-6	1.75	15.0	63	2.93	0.50	12	0.25
RW1-C12-BE-7	1.75	15.0	73	2.93	0.50	12	0.25
RW1-C12-BE-8	1.75	15.0	83	2.93	0.60	12	0.25
RW1-C12-BE-9	1.75	15.0	95	3.81	0.60	12	0.25
RW1-C12-BE-10	1.75	20.0	85	3.52	0.60	12	0.25
RW1-C12-BE-11	1.75	15.0	85	3.66	0.60	12	0.25

Table 6.3 – List of Simulated Models in PW4-C20-BE Series

Specimen	**Shear Span**	**ALR**	$f_{y,BE}$	$\rho_{vert,BE}$	$\rho_{t,web}$	l_{BE}	l_{BE}/l_w
	--	%	ksi	%	%	in	--
PW4-C20-BE-1	1.50	7.5	63	3.44	0.65	25	0.21
PW4-C20-BE-2	1.50	10.0	63	3.44	0.65	25	0.21
PW4-C20-BE-3	1.50	12.5	63	3.44	0.65	25	0.21
PW4-C20-BE-4	1.50	7.5	63	3.13	0.65	25	0.21
PW4-C20-BE-5	1.50	7.5	75	3.13	0.65	25	0.21
PW4-C20-BE-6	1.50	10.0	77	2.41	0.65	30	0.25
PW4-C20-BE-7	1.50	15.0	60	3.44	0.65	30	0.25
PW4-C20-BE-8	1.75	10.0	79	3.44	0.65	30	0.25

Specimen	**Shear Span**	**ALR**	$f_{y,BE}$	$\rho_{vert,BE}$	$\rho_{t,web}$	l_{BE}	l_{BE}/l_w
PW4-C20-BE-9	1.50	15.0	63	2.91	0.65	30	0.25
PW4-C20-BE-10	1.75	15.0	63	3.44	0.65	30	0.25
PW4-C20-BE-11	1.75	10.0	63	3.44	0.65	30	0.25
PW4-C20-BE-12	1.75	15.0	67	4.37	0.65	30	0.25
PW4-C20-BE-13	1.75	15.0	90	3.44	0.65	30	0.25
PW4-C20-BE-14	1.75	20.0	67	3.44	0.65	30	0.25
PW4-C20-BE-15	1.50	7.5	90	2.82	0.65	30	0.25
PW4-C20-BE-16	1.50	6.0	80	3.13	0.65	30	0.25
PW4-C20-BE-17	1.50	7.5	65	3.13	0.65	30	0.25

Table 6.4 – List of Results for Simulated Models in the RW1-C12-BE Series

Specimen	$V_{max}/A_{cv}f'_c{}^{0.5}$	V_b/V_n	**Story Drift**	**Hinge Rotation**	$\varepsilon_{t,ATENA}/\varepsilon_{t,PSRP}$	c_{ATENA}/c_{PSRP}	**Failure Mode**
	--	--	%	rad	--	--	--
RW1-C12-BE-1	6.16	0.84	2.16	0.0208	0.28	0.94	CB
RW1-C12-BE-2	6.51	0.88	2.22	0.0209	0.26	0.99	CB
RW1-C12-BE-3	6.85	0.93	2.29	0.0213	0.25	0.87	CB
RW1-C12-BE-4	7.25	0.98	1.67	0.0149	0.30	0.74	CS
RW1-C12-BE-5	7.60	1.03	1.45	0.0132	0.34	0.82	CS
RW1-C12-BE-6	6.14	0.83	2.16	0.0208	0.35	0.98	CB
RW1-C12-BE-7	6.48	0.88	2.37	0.0226	0.29	0.95	CB
RW1-C12-BE-8	6.82	0.82	2.35	0.0220	0.33	0.87	CB
RW1-C12-BE-9	8.21	0.99	1.63	0.0138	0.34	0.73	CS
RW1-C12-BE-10	8.18	0.98	1.62	0.0144	0.32	0.77	CS
RW1-C12-BE-11	8.03	0.96	1.89	0.0164	0.30	0.85	CB

Table 6.5 – List of Results for Simulated Models in the PW4-C20-BE Series

Specimen	$V_{max}/A_{cv}f'_c{}^{0.5}$	V_b/V_n	**Story Drift**	**Hinge Rotation**	$\varepsilon_{t,ATENA}/\varepsilon_{t,PSRP}$	c_{ATENA}/c_{PSRP}	**Failure Mode**
	--	--	%	rad	--	--	--
PW4-C20-BE-1	6.37	0.67	1.92	0.0142	0.17	0.84	CB
PW4-C20-BE-2	6.89	0.72	1.53	0.0112	0.17	0.90	CS
PW4-C20-BE-3	7.08	0.74	1.24	0.0090	0.20	0.86	CS
PW4-C20-BE-4	6.19	0.65	1.80	0.0136	0.16	0.81	CB
PW4-C20-BE-5	7.01	0.74	1.71	0.0119	0.19	0.79	CB
PW4-C20-BE-6	6.83	0.72	1.66	0.0127	0.22	0.80	CB
PW4-C20-BE-7	7.59	0.80	1.19	0.0087	0.23	0.82	CS
PW4-C20-BE-8	6.18	0.65	1.75	0.0130	0.21	0.78	CB
PW4-C20-BE-9	7.47	0.71	1.40	0.0104	0.22	0.89	CS
PW4-C20-BE-10	6.97	0.73	1.92	0.0140	0.23	0.91	CB
PW4-C20-BE-11	6.49	0.68	1.81	0.0134	0.20	0.82	CB
PW4-C20-BE-12	7.74	0.81	1.00	0.0070	0.24	0.86	CS
PW4-C20-BE-13	7.99	0.84	1.13	0.0074	0.26	0.79	CS
PW4-C20-BE-14	7.49	0.79	1.48	0.0109	0.28	0.94	CS

Specimen	V_{max}/ $A_{cv}f'_c{}^{0.5}$	V_b/V_n	Story Drift	Hinge Rotation	$\varepsilon_{t,ATENA}$/ $\varepsilon_{t,PSRP}$	c_{ATENA}/ c_{PSRP}	Failure Mode
PW4-C20-BE-15	6.16	0.65	1.92	0.0151	0.26	0.69	CB
PW4-C20-BE-16	7.00	0.73	1.94	0.0133	0.20	0.77	CB
PW4-C20-BE-17	6.82	0.72	2.73	0.0156	0.19	0.82	CB

6.2.2 Impact of Boundary Element Length

With the models defined in the previous section, it is now possible to determine if it is possible to prevent CS failure by confining a greater length of the wall. The current ACI 318-14 requirements result in large strains in the unconfined web region, leading to early concrete crushing; by confining the full length of the compression region, only confined concrete elements are subjected to compression. This section investigates both (1) increased shear demands and (2) the confinement length necessary to reach the increased shear demands while not exhibiting CS failure.

To determine the confinement length necessary to reach greater shear demands, the PSRP and ATENA neutral axes are calculated for each simulation and then related to the length of confinement provided in the model. Figure 6.11 and Figure 6.12 thus relate failure mode to both shear demand and the length of confined reinforcement relative to the PSRP neutral axis. Figure 6.11 shows that CS failures occur (1) above 8.0$\sqrt{f'c}$ psi (0.66$\sqrt{f'c}$ MPa) and (2) above l_{be}/c_{PSRP} = 0.9 for walls with CSAR = 12. Figure 6.12 shows that CS failures occur (1) above 7$\sqrt{f'c}$ psi (0.58$\sqrt{f'c}$ MPa) and (2) above l_{be}/c_{PSRP} = 1.0 for walls with CSAR = 20. These results are summarized in Table 6.6.

Table 6.6 – Maximum Shear Demands and Required Confinement Lengths for CSARs = 12 and 20

CSAR	V_{max}/ $A_{cv}f'_c{}^{0.5}$	L_{be}/ c_{PSRP}
12	8.0	0.9
20	7.0	1.0

These results show that, regardless of the confinement length, any shear demand which exceeds the CSAR-specific shear demand limit will result in CS failure. This is the maximum possible shear demand that the wall is able to resist before exhibiting a CS failure. The required confinement lengths for CSARs of 12 and 20 both exceed that which is required by ACI 318-14, which stipulates that the boundary element length be the greater of c/2 and c-0.1l_w.

Figures 6.13-6.14 are similar to the previous two figures, but instead normalize boundary element length by the ATENA neutral axis rather than that determined by PSRP. Note that for CSAR = 12, the necessary confined length when considering the ATENA neutral axis is 1.0 rather than the 0.9 value determined by PSRP analysis. This relates back to the discussion of strain distributions in Section 6.1, specifically to the lack of accuracy provided by PSRP analysis in predicting the neutral axis in low-CSAR walls. The difference between c_{ATENA} and c_{PSRP} at low CSARs is particularly interesting in the context of the ACI 318-14 boundary element requirement noted above. In effect, current ACI regulations result in a relatively greater portion of low-CSAR wall compression regions being confined than is confined in equivalent high-CSAR walls. This is troublesome as it is the high-CSAR walls that at greater risk for CS failure.

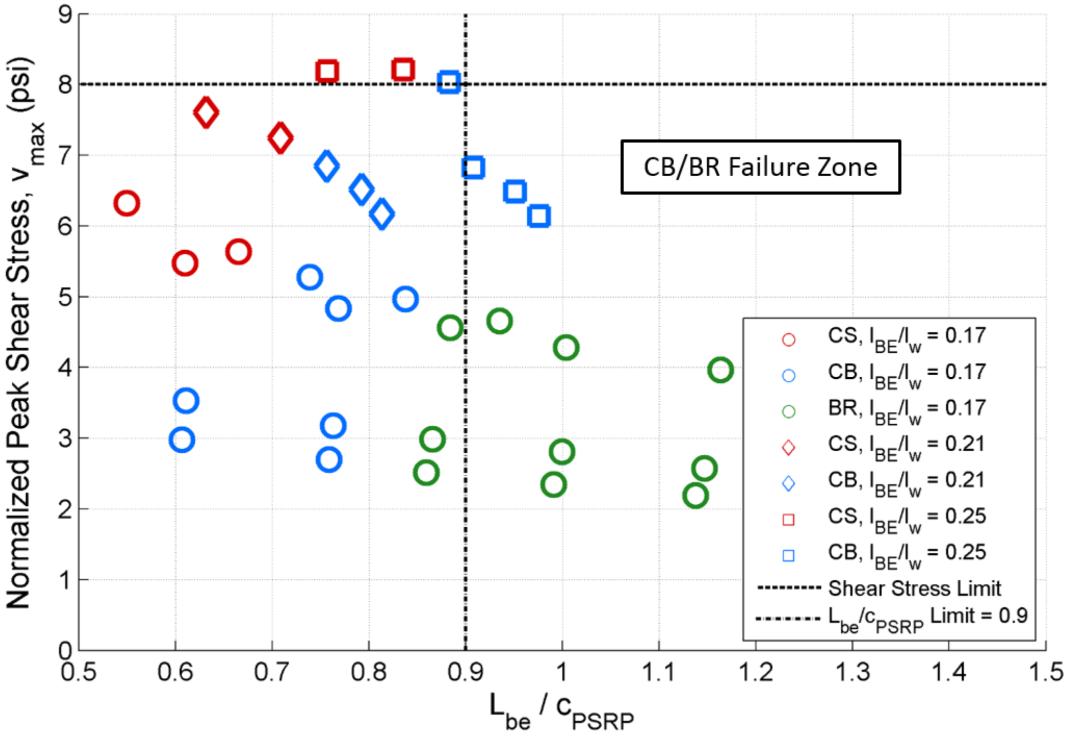

Figure 6.11 – Peak Shear Stress vs. Length of Conf. Region over Comp. Region (PSRP) (CSAR = 12)

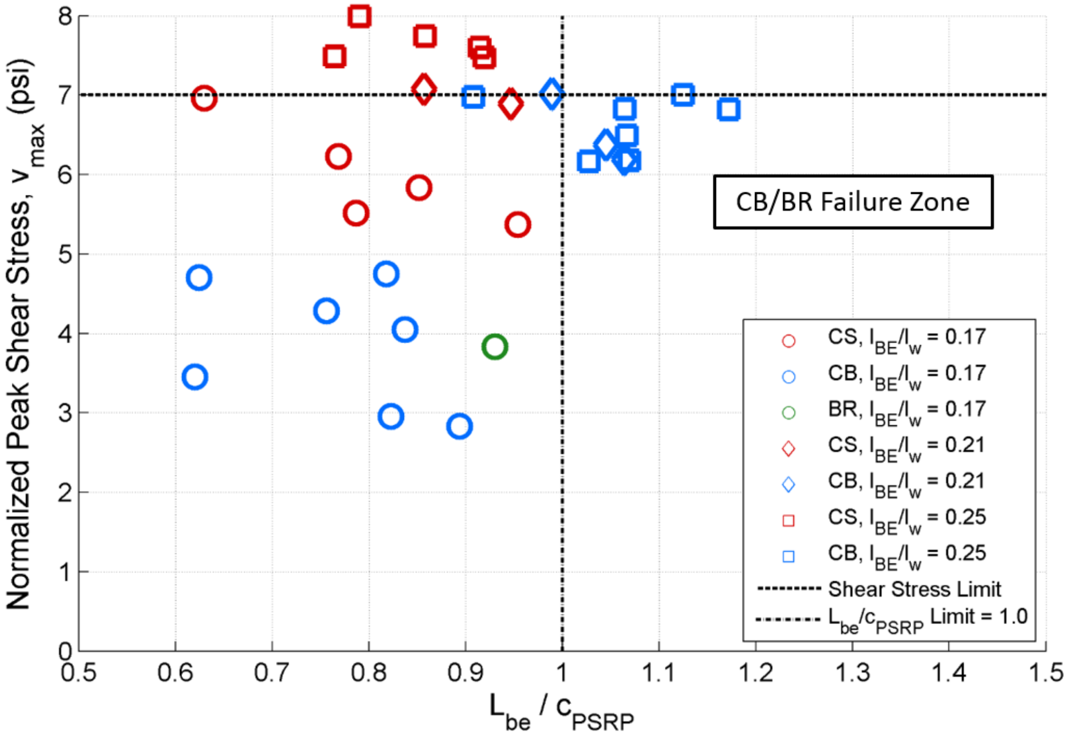

Figure 6.12 – Peak Shear Stress vs. Length of Conf. Region (PSRP) over Comp. Region (CSAR = 20)

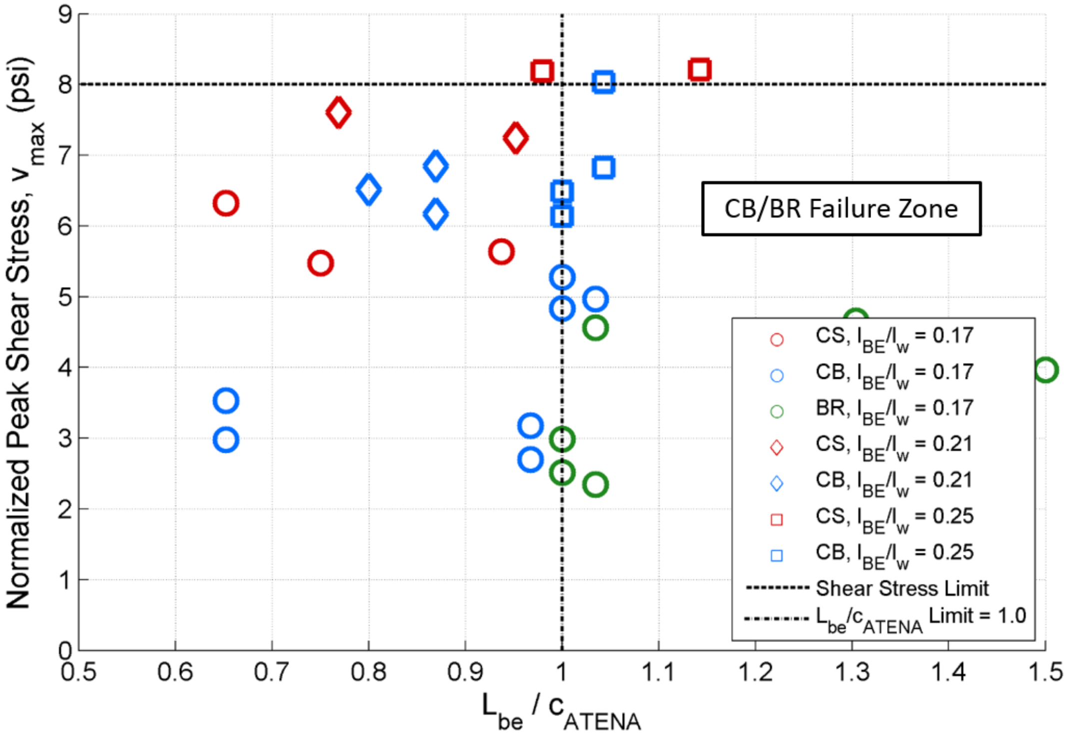

Figure 6.13 – Peak Shear Stress vs. Length of Conf. Region over Comp. Region (ATENA) (CSAR = 12)

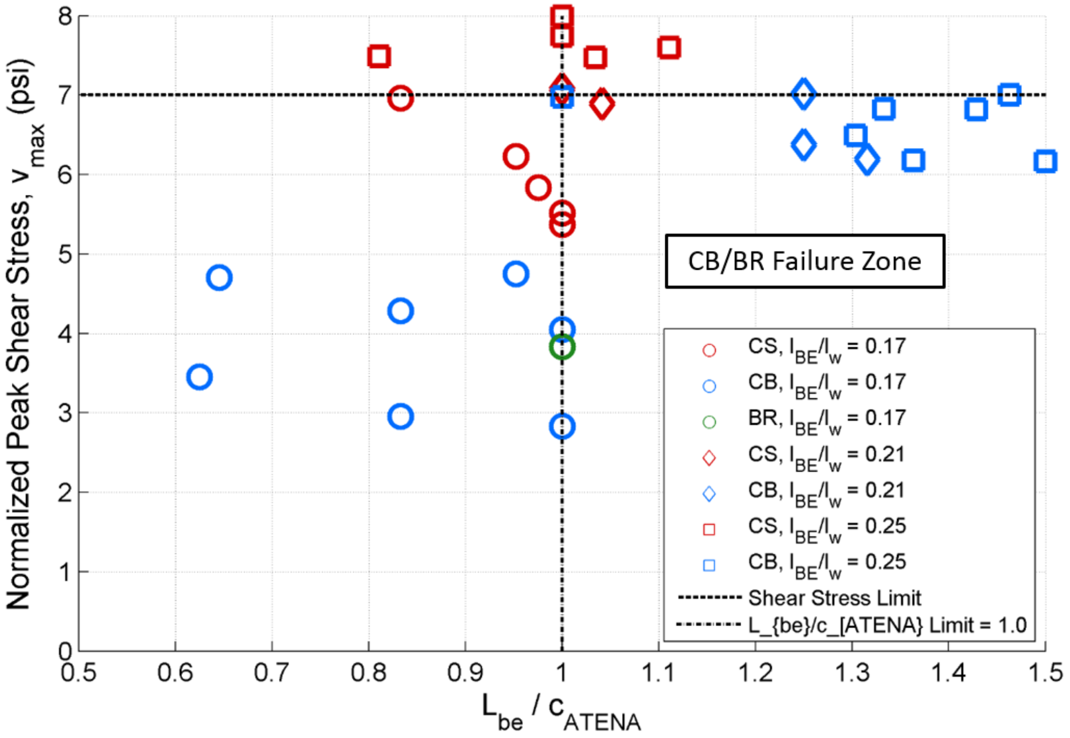

Figure 6.14 – Peak Shear Stress vs. Length of Conf. Region (ATENA) over Comp. Region (CSAR = 20)

6.2.3 Required Length of Confining Boundary Element Reinforcement (α_{BE})

The previous section defined the confinement length required at each CSAR to prevent CS failures at increased shear demands. A parameter is defined below that determines the required length of confinement for a given wall design.

Currently the ACI Code allows a shear stress demand of $10\sqrt{f'c}$ psi ($0.83\sqrt{f'c}$ MPa) and requires a confined boundary element length of max{c/2, c-0.1l_w}. On the basis of the data above, new limits on shear stress demand and requirement for boundary element length are proposed. The new approach for extending the confined region of the planar shear walls increases the peak shear stress limit determined for current ACI requirements in Chapter 5.

This new requirement for confinement length is characterized here by the parameter α_{BE} (Eq. 6.1). Figures 6.15-6.16 plot this parameter vs. CSAR, and the results are further detailed in Table 6.7.

$$\alpha_{BE} = \frac{\text{Length of Confining Reinforcement}}{\text{Neutral Axis Determined by PSRP}} \qquad \textit{(Eq. 6.1)}$$

Table 6.7 – α_{BE} Parameter for Varied CSAR

	CSAR = 8	**CSAR = 12**	**CSAR = 20**
α_{BE}	0.85	0.9	1.0

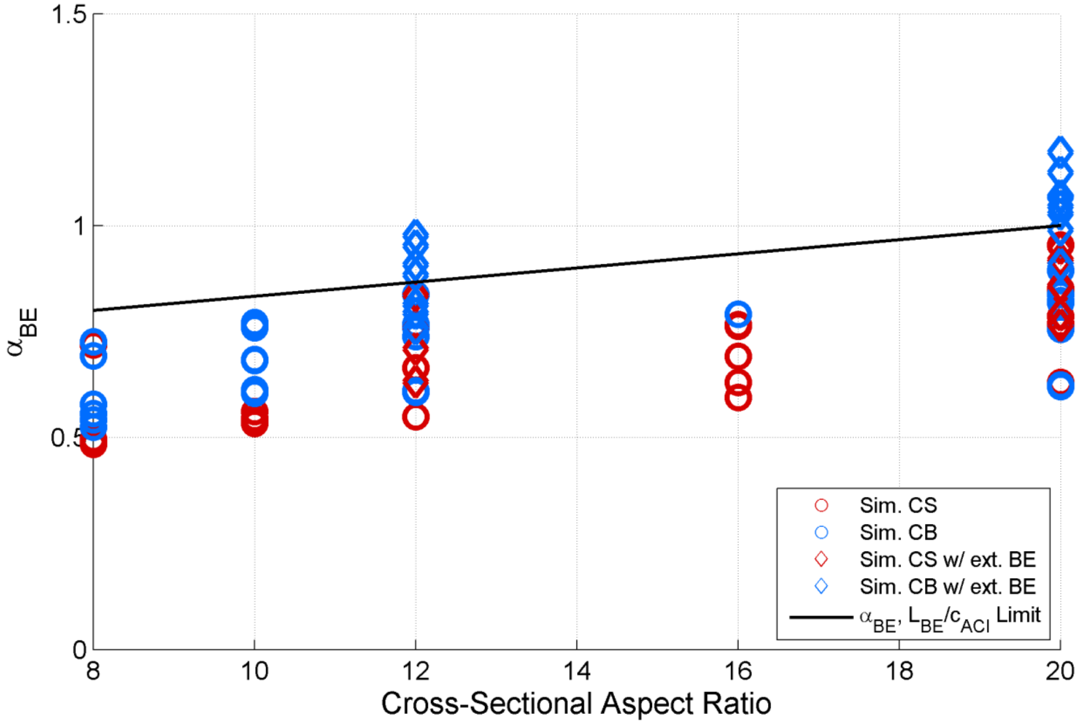

Figure 6.15 – Length of Confined Region over Comp. Region (PSRP) vs. CSAR

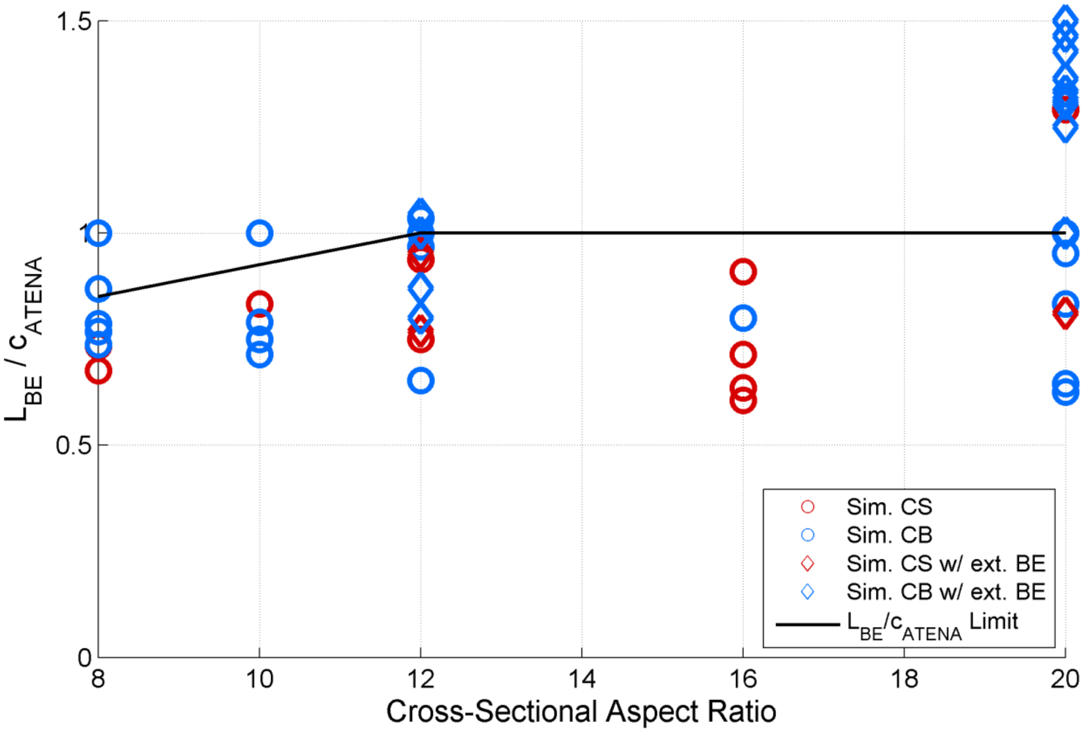

Figure 6.16 – Length of Confined Region over Comp. Region (ATENA) vs. CSAR

6.3 DESIGN RECOMMENDATIONS

The above analysis shows that it is possible to define a greater shear demand limit than was specified in Chapter 5 (Figure 6.17) by providing a greater length of confinement. Both the required confinement length (α_{BE}) and shear demand limit vary based on the wall geometry (i.e., cross-sectional aspect ratio). This section will provide design recommendations and a proposed design process for walls that implements the findings of Section 6.2.

6.3.1 Proposed Design Process

There are three essential parameters essential to achieving a wall design that prevents CS failure: CSAR, shear demand, and the confinement length. The CSAR determines the necessary confinement length to prevent CS failure at a given shear demand; the shear limit for current ACI BE length requirements is detailed in Figure 6.17. The increased shear demand limit for designs which confine the required α_{BE} are shown in Figure 6.18.

It is recommended for simplicity that α_{BE} is taken as 1.0 for all CSARs. The value only decreases marginally from 1.0 for CSARs less than 20, and it is conservative to simply confine the full compression region. This is the end result of CS analysis: by confining the full compression region, it is possible to reach greater shear demands while avoiding CS failure, which characteristically initiates at the web/boundary element interface. With current regulations, this interface is often subjected to large compressive strains and results in CS failure.

The proposed design process which includes consideration of these two shear demand limits is as follows:

- Determine the cross-sectional aspect ratio of the wall design.

- Determine if the wall will be subjected to peak shear stresses higher than those allowable by the current ACI 318-14 boundary element provisions (e.g., $5.5\sqrt{f'c}$ psi ($0.46\sqrt{f'c}$ MPa) at CSAR = 12 and $5\sqrt{f'c}$ psi ($0.42\sqrt{f'c}$ MPa) at CSAR = 20). This limit is shown in full in Figure 6.17.
- If the lower peak shear stress bound of Figure 6.17 is sufficient, design can proceed with l_{BE} = max{$c_{PSRP}/2$, c_{PSRP}-0.1l_w}.
- If upper peak shear stress bound of Figure 6.18 is required, it is necessary to confine the full compression region.

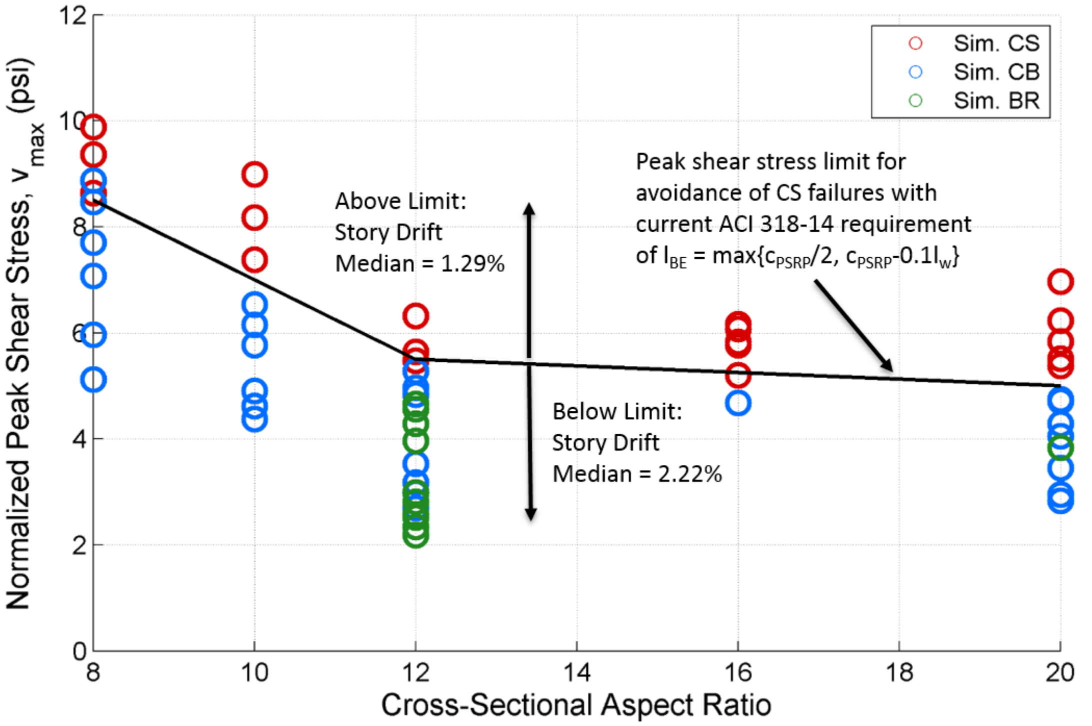

Figure 6.17 – Peak Shear Stress vs. CSAR for models with LBE meeting ACI requirements

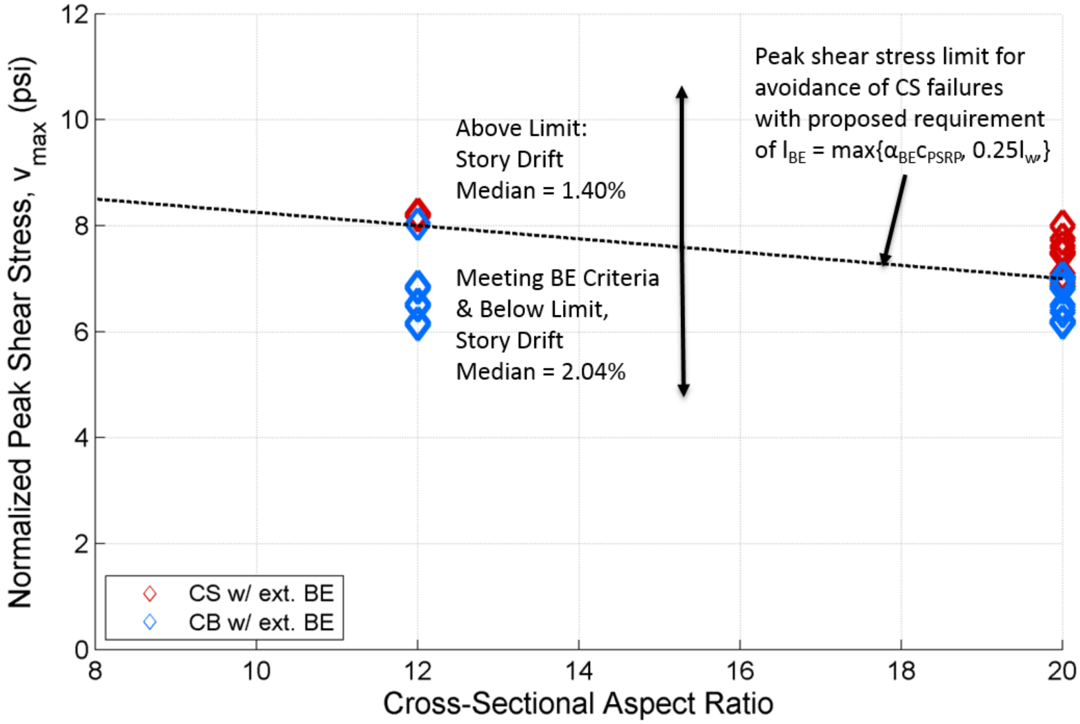

Figure 6.18 – Peak Shear Stress vs. CSAR for models with LBE extended beyond ACI requirements

6.3.2 Updated Fragility Curves per Failure Mode

The two limits for the boundary element length refer to different peak shear stress bounds, both of which are designed to prevent the loss of deformation capacity observed in compression-shear failure. The design goal is to create sections which fail in either BR or CB modes, and this is only prevented at high shear stress demands by extending the confinement. The additional models run in this chapter achieved higher shear stress demands at larger confined lengths and did not exhibit significantly different deformation capacity than was observed in the Chapter 5 models and fragility curves. These fragility curves are updated with new models below; note that they are defined in the same fashion as those in Chapter 5, as detailed by Eq. 5.2-5.4.

There are three different groups of fragility curves below. Figures 6.19-6.20 present the fragility curves for only the extended boundary element models simulated in Chapter 6. The fragility curves which consider only Chapter 5 models are reproduced in Figures 6.21-6.22. This data is summarized in Table 6.8 and Table 6.9.

The Chapter 5 models exhibit greater deformation capacity than the Chapter 6 models, but this is due to the high CSAR (only values of 12 and 20) of models run in the extended boundary element study. If only CSARs of 12 and greater are considered for both chapters, as shown in Table 6.9, the median deformation capacity of CB failures in the two different studies is identical (story drift = 1.93%, hinge rotation = 0.015 rad). The CS failures in Chapter 6 actually exhibit greater deformation capacity than CS failures simulated in Chapter 5 (1.45% to 1.17% story drift, 0.011 rad to 0.009 rad hinge rotation. This shows that the extended confinement detailed in this chapter enables CB failures at higher shear demands to exhibit the same deformation capacity as CB failures at lower shear demands which do not confine the full compression region.

Fragility curves which include all simulations in Chapters 5 and 6 are presented in Figures 6.23-6.24.

Table 6.8 – Medians and Coefficients of Variation for Failure Modes of Planar Walls for Both Chapter 6 Ext. BE Models and Chapter 5 Standard BE Models

Output Parameter	**Failure Mode**	**Chapter 5 Models, Standard BE Length**			**Chapter 6 Models, Extended BE Length**		
		#	**Median**	**COV**	**#**	**Median**	**COV**
Story Drift (%)	BR	18	2.30	0.17	--	--	--
	CB	38	2.08	0.21	11	1.93	0.14
	CS	20	1.30	0.15	17	1.45	0.16
Hinge Rotation (rad)	BR	18	0.020	0.17	--	--	--
	CB	38	0.018	0.24	11	0.015	0.23
	CS	20	0.009	0.23	17	0.011	0.25

Table 6.9 – Medians and Coefficients of Variation for Failure Modes of Planar Walls for Both Chapter 6 Ext. BE Models and Chapter 5 Standard BE Models (CSAR ≥ 12)

Output Parameter	**Failure Mode**	**Chapter 5 Models, Standard BE Length**			**Chapter 6 Models, Extended BE Length**		
		#	**Median**	**COV**	**#**	**Median**	**COV**
Story Drift (%)	BR	6	2.13	0.27	--	--	--
	CB	11	1.93	0.13	11	1.93	0.14
	CS	11	1.17	0.16	17	1.45	0.16
Hinge Rotation (rad)	BR	6	0.016	0.29	--	--	--
	CB	11	0.015	0.13	11	0.015	0.23
	CS	11	0.009	0.15	17	0.011	0.25

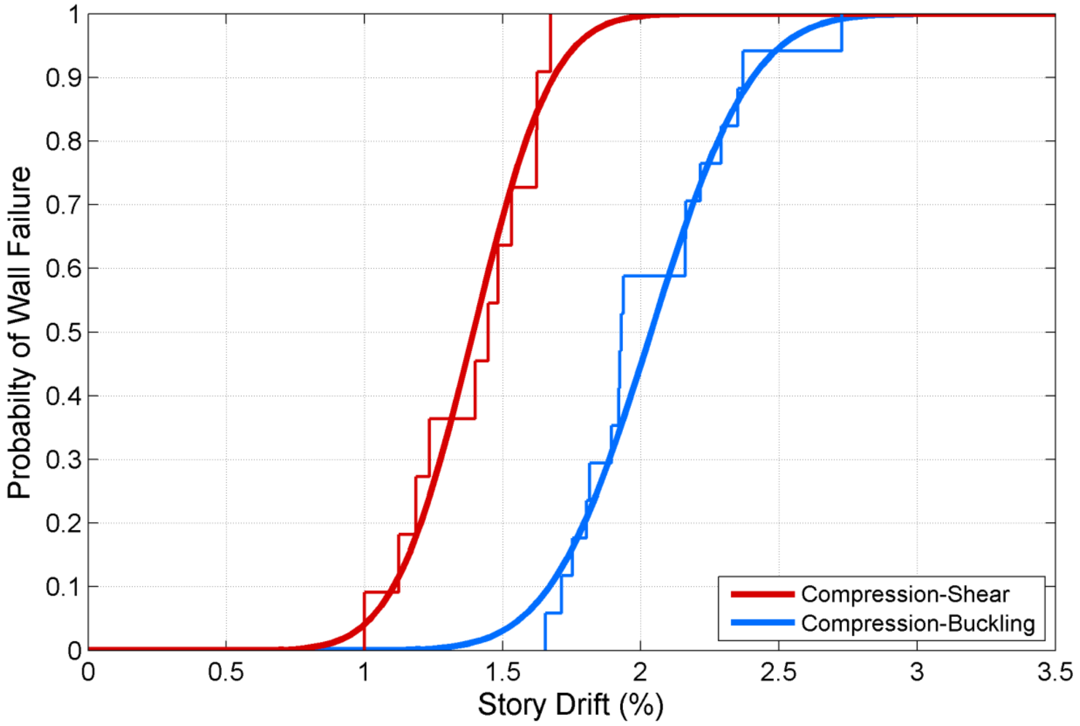

Figure 6.19 – Fragility Curves for Different Failure Modes, Story Drift (Ext. BE Models)

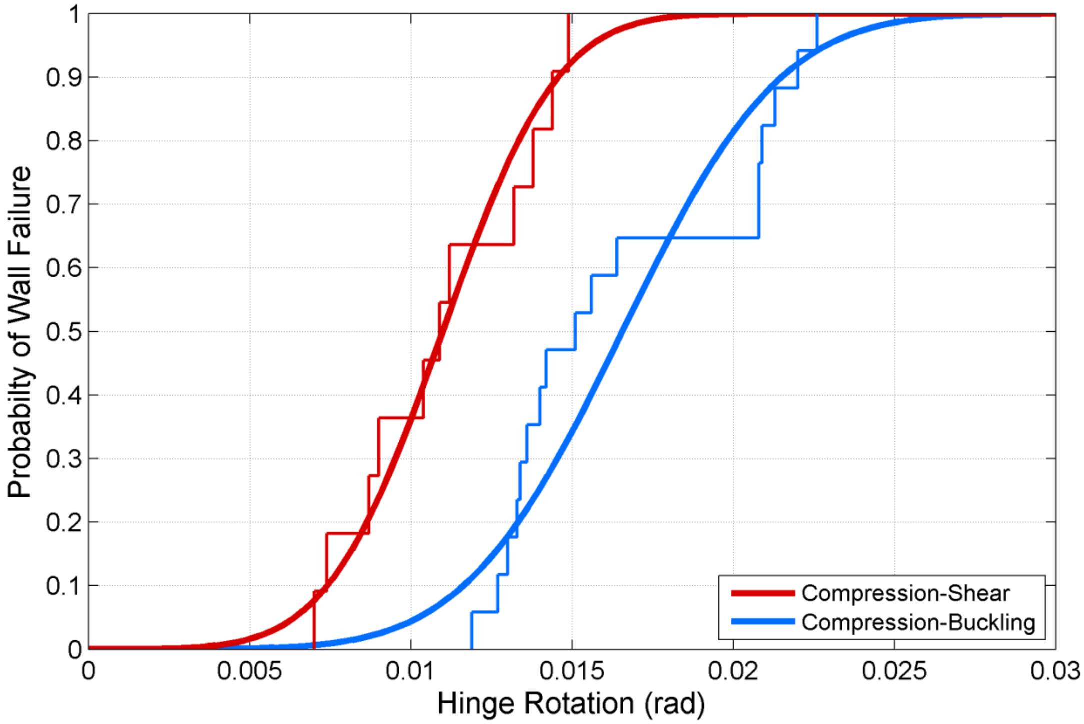

Figure 6.20 – Fragility Curves for Different Failure Modes, Hinge Rotation (Ext. BE Models)

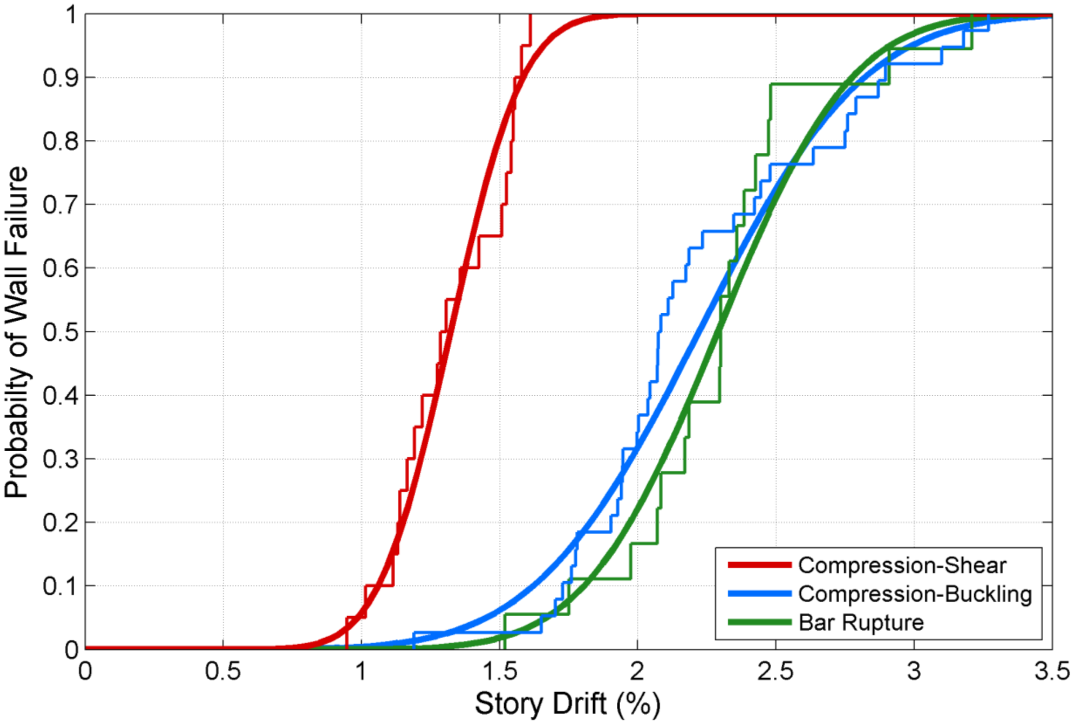

Figure 6.21 – Fragility Curves for Planar Wall Failure Modes, Story Drift (All Simulated Models)

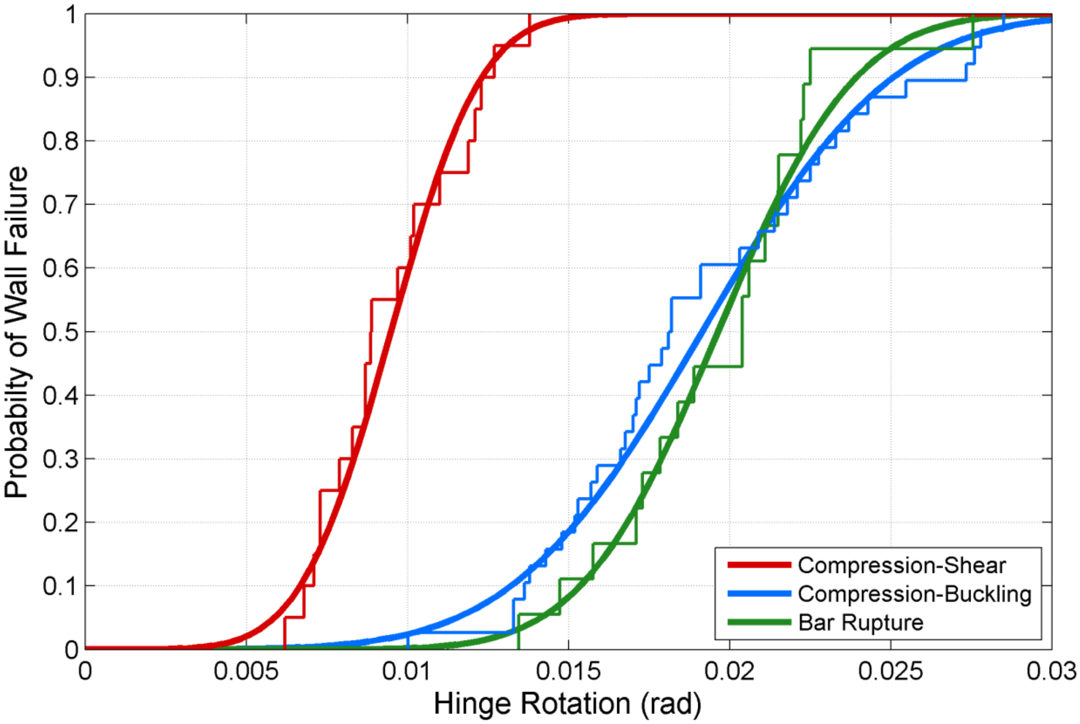

Figure 6.22 – Fragility Curves for Planar Wall Failure Modes, Hinge Rotation (All Simulated Models)

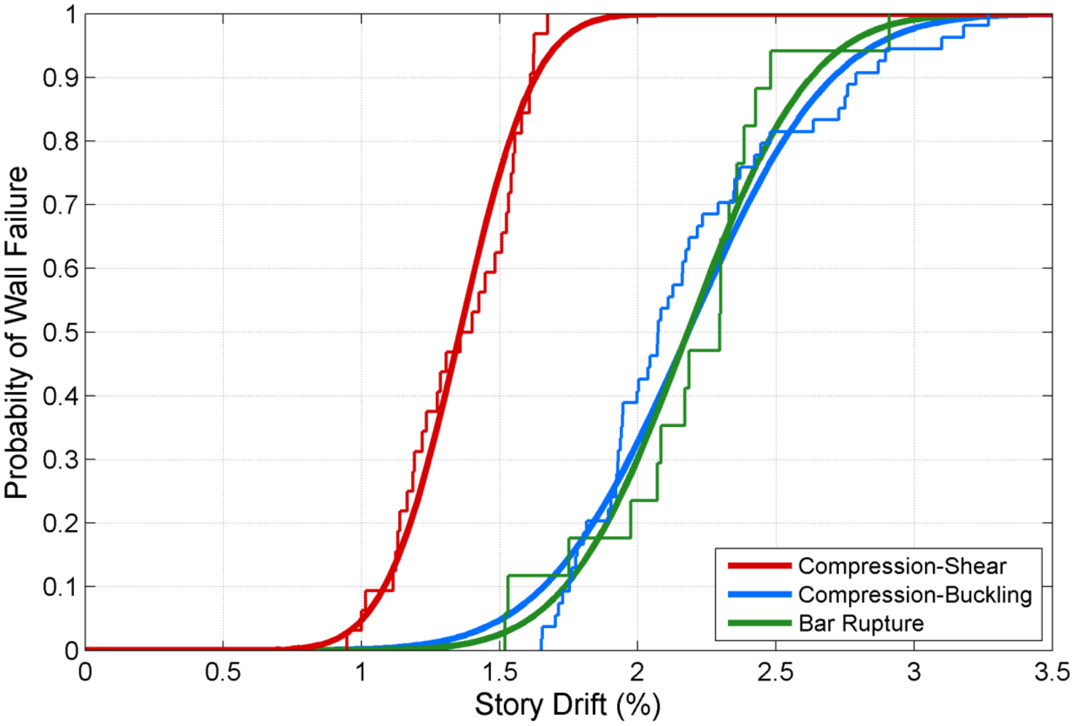

Figure 6.23 – Fragility Curves for Different Failure Modes, Story Drift

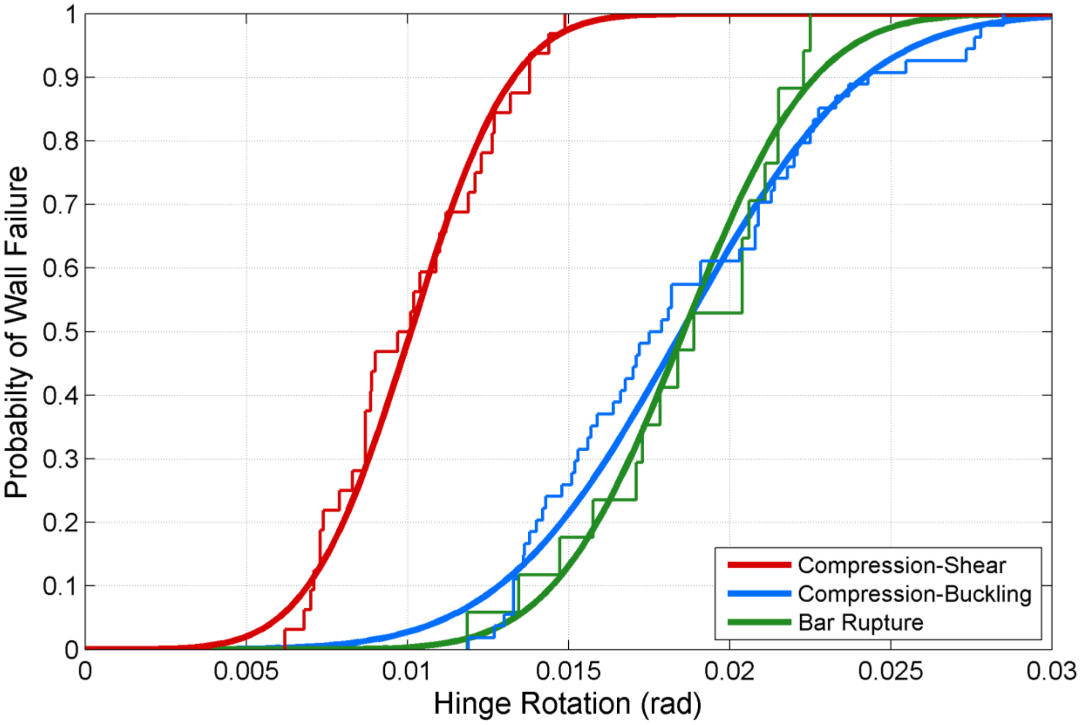

Figure 6.24 – Fragility Curves for Different Failure Modes, Hinge Rotation

6.4 CONCLUSIONS

PSRP analysis predicts larger tensile strains at failure than is observed in non-linear analysis, and accuracy in prediction of the neutral axis is impacted by the cross-sectional aspect ratio. The lack of accuracy in prediction of the neutral axis means that current design criteria for walls are more conservative for specimens of low CSAR than high CSAR.

It is possible to prevent CS failure in walls subjected to shear demands that exceed the limits specified in Chapter 5. The critical issue in development of CS failure is crushing at the web/boundary element interface, and moving this interface away from critical behavior (i.e., outside the region subjected to compression) allows for prevention of CS failure at greater shear demands than are possible with the current ACI 318-14 boundary element length requirement.

There are two basic design guidelines for prevention of CS failure based on the findings of this chapter.

1. Design planar shear walls to be subjected to peak shear stresses less than $7.0\sqrt{f'c}$ psi ($0.58\sqrt{f'c}$ MPa).
2. Confine the full length of the compression region.

7 SUMMARY, CONCLUSIONS, AND RECOMMENDATIONS FOR FUTURE WORK

Currently, within the structural engineering community, there is the expectation that Code-based design of slender concrete walls will result is a ductile tension-controlled flexural failure. However, damage to walls observed following recent earthquakes and observed in the laboratory indicates that compression failures are likely and that damage may extend into the web of the wall beyond the highly stress flexural compression zone of the wall. Additionally, review of existing experimental data suggests that shear demand, axial load and cross-sectional configuration affect flexural response and the deformation capacity of flexural walls. Comprehensive laboratory investigation of these parameters and their impact on the behavior of flexural walls is not feasible due to cost and the limitations of testing laboratories. Thus, a numerical investigation was conducted.

The research presented here uses a validated, high-resolution finite element model to extend the experimental data set and study the impact of shear stress demand, cross-sectional aspect ratio and axial load ratio on flexural wall failure modes and deformation capacity. To that end, the primary objectives of the research presented in this thesis were:

1. To develop a nonlinear three-dimensional finite element (FE) model capable of predicting the stiffness, strength, deformation capacity, and failure mode of wall test specimens that yield in flexure prior to failure.
2. To use this model to determine the influence of untested parameters on walls expected to respond primarily in flexure, including cross-sectionally slender walls, walls with high shear stress demand and walls with high axial load ratios.
3. To provide design recommendations that inhibit undesirable failure modes and maximize the deformation capacity of walls.

7.1 RESEARCH SUMMARY

7.1.1 Model Development and Evaluation

Two FE programs, Abaqus (www.3ds.com) and ATENA (www.cervenka.cz), were considered for use in this research study. Both were evaluated with respect to accuracy and numerical robustness with which the nonlinear response of reinforced concrete components was simulated. Analyses of concrete walls conducted using Abaqus were found to be computationally expensive and did not exhibit numerical stability beyond the point of specimen yield. While ATENA models were not successfully run using cyclic loading protocols, using ATENA it was possible to accurately simulate the response envelope for cyclically loaded walls through to failure. Thus, ATENA was selected as the software package to be used in this research.

Using a database of 23 experimental tests of flexural walls, a modelling approach in ATENA was developed and calibrated. Model development determined appropriate levels of mesh refinement, the extent to which reinforcing steel could be modeled as smeared versus discrete reinforcement, impact of using a symmetric boundary condition, etc.; this development process was accomplished by comparing simulated and measured response for laboratory test specimens. As 65% of the database walls failed due to concrete crushing, the concrete material parameters were critical to the accuracy of the simulations. For most concrete model parameters, the calibration process consisted of validating recommended default values. However, concrete deformation capacity in compression was calibrated to provide accurate simulation of the measured deformation capacity of compression-controlled flexural walls tested in the laboratory; the calibrated value resulted in a concrete crushing energy that fell within the range of values determined by Jansen and Shah (114 to 171 lb/in (20-30 N/mm)) from laboratory tests of plain concrete cylinders. Deformation predictions for BR failures were based on a calibrated buckle/rupture model.

The model simulates well the envelope to the cyclic response curve, including failure, for wall test specimens exhibiting both bar rupture and compression-buckling failure modes. Specimen strength is simulated accurately and precisely for BR and CB failures (average ratio of simulated to measured strength of 0.99 with a COV of 0.05). Deformation capacity is also modeled accurately and precisely for both failure modes (average ratio of simulated to measured deformation capacity of 0.98 with a COV of 0.06). The ATENA model typically simulates an initial stiffness that is greater than that measured in the laboratory (average ratio of simulated to measured secant stiffness to yield of 0.91 with a COV of 0.29). This is attributed to the fact that the ATENA model does not simulate initial cracking due to shrinkage and temperature; this could be incorporated into the model to achieve improved accuracy.

7.1.2 Numerical Investigation of Wall Behavior and Failure Modes

The simulated failure modes were identified and quantified using five reference walls that spanned the dataset in the key study parameters The analyses presented in this chapter show that Specimen S6 exhibited behavior not adequately explained by either the CB or BR failure designations, with shear playing a significant role in the compression failure that resulted in an early loss of load-carrying capacity. This behavior was defined as a compression-shear (CS) failure.

7.1.3 Parameter Study to Investigate Impact of Design Parameters on Failure Mode

An extensive study was conducted with the main intent of studying the impact of CSAR and peak normalized shear stress demand. This study used several base specimens to provide a range of different specimen geometries (i.e., CSAR) and varied design parameters to achieve different shear demands. The primary parameters varied were the axial load ratio and shear span, with the longitudinal reinforcement ratio varied for a smaller selection of models. The results indicate that the compressive failure modes were affected by the CSAR and normalized shear stress demand, with a change in location of compression failure for these walls leading to reduced drift capacity; specifically, higher shear demands result in simultaneous concrete crushing across the length of the boundary element rather than concentrated crushing in the boundary element core. High-CSAR walls (i.e., CSAR = 20) with peak shear stresses above $5\sqrt{f'c}$ psi ($0.42\sqrt{f'c}$ MPa) exhibited the lowest drift capacity.

7.1.4 Design To Prevent CS Failure

Currently, ACI 318-14 requires that walls in regions of high seismicity with large flexural compression demand include special boundary elements with heavy confining reinforcement. These special boundary elements must extent from the extreme compression fiber of the wall into wall depth a distance equal to the greater of 1) half the neutral axis depth or 2) the neutral axis depth less 10% of the wall length. Thus, current ACI Code requirements result in confinement of only a portion of the concrete compression zone. Given the potential for concrete crushing to initiate at the web-boundary element interface, the parameter study of Chapter 5 was extended to include boundary element length as a study parameter. This enabled an investigation of the relationship between the boundary element confinement length and failure mode.

7.2 CONCLUSIONS

7.2.1 Modeling Flexural Walls.

The ATENA model provided accurate simulation of stiffness, strength, and deformation capacity for walls spanning key study parameters and all failure modes. Key model attributes used to achieve this were:

1. Mesh scheme: designed such that the critical compressive region is finely meshed, with coarser meshes used at higher sections of the wall. Contact surfaces were defined between the different meshed regions to ensure compatibility.
2. Smeared reinforcement: all concrete elements in the wall contained an amount of smeared reinforcement. The lack of plain concrete elements reduced issues with numerical stability.

Concrete material model parameters calibrated to achieve accurate prediction of measured behavior were:

1. Compressive plastic deformation capacity: calibrated to provide accurate simulation of the drift capacity of wall test specimens exhibiting crushing failure in the laboratory. The calibrated value is consistent with previous research by Janssen and Shah ().
2. Compression yield surface dilation parameter: calibrated both to match experimental data and to provide numerical stability in the model.
3. Shear retention factor: calibrated for model stability and to avoid sliding failures not observed experimentally.
4. Tension stiffening: calibrated to provide numerical stability while not significantly affective simulation results.

7.2.2 Failure Modes for Flexural Walls

1. Flexural walls were observed to simulate three failure mechanisms
    a. Buckling-rupture (BR) failure, characterized by the longitudinal boundary element reinforcement reaching the buckle/rupture limit prior to crushing of the boundary element core concrete. There is limited shear influence.
    b. Compression-buckling (CB) failure, characterized by concrete crushing in the boundary element core occurring prior to the longitudinal reinforcement reaching the buckle/rupture limit. There may be significant diagonal shear stresses, but CB failures do not exhibit significant strength loss due to shear demand prior to crushing of the boundary element core. The primary shear strut terminates in the boundary element well above the critical section, resulting in high vertical stresses in the boundary element core but lesser minimum principal stresses (i.e., the interaction of shear and vertical stresses) at the web/boundary element interface. Crushing first occurs at the outermost fiber of the boundary element and progresses through the boundary element core and toward the web/boundary element interface. With adequate confining reinforcement, the wall maintains lateral-load carrying capacity as the neutral axis progresses toward the web/boundary element interface. This allows for greater plastic deformation than is observed in CS failures.
    c. Compression-shear (CS) failure, characterized by concrete crushing across the length of the boundary element occurring prior to the longitudinal reinforcement reaching the buckle/rupture limit defined in Section 3.4. There are significant diagonal shear stresses and the primary shear strut causes the loss of strength near the web/boundary element interface. This results in the formation of a second shear strut below the original diagonal

shear transfer, leading to the development of larger shear stresses across a greater portion of the web/boundary element interface. Initial crushing occurs at both the web/boundary element interface and the outermost fiber of the boundary element core, and the specimen loses lateral-load carrying capacity as crushing occurs across the length of the boundary element. Significant minimum principal strains are present across the length of the boundary element and into the web.

2. The deformation capacity exhibited by BR and CB failures is significantly greater than that exhibited by CS failures. Approximately the same deformation capacity is achieved by walls exhibiting BR and CB failures, and the design of walls exhibiting BR and CB failures is approximately the same. Increasing axial load ratio influences the transition from BR to CB failure.
3. The two parameters most influential in compression-shear failure are the shear demand and cross-sectional aspect ratio. Walls with a CSAR greater than 10 (“thin” walls) are subject to compression-shear failures at relatively low shear demands, if designed in accordance with current ACI Code requirements. In walls with a slender cross-section and moderate-to-high levels of peak shear stress (i.e., greater than $5\sqrt{f'c}$ psi ($0.42\sqrt{f'c}$ MPa)).
4. Planar walls develop vertical strain profiles that differ from the linear, plane-sections-remain plane (PSRP) profile typical employed for design and analysis. There is a nearly flat tensile strain response observed in most of the walls in this study, and the non-linearity of this strain distribution is exacerbated by CSAR and shear demand. This changes the local deformation demands and shows that PSRP assumptions are inaccurate for modern wall designs. PSRP-based design that intends for wall response to be dominated by the tensile response of the longitudinal reinforcement overestimates the strain in the tensile reinforcement, resulting in behavior that is highly influenced by concrete crushing.

Design Recommendations

1. *Design planar shear walls to be subjected to peak shear stresses less than* $7.0\sqrt{f'c}$ *psi* ($0.58\sqrt{f'c}$ *MPa).* High-CSAR walls exhibit CS failures above shear stresses of $5\sqrt{f'c}$ psi ($0.42\sqrt{f'c}$ MPa) when designed to current ACI Code requirements for the boundary element length. Even with extended boundary element reinforcement, CS failures develop at shear stresses greater than $7\sqrt{f'c}$ psi ($0.58\sqrt{f'c}$ MPa).
2. *Confine the full length of the compression region in walls subjected to peak shear stress demands greater than* $5\sqrt{f'c}$ *psi* ($0.42\sqrt{f'c}$ *MPa).* It is possible to improve behavior by suppressing a CS failure through the extension of the length of the well-confined boundary element region. Current ACI 318-14 requirements on confined length are inadequate and do not consider the length of the confined region relative to the neutral axis to be a significant factor in design.

7.3 FUTURE WORK

The following items were not studied in this research but are promising areas of future work.

- Uniformly-Distributed Reinforcement: There is promise shown in the vertical strain distributions of walls with uniformly-distributed longitudinal reinforcement. Walls designed with heavily-reinforced boundary elements and lightly-reinforced web regions have highly non-uniform vertical stiffness, which results in the non-linearity of the vertical strain distribution; however, the uniform stiffness of a uniformly-distributed wall allows for a more linear distribution. Limited studies conducted with more uniformly-distributed reinforcement configurations showed promise in (1) developing a vertical strain distribution closer to that assumed in a plane section analysis and (2) helping avoid the development of compression-shear failure.

- Non-Planar Walls: Modern design practice relies heavily on non-planar shear walls. These walls should be assessed in a similar fashion to the analysis of planar walls in this thesis. Many of the biggest issues in planar walls (e.g. stress gradient between web and boundary element) are likely even more significant in non-planar wall designs.
- Cyclic loading: Cyclic loading was not achieved in this study. The impact of load protocol is of interest and would add further depth to the understanding of wall behavior. This study would necessitate a concrete constitutive model capable numerical stability when subjected to cyclic loading.
- Axial load ratios exceeding 30%: Axial loads over 20% were not considered in this study. High-ALR walls may result in different wall behavior than is observed with ALRs less than 20%. The failure mode and deformation capacity of these walls is worth further investigation. Because many walls are coupled and coupling results in a wall pier with a high axial load
- Impact of concrete strength: The concrete strength was not varied in this study and there is limited experimental data available for walls built with high-strength concrete. This is particularly relevant as high-strength concrete is being used more commonly in practice.

BR failure development (low shear demand at low CSAR): Numerical stability issues at low axial loads made it difficult to study bar rupture failures to the same degree as the compression failures. There are a lack of models run at low ALRs and shear demands for walls, and particularly low-CSAR walls. It is possible to better understand the development, behavior, and deformation capacity of BR failures across a range of CSARs.

REFERENCES

ACI Committee 318, and American Concrete Institute. 2011. Building Code Requirements for Structural Concrete (ACI 318-11) and Commentary. Farmington Hills, MI: American Concrete Institute.

ACI Committee 318, and American Concrete Institute. 2014. Building Code Requirements for Structural Concrete (ACI 318-14): An ACI Standard : Commentary on Building Code Requirements for Structural Concrete (ACI 318R-14), an ACI Report.

ATC-58, 2012. *Seismic Performance Assessment of Buildings, Volume 1 – Methodology (FEMA P-58-1),* Prepared by the Applied Technology Council for the Federal Emergency Management Agency.

Berry, Matt, Dawn Lehman, and Laura Lowes. 2008. "Lumped-Plasticity Models for Performance Simulation of Bridge Columns." ACI Structural Journal 105 (3). doi:10.14359/19786.

Birely, Anna. 2012. "Seismic Performance of Slender Reinforced Concrete Walls." Ph.D. dissertation, Seattle, WA: Dept. of Civil and Environmental Engineering, University of Washington.

Birely, Anna, Laura Lowes, and Dawn Lehman. 2011. "Investigation of Performance of Slencer RC Structural Walls." Database report. Department of Civil and Environmental Engineering: University of Washington.

CEB-FIP Model Code 1990:: Contribution a La 27e Session Pleniere Du CEB, Paris, Septembre 1990. [3]: Addendum. 1990. CEB Bulletin D'information 198. Lausanne: Comite Euro-International du Beton.

Červenka, Jan, and Vassilis K. Papanikolaou. 2008. "Three Dimensional Combined Fracture–plastic Material Model for Concrete." International Journal of Plasticity 24 (12): 2192–2220. doi:10.1016/j.ijplas.2008.01.004.

Červenka, Vladimir. 1985. "Constitutive Model for Cracked Reinforced Concrete." ACI Journal Proceedings 82 (6). doi:10.14359/10409.

Červenka, Vladimir, Jan Červenka, and Radomir Pukl. 2002. "ATENA — A Tool for Engineering Analysis of Fracture in Concrete." Sadhana 27 (4): 485–92. doi:10.1007/BF02706996.

Červenka, Vladimir, Libor Jendele, and Jan Cervenka. 2013. "ATENA Program Documentation: Part 1 Theory." Cervenka Consulting, Prague, Czech Republic.

Červenka, Vladimír, and Radomír Pukl. 1992. "Computer Models of Concrete Structures." Structural Engineering International 2 (2): 103–7. doi:10.2749/101686692780615905.

Coleman, J, and Enrico Spacone. 2001. “Localization Issues in Force-Based Frame Elements.” Journal of Structural Engineering 127 (11): 1257–65. doi:10.1061/(ASCE)0733-9445(2001)127:11(1257).

Comite Europeen De Normalization. 2014. Eurocode 2 : Design of Concrete Structures.

Dazio, Alessandro, Katrin Beyer, and Hugo Bachmann. 2009. “Quasi-Static Cyclic Tests and Plastic Hinge Analysis of RC Structural Walls.” Engineering Structures 31 (7): 1556–71. doi:10.1016/j.engstruct.2009.02.018.

De Borst, R. 1986. “Non-Linear Analysis of Frictional Materials.” Ph.D. thesis, The Netherlands: Delft University of Technology.

Hordijk, D.A. 1991. “Local Approach to Fatigue of Concrete.” Ph.D. thesis, The Netherlands: Delft University of Technology.

Jansen, Daniel C., and Surendra P. Shah. 1997. “Effect of Length on Compressive Strain Softening of Concrete.” Journal of Engineering Mechanics 123 (1): 25–35. doi:10.1061/(ASCE)0733-9399(1997)123:1(25).

Kupfer, H, H.K. Hilsdorf, and H Rusch. 1969. “Behavior of Concrete Under Biaxial Stresses.” ACI Journal Proceedings 66 (8). doi:10.14359/7388.

Liu, H. 2004. “Effect of Concrete Strength on the Response of Ductile Shear Walls.” MS thesis, Montreal, QB: Dept. of Civil Engineering and Applied Mechanics, McGill University.

Menetrey, P., and William, K.J. 1995. “Triaxial Failure Criterion for Concrete and Its Generalization.” ACI Structural Journal 92 (3). doi:10.14359/1132.

Menegotto, M., and E. Pinto. 1973. Method of Analysis for Cyclically Loaded Reinforced Concrete Plane Frames Including Changes in Geometry and Non-Elastic Behavior of Elements Under Combined Normal Force and Bending, *Proceedings, IABSE Symposium on Resistance and Ultimate Deformability of Structures Acted on by Well-Defined Repeated Loads*, Lisbon.

Moehle, J. 2011. “February 27, 2010 Chile Earthquake Reconnaissance Team Investigation: Reinforced Concrete Buildings.” Powerpoint presentation.

NIST, 2013. “Recommendations for Seismic Design of Reinforced Concrete Wall Buildings Based on Studies of the 2010 Chile Earthquake,” NEHRP Consultants Joint Venture for the National Institute of Standards and Technology, Gaithersburg, MD, Tech. Rep. No. GCR 13-917-25.

Oesterle, R., A. Aristizabal-Ochoa, J. Carpenter, H. Russell, and W. Corley. 1976. “Earthquake resistant structural walls - tests of isolated walls,” Portland Cement Association/National Science Foundation, Washington, D.C., Tech. Rep. No. NSF/RA-760815.

Oh, Young-Hun, Sang Whan Han, and Li-Hyung Lee. 2002. “Effect of Boundary Element Details on the Seismic Deformation Capacity of Structural Walls.” Earthquake Engineering & Structural Dynamics 31 (8): 1583–1602. doi:10.1002/eqe.177.

Orakcal, Kutay, and John Wallace. 2006. “Flexural Modeling of Reinforced Concrete Walls - Experimental Verification.” ACI Structural Journal 103 (2). doi:10.14359/15177.

Palermo, Dan, and Frank J. Vecchio. 2007. “Simulation of Cyclically Loaded Concrete Structures Based on the Finite-Element Method.” Journal of Structural Engineering 133 (5): 728–38. doi:10.1061/(ASCE)0733-9445(2007)133:5(728).

Pugh, Josh. 2012. “Numerical Simulation of Walls and Seismic Design Recommendations for Walled Buildings.” Ph.D. dissertation, Seattle, WA: Dept. of Civil and Environmental Engineering, University of Washington.

Stevens, N.J., M. Uzumeri, and M.P. Collins. 1991. “Reinforced Concrete Subjected to Reversed Cyclic Shear--Experiments and Constitutive Model.” ACI Structural Journal 88 (2). doi:10.14359/2880.

Tran, Thien Anh. 2012. “Experimental and Analytical Studies of Moderate Aspect Ratio Reinforced Concrete Structural Walls.” Ph.D. dissertation, Los Angeles, CA: Dept. of Civil and Environmental Engineering, University of California, Los Angeles.

Vallenas, J., B. V.V., and E. Popov. 1979. “Hysteretic behavior of reinforced concrete structural walls,” Earthquake Engineering Research Center, Berkeley, CA, Tech. Rep. No. UCB/EERC-79/20.

Vecchio, F.J., and M. Nieto. 1991. “Shear-Friction Tests on Reinforced Concrete Panels.” ACI Structural Journal 88 (3). doi:10.14359/3132.

Vecchio, Frank, and Collins. 1986. “The Modified Compression-Field Theory for Reinforced Concrete Elements Subjected to Shear.” ACI Journal Proceedings 83 (2). doi:10.14359/10416.

Vos, E., and H. W. Reinhardt. 1982. “Influence of Loading Rate on Bond Behaviour of Reinforcing Steel and Prestressing Strands.” Matériaux et Constructions 15 (1): 3–10. doi:10.1007/BF02473553.

Wallace, John W. 2012. “Behavior, Design, and Modeling of Structural Walls and Coupling Beams — Lessons from Recent Laboratory Tests and Earthquakes.” International Journal of Concrete Structures and Materials 6 (1): 3–18. doi:10.1007/s40069-012-0001-4.

Wallace, John W., and John H. Thomsen IV. 1995. “Seismic Design of RC Structural Walls. Part II: Applications.” Journal of Structural Engineering 121 (1): 88–101. doi:10.1061/(ASCE)0733-9445(1995)121:1(88).

Welt, Travis. 2015. “Detailing for Compression in Reinforced Concrete Wall Boundary Elements: Experiments, Simulations, and Design Recommendations.” Ph.D. dissertation, Urbana-Champaign, IL: Dept. of Civil and Environmental Engineering, University of Illinois.

Appendix A WALL DATA AND RESULTS

This appendix will detail the parameter inputs, response quantities, and load-displacement figures for all specimens simulated in this study.

Experimental Specimens

Specimens PW1-PW3 from Birely (2012) were not included in the main data set as they included lap splices at a critical wall section. This experimental program was designed to evaluate the performance of typical wall designs representative of modern mid-rise buildings located on the west coast of the United States. The main parameters varied were the shear span and concentration of steel in the boundary element. The tests also studied the impact of lap splices on wall response. These specimens were modeled using typical parameters and exhibited stable behavior.

Tables A.1-A.8 present the data necessary to fully define and evaluate numerical models for all walls in the database. Statistics for all parameters are also included.

Parameters listed in the tables below are defined as follows:

- l_w = horizontal length of wall parallel to web.
- t_w = wall thickness.
- h = specimen height.
- h_{eff} = effective loading height.
- CSAR = cross-sectional aspect ratio.
- Shear Span = $h_{eff}/l_{w.}$
- ALR = axial load ratio.
- V_{max} = maximum base shear resisted by the wall.
- V_n = Nominal shear strength of the wall per ACI 318-14. Calculated using reported material strengths.
- Δ_{ult} = specimen drift capacity. Defined as the drift at which the lateral load-carrying capacity of the wall dropped to 80% of the historic maximum.
- f'_c = compressive concrete strength.
- $f_{y,BE}$ = yield strength of longitudinal boundary element reinforcing steel.
- $E_{s,BE}$ = Elastic modulus of longitudinal boundary element reinforcing steel.
- $f_{u,BE}$ = ultimate strength of longitudinal boundary element reinforcing steel.
- $\varepsilon_{u,BE}$ = rupture strain of longitudinal boundary element reinforcing steel.
- $f_{y,v}$ = yield strength of longitudinal web reinforcing steel.
- $E_{s,v}$ = Elastic modulus of longitudinal web reinforcing steel.
- $f_{u,v}$ = ultimate strength of longitudinal web reinforcing steel.
- $\varepsilon_{u,v}$ = rupture strain of longitudinal web reinforcing steel.
- $\rho_{vert,BE}$ = longitudinal reinforcement ratio for wall end region.
- $\rho_{vert,web}$ = longitudinal reinforcement ratio for wall web.
- ρ_{gross} = total gross longitudinal reinforcement ratio.
- $\rho_{t,web}$ = transverse reinforcement ratio for wall web.
- ρ_{vol} = volumetric reinforcement ratio for wall end region.
- $\rho_{vert,BE}$ = longitudinal reinforcement ratio for wall end region.

- h_x = horizontal spacing of vertical reinforcement for wall end region.
- s_{vert} = longitudinal spacing of confining reinforcement for wall end region.
- d_b = diameter of longitudinal reinforcement for wall end region.
- ACI BE = classification of boundary element confinement per ACI 318-14 (i.e., NBE, OBE, SBE).

Table A.1 – Geometry and Loading Information for Experimental Wall Database

Specimen	Author	Geometry					Loading	
		l_w	t	h	h_{eff}	CSAR	Shear Span	ALR
		in.	in.	in.	in.	--	--	%
WSH1	Dazio, et al.	78.7	5.91	158.7	179.5	13.3	2.28	5.5
WSH2	Dazio, et al.	78.7	5.91	158.7	179.5	13.3	2.28	6.3
WSH3	Dazio, et al.	78.7	5.91	158.7	179.5	13.3	2.28	6.4
WSH4	Dazio, et al.	78.7	5.91	158.7	179.5	13.3	2.28	6.3
WSH5	Dazio, et al.	78.7	5.91	158.7	179.5	13.3	2.28	13.7
WSH6	Dazio, et al.	78.7	5.91	158.7	177.9	13.3	2.26	11.4
W1	Liu	47.2	7.78	147.6	147.6	6.0	3.13	7.6
W2	Liu	47.2	7.78	147.6	147.6	6.0	3.13	3.5
PW1	Birely	120	6	144	340.8	20.0	2.84	9.9
PW2	Birely	120	6	144	249.6	20.0	2.08	13.3
PW3	Birely	120	6	144	240	20.0	2.00	10.4
PW4	Birely	120	6	144	240	20.0	2.00	12.2
RW1	Thomsen, et. al	48	4	144	150	12.0	3.13	10.5
RW2	Thomsen, et. al	48	4	144	150	12.0	3.13	9.2
S5	Vallenas, et al.	95	4.49	120	151.6	21.1	1.60	4.8
S6	Vallenas, et al.	95	4.49	120	151.6	21.1	1.60	4.8
WR20	Oh, et al.	59.1	7.87	78.7	118.1	7.5	2.00	10.4
WR10	Oh, et al.	59.1	7.87	78.7	118.1	7.5	2.00	9.8
WR0	Oh, et al.	59.1	7.87	78.7	118.1	7.5	2.00	10.8
R1	Oesterle, et al.	75	4	176	180	18.8	2.40	0.0
R2	Oesterle, et al.	75	4	176	180	18.8	2.40	0.0
RW-A20-P10-S38	Tran	48	6	96	96	8.0	2.00	7.3
RW-A20-P10-S63	Tran	48	6	96	96	8.0	2.00	7.3
RW-A15-P10-S51	Tran	48	6	72	72	8.0	1.50	7.7
RW-A15-P10-S78	Tran	48	6	72	72	8.0	1.50	6.4
RW-A15-P2.5-S64	Tran	48	6	72	72	8.0	1.50	1.6

Table A.2 – Geometry and Loading Statistics for Experimental Wall Database

	CSAR	**Shear Span**	**ALR**
	--	--	%
Mean	13.0	2.22	7.6
Std. Deviation	5.3	0.51	3.7
COV	0.41	0.23	0.49

Table A.3 – Materials Information for Experimental Wall Database

Specimen	**Materials**								
	f'_c	$f_{y,be}$	$E_{s,be}$	$f_{u,be}$	$\varepsilon_{u,be}$	$f_{y,v}$	$E_{s,v}$	$f_{u,v}$	$\varepsilon_{u,v}$
	psi	ksi	ksi	ksi	in/in	ksi	ksi	ksi	in/in
WSH1	6526	79.4	29000	89.9	0.05	84.6	29000	87.1	0.02
WSH2	5874	84.6	29000	108.4	0.08	70.3	29000	77.5	0.06
WSH3	5685	87.2	29000	105.2	0.08	82.6	29000	101.6	0.07
WSH4	5932	83.5	29000	97.9	0.07	84.7	29000	103.6	0.08
WSH5	5555	84.7	29000	103.6	0.08	75.3	29000	81.0	0.05
WSH6	6613	83.5	29000	97.9	0.07	84.7	29000	103.6	0.08
W1	4801	66.4	29000	91.4	0.18	67.4	29000	84.2	0.17
W2	10245	66.4	29000	91.4	0.18	67.4	29000	84.2	0.17
PW1	5231	84.0	29000	100.8	0.12	75.7	29000	77.0	0.06
PW2	5843	84.0	29000	100.8	0.12	75.7	29000	77.0	0.06
PW3	4980	51.3	29000	77.9	0.20	51.3	29000	77.9	0.20
PW4	4272	67.1	29000	109.5	0.12	75.7	29000	77.0	0.06
RW1	4580	63.0	29000	93.0	0.10	65.0	29000	85.0	0.08
RW2	4925	63.0	29000	93.0	0.10	65.0	29000	85.0	0.08
S5	5004	69.9	29000	99.6	0.15	73.5	29000	105.9	0.12
S6	5033	69.9	29000	99.6	0.15	73.5	29000	105.9	0.12
WR20	4960	65.1	29000	89.5	0.15	49.6	29000	64.5	0.18
WR10	5250	65.1	29000	89.5	0.15	49.6	29000	64.5	0.18
WR0	4772	65.1	29000	89.5	0.15	49.6	29000	64.5	0.18
R1	6490	74.2	29000	111.0	0.18	75.7	29000	101.5	0.18
R2	6735	65.3	29000	102.7	0.18	77.6	29000	100.2	0.18
RW-A20-P10-S38	6830	68.4	29000	88.9	0.19	61.4	29000	71.3	0.07
RW-A20-P10-S63	7050	68.4	29000	88.9	0.19	61.4	29000	71.3	0.07
RW-A15-P10-S51	7070	68.4	29000	88.9	0.19	61.4	29000	71.3	0.07
RW-A15-P10-S78	8090	68.4	29000	88.9	0.19	61.4	29000	71.3	0.07
RW-A15-P2.5-S64	8340	68.4	29000	88.9	0.19	61.4	29000	71.3	0.07

Table A.4 – Materials Statistics for Experimental Wall Database

	f'_c	$f_{y,be}$	$E_{s,be}$	$f_{u,be}$	$\varepsilon_{u,be}$	$f_{y,v}$	$E_{s,v}$	$f_{u,v}$	$\varepsilon_{u,v}$
	psi	ksi	ksi	ksi	in/in	ksi	ksi	ksi	in/in
Mean	6026	17.7	29000	95.6	0.14	68.5	29000	89.3	0.11
Std. Deviation	1369	9.2	0.0	8.1	0.05	11.0	0.0	13.8	0.05
COV	0.23	0.13	0.00	0.34	0.34	0.16	0.00	0.17	0.52

Table A.5 – Geometry and Loading Information for Experimental Wall Database

	Flexural Data				**Shear Data**				**Drift Data**		
Specimen	**My**	M_n	$M_{b,max}$	M_b/M_n	V_n	$V_{b,max}$	$V_{max}/A_{cv}f'^{0.5}_c$	V_b/V_n	**Δy**	**Δu**	**FM**
	k-ft	k-ft	k-ft	--	kips	kips	psi	--	%	%	--
WSH1	930	1100	1130	1.03	173.5	75.5	2.01	0.44	0.24	1.04	BR
WSH2	960	1085	1210	1.12	153.0	80.9	2.27	0.53	0.27	1.75	BR
WSH3	1140	1390	1530	1.10	152.6	102.4	2.92	0.67	0.32	2.07	BR
WSH4	1130	1400	1480	1.06	159.2	99.2	2.77	0.62	0.29	1.6	CB
WSH5	1210	1350	1460	1.08	156.9	97.4	2.81	0.62	0.2	1.52	BR
WSH6	1530	1810	2010	1.11	163.2	135.4	3.58	0.83	0.31	2.04	CB
W1	615	740	725	0.98	149.9	58.8	2.31	0.39	0.64	2.98	CB
W2	650	790	765	0.97	190.7	62.1	1.67	0.33	0.55	2.91	BR
PW1	4260	4930	5190	1.22	256.8	182.8	3.51	0.71	0.38	1.53	BR
PW2	4880	5590	6080	1.25	262.7	292.2	5.31	1.11	0.45	1.5	CB
PW3	2960	3880	4480	1.51	254.2	224.1	4.41	0.88	0.24	1.22	CB
PW4	3660	4290	4360	1.19	246.7	217.9	4.63	0.88	0.4	1.01	CB
RW1	330	390	420	1.07	67.2	33.4	2.57	0.5	0.48	2.26	BR
RW2	330	385	450	1.16	68.1	35.7	2.65	0.52	0.55	2.35	CB
S5	1880	2200	2600	1.18	232.8	205.5	6.81	0.88	0.31	1.47	CB
S6	1880	2200	2450	1.12	233.0	194.3	6.42	0.83	0.32	1.65	CB
WR20	790	875	970	1.11	130.1	98.3	3	0.76	0.35	2.82	CB
WR10	795	880	950	1.08	150.5	96.7	2.87	0.64	0.47	2.82	CB
WR0	790	870	940	1.08	128.9	95.4	2.97	0.74	0.52	2.14	CB
R1	295	350	410	1.17	118.7	27.5	1.1	0.23	0.17	2.52	BR
R2	510	615	755	1.23	121.4	50.4	2	0.42	0.33	3.25	BR
RW-A20-P10-S38	680	760	960	1.26	108.3	108.0	4.5	1.00	0.55	3.14	CB
RW-A20-P10-S63	1135	1240	1400	1.13	159.8	166.9	6.9	1.04	0.66	3.00	CB
RW-A15-P10-S51	710	710	810	1.14	144.5	135.5	5.6	0.94	0.56	3.31	CB
RW-A15-P10-S78	1045	1090	1160	1.07	206.8	193.2	7.5	0.93	0.67	3.00	CB
RW-A15-P25-S64	845	725	715	0.99	186.8	150.6	5.7	0.81	0.61	3.00	CB

Table A.6 – Geometry and Loading Statistics for Experimental Wall Database

	M_b/M_n	$V_{max}/A_{cv}f'_c{}^{0.5}$	V_b/V_n	Δy	Δu
	--	psi	--	%	%
Mean	1.13	3.80	0.70	0.42	2.23
Std. Deviation	0.11	1.79	0.23	0.15	0.74
COV	0.09	0.47	0.33	0.36	0.33

Table A.7 – Geometry and Loading Information for Experimental Wall Database

Specimen	**Reinforcing Steel**					**Confinement**				
	$\rho_{vert,BE}$	$\rho_{vert,web}$	ρ_{gross}	$\rho_{t,web}$	ρ_{vol}	h_x	s_{vert}	s_{vert}/d_b	h_x/s	**ACI BE**
	%	%	%	%	%	in	in	--	--	--
WSH1	1.57	0.30	0.54	0.25	1.01	2.95	2.95	7.50	1.00	NBE
WSH2	1.57	0.30	0.54	0.25	1.01	2.95	2.95	7.50	1.00	NBE
WSH3	1.74	0.54	0.82	0.25	0.96	3.94	2.95	6.25	1.33	OBE
WSH4	1.74	0.54	0.82	0.25	0.00	--	--	--	--	NBE
WSH5	0.77	0.27	0.39	0.25	0.75	3.94	1.97	6.25	2.00	OBE
WSH6	1.74	0.54	0.56	0.25	1.44	3.94	1.97	6.25	2.00	NBE
W1	3.07	0.34	1.24	0.40	2.26	7.09	3.94	5.00	1.80	OBE
W2	3.07	0.34	1.24	0.47	2.26	7.09	3.94	5.00	1.80	NBE
PW1	3.50	0.28	1.32	0.28	1.24	3.00	2.00	4.00	1.50	SBE
PW2	3.50	0.28	1.32	0.28	1.24	3.00	2.00	4.00	1.50	SBE
PW3	1.86	1.57	1.69	0.28	1.37	3.00	1.75	3.50	1.71	SBE
PW4	3.50	0.28	1.32	0.28	1.24	3.00	2.00	4.00	1.50	SBE
RW1	2.95	0.33	1.12	0.33	0.78	2.00	3.00	8.00	0.67	NBE
RW2	2.95	0.33	1.12	0.33	1.17	6.00	2.00	5.33	3.00	NBE
S5	5.66	0.55	1.75	0.55	0.84	2.70	1.34	2.14	2.02	SBE
S6	5.66	0.55	1.75	0.55	0.84	2.70	1.34	2.14	2.02	SBE
WR20	1.27	0.32	0.67	0.28	1.43	3.94	7.87	15.38	0.50	NBE
WR10	1.27	0.32	0.67	0.36	2.85	3.94	3.94	7.69	1.00	OBE
WR0	1.27	0.32	0.67	0.28	0.00	--	--	--	--	NBE
R1	1.47	0.28	0.47	0.31	0.80	5.50	4.00	10.67	1.38	NBE
R2	4.00	0.28	0.96	0.31	4.41	2.75	1.33	2.66	2.07	SBE
RW-A20-P10-S38	3.23	0.27	1.29	0.27	2.23	2.00	2.00	4.00	1.00	SBE
RW-A20-P10-S63	7.11	0.61	2.84	0.61	2.23	2.00	2.00	2.67	1.00	SBE
RW-A15-P10-S51	3.23	0.32	1.32	0.32	2.23	2.00	2.00	4.00	1.00	SBE
RW-A15-P10-S78	6.06	0.73	2.56	0.73	2.23	2.00	2.00	2.67	1.00	SBE
RW-A15-P2.5-S64	6.06	0.61	2.48	0.61	2.23	2.00	2.00	4.00	1.00	SBE

Table A.8 – Geometry and Loading Statistics for Experimental Wall Database

	$\rho_{vert,BE}$	$\rho_{vert,web}$	ρ_{gross}	$\rho_{t,web}$	ρ_{vol}	s_{vert}/d_b	h_x/s
	%	%	%	%	%	--	--
Mean	3.07	0.44	1.21	0.36	1.50	5.4	1.4
Std. Deviation	1.77	0.27	0.66	0.14	0.94	3.0	0.6
COV	0.58	0.61	0.54	0.38	0.63	0.55	0.39

Listed below are all results for simulated ATENA models in this study. Table A.9 lists all simulated results for experimental specimens. Simulated results for parameter study designs are listed in Table A.10.

Table A.9 – List of Results for Simulated Response of Experimental Specimens

Specimen	**ALR**	**Shear Span**	**$V_{max}/A_{cv}f'_c{}^{0.5}$**	**V_b/V_n**	**Story Drift**	**Hinge Rotation**	**EI_{eff}/EI_g**	**Failure Mode**
	%	--	psi	--	%	rad	--	--
WSH2	6.3	2.28	2.22	0.52	1.75	0.0147	0.24	4
WSH3	6.4	2.28	2.85	0.60	2.07	0.0158	0.23	4
WSH4	6.3	2.28	2.85	0.60	1.76	0.0136	0.26	2
WSH5	13.7	2.28	2.79	0.61	1.52	0.0135	0.36	4
WSH6	11.4	2.28	3.55	0.77	2.00	0.0168	0.30	2
W1	7.6	3.12	2.41	0.41	2.87	0.0228	0.25	2
W2	3.5	3.12	1.74	0.34	2.91	0.0215	0.19	4
PW1	9.9	2.84	3.51	0.71	1.53	0.0119	0.45	4
PW2	13.3	2.08	5.15	1.08	1.61	0.0126	0.38	1
PW3	10.4	2.00	3.99	0.99	1.19	0.0100	0.33	2
PW4	12.2	2.00	5.01	1.15	1.82	0.0144	0.37	2
RW1	10.5	3.13	2.52	0.49	2.30	0.0179	0.25	4
RW2	9.2	3.13	2.41	0.48	2.18	0.0166	0.23	2
S6	4.8	1.60	6.27	0.80	1.58	0.0089	0.21	1
WR10	9.8	2.00	2.98	0.64	2.75	0.0255	0.27	2
WR0	10.8	2.00	3.09	0.73	2.11	0.0203	0.30	2
R1	0.0	2.40	1.05	0.21	2.47	0.0222	0.12	4
R2	0.0	2.40	1.89	0.38	3.21	0.0275	0.16	4
RW-A20-P10-S38	7.32	2.00	4.23	0.93	3.10	0.0278	0.33	2
RW-A20-P10-S63	7.29	2.00	6.73	1.02	3.27	0.0276	0.40	2
RW-A15-P10-S51	7.71	1.50	5.56	0.93	3.18	0.0273	0.27	2
RW-A15-P10-S78	6.40	1.50	7.85	0.98	2.76	0.0233	0.29	2

Table A.10 – Results for all Parameter Study Specimens

Specimen	ALR	Shear Span	$V_{max}/A_{cv}f'_c{}^{0.5}$	V_b/V_n	Story Drift	Hinge Rotation	EI_{eff}/EI_g	Failure Mode
	%	--	psi	--	%	rad	--	--
PW4-C20-1	5.0	1.50	5.37	0.88	1.19	0.0073	0.23	CS
PW4-C20-2	7.5	1.50	5.84	0.95	1.29	0.0083	0.25	CS
PW4-C20-3	10.0	1.50	6.23	0.88	1.14	0.0073	0.26	CS
PW4-C20-4	15.0	1.50	6.97	0.97	1.02	0.0068	0.29	CS
PW4-C20-5	5.0	2.25	3.83	0.74	2.19	0.0171	0.34	BR
PW4-C20-6	7.5	2.25	4.05	0.79	2.04	0.0157	0.37	CB
PW4-C20-7	10.0	2.25	4.28	0.83	1.95	0.0152	0.39	CB
PW4-C20-8	15.0	2.25	4.70	0.91	1.73	0.0133	0.43	CB
PW4-C20-9	5.5	3.00	2.83	0.46	2.07	0.0153	0.44	CB
PW4-C20-10	7.5	3.00	2.95	0.48	1.90	0.0148	0.47	CB
PW4-C20-11	15.0	3.00	3.46	0.67	1.94	0.0159	0.58	CB
PW4-C20-12	10.0	1.50	4.75	0.92	1.93	0.0138	0.24	CB
PW4-C20-13	10.0	1.50	5.52	0.91	1.55	0.0102	0.25	CS
PW16-C16-1	10.0	1.50	6.16	1.00	0.95	0.0062	0.32	CS
PW16-C16-2	9.0	2.00	4.67	0.91	1.70	0.0133	0.43	CB
PW16-C16-3	15.0	2.00	5.83	0.96	1.22	0.0097	0.51	CS
PW16-C16-4	15.0	2.00	6.07	1.00	1.11	0.0087	0.53	CS
PW16-C16-5	12.5	2.00	5.77	0.95	1.13	0.0087	0.51	CS
PW16-C16-6	10.0	2.00	5.20	0.86	1.17	0.0089	0.48	CS
RW1-C12-1	2.5	1.75	3.96	0.70	2.33	0.0204	0.24	BR
RW1-C12-2	5.0	1.75	4.29	0.75	2.36	0.0206	0.24	BR
RW1-C12-3	7.5	1.75	4.56	0.80	2.17	0.0189	0.26	BR
RW1-C12-4	10.0	1.75	4.84	0.85	2.07	0.0182	0.29	CB
RW1-C12-5	15.0	1.75	5.48	0.96	1.42	0.0127	0.32	CS
RW1-C12-6	2.5	2.50	2.57	0.50	1.98	0.0173	0.31	BR
RW1-C12-7	5.0	2.50	2.81	0.54	2.48	0.0223	0.34	BR
RW1-C12-8	7.5	2.50	2.99	0.58	2.43	0.0225	0.37	BR
RW1-C12-9	10.0	2.50	3.18	0.61	2.35	0.0214	0.40	CB
RW1-C12-10	15.0	2.50	3.53	0.68	1.78	0.0170	0.45	CB
RW1-C12-11	2.5	3.13	2.19	0.42	2.30	0.0215	0.35	BR
RW1-C12-12	5.0	3.13	2.34	0.45	2.30	0.0204	0.37	BR
RW1-C12-13	7.5	3.13	2.52	0.48	2.38	0.0211	0.43	BR
RW1-C12-14	10.0	3.13	2.70	0.52	2.23	0.0209	0.44	CB
RW1-C12-15	15.0	3.13	2.98	0.57	1.78	0.0171	0.51	CB
RW1-C12-16	2.5	1.75	4.66	0.82	2.08	0.0184	0.31	BR

Specimen	ALR	Shear Span	$V_{max}/A_{cv}f'_c{}^{0.5}$	V_b/V_n	Story Drift	Hinge Rotation	EI_{eff}/EI_g	Failure Mode
	%	--	psi	--	%	rad	--	--
RW1-C12-17	5.0	1.75	4.96	0.87	2.19	0.0191	0.28	CB
RW1-C12-18	7.5	1.75	5.28	0.93	2.08	0.0179	0.30	CB
RW1-C12-19	10.0	1.75	5.64	0.99	1.61	0.0138	0.32	CS
RW1-C12-20	15.0	1.75	6.32	0.96	1.28	0.0110	0.35	CS
RW10-C10-1	10.0	1.50	5.77	0.93	2.04	0.0175	0.25	CB
RW10-C10-2	12.5	1.50	6.15	0.99	2.00	0.0172	0.28	CB
RW10-C10-3	15.0	1.50	6.53	0.95	1.65	0.0143	0.33	CB
RW10-C10-4	10.0	2.00	4.37	0.84	2.44	0.0221	0.34	CB
RW10-C10-5	12.5	2.00	4.62	0.89	2.07	0.0191	0.37	CB
RW10-C10-6	15.0	2.00	4.90	0.94	1.94	0.0182	0.37	CB
RW10-C10-7	15.0	1.50	7.38	0.94	1.51	0.0121	0.30	CS
RW10-C10-8	15.0	1.50	8.18	0.98	1.53	0.0119	0.33	CS
RW10-C10-9	15.0	1.50	8.99	0.92	1.36	0.0101	0.31	CS
RW-C8-1	15.0	2.00	7.70	1.03	2.42	0.0218	0.46	CB
RW-C8-2	15.0	2.00	8.47	0.99	2.48	0.0225	0.48	CB
RW-C8-3	15.0	2.00	8.87	0.99	2.13	0.0181	0.50	CB
RW-C8-4	15.0	2.00	9.37	1.04	1.54	0.0123	0.51	CS
RW-C8-5	15.0	2.00	9.89	1.05	1.56	0.0071	0.55	CS
RW-C8-6	10.0	2.00	5.12	0.77	2.90	0.0285	0.35	CB
RW-C8-7	10.0	2.00	7.08	0.99	2.79	0.0237	0.42	CB
RW-C8-8	10.0	2.00	5.97	0.90	2.64	0.0243	0.37	CB
RW-C8-9	5.0	2.00	8.64	0.93	1.31	0.0079	0.48	CS
RW1-C12-BE-1	15.0	1.75	6.16	0.84	2.16	0.0208	0.42	CB
RW1-C12-BE-2	15.0	1.75	6.51	0.88	2.22	0.0209	0.38	CB
RW1-C12-BE-3	15.0	1.75	6.85	0.93	2.29	0.0213	0.38	CB
RW1-C12-BE-4	15.0	1.75	7.25	0.98	1.67	0.0149	0.38	CS
RW1-C12-BE-5	20.0	1.75	7.60	1.03	1.45	0.0132	0.40	CS
RW1-C12-BE-6	15.0	1.75	6.14	0.83	2.16	0.0208	0.36	CB
RW1-C12-BE-7	15.0	1.75	6.48	0.88	2.37	0.0226	0.34	CB
RW1-C12-BE-8	15.0	1.75	6.82	0.82	2.35	0.0220	0.38	CB
RW1-C12-BE-9	15.0	1.75	8.21	0.99	1.63	0.0138	0.41	CS
RW1-C12-BE-10	20.0	1.75	8.18	0.98	1.62	0.0144	0.41	CS
RW1-C12-BE-11	15.0	1.75	8.03	0.96	1.89	0.0164	0.41	CB
PW4-C20-BE-1	7.5	1.50	6.37	0.67	1.93	0.0142	0.26	CB
PW4-C20-BE-2	10.0	1.50	6.89	0.72	1.53	0.0112	0.28	CS
PW4-C20-BE-3	12.5	1.50	7.08	0.74	1.24	0.0090	0.29	CS
PW4-C20-BE-4	7.5	1.50	6.19	0.65	1.80	0.0136	0.29	CB

Specimen	ALR	Shear Span	$V_{max}/A_{cv}f'_c{}^{0.5}$	V_b/V_n	Story Drift	Hinge Rotation	EI_{eff}/EI_g	Failure Mode
	%	--	psi	--	%	rad	--	--
PW4-C20-BE-5	7.5	1.50	7.01	0.74	1.71	0.0119	0.25	CB
PW4-C20-BE-6	10.0	1.50	6.83	0.72	1.66	0.0127	0.27	CB
PW4-C20-BE-7	15.0	1.50	7.59	0.80	1.19	0.0087	0.31	CS
PW4-C20-BE-8	10.0	1.75	6.18	0.65	1.75	0.0130	0.33	CB
PW4-C20-BE-9	15.0	1.50	7.47	0.71	1.40	0.0104	0.30	CS
PW4-C20-BE-10	15.0	1.75	6.97	0.73	1.92	0.0140	0.37	CB
PW4-C20-BE-11	10.0	1.75	6.49	0.68	1.81	0.0134	0.34	CB
PW4-C20-BE-12	15.0	1.75	7.74	0.81	1.00	0.0070	0.40	CS
PW4-C20-BE-13	15.0	1.75	7.99	0.84	1.13	0.0074	0.41	CS
PW4-C20-BE-14	20.0	1.75	7.49	0.79	1.48	0.0109	0.40	CS
PW4-C20-BE-15	7.5	1.50	6.16	0.65	1.92	0.0151	0.25	CB
PW4-C20-BE-16	6.0	1.50	7.00	0.73	1.94	0.0133	0.34	CB
PW4-C20-BE-17	7.5	1.50	6.82	0.72	2.73	0.0156	0.27	CB

Experimental Load-Displacement Response

Figures A.1-A.22 present the measured and simulated responses for all modeled experimental specimens. This set includes Specimens PW1-PW3, which were not included in Chapter 3. These figures are identical to the example figures detailed in Section 3.7.1.

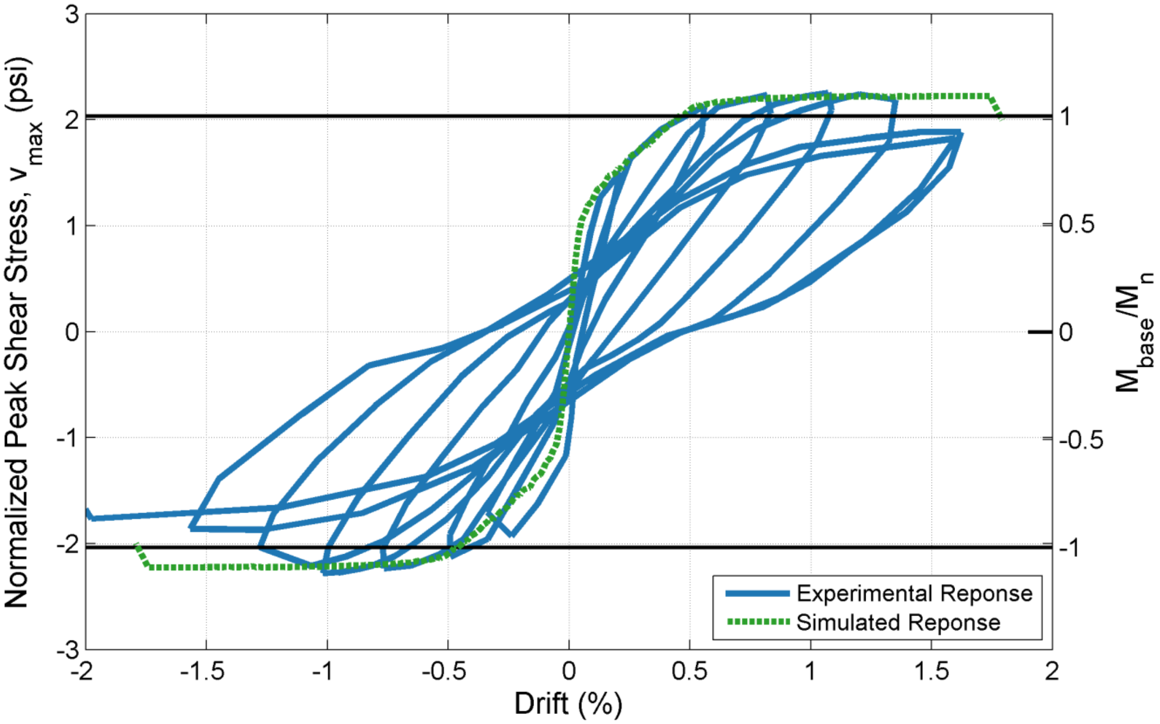

Figure A.1 – Specimen WSH2 Normalized Peak Shear Stress vs. Drift

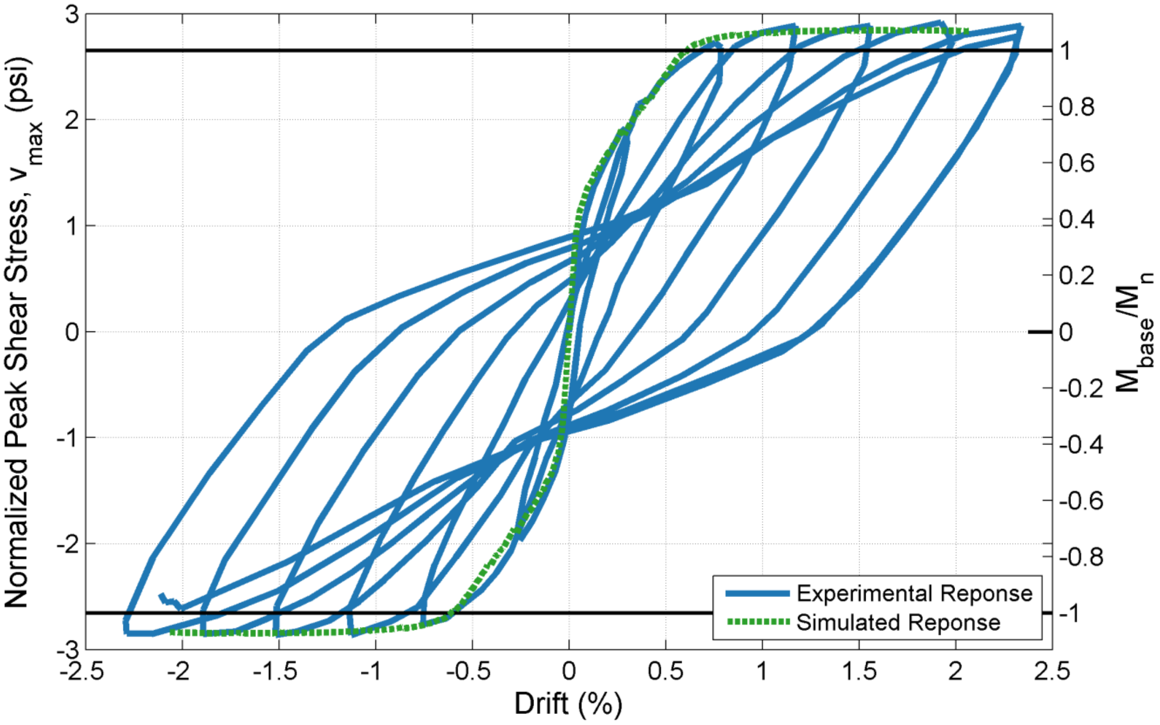

Figure A.2 – Specimen WSH3 Normalized Peak Shear Stress vs. Drift

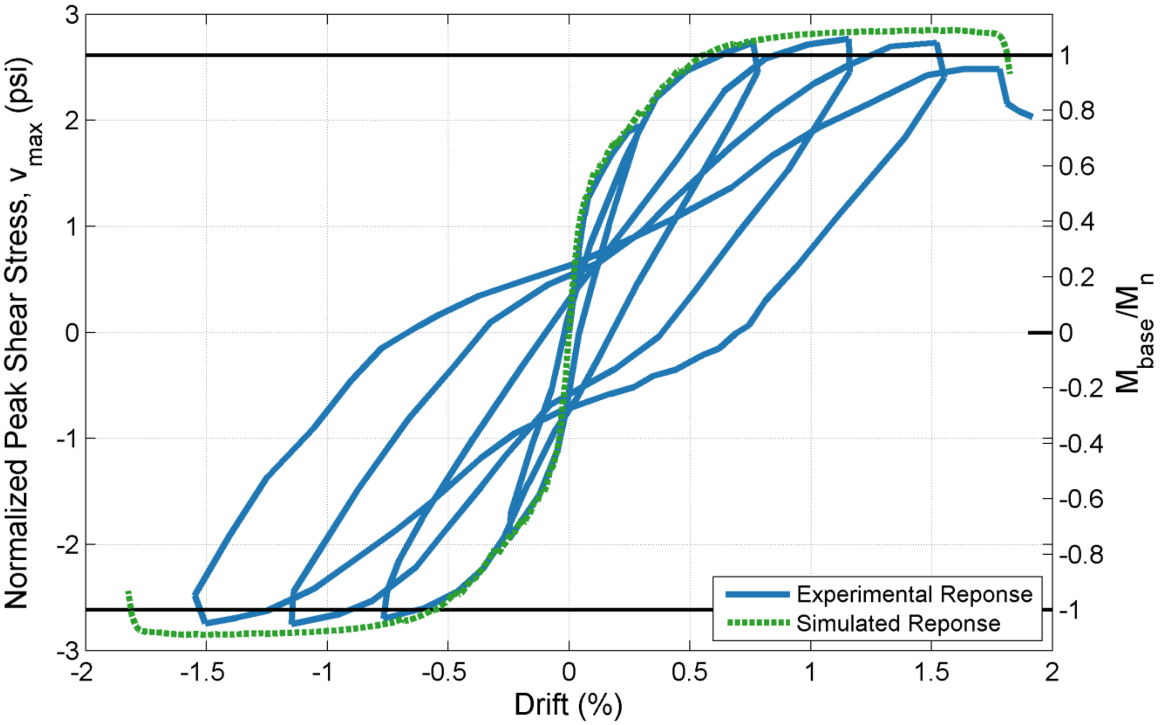

Figure A.3 – Specimen WSH4 Normalized Peak Shear Stress vs. Drift

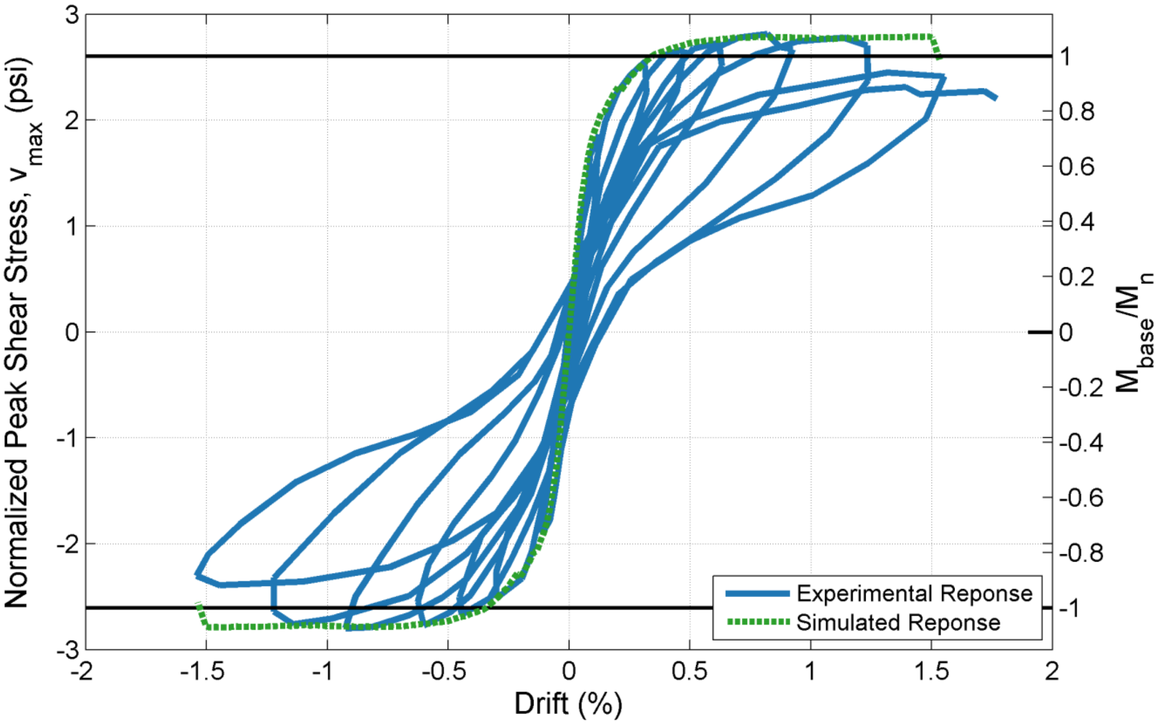

Figure A.4 – Specimen WSH5 Normalized Peak Shear Stress vs. Drift

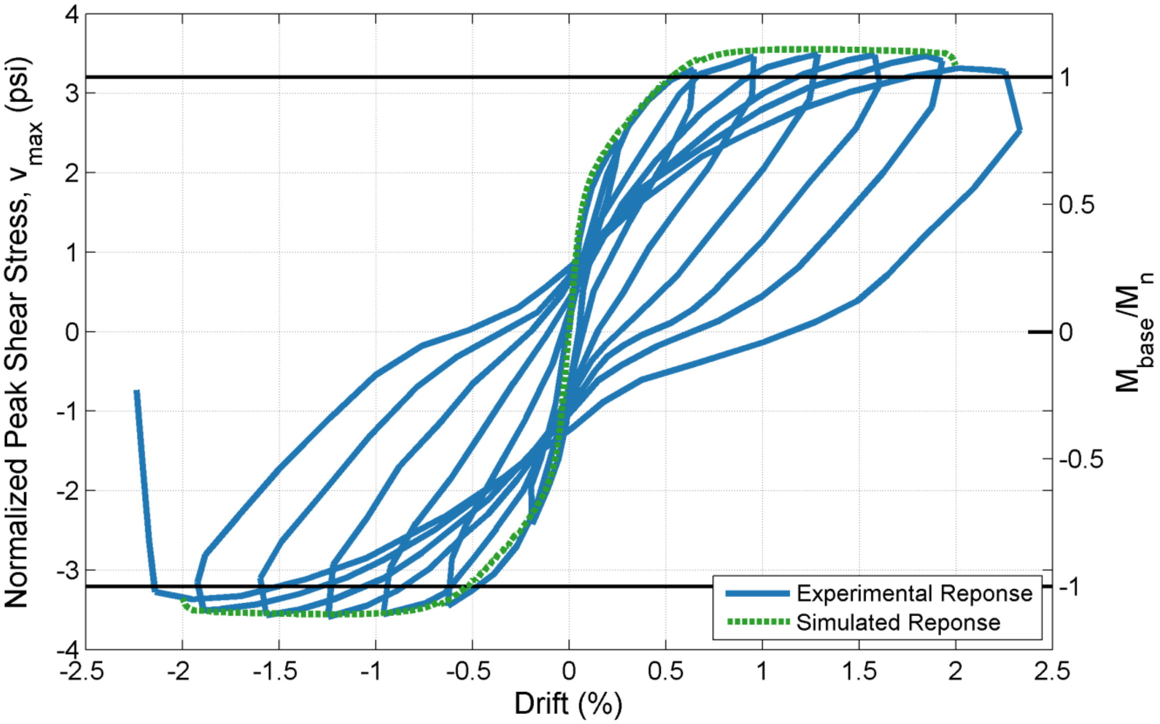

Figure A.5 – Specimen WSH6 Normalized Peak Shear Stress vs. Drift

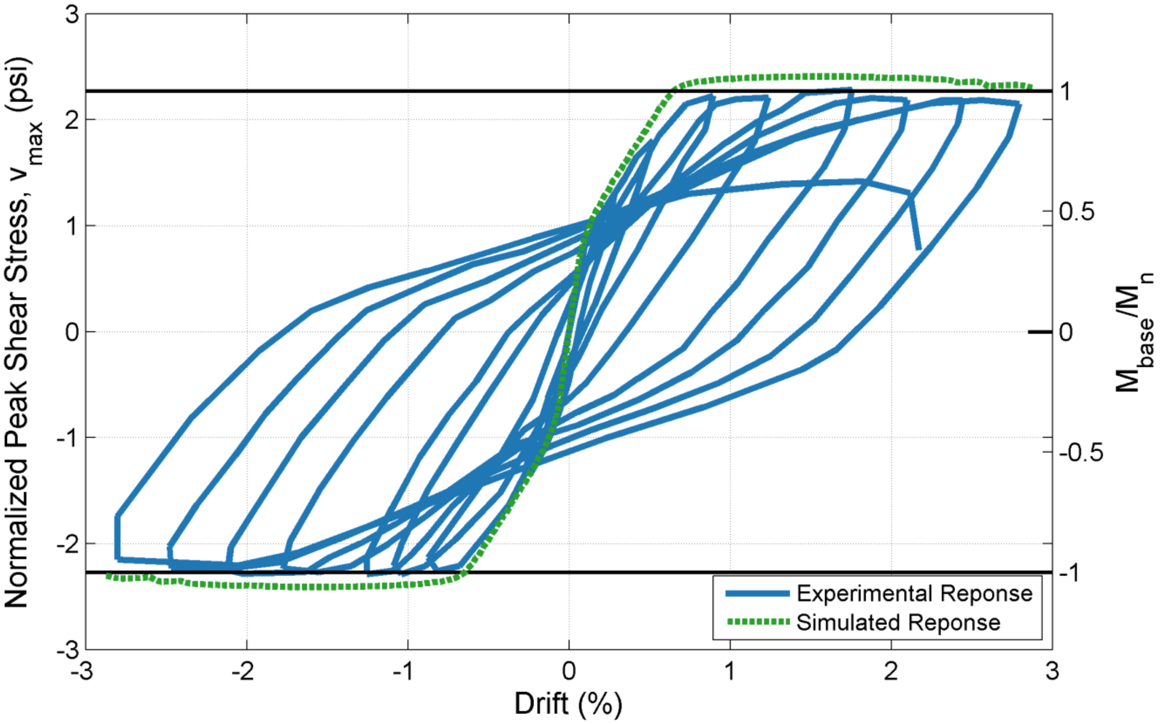

Figure A.6 – Specimen W1 Normalized Peak Shear Stress vs. Drift

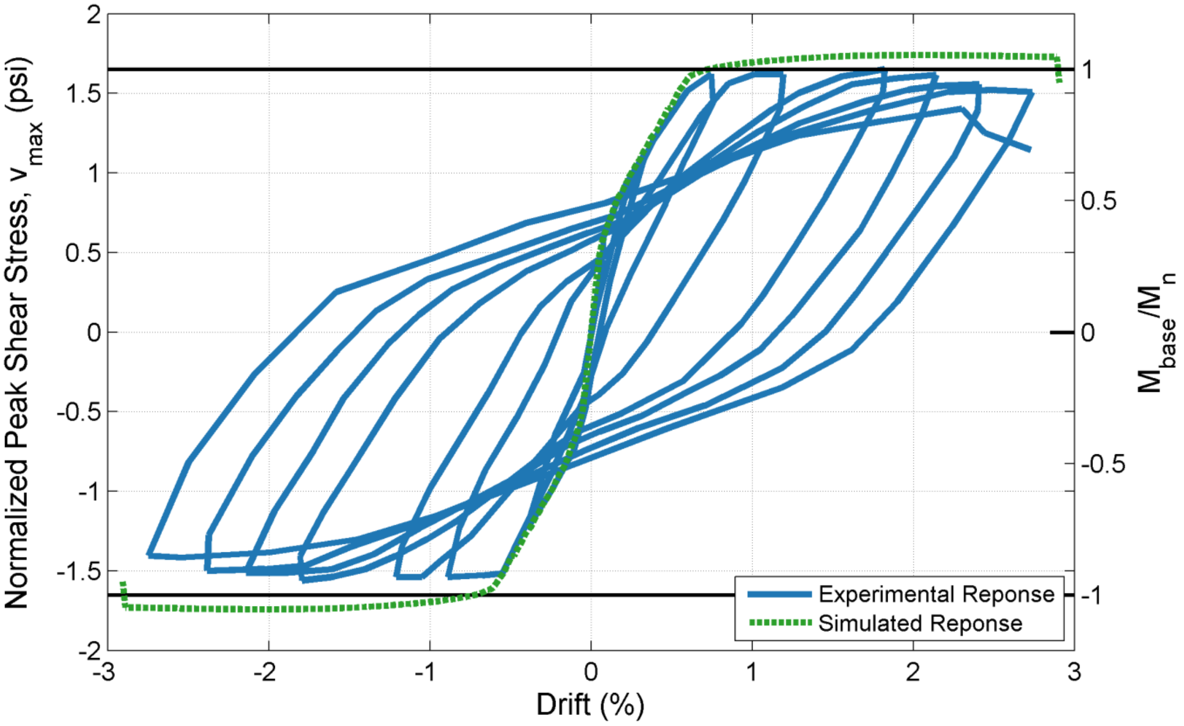

Figure A.7 – Specimen W2 Normalized Peak Shear Stress vs. Drift

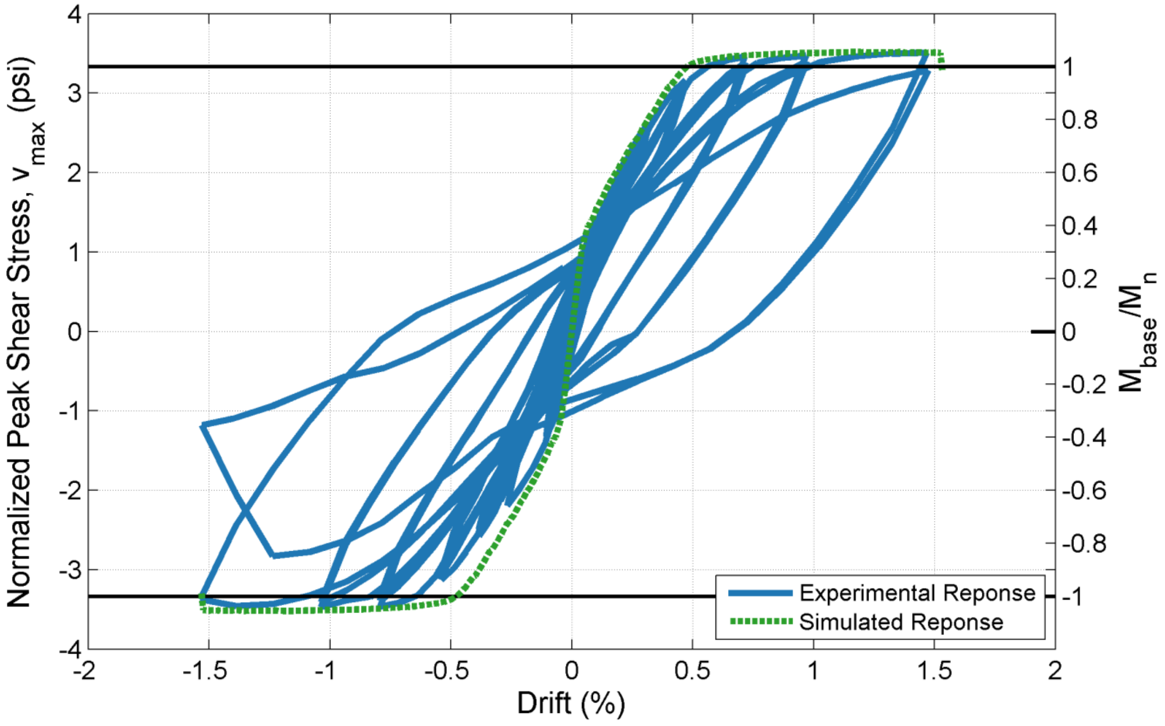

Figure A.8 – Specimen PW1 Normalized Peak Shear Stress vs. Drift

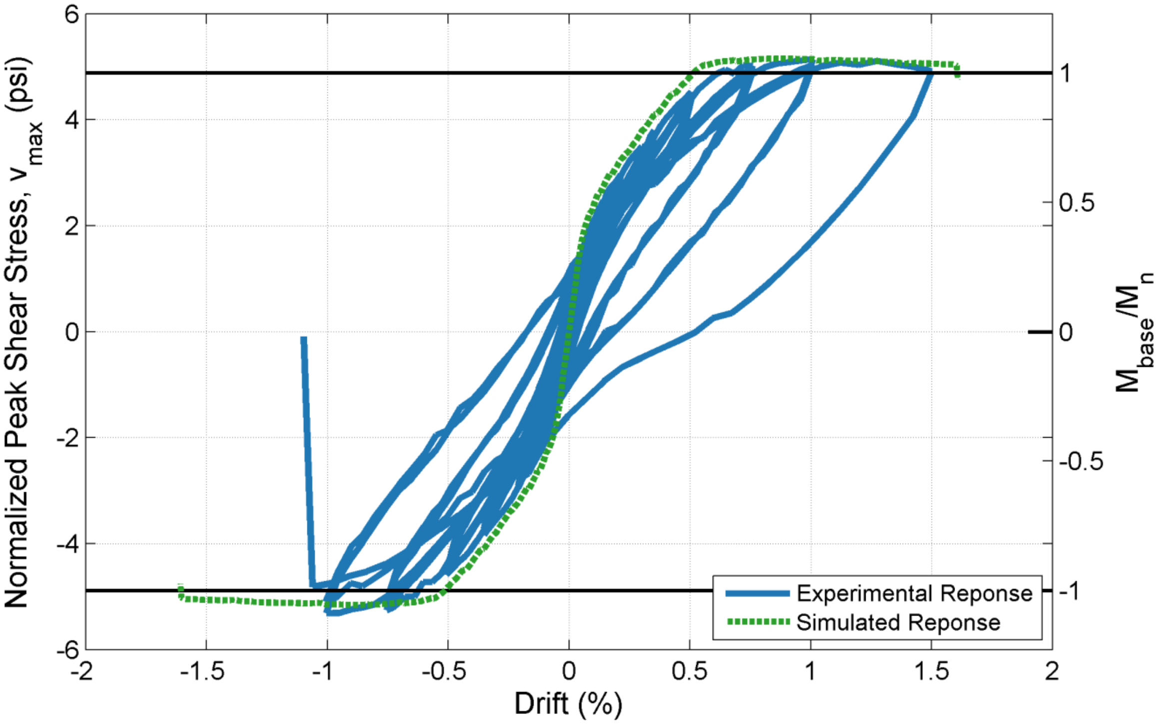

Figure A.9 – Specimen PW2 Normalized Peak Shear Stress vs. Drift

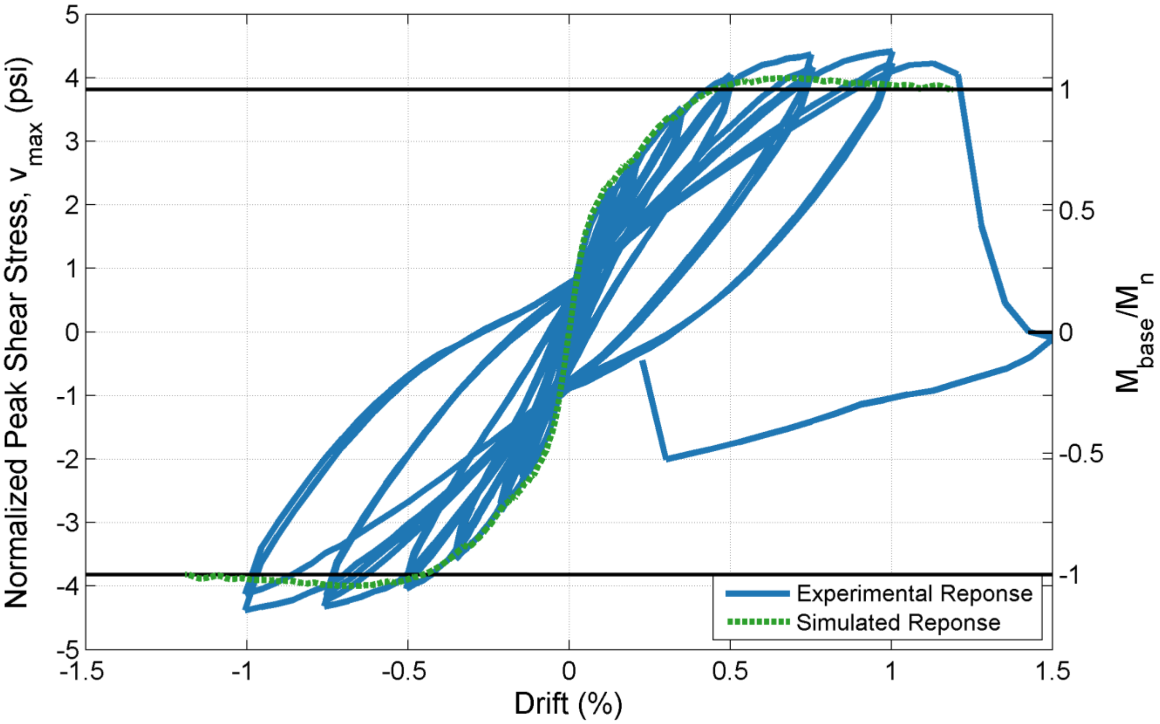

Figure A.10 – Specimen PW3 Normalized Peak Shear Stress vs. Drift

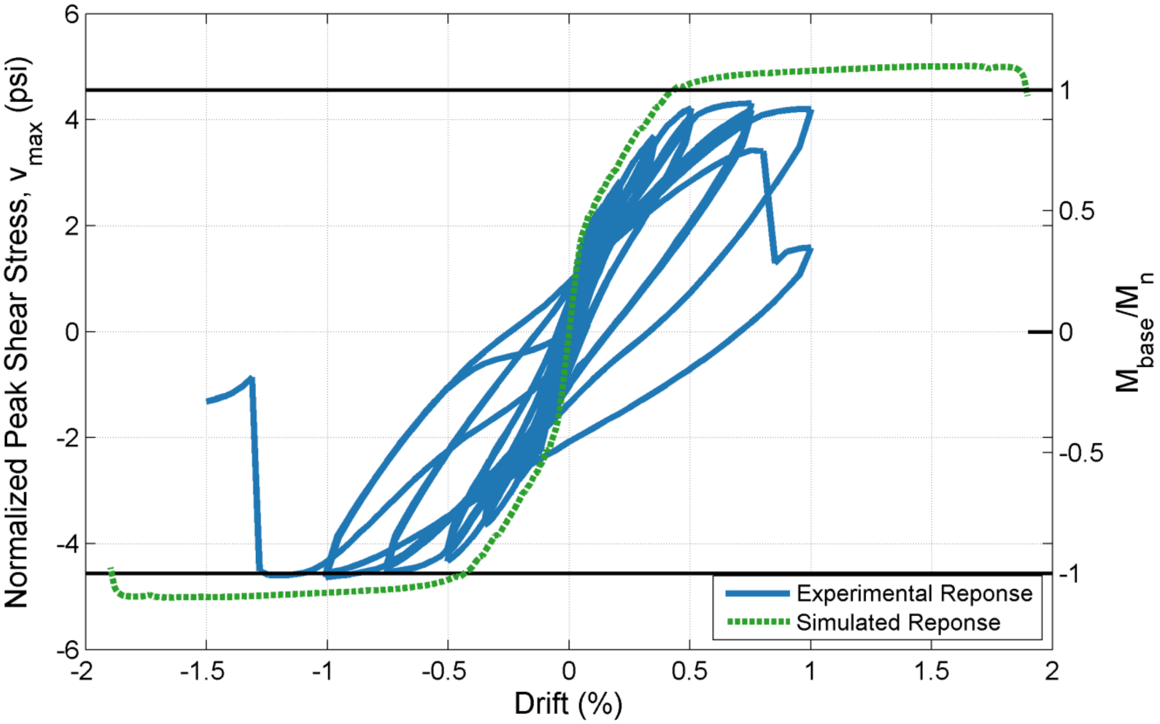

Figure A.11 – Specimen PW4 Normalized Peak Shear Stress vs. Drift

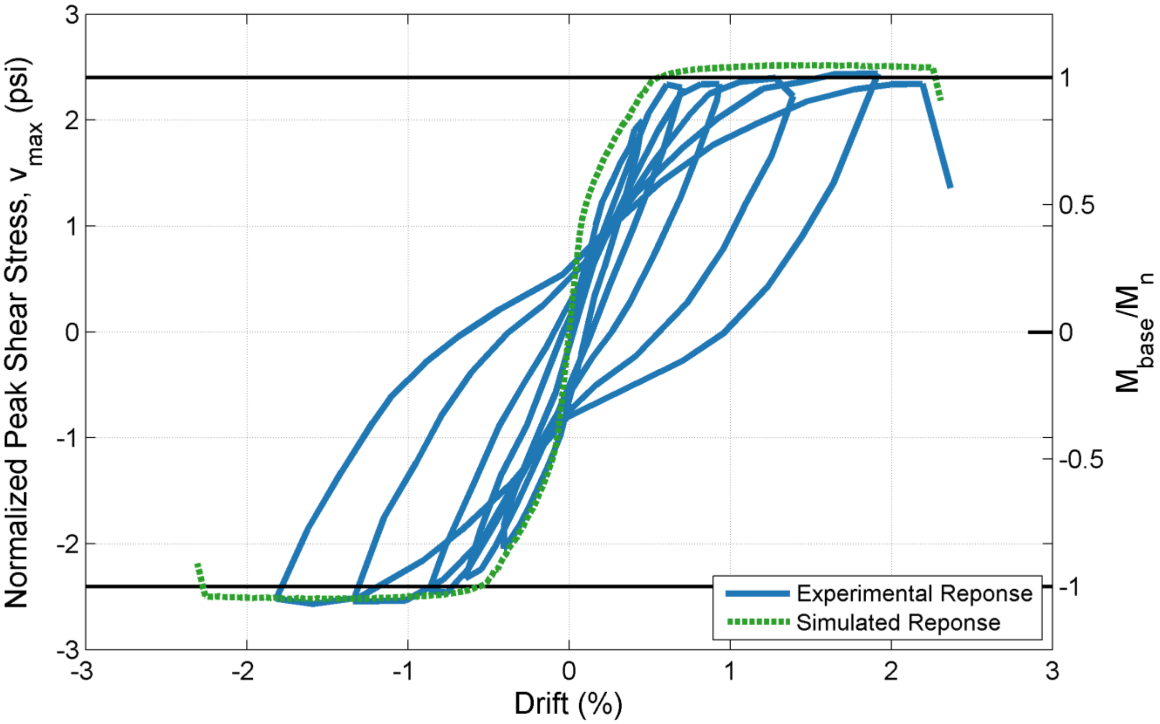

Figure A.12 – Specimen RW1 Normalized Peak Shear Stress vs. Drift

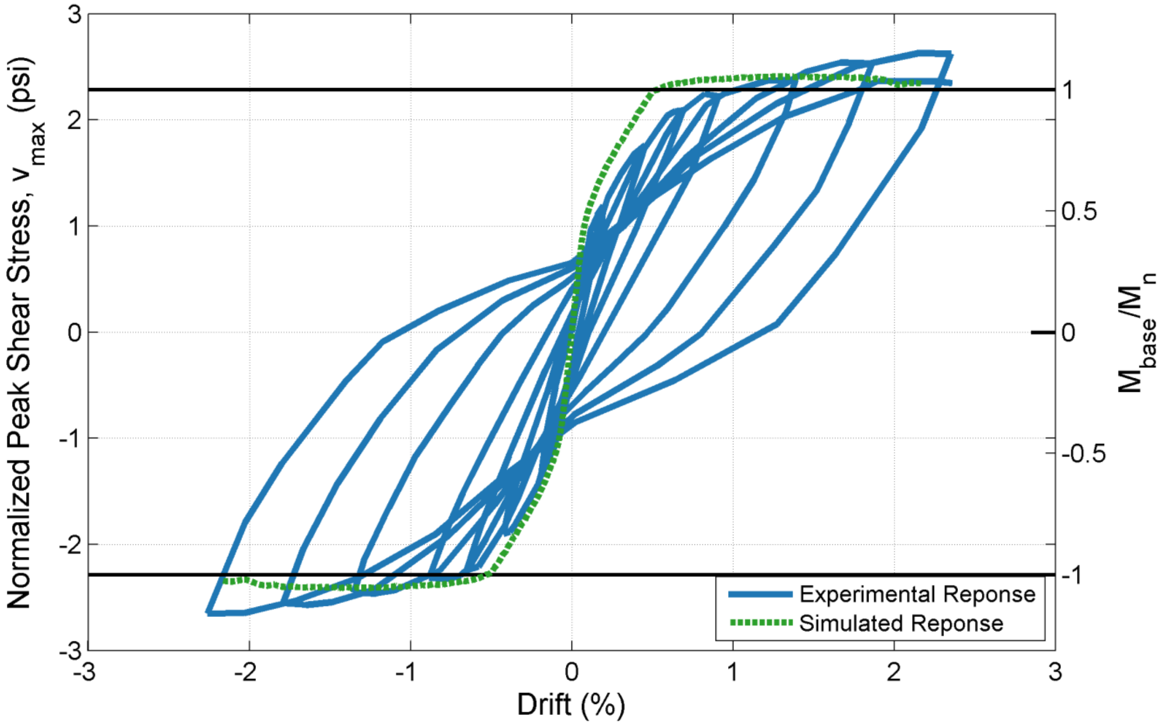

Figure A.13 – Specimen RW2 Normalized Peak Shear Stress vs. Drift

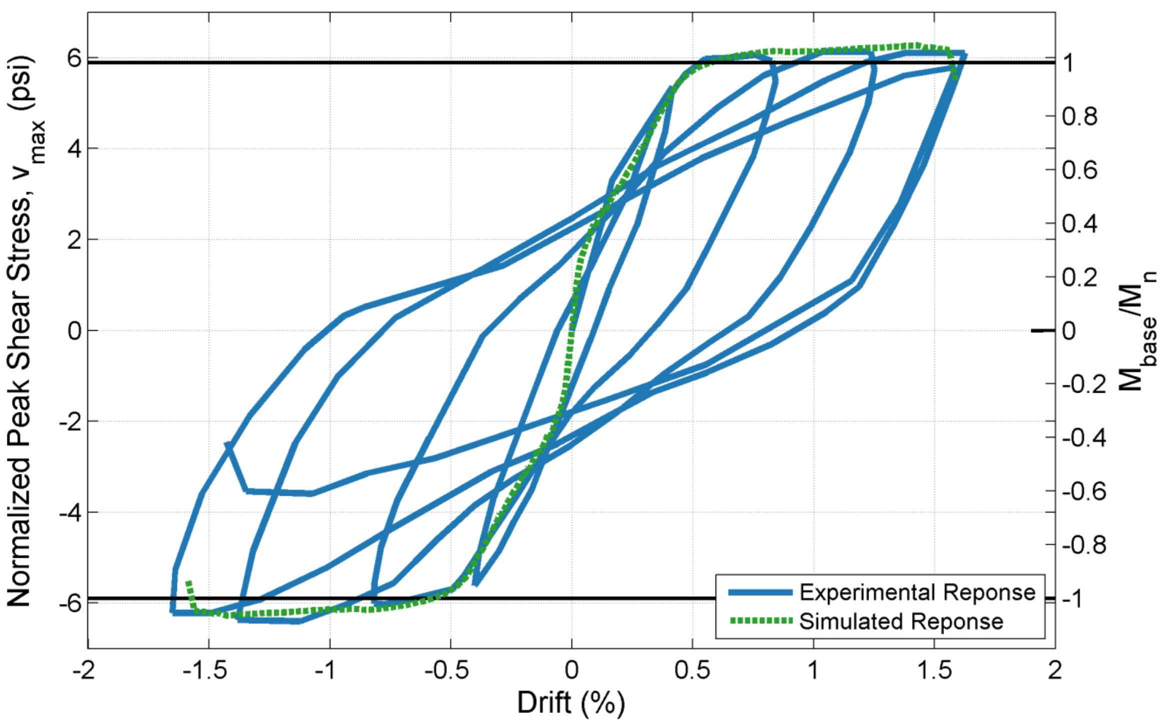

Figure A.14 – Specimen S6 Normalized Peak Shear Stress vs. Drift

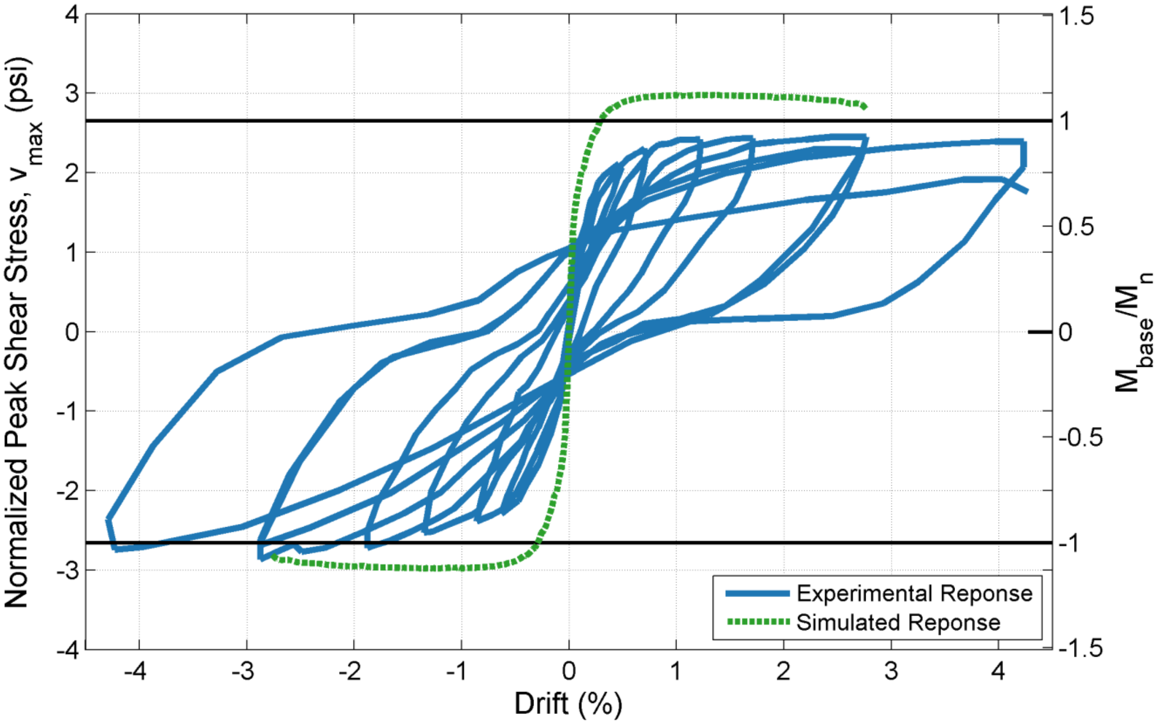

Figure A.15 – Specimen WR10 Normalized Peak Shear Stress vs. Drift

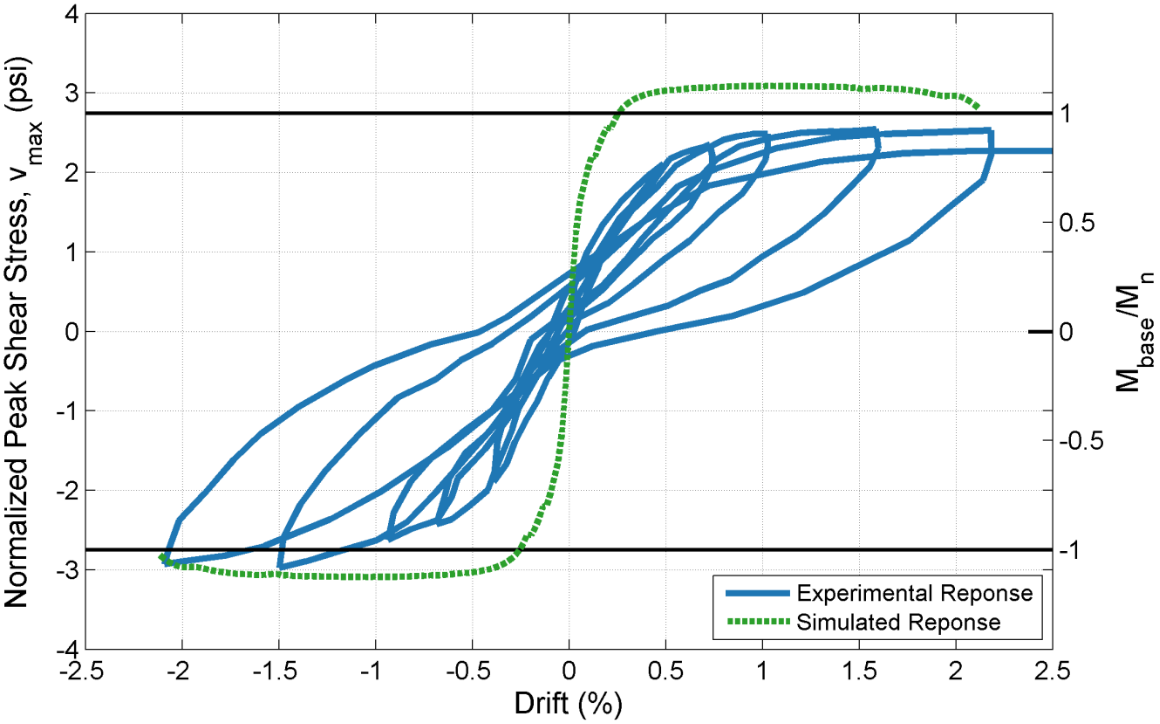

Figure A.16 – Specimen WR0 Normalized Peak Shear Stress vs. Drift

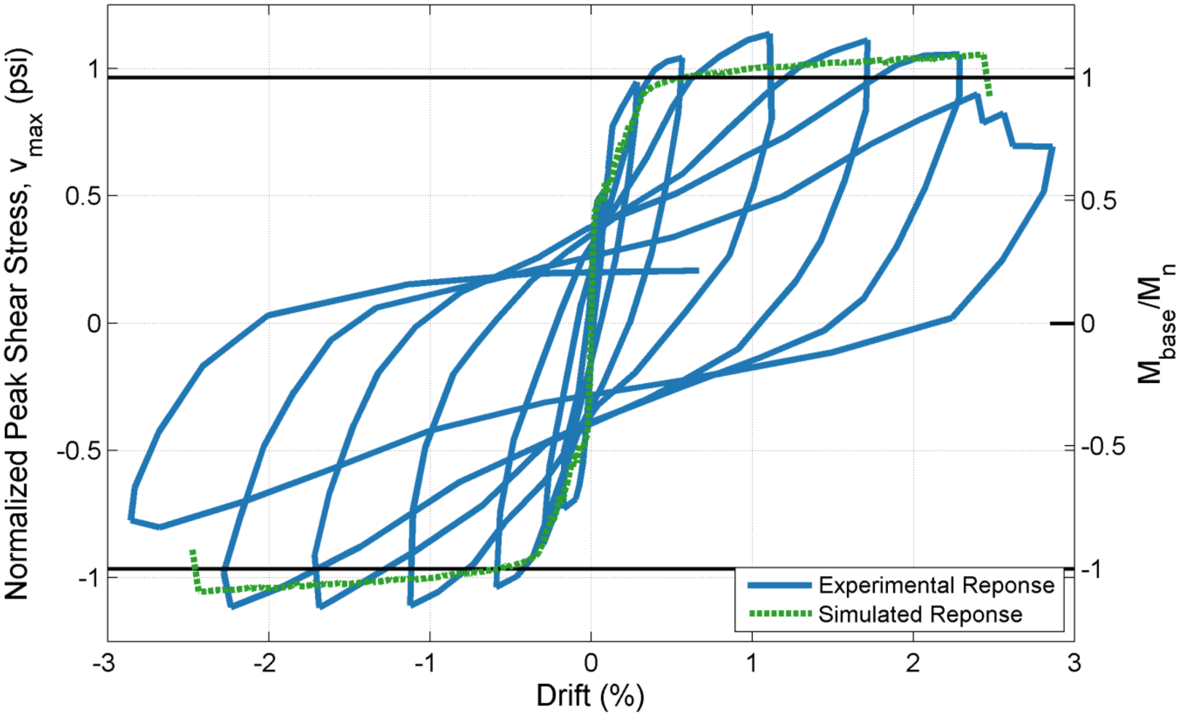

Figure A.17 – Specimen R1 Normalized Peak Shear Stress vs. Drift

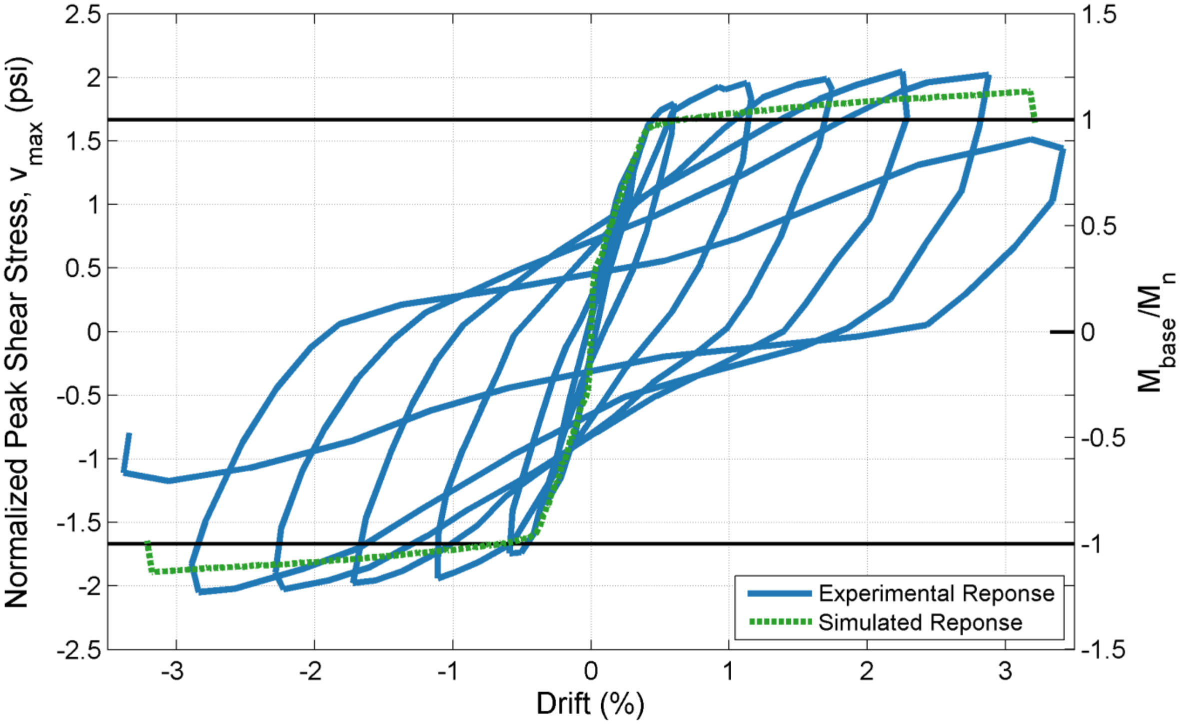

Figure A.18 – Specimen R2 Normalized Peak Shear Stress vs. Drift

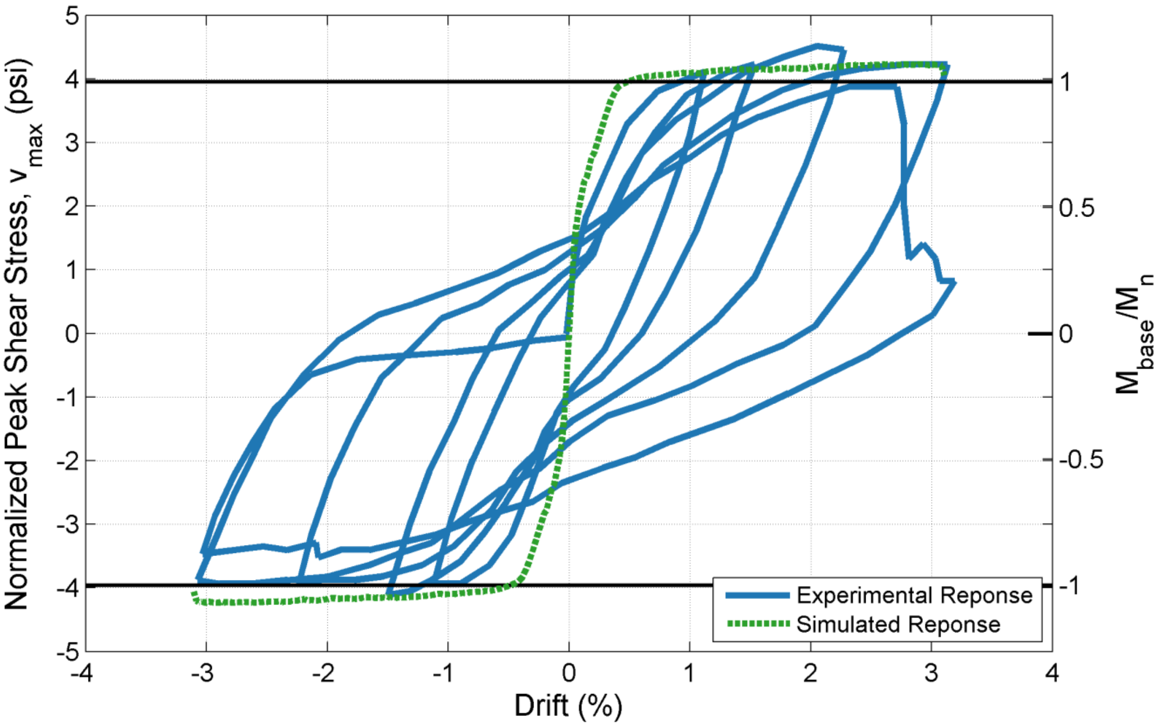

Figure A.19 – Specimen RW-A20-P10-S38 Normalized Peak Shear Stress vs. Drift

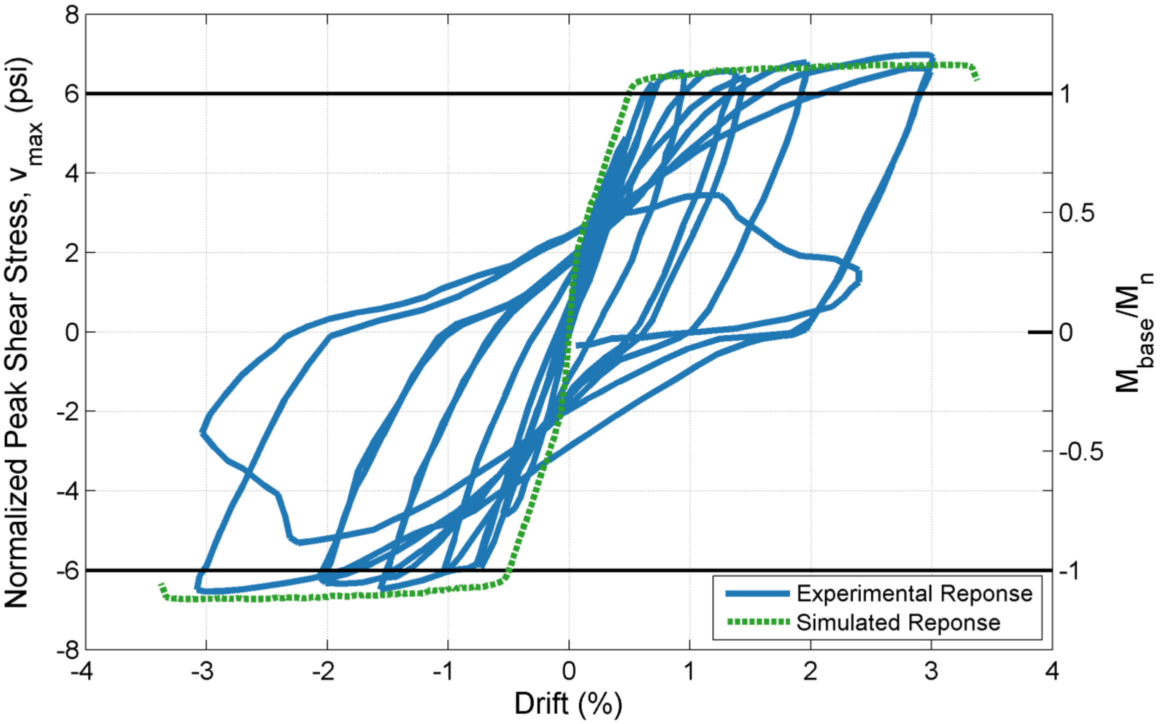

Figure A.20 – Specimen RW-A20-P10-S63 Normalized Peak Shear Stress vs. Drift

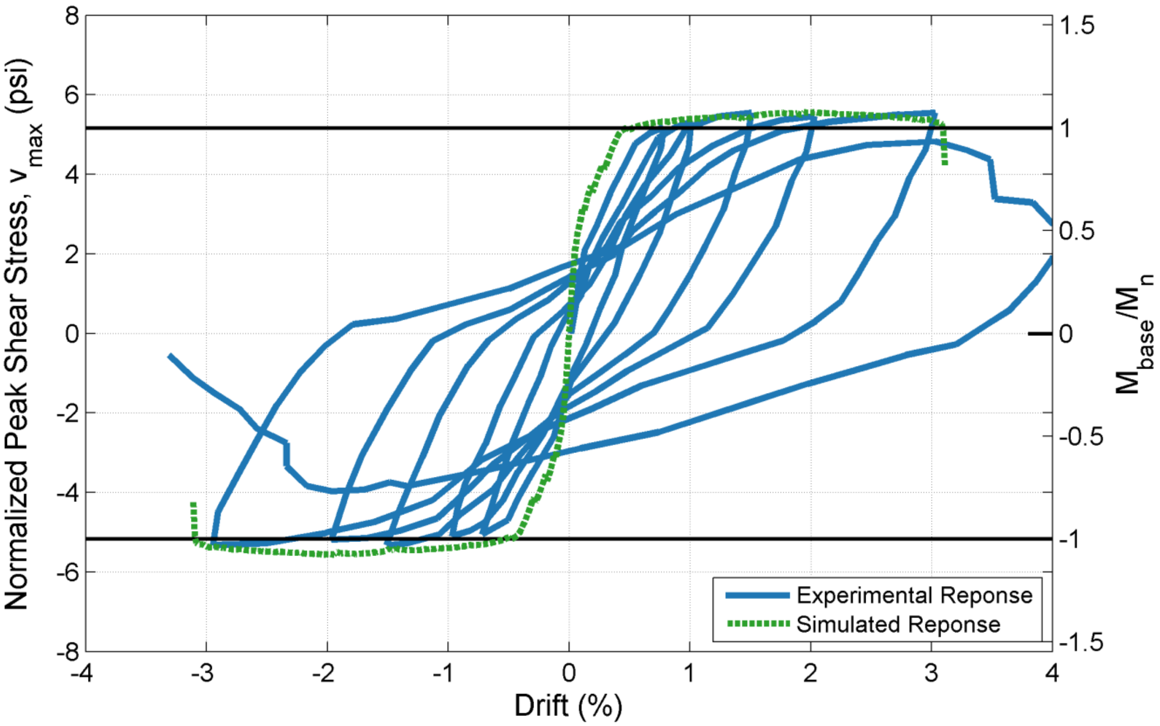

Figure A.21 – Specimen RW-A15-P10-S51 Normalized Peak Shear Stress vs. Drift

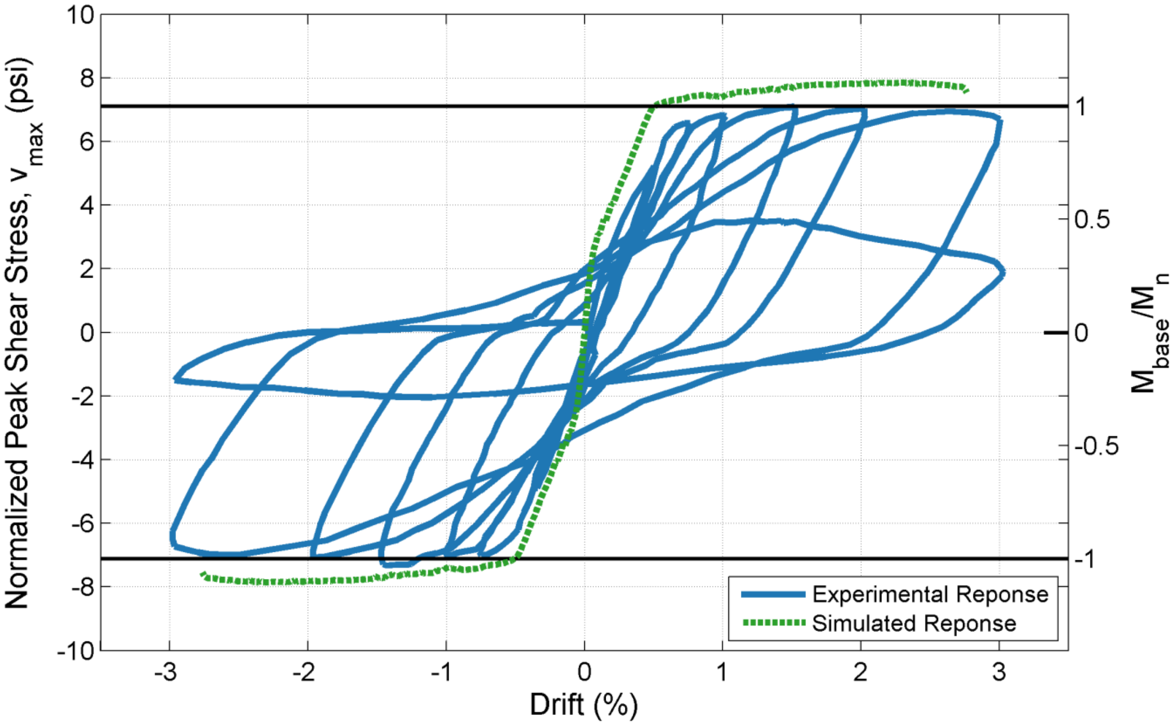

Figure A.22 – Specimen RW-A15-P10-S78 Normalized Peak Shear Stress vs. Drift

Appendix B EFFECTIVE FLEXURAL STIFFNESS

The effective stiffness, EI_{eff}/EI_g, is calculated for all models conducted in this research. EI_{eff} is defined as the secant stiffness to yield (Eq. B.1). System yield was defined as the point at which wall reinforcement first reached yield strain in tension, as measured in the ATENA analysis. The base shear at this point of yield is defined as V_y. Note that the gross system stiffness is calculated with $E_c = 57{,}000\sqrt{f'c}$ (psi).

The ATENA results allowed for calculation of the shear deformations in each model, allowing for greater accuracy in determining the flexural stiffness. The shear deformation was calculated at a distance $l_w/2$ above the base of the specimen; this is consistent with the definition of the hinge length in Chapter 5. The shear deformations did not significantly impact the flexural stiffness for low-CSAR specimens and only provided up to a 5% increase for high-CSAR specimens (CSAR > 12).

$$\mathrm{EI_{eff}} = \mathrm{V_y h_{eff}^3}/3\Delta_{\mathrm{flex}}, \text{where } \Delta_{\mathrm{flex}} = \Delta_{\mathrm{total}} - \Delta_{\mathrm{shear}} \qquad \textit{(Eq. B.1)}$$

Where V_y is the base shear at the point of system yield, defined by yield of the longitudinal reinforcing in the ATENA model. Δ_{shear} is defined as the shear deformation at a height $l_w/2$ from the specimen base.

Figures B.1-B.5 show the impact of ALR, shear span, CSAR, and peak shear stress on the effective flexural stiffness of all simulations conducted in this study. The following are takeaways from this analysis:

- There is a strong relationship between axial load ratio and the effective flexural stiffness. For each base specimen, the change from a low ALR (<5%) to high ALR (>10%) resulted in roughly a 10% gain in effective flexural stiffness.
- There is no relationship between CSAR and EI_{eff}/EI_g.
- There exists a strong correlation between the shear span and the effective stiffness, which matches intuition. Specimens with a low shear span (<2.0) undergo more cracking and loss of stiffness prior to reaching M_n, while models with a high shear span (>2.5) are able to retain much of their stiffness up to M_n. This idea is reinforced in Figure B.5, which shows a strong relationship between effective flexural stiffness and $\varepsilon_{t,ATENA}/\varepsilon_{t,ACI}$. As response becomes more non-linear (i.e., lower value of $\varepsilon_{t,ATENA}/\varepsilon_{t,ACI}$), there is a decline in the effective flexural stiffness
- There is a relationship between the peak shear stress and the effective flexural stiffness, but this mostly a function of the axial load ratio necessary to reach high shear demands.

The effective flexural stiffness generally falls from 20 to 50% of the gross section stiffness. Models with a high shear span and high axial load ratio are often able to achieve results greater than 40%, with shear span being more influential than ALR. The assumption of 50% effective flexural stiffness for all walls is non-conservative.

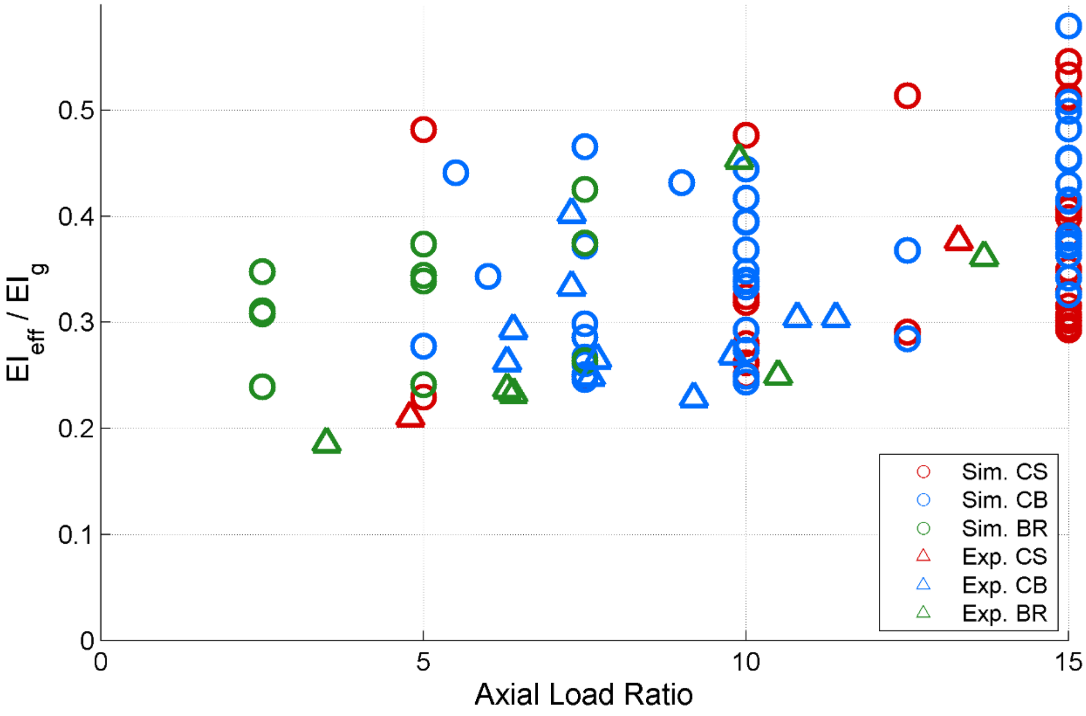

Figure B.1 – Effective Flexural Stiffness vs. Axial Load Ratio

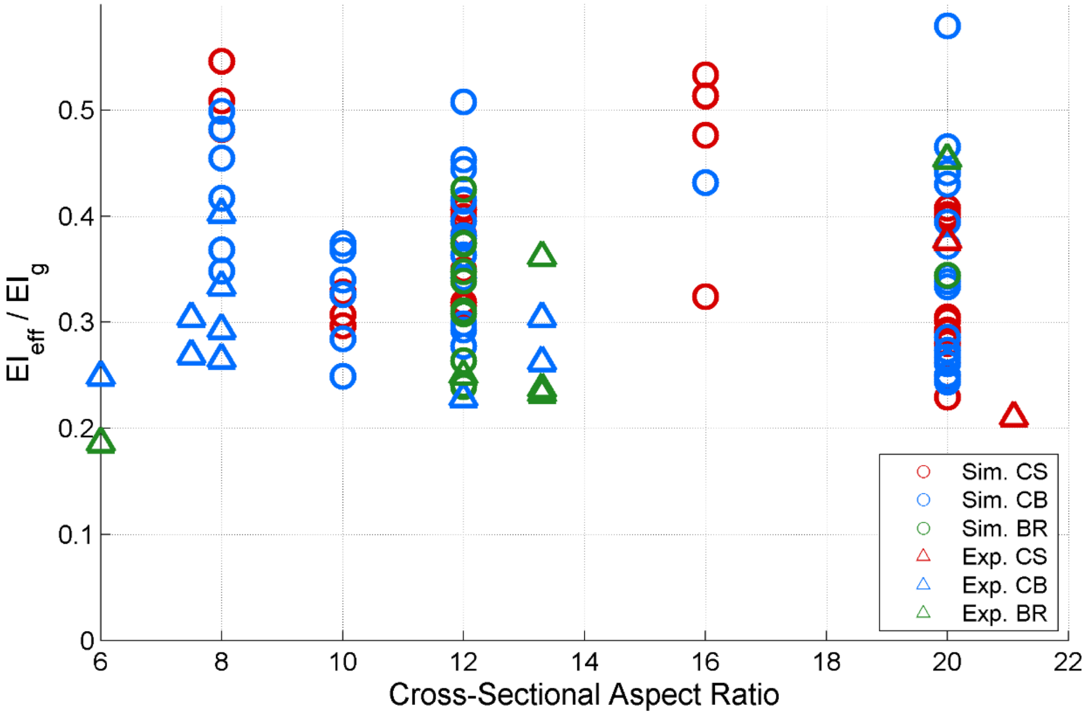

Figure B.2 – Effective Flexural Stiffness vs. CSAR

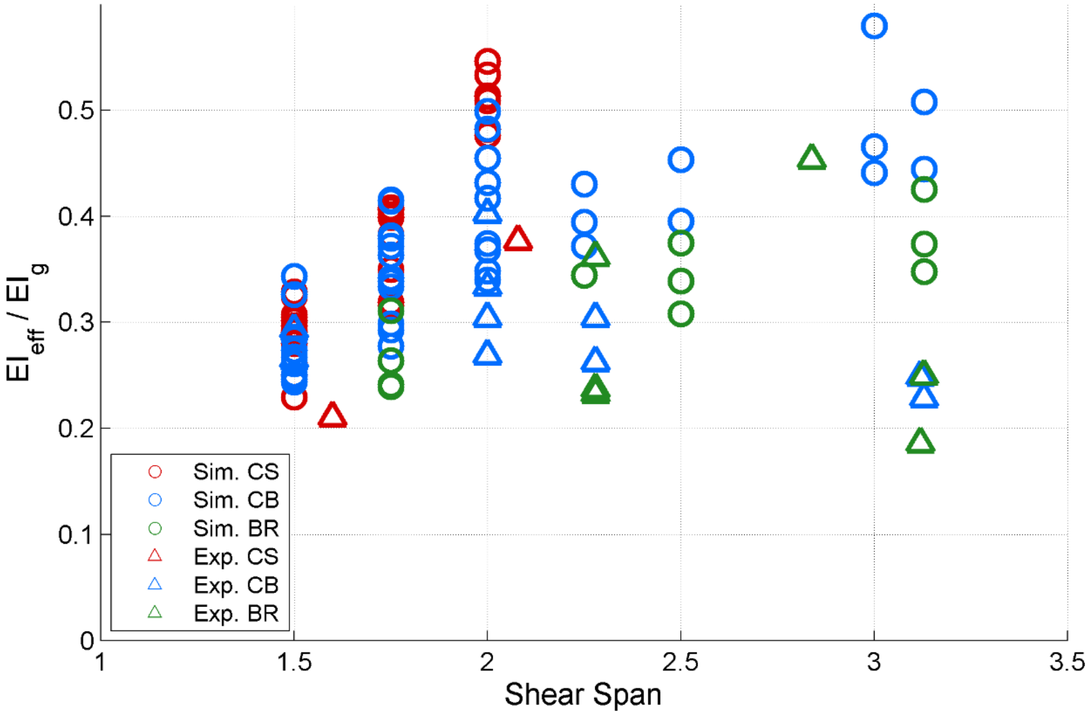

Figure B.3 – Effective Flexural Stiffness vs. Shear Span

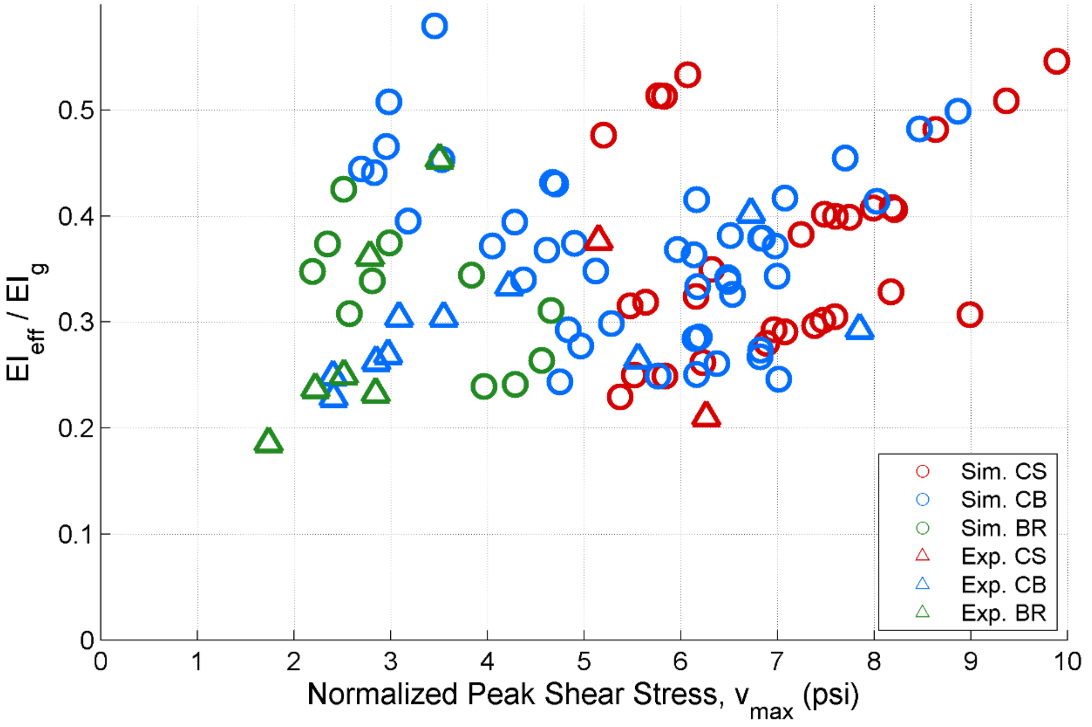

Figure B.4 – Effective Flexural Stiffness vs. Peak Shear Stress

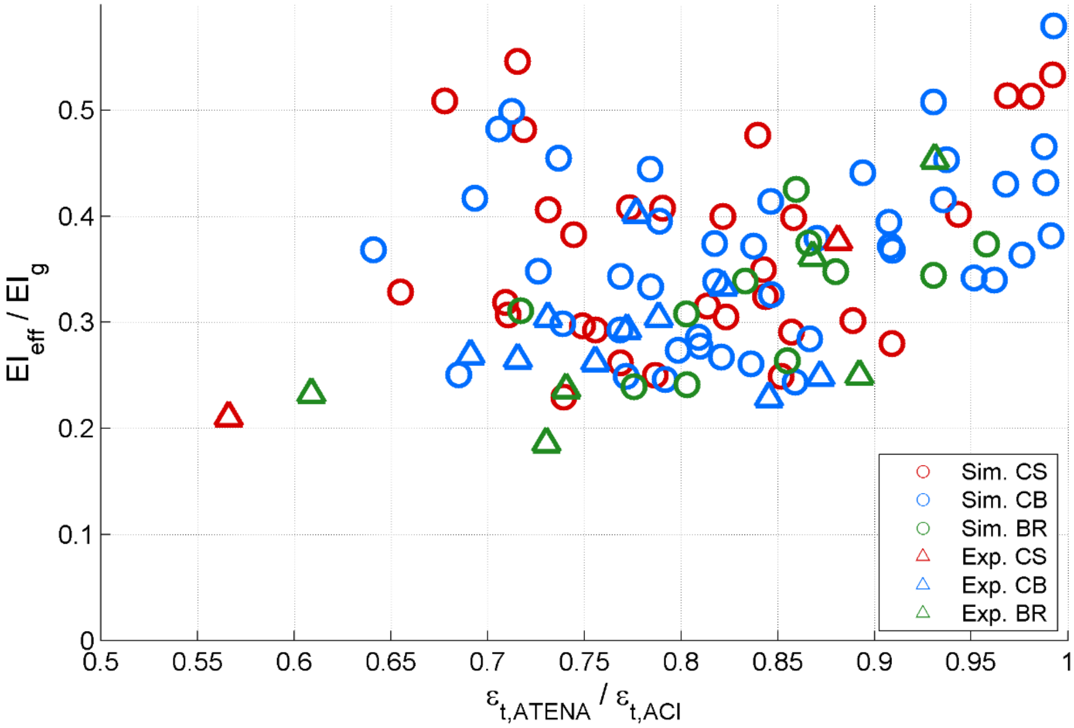

Figure B.5 – Effective Flexural Stiffness vs. $\varepsilon_{t,ATENA}/\varepsilon_{t,ACI}$

Appendix C EVALUATION OF FEM SOFTWARE

The non-linear modeling of concrete is a difficult task, which is unfortunate as the use of concrete in lateral force resisting systems has increased in recent years. There are a number of problems which plague reinforced concrete modeling, including tensile response, bar buckling, tension stiffening, system softening, and confinement. Confinement is particularly important to concrete analysis as it provides a large amount of the ductility that is desired in lateral systems. Most analysis currently being conducted employs values determined by a concrete model that was calibrated through experimental data. Examples of these models include Saatcioglu & Razvi (1992) and Mander (1988). However, there is not much documentation regarding the explicit modeling of transverse reinforcement in reinforced concrete models. It would useful to determine a program and method by which the impact of tie size, spacing, material properties, and detailing could be fully implemented into the analysis. The ultimate goal of this work would be to develop a model by which it is possible to relate crushing energy to transverse reinforcement detailing.

The objective of this report is to develop an understanding of the effectiveness of modeling transverse reinforcement in two finite element software packages: ABAQUS and ATENA. The program which is best able to correctly model behavior has been utilized to analyze a recent concrete prism compression test in an attempt to validate model results.

Test Specimen

The model for this issue was as simple as possible to best isolate the behavior of interest. The specimen consisted of a rectangular compression block with rectangular ties bounding the concrete, as shown in Figures C.1-C.2. This means that the specimen was wholly confined and that there was no cover concrete present in the analysis. The boundary conditions consisted of one pin and rollers across the left of the bottom surface, allowing for the release of horizontal force and only restraining force in the vertical direction.

To load the problem, a displacement boundary condition was applied across the top surface. The ATENA model utilized an elastic plate on top of the concrete to apply the load at four distinct points, while the ABAQUS model did not include any loading apparatus. This is because the displacement control was spread across the surface and no plate was needed to ensure equal deformation across the plane. It was necessary to use displacement control as much of the critical behavior took place after significant softening had occurred and the tangent stiffness of the system was negative.

The behavior of the structure was characterized by load-displacement plots which report the reaction at the base of the specimen plotted vs. the displacement along the top of the specimen. This is the same data that is available for the prism tests which were used to validate the confinement models. This graph allows for the calculation of average concrete stress, the key output, as well as also yielding the relative ductility of systems with different levels of transverse reinforcement.

The experimental prism test was conducted by Travis Welt in March 2014 at the CERL facility in Champaign, Illinois, as part of the NIST Wall Project. The specimen is similar to the model, with 1.1% transverse reinforcement and dimensions of 8”x15”x40”. Unlike the model, 2.6% vertical reinforcement was included. Tests were conducted with both monotonic and cyclic loading, and with different levels of detailing. The specimen selected for this analysis is CS5, a prism loaded monotonically determined by ACI 318-11 “Special” boundary element detailing. Figures C.3-C.4 show the specimen in elevation and plan view.

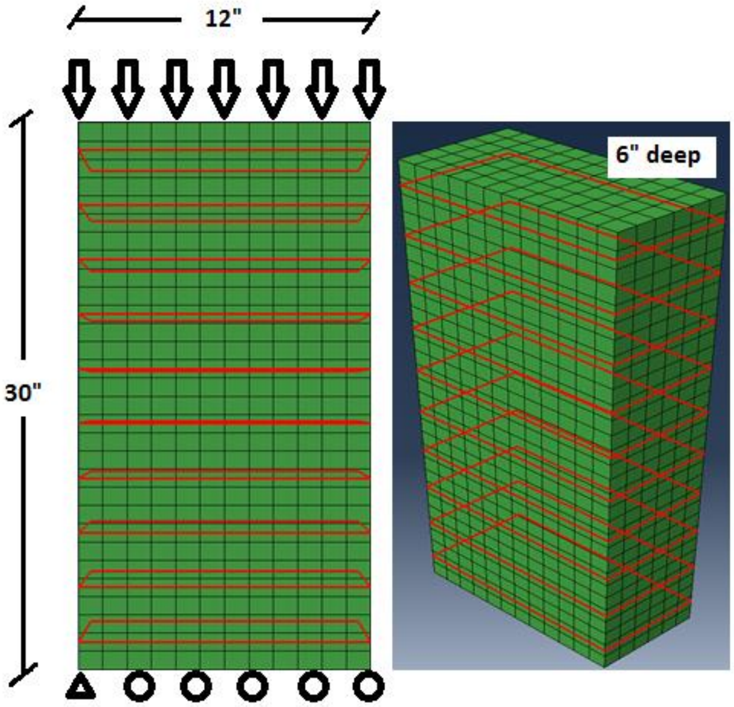

Figure C.1 – Annotated Visual Representation of ABAQUS Model

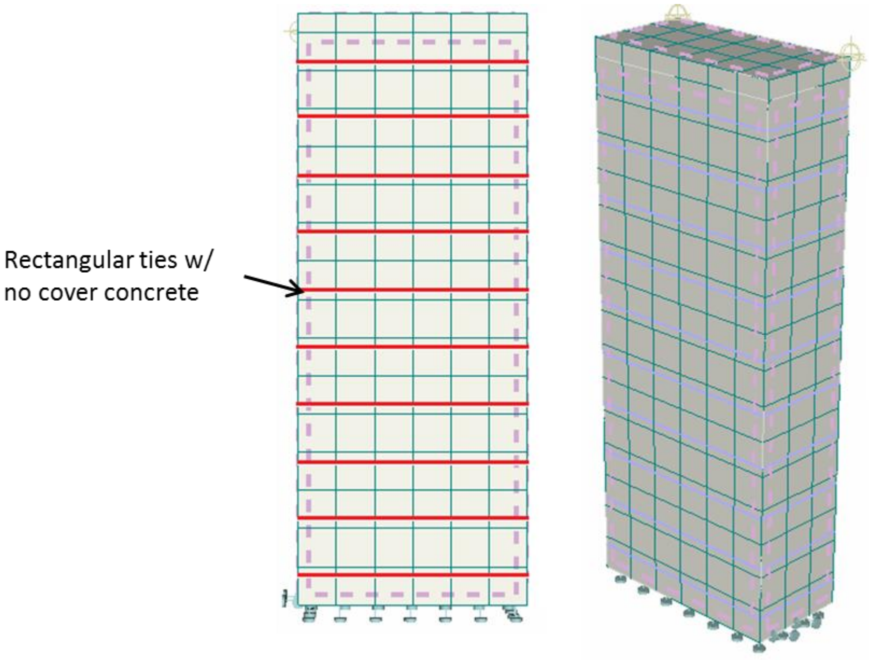
Rectangular ties w/ no cover concrete

Figure C.2 – Visual Representation of ATENA Model (not to scale)

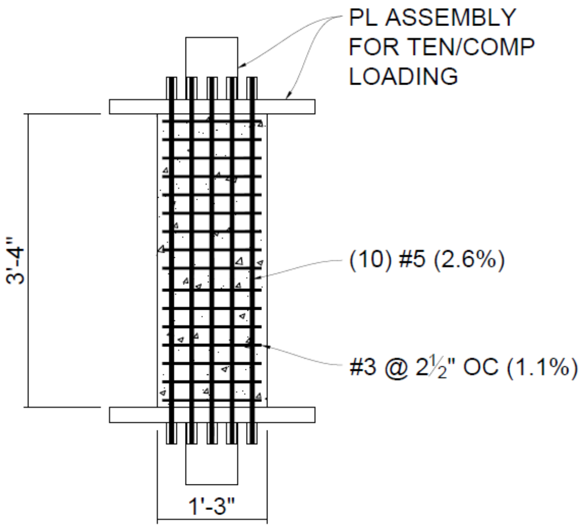

Figure C.3 – CS5 Elevation

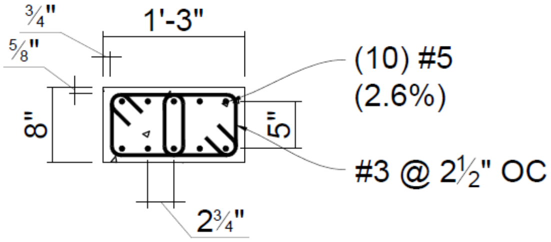

Figure C.4 – CS5 Base Section

Analysis Background

Two finite element method programs are evaluated in this report: ABAQUS and ATENA. ABAQUS is a commercial finite element software used for the analysis of continua. The main concrete constitutive model available in this software package is Concrete Damaged Plasticity, a model developed by Lee & Fenves (1998) which has been utilized in a number of other research projects.

ATENA is a finite element software developed by Cervenka Consulting for the analysis of reinforced concrete continua. The concrete model evaluated in this study is "Nonlinear Cementitious 2" (NC2). The main benefit of this material model with respect to this study is that its behavior is regularized in both compression and tension, which bypasses much of the issue with mesh sensitivity.

The main non-linearity in this analysis was related to the concrete material non-linearity, and the main objective of the analysis was to isolate the impact of confinement on the material model. Geometric non-linearity was not a particularly impactful consideration due to the geometry and loading of the problem.

In both software packages, linear brick elements were used to model concrete; in ABAQUS, this element is labeled as "C3D8" and as a "linear brick element" in ATENA. The reason for this element formulation is that the analysis needed to be three-dimensional to capture the impact of confinement, and the linear formulation was capable of handling the compressive behavior which was experienced. As elements won't be subjected to extreme bending situations, the issue of element lock-up that is often associated with linear elements was not an issue.

Steel was modeled by 2-node truss elements, “T3D2” elements in ABAQUS and “reinforcement elements” in ATENA. In ABAQUS, the reinforcement was attached to the concrete by an “embedded region” constraint, allowing the two materials to act in tandem. With ATENA, reinforcement is implicitly embedded in the concrete which it contacts; the connection between the two was assumed to be perfect. The material formulation for steel was bi-linear.

The material formulations for concrete utilized the models noted earlier. The main concrete and steel properties are included in Table C.1. As the only goal of this initial evaluation was to evaluate different parameters in relation to each other, the exact values of the material properties are not hugely important, as long as they are held constant throughout all analyses. The material properties for the prism were primarily obtained through experiments. The concrete stiffness was estimated by $E_c = 57000\sqrt{f'c}\ (psi)$ and the ultimate strain of the steel was assumed to be 12%. Prism material properties are listed in Table C.2.

In ABAQUS, a static general load case was utilized for analysis. In ATENA, a Newton-Raphson algorithm with line search was used.

Table C.1 – Parameter Study Material Properties

	Parameter	Value	
Concrete	ε_{peak}	0.001	in/in
	ε_{ult}	0.007	in/in
	f'_c	5.0	ksi
	E_c	4500	ksi
Steel	f_y	60	ksi
	f_u	75	ksi
	B_s	0.02	(-)
	E_s	29000	ksi

Table C.2 – Prism CS5 Material Properties

	Parameter	Value	
Conc.	f'_c	4.1	ksi
	E_c	3500	ksi
Vert. Steel	f_y	82.4	ksi
	f_u	98.9	ksi
	ε_{ult}	0.12	in/in
Tie Steel	f_y	68.5	ksi
	f_u	100.2	ksi
	ε_{ult}	0.12	in/in

Analysis Process

The simplest analysis performed was a first-order elastic model. This model is very predictable as the model is mechanically simple. As the stiffness of a block is $\frac{AE}{L}$, it is a trivial exercise to calculate the expected system response. The analysis in both ATENA and ABAQUS was about 0.1% stiffer than this prediction due to the presence of the confinement, but this is expected. When dealing with an elastic material, transverse reinforcement is not particularly impactful.

It was also important to run a "control" test case. Before building any models with transverse reinforcement, a concrete block with no confinement was analyzed in both software packages. This provides the analysis with a baseline for measuring the impact of confinement.

Scope

Beyond the simplified models, a standard parameter study was conducted. Table C.3 shows the test matrix for the first set of analyses in both software packages.

Table C.3 – Test matrix for all analyses, ABAQUS (left) & ATENA (right)

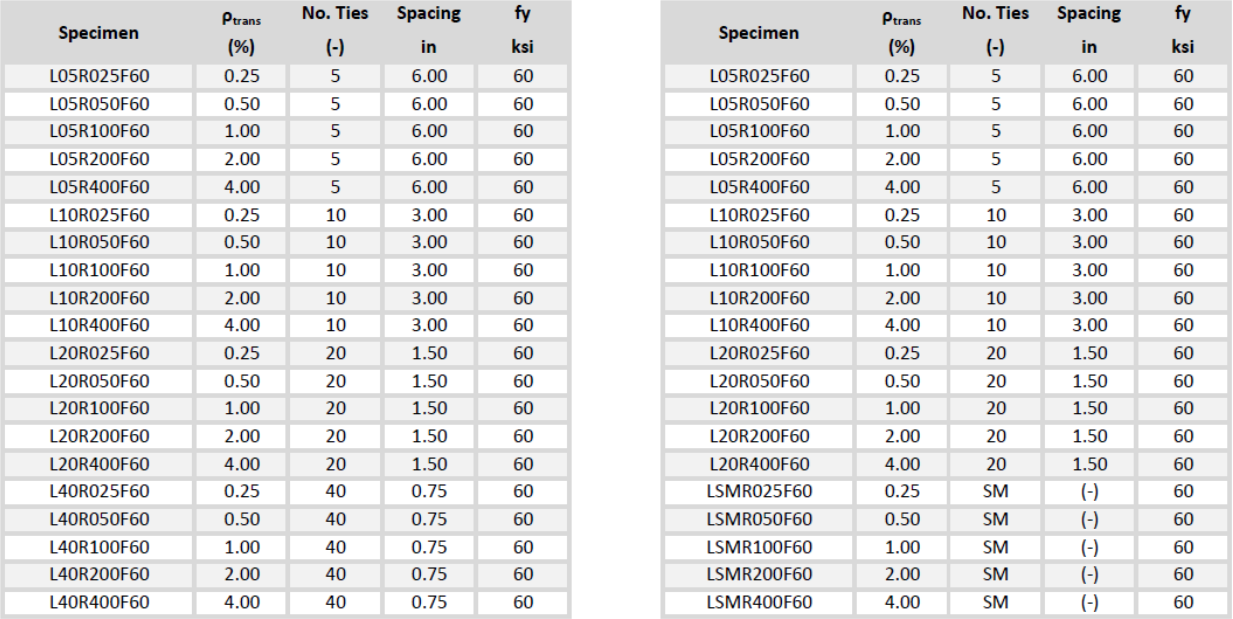

Specimen	ρ_{trans}	No. Ties	Spacing	fy
	(%)	(-)	in	ksi
L05R025F60	0.25	5	6.00	60
L05R050F60	0.50	5	6.00	60
L05R100F60	1.00	5	6.00	60
L05R200F60	2.00	5	6.00	60
L05R400F60	4.00	5	6.00	60
L10R025F60	0.25	10	3.00	60
L10R050F60	0.50	10	3.00	60
L10R100F60	1.00	10	3.00	60
L10R200F60	2.00	10	3.00	60
L10R400F60	4.00	10	3.00	60
L20R025F60	0.25	20	1.50	60
L20R050F60	0.50	20	1.50	60
L20R100F60	1.00	20	1.50	60
L20R200F60	2.00	20	1.50	60
L20R400F60	4.00	20	1.50	60
L40R025F60	0.25	40	0.75	60
L40R050F60	0.50	40	0.75	60
L40R100F60	1.00	40	0.75	60
L40R200F60	2.00	40	0.75	60
L40R400F60	4.00	40	0.75	60

Specimen	ρ_{trans}	No. Ties	Spacing	fy
	(%)	(-)	in	ksi
L05R025F60	0.25	5	6.00	60
L05R050F60	0.50	5	6.00	60
L05R100F60	1.00	5	6.00	60
L05R200F60	2.00	5	6.00	60
L05R400F60	4.00	5	6.00	60
L10R025F60	0.25	10	3.00	60
L10R050F60	0.50	10	3.00	60
L10R100F60	1.00	10	3.00	60
L10R200F60	2.00	10	3.00	60
L10R400F60	4.00	10	3.00	60
L20R025F60	0.25	20	1.50	60
L20R050F60	0.50	20	1.50	60
L20R100F60	1.00	20	1.50	60
L20R200F60	2.00	20	1.50	60
L20R400F60	4.00	20	1.50	60
LSMR025F60	0.25	SM	(-)	60
LSMR050F60	0.50	SM	(-)	60
LSMR100F60	1.00	SM	(-)	60
LSMR200F60	2.00	SM	(-)	60
LSMR400F60	4.00	SM	(-)	60

A short analysis of the impact of yield strength was also conducted. These tests are shown in Table C.4.

Table C.4 – Test matrix for verifying material strengths

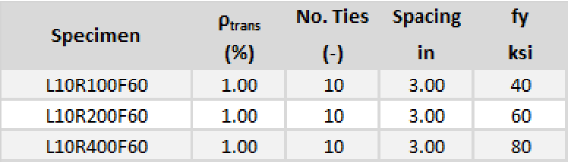

Specimen	ρ_{trans}	No. Ties	Spacing	fy
	(%)	(-)	in	ksi
L10R100F60	1.00	10	3.00	40
L10R200F60	1.00	10	3.00	60
L10R400F60	1.00	10	3.00	80

The objective of these tests was to determine the ability of the software to model confinement, as well as determine what the impacts of tie size, spacing, and material strength. By evaluating the model with each parameter investigated separately, it was possible to discern the program's interpretation of each variable.

The model validation will consist of one FE model compared to the experimental results of specimen CS5.

ABAQUS

Figures C.5-C.8 show load-displacement curves, with each plots representing a different tie spacing. The load is normalized by f'$_c$A$_g$, and the displacement is normalized by the specimen height.

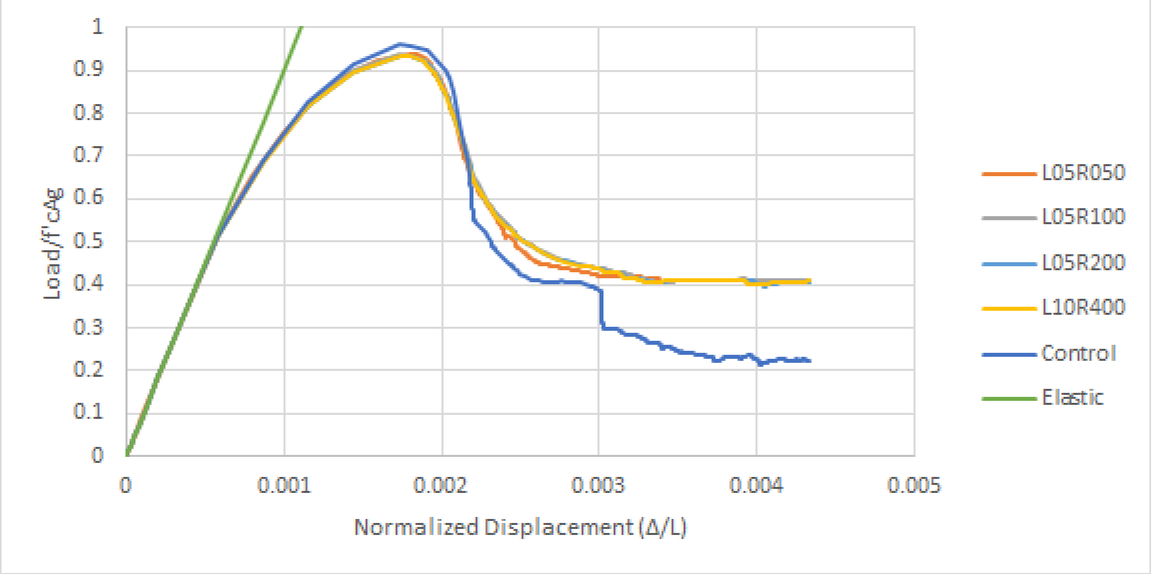

Figure C.5 – Load-displacement response for 6" tie spacing (L05, ABAQUS)

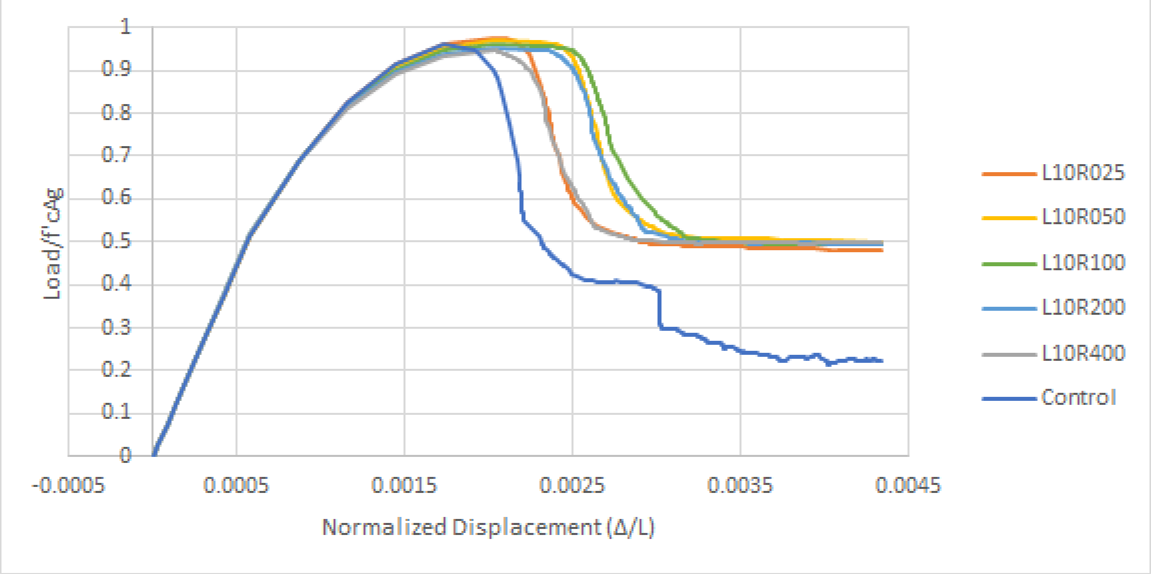

Figure C.6 – Load-displacement response for 3" tie spacing (L10, ABAQUS)

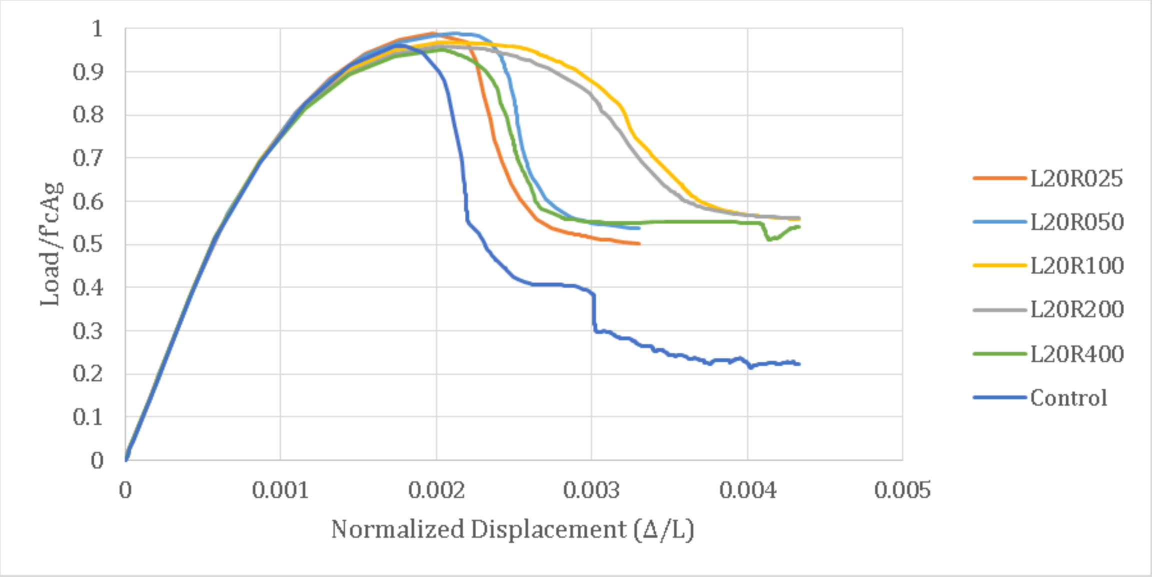

Figure C.7 – Load-displacement response for 1.5" tie spacing (L20, ABAQUS)

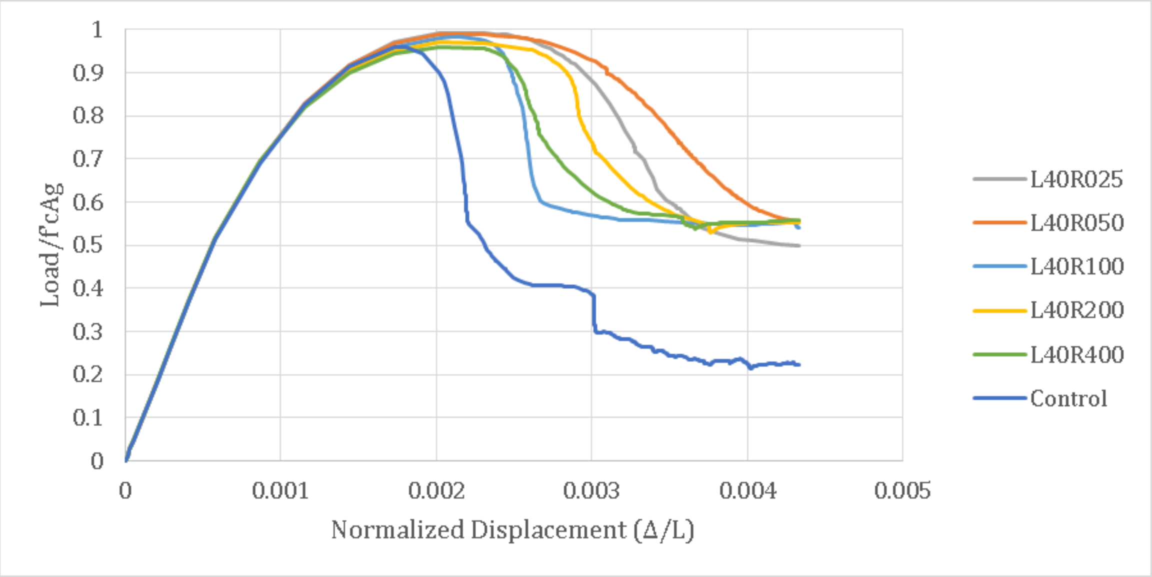

Figure C.8 – Load-displacement response for 0.75" tie spacing (L40, ABAQUS)

<u>ATENA</u>

Figures C.9-C.12 show the load-displacement results for analyses in ATENA 3D in the same fashion as the previous section.

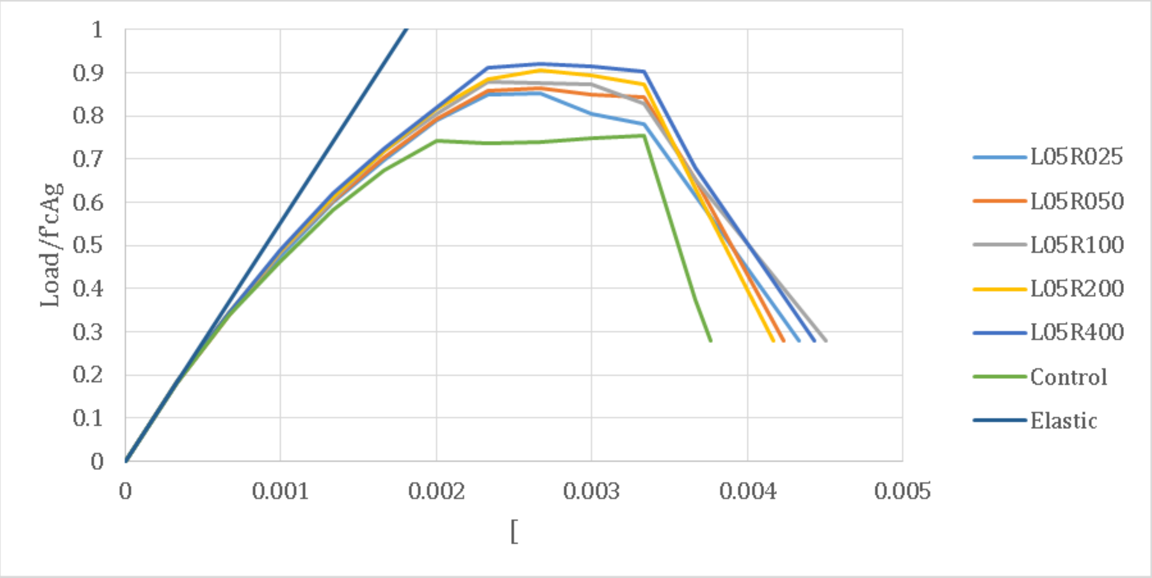

Figure C.9 – Load-displacement response for 6" tie spacing (L05, ATENA)

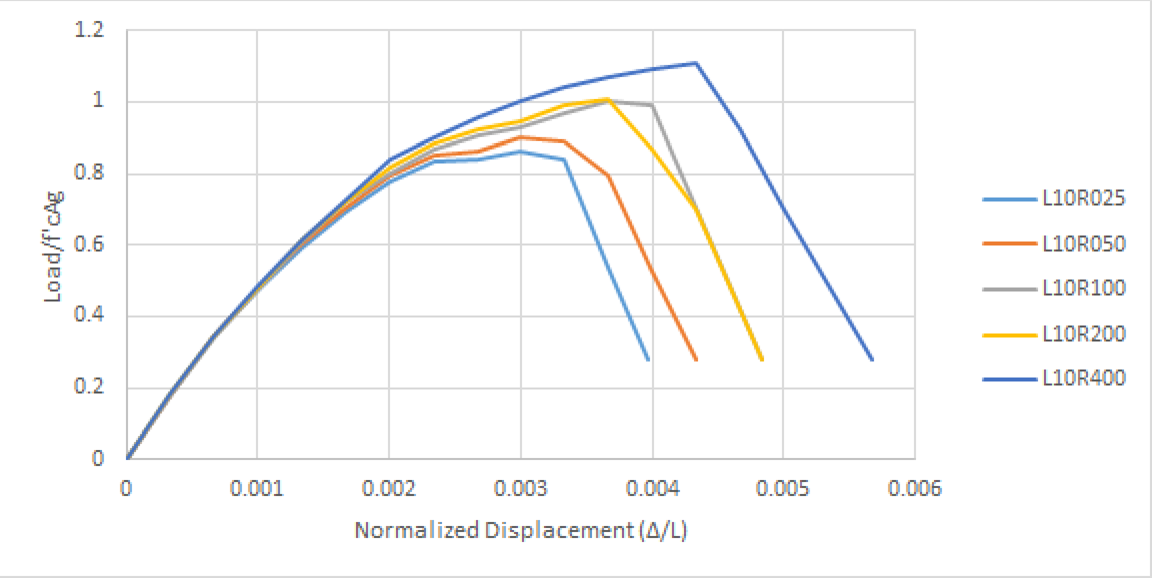

Figure C.10 – Load-displacement response for 3" tie spacing (L10, ATENA)

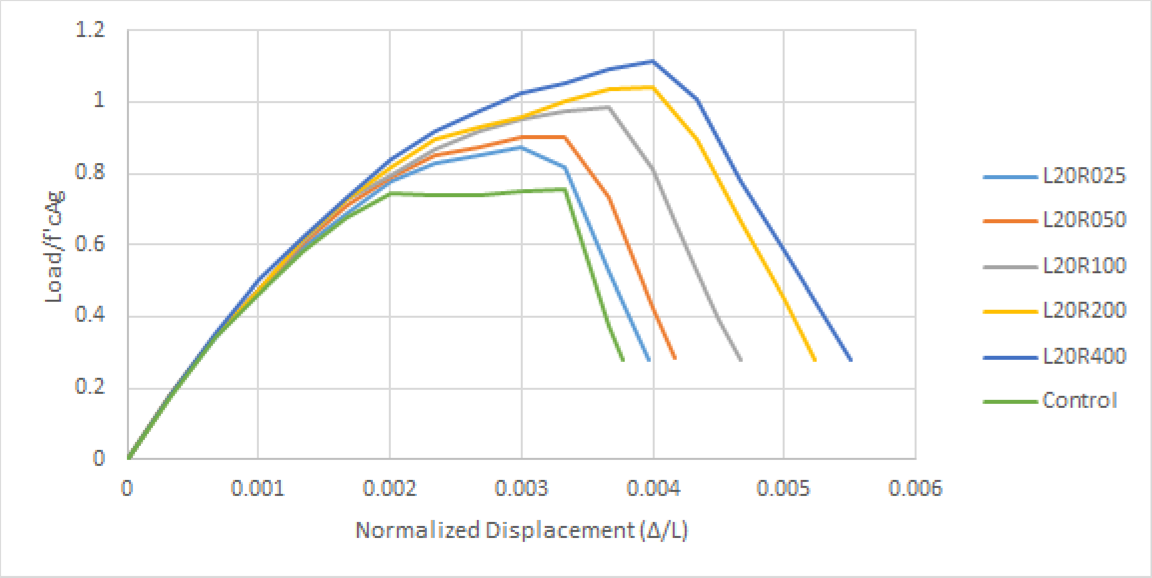

Figure C.11 – Load-displacement response for 1.5” tie spacing (L20, ATENA)

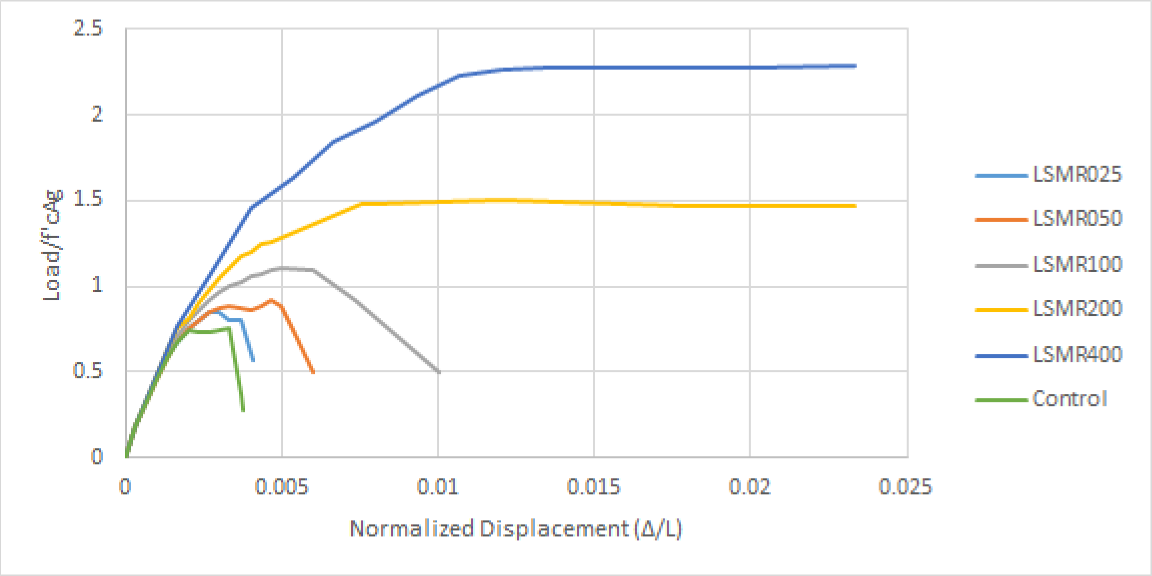

Figure C.12 – Load-displacement response for smeared reinforcement (LSM, ATENA)

<u>Software Evaluation and Discussion</u>

There were a few general issues with the ABAQUS analyses. First, there was very little change in peak stress recorded with different levels and layouts of reinforcement. This is in direct opposition to experimental data and all established confinement models. With greater reinforcement, there should be a greater level of pressure resisting the deformation of the specimen. The fact that the peak value is essentially f’$_c$ for all models shows that there is a real issue with how ABAQUS is treating confinement.

Though it would be expected to see greater levels of reinforcement also result in increased ductility (i.e., greater ultimate strain), actual behavior peaked at 1-2% reinforcement and decreased beyond 4%. Intuitively, this does not make sense. What appears to be happening is that the greater tie area increases the tie stiffness, which results in more localized deformation occurring around the tie. Fewer ties are thus engaged with extreme levels of transverse reinforcement.

The impact of layout and tie spacing was a little more straightforward, though still not entirely intuitive. At low levels of transverse reinforcement (0.5%), the change with tie spacing was significant. As shown in Figures C.13-C.14, the impact of confinement increased as the tie spacing decreased; however, at a higher reinforcement ratio (2.0%), the ultimate strain reached a peak at L20 (1.5" spacing) and decreased at L40 (0.75" spacing). It is clear from the analysis that the spacing of the bars is significant, but the behavior is somewhat surprising as a closer spacing yielded greater results for all other analyses.

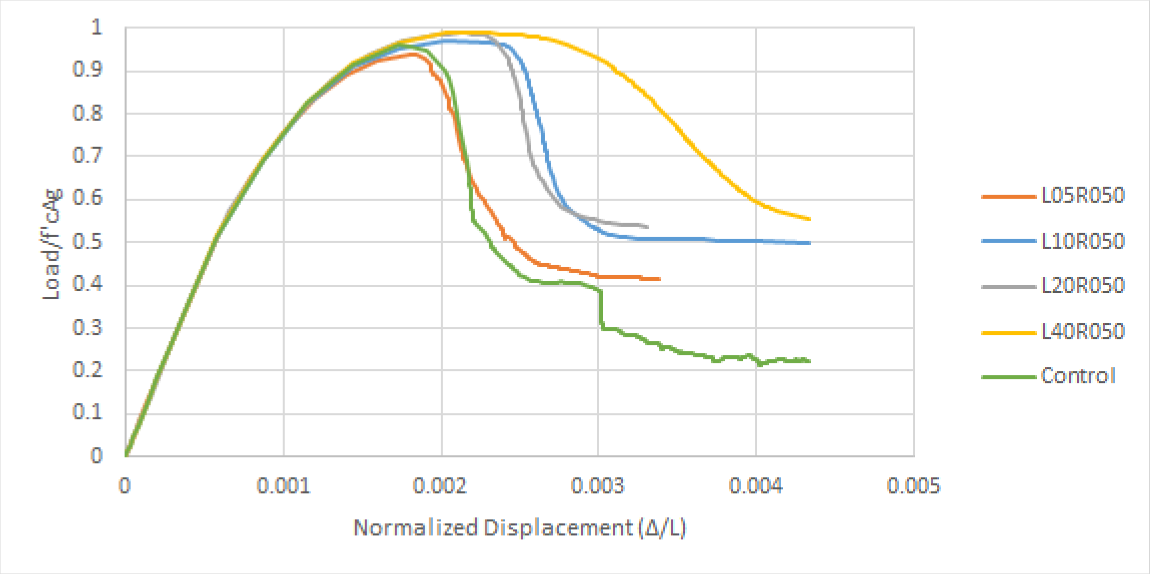

Figure C.13 – Load-displacement plot at different tie spacings (ABAQUS, ρ=0.5%)

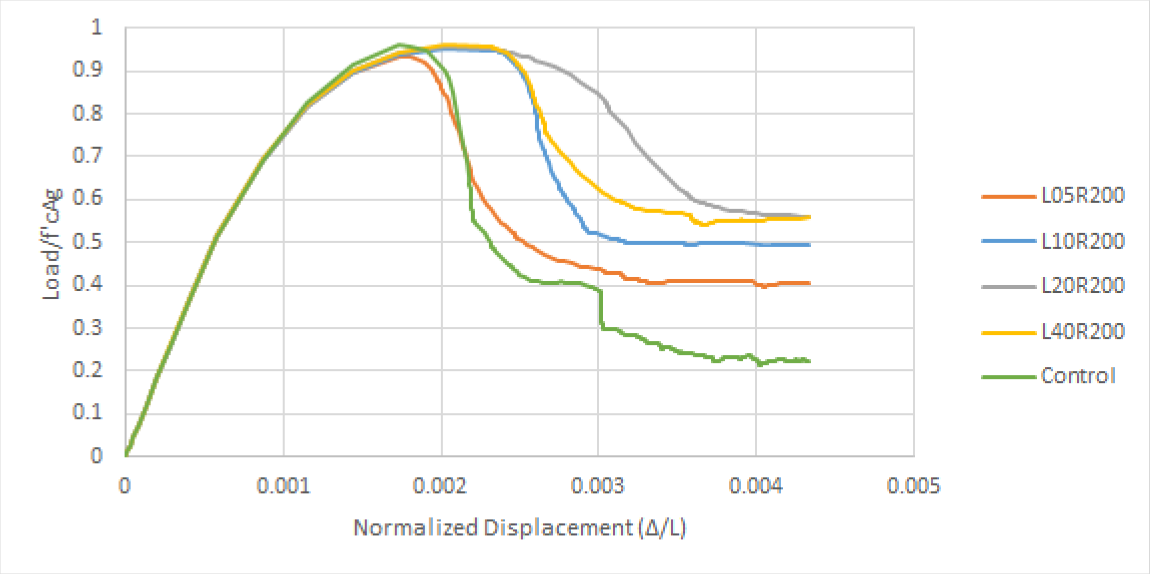

Figure C.14 – Load-displacement plot at different tie spacings (ABAQUS, ρ=2.0%)

Figure C.15 shows that, as expected, the yield strength of the ties does affect behavior. Keeping the reinforcement ratio constant at 1.0% and changing the material stress and bar area, it was possible to compare ties of 40, 60, and 80 ksi. The 80 ksi ties have the same tensile capacity at yield, but are less stiff and therefore less able to provide confinement.

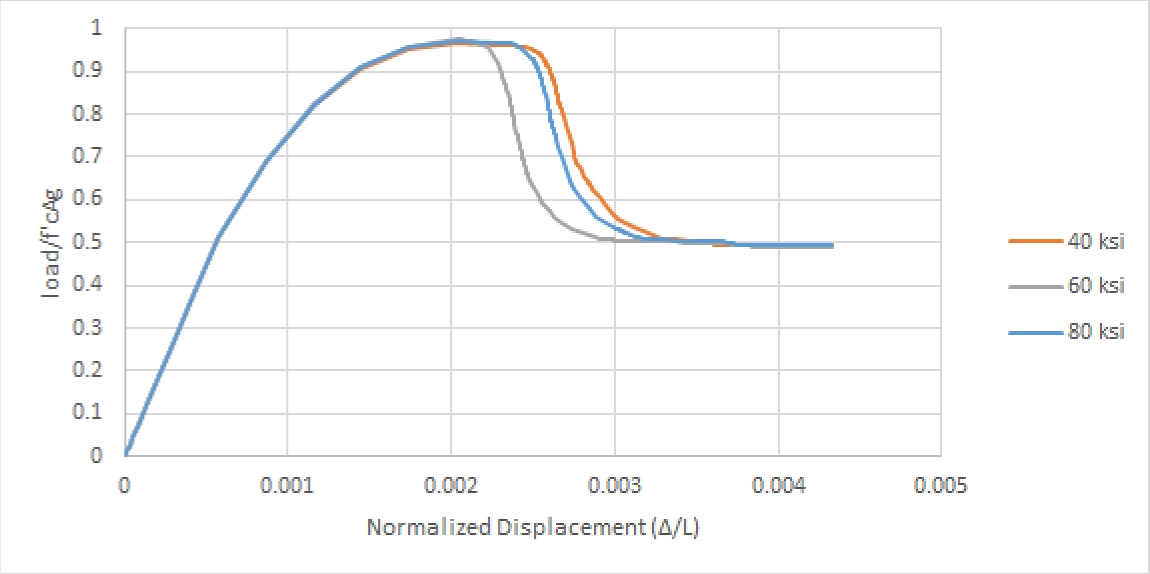

Figure C.15 – Load-displacement plots at different steel yield stress (ABAQUS, ρ=1.0%)

ATENA

The ATENA analyses generally yielded better results for discrete transverse modeling. In all cases, Figure C.9-C.12 show that increased reinforcement resulted in both improved peak stress and ultimate compressive strain; it's also of interest that the model predicts a capacity of less than f'_cA_g for the unreinforced section. As with ABAQUS, the confinement provides a very small effect at the large tie spacing of 6"; however, at smaller tie spacings that are more typical in structural walls, the transverse reinforcement affects the results as expected, with more reinforcement resulting in greater confinement.

Figures C.16-C.17 show the impact of layout on the analysis. At low levels of reinforcement, the layout is mostly significant, but it is influential at greater reinforcement ratios.

ATENA offers the capacity for a "smeared reinforcement" across any concrete element. The issue shown in this analysis is that it does not appear to correctly model post-peak behavior, as the concrete specimen does not lose strength at high displacements. While the initial stiffness and peak stress are reasonable, the ultimate strain predicted by the model does not conform to typical concrete compressive behavior.

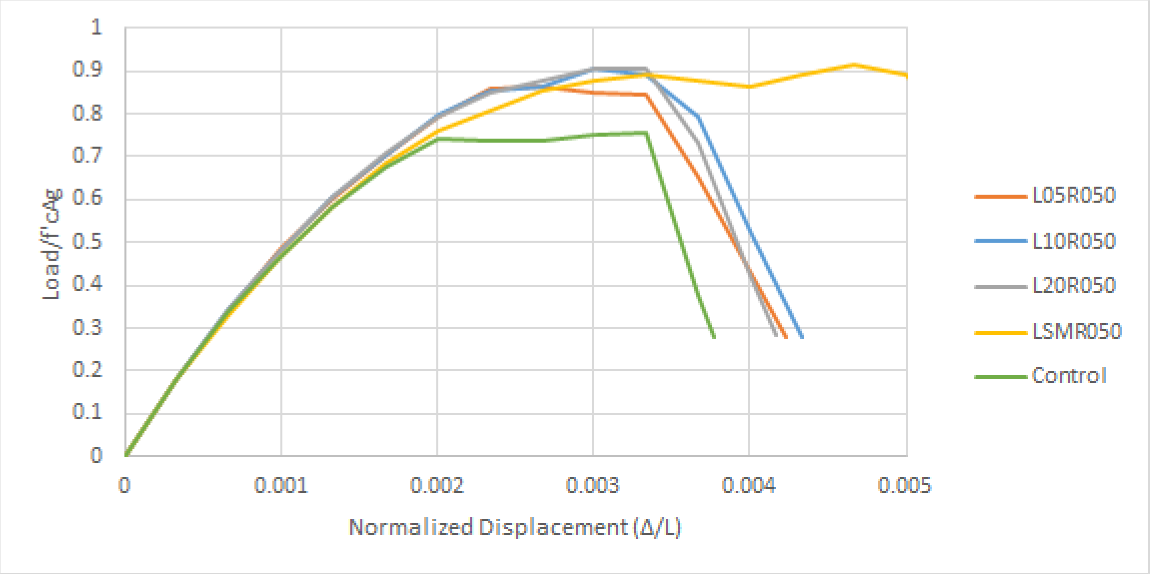

Figure C.16 – Load-displacement plots at different tie spacings (ATENA, ρ=0.5%)

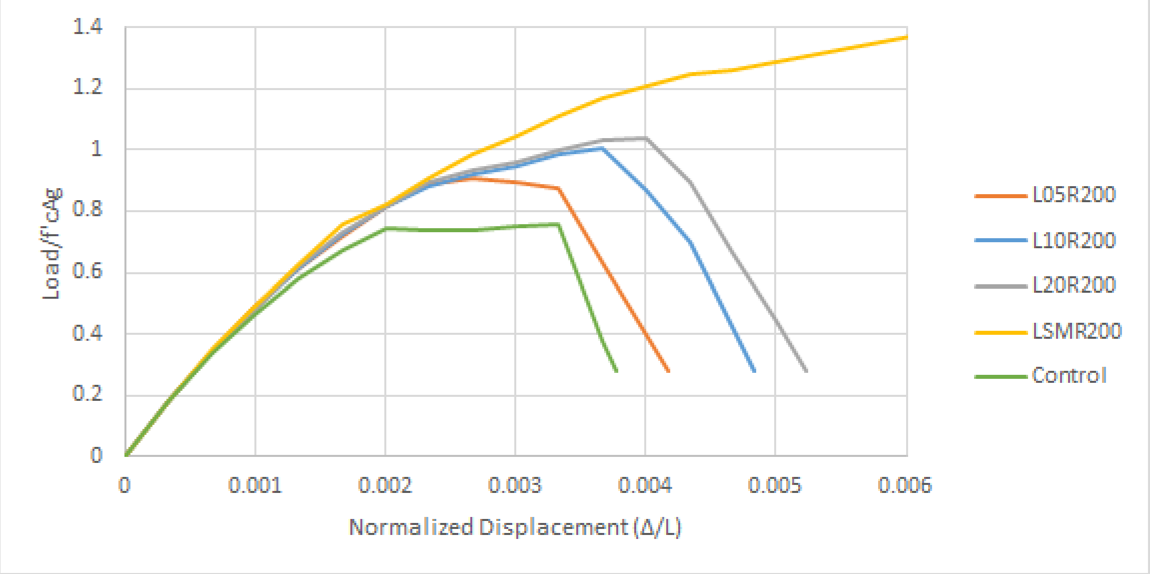

Figure C.17 – Load-displacement plots at different tie spacings (ATENA, ρ=2.0%)

Prism Results and Discussion

As the ABAQUS model did not fully model the expected behavior of the transverse reinforcement, ATENA will be used to model the prism. Reinforcement was explicitly modeled in ATENA due to the issues with smeared reinforcement discussed earlier in this report. Figure C.18 plots the ATENA model prediction against the CS5 experimental data.

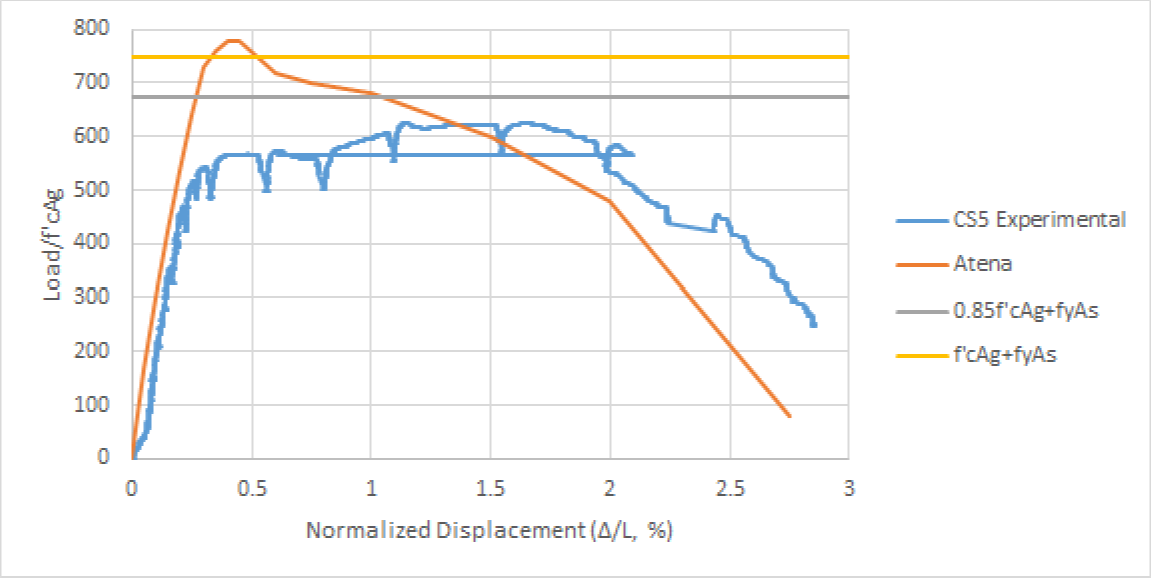

Figure C.18 – Load-displacement plot for ATENA model and CS5 experimental data

This result overestimates the peak strength. A possible explanation for this is that the cover concrete spalled early on in the experiment, and the model failed to capture this behavior to the full extent. As it was reported that the compression steel had yielded at the peak strength of the prism, it is possible to approximate the approximate stress of the concrete. If it is assumed that the cover is acting with the core, then the average compressive stress is 3.1 ksi, or 0.75f'_cA_g. If the core acts alone and the cover concrete is fully ignored, this becomes 0.99f'_cA_g. The model predicts a peak concrete stress of 1.07f'_cA_g, assuming that the full section, including cover, is acting in compression and that the compression reinforcement has yielded. These results are not entirely dissimilar, and may be the reason for the large difference in peak strengths predicted by the model.

Another potential issue is that the damage did not occur correctly in the model because of the assumption of material homogeneity. In an experiment, issues with consolidation and mixing can leave concentrated areas of the model as potential weak points in the analysis. As shown in Figure C.19, the damage for the walls occurred at the top. The damage pattern for the wall, when filtering out small cracks as in Figure 20L, tends to agree that the most damage occurs at the top. However, the cracked cover concrete at the top still retains some strength, which is different form the experimental case, where the impact of the cover concrete was likely minimal.

Despite the difference in peak stress, there are some similarities in the experimental and model data. They both soften at similar rates, with the difference in displacement at peak strength likely being due to the difference in cover concrete at the top of the specimen.

The promise of this analysis is that it shows that the impact of transverse reinforcement detailing can be determined through this kind of model. The extension of this work is to look at the impact of cyclic loading and ACI-defined detailing standards on the effective concrete crushing energy provided by transverse reinforcement.

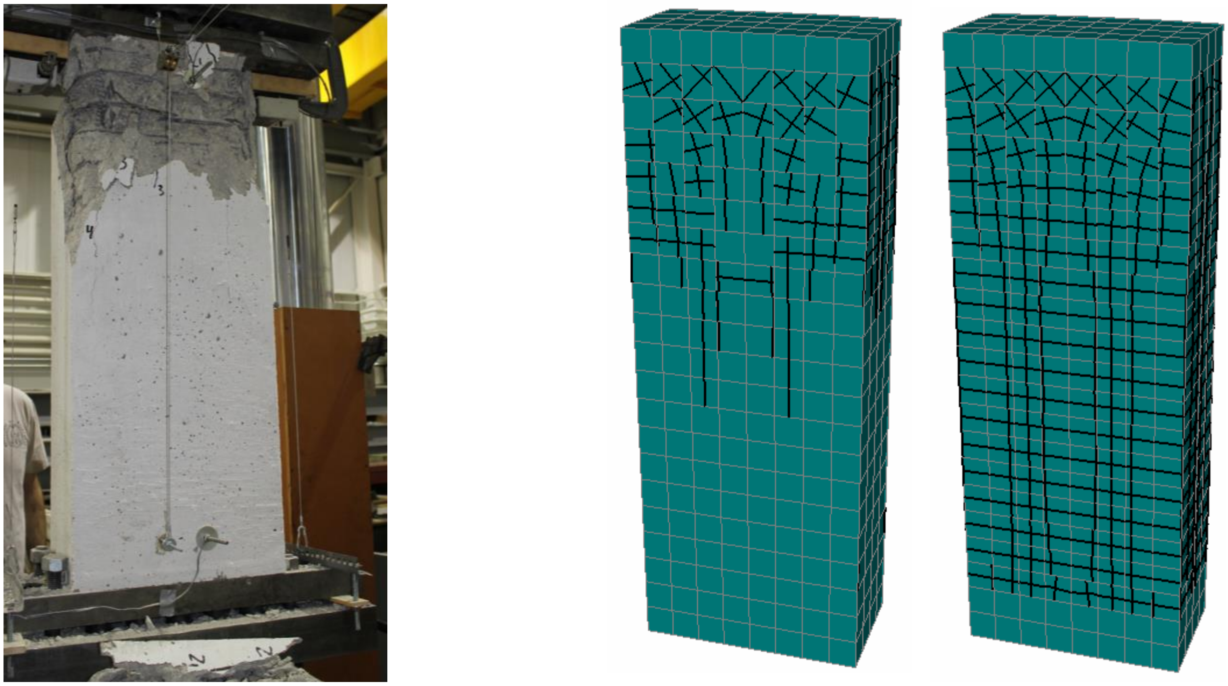

Figure C.19 – CS5 damage at 0.7% drift, experimental (L) and modeled (R)

Critique

The results of the parameter study are informative, but there are assumptions here which should likely be investigated in further work. This analysis focused on global behavior, but there may be some issue with the tie/concrete interface at a local level. With greater spacing, there was very little impact of confinement, but this may be due to a mesh sensitivity issue, where the system fails due to excessive deformation of an element which does not have any direct connection to transverse reinforcement. In a brief look at this issue in ATENA, the results did not seem to change appreciably with different element sizes; however, this is far from an exhaustive study and this could prove to be influential. The results in ABAQUS did seem to be affected significantly by the ratio of element size to tie spacing. It may also be valuable to perform modeling where the tie is not connected to the concrete to assess the impact of the concrete-steel interaction.

Another potential topic for a future study is the impact of confinement on singular elements, rather than systems. This particular work assumes that the impact of confinement is better understood in system that resembles a structural wall boundary element, but the local behavior of a single element could yield different results, and this would increase understanding of the software's capacity. This could also help in understanding why the ATENA model predicted such low values of peak stress for the lesser-confined models.

Perhaps the biggest assumption of this analysis was in relation to the reinforcement. As noted earlier, the concrete was assumed to have a perfect connection with the ties, and this may be inaccurate. In the prism test, it's assumed that the bars act in a perfectly vertical plane with no 3D behavior, but it is likely that buckling causes some of the loss in strength, and that behavior is not considered in this analysis.

Regarding the prism test, behavior differs in that the experimental cover concrete spalled at the stop, while the modeled prism retained some residual strength. It is possible that a better model be developed between the core and cover concrete which somehow takes into account the tendency of the cover concrete to rapidly lose strength.

Conclusion

It appears that the ATENA model is better able to account for explicit transverse reinforcement than ABAQUS. There are still aspects remaining for investigation in this software package, mainly regarding the smeared reinforcement and attempting to understand the dramatically over-estimated results predicted by this model.

Going forward, the main takeaway from the prism study is the need to distinguish between cover and confined concrete in these models. Further analyses of these prisms should be conducted, but it does seem that the lack of contribution from cover concrete to peak stress is the reason for the discrepancy in the results, and being able to properly model this would be a large step toward understanding the behavior of confined concrete structures.

References

ACI, *Building Code Requirements for Structural Concrete (ACI 318-11) and Commentary*(ACI 318-11), American Concrete Institute, Committee 318, Farmington Hills, MI, 2011.

ATC-104 NIST Structural Wall Project. Unpublished raw data, *National Institute of Standards and Technology*. 2014.

J. Mander, M. Priestley, and R. Park, “Observed stress-strain behavior of confined concrete,” *ASCE Journal of Structural Engineering*, vol. 114, no. 8, pp. 1827–1849, 1988.

M. Saatcioglu and S. Razvi, “Strength and ductility of confined concrete,” *ASCE Journal of Structural Engineering*, vol. 81, no. 6, pp. 1590–1607, 1992.

Appendix D WALL MODELING IN OPENSEES

Prior to development of the FE model in ATENA, preliminary studies were conducted in OpenSees using the Pugh (2012) regularized distributed-plasticity method. This allowed for investigation of key parameters in wall design, primarily axial load ratio, established as a key parameter by Birely (2012). The ultimate findings were similar to what was eventually determined in ATENA: axial load ratio has an impact on the determination of failure mode between CB and BR, but does not have a significant impact on wall deformation capacity. These findings helped to motivate the development of the ATENA FE model as it was necessary to investigate the shear demand, a parameter which was not captured by a PSRP model such as the one used below.

Model Background

Numerical simulation of the shear walls was conducted in OpenSees utilizing fiber-type distributed-plasticity beam column elements and following the method developed by Pugh (2012). As shown in Pugh (2012), this model is able to predict wall behavior with both low computational demand and mesh sensitivity. It was developed through a study of 21 planar wall experimental tests, using this data to find an appropriate regularization scheme through which wall behavior could be accurately predicted.

The model employs force-based beam column elements (force-BeamColumn). Each wall was meshed as a cantilever with a fixed base and a series of connected beam column elements. Self-weight and applied axial load were applied as one concentrated load at the top of the specimen. Moment was accounted for by the method shown in Figure D.1.

Or

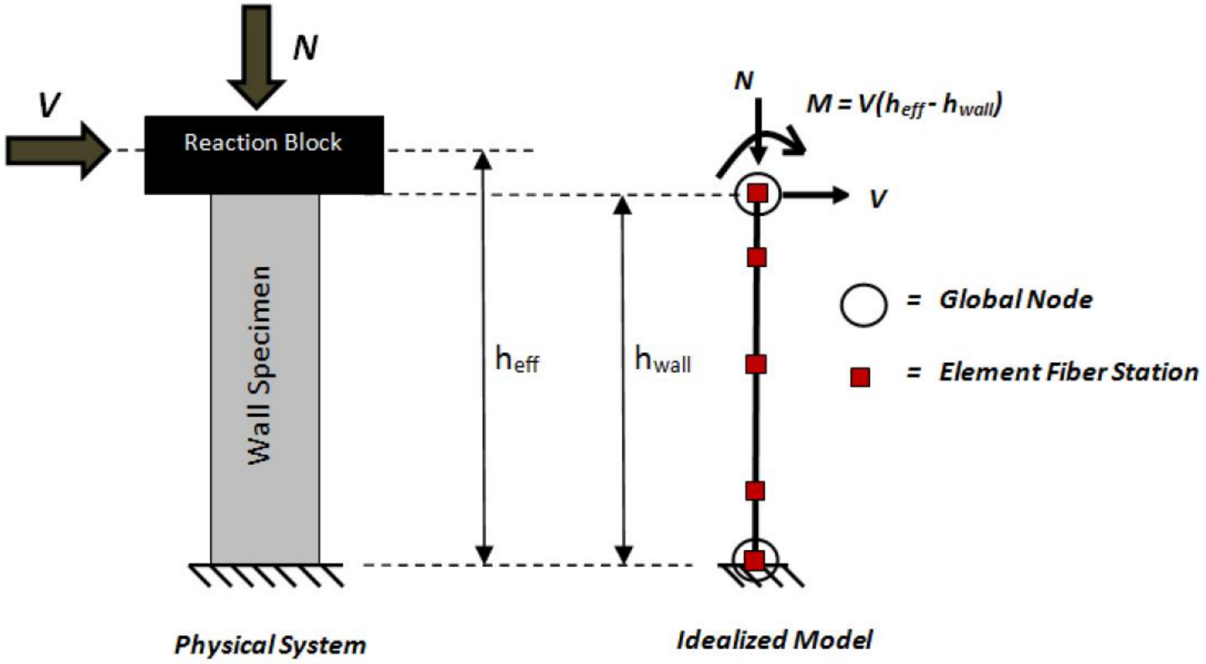

Figure D.1 – Idealized OpenSees Model (Pugh,2012)

Concrete was modeled using the Concrete02 material in OpenSees, which is based on the Honegstad stress-strain curve and allows for linear tension stiffening. A linear effective shear stiffness model was added to the flexural section through the 'section aggregator' command. Steel is modeled as bi-linear using Steel02 in OpenSees. Material regularization was also utilized to remove mesh sensitivity. Though the basic model was able to accurately predict specimen strength, drift was sensitive to the number of elements used for the analysis.

Material regularization was implemented by altering the post-peak response of each material according to the fiber section characteristic length. By changing the steel and concrete in this manner, it is possible to achieve objective response and achieve the same findings when using different numbers of elements in analysis. Figure D.2 shows the impact of regularization on the model. Shown in Figure D.3 is a verification of the model, with the predicted behavior plotted against the experimental data.

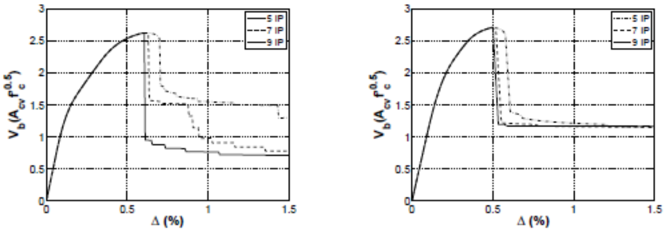

(a) WSH4 (Basic) (b) OhWR0 (Basic)

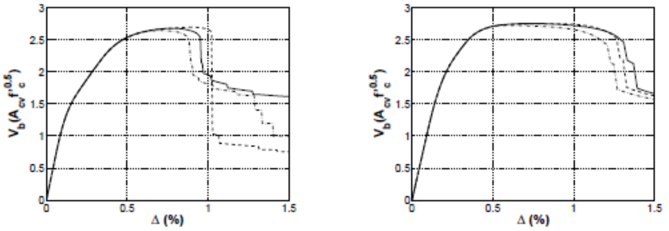

(c) WSH4 (Partial Reg.) (d) OhWR0 (Partial Reg.)

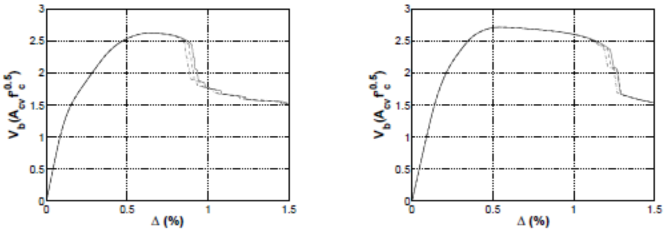

(e) WSH4 (Full Reg.) (f) OhWR0 (Full Reg.)

Figure D.2 – Regularization Response Comparison (Pugh, 2012)

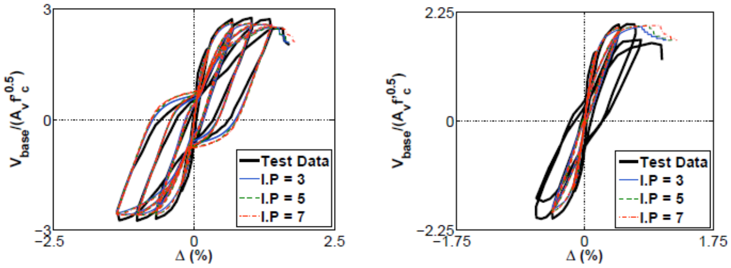

(a) CB Failure (WSH4)

(b) Rupture Failure (WSH1)

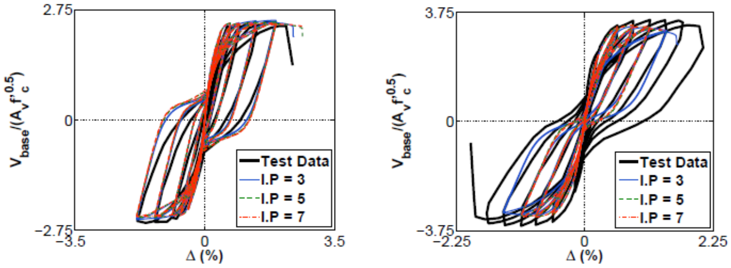

(c) BR Failure (RW1)

(d) CB Failure - High Shear Demand (WSH6)

Figure D.3 – Specimen Load Displacement Curves (Pugh, 2012)

Implementation

The OpenSees model was then utilized to study the impact of different parameters on shear wall response and provide a guideline for future test specimens of interest. Two specimens were studied and compared against the same 21-wall data set used to create the model. The key parameters studied were reinforcement ratio in both the boundary element and web and the axial load ratio. These studies helped determine what experimental tests would provide the most insight into wall behavior.

Shown in Figure D.4 is a typical set of hysteretic plots for a typical wall that is subjected to different axial load ratios. The most obvious result of these analyses was that axial load ratio appears to determine the failure mode of the shear walls; however, the data in Figure D.6 does not show a significant relationship between axial load ratio and deformation capacity. The model did not show a significant influence of reinforcement ratio in either of these areas.

When the cover concrete reached the ACI limit of 0.003 in/in compressive strain, the strain present in the boundary element reinforcement, ε_t, correlated strongly with the axial load ratio, as shown in Figure 4. The relationship between ε_t and the failure mode is also of interest, as at values above 0.02 we tend to see failures in rupture of the boundary element reinforcement. The three specimens which exhibit three tension rupture failures at high axial load ratios in Figure D.5 all utilize steel which featured a very low ultimate strain. It would be advantageous to conduct further testing to see if these failures were a result of this low material property.

In summary:

- Axial load ratio appears to have a strong impact in the determination of failure mode between CB and BR.
- There does not appear to be a strong relationship between axial load ratio and ultimate drift, as plotted in Figure D.6.

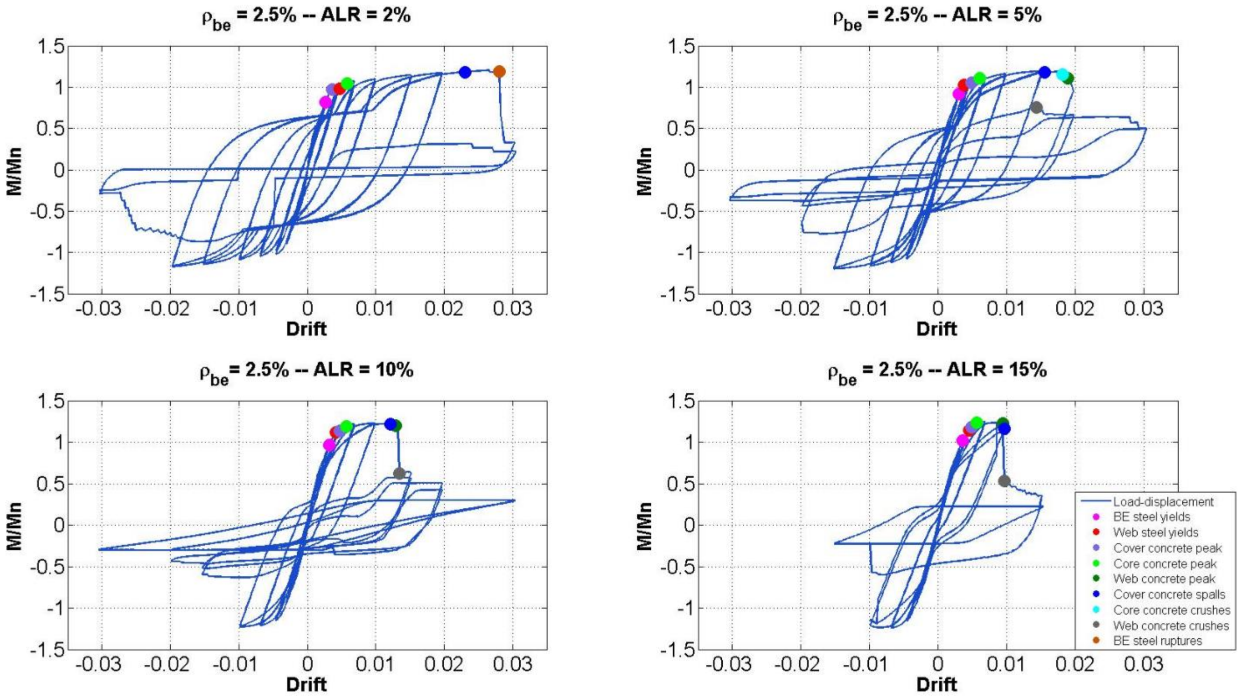
ρ_{be} = 2.5% -- ALR = 2%

ρ_{be} = 2.5% -- ALR = 5%

ρ_{be} = 2.5% -- ALR = 10%

ρ_{be} = 2.5% -- ALR = 15%

Figure D.4 – Predicted Load Displacement Response of TSW01 at Various ALR

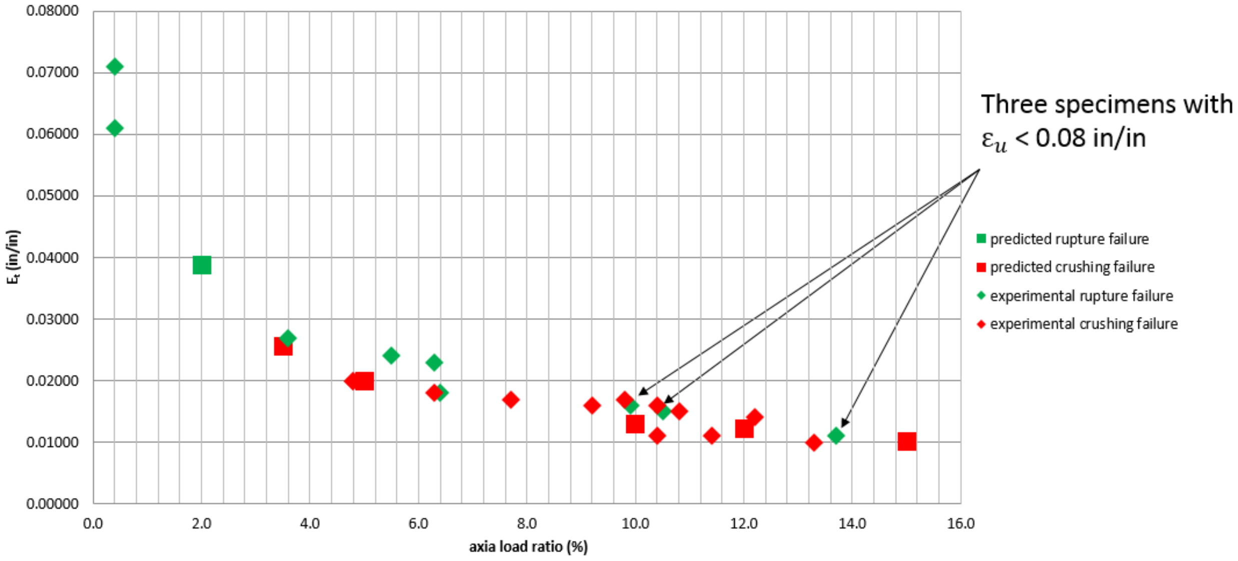
Three specimens with ε_u < 0.08 in/in

Figure D.5 – Relationship between Axial Load Ratio and Steel Strain at ACI Compressive Strain Limit

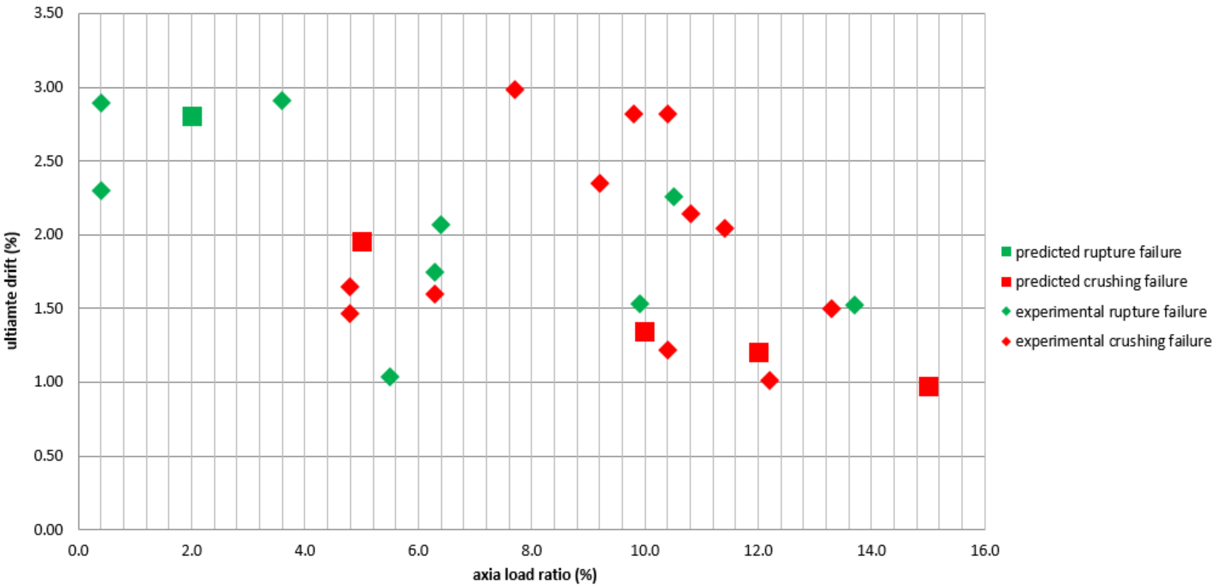

Figure D.6 – Plot of Ultimate Drift as a Function of Axial Load Ratio

Recommendations

For future testing, it would be useful to look at the impact of axial load ratio on different walls. By conducting analyses on walls with similar aspect ratios, reinforcement ratios, and material properties, it would be possible to better determine if there is a correlation between axial load ratio, ε_t, and failure mode. It would also be useful to hold the axial load ratio constant and test with different boundary element reinforcement ratios to see if there is a significant change in either ultimate drift or failure mode.